Phase Separation in Binary Phospholipid Vesicles Studied Using Fluorescence Microscopy Techniques

Paul Beales

Thesis submitted for the degree of Doctor of Philosophy

The University of Edinburgh

2005

Abstract

Lipids are naturally occurring, water insoluble molecules that make up the major constituents of the cell membranes of living organisms. Lipids have a hydrophilic (water-loving) head group and a hydrophobic (water-hating) tail or tails. The amphiphilic nature of lipid molecules causes them to spontaneously self-assemble into structures in aqueous solution such that their hydrophobic portions are hidden from, and their hydrophilic heads are exposed to, the aqueous environment. The class of lipids of interest in this thesis are known as *phospholipids*. Phospholipids form bilayer membranes on contact with water which close up into spherical vesicles.

In this thesis I study Giant Unilamellar Vesicles (GUVs) consisting of a mixture of two phospholipids with identical hydrophobic tails but different hydrophilic head groups. GUVs are between 5 and 200 microns in diameter so can be studied using optical observation techniques. This size range and membrane geometry is also comparable to that of the cell membranes of living organisms, hence the study of simple lipid model membrane systems in the form of GUVs may give insight into any heterogeneous structure of living membranes such as the possible existence of '*lipid rafts*'. Improved understanding of GUVs with only a small number of lipid components could also be of use for *in vivo* drug delivery systems where drugs are transported in encapsulated form to a target site where they are released.

The binary lipid GUVs were studied by fluorescence multiphoton and confocal microscopy, techniques which allow the collection of digital images in the form of thin, in-focus sections through the sample. This results in clear, high resolution images of the GUVs. Amphiphilic fluorophores, which preferentially partition between lipid phases, were added to the lipids in trace amounts to enable the detection of domains of different lipid phases in the membrane of the vesicles. GUVs were obtained by electroformation in formation chambers which were designed and constructed especially for this project. Domain formation was observed as the vesicles were slowly cooled from the high temperature fluid (L_α) phase through a region of gel-fluid phase coexistence.

In samples consisting of mixtures of DPPC and DPPE lipids, domain growth was observed not to follow the expected equilibrium mole fractions for each phase as predicted by the lever rule using phase diagrams from the published literature. The very low diffusion constant of the DPPE-rich gel domains which formed resulted in gel domains being unable to alter their composition, as required by the equilibrium phase diagram, at cooling rates as slow as between 0.1 and 0.2 °C/min. This meant that the fluid and gel phases could not remain in equilibrium with each other and so the fluid phase behaved like an isolated system, phase separating on further cooling in a manner which resulted in a non-equilibrium 'tree-ring' growth of the gel

domains. Observed mole fractions of gel phase as a function of temperature were in close agreement with this 'tree-ring' model.

The morphology of the observed gel domains was seen to reflect the molecular structure of the gel phase formed. The DPPE-rich L_{β} gel phase of DPPC/DPPE mixtures resulted in domains which lack long-range molecular ordering, giving rise to domains that are isotropic in the plane of the membrane on micron length scales. In DPPC/DPPS membrane systems, the gel that formed was of the $L_{\beta'}$ type which has long-range (of order microns) orthorhombic packing; the resultant domains showed straight edges and sharp corners (under optical resolution) and were often near-hexagonal in shape. This was also compared with images obtained by other researchers in the group on the DLPC/DPPC system where stripe domains of the rippled gel ($P_{\beta'}$) are observed, reflecting its directional anisotropy in the two-dimensional membrane geometry and its long-range order of molecular packing.

Further discussion is given to the movement and interaction of the inherently circular domains in the DPPC/DPPE system as well as a brief examination of phenomena in single component DPPC and DPPE vesicles. GUVs containing DPPA and DPPG lipids are briefly considered. I also discuss detection of phenomena such as membrane adhesion and vesicle lysis, offering qualitative explanations for the observed behaviour.

Acknowledgements

I would like to thank my supervisors, Professor Wilson Poon and Dr Stefan Egelhaaf, for their enthusiasm, ideas and encouragement during this project.

I would also like to thank Vernita Gordon for enthusiastic discussions and the sharing of ideas between both our research. It was invaluable to be able to bounce silly ideas off her.

I am also grateful to the technicians: Andrew Downie for constructing the electroformation chambers and discussions on practical aspects of their design, Andrew Garrie for making the ITO-coated plates and discussions on choices of adhesives, and Hugh Vass for discussions on temperature control.

Thanks also go to COSMIC for the allocation of time on the confocal microscope. Jochen Arlt and Andrew Garrie provided technical support.

Many thanks to all those with whom I have had discussions with on various aspects of my work. These include Mike Cates, Peter Olmsted, Fred Mackintosh, Helmut Möhwald, Didier Roux, Reinhard Lipowsky, Richard Templer and all the members of the so-called 'Biophysics Breakfast Club'.

Thank you to Lorna Dougan for encouragement, motivation and being there when I've needed someone to talk (or rant!) to, also for providing fun and distraction when it has been needed to keep me sane.

Finally, the largest proportion of my gratitude must go to my parents for supporting me throughout my entire education both financially and by encouragement.

Contents

Chapter 1

Introduction

The main constituents of the cell membranes of living organisms are lipids. The amphiphilic nature of lipids causes them to self-assemble into structures when in aqueous solution. Living membranes are one such aggregate in the form of a lipid bilayer which acts as a solvent for membrane proteins to diffuse in (*the fluid mosaic model* [1]). In recent years there has been experimental evidence to suggest the existence of heterogeneities in the fluid membranes of living organisms, termed *'lipid rafts'*, which may play an important role in cellular processes including cell signalling, adhesion and endocytosis. The membranes of living organisms are made up of around 800 to 1000 different lipid species and so are too complex to be studied in detail by physicists. However, simpler model membrane systems with only a few lipid components can be studied to gain insight into the biophysics of cell membranes.

In this thesis I study the phase separation of binary lipid membranes in the form of giant unilamellar vesicles (GUVs), spherical bilayers between 5 and 200 μm in diameter: a similar size range to living cells. Fluorescent lipids are used to label domains of different lipid phases so that phase separation within the membrane can be observed using fluorescence multiphoton or confocal microscopy. Fluorescence microscopy has already been shown to be a valuable tool for the study of micron-sized heterogeneities in the lipid membranes of GUVs [2–12]. In these binary vesicle systems, a solid-like phase known as a gel phase forms within the fluid membrane on cooling from a homogeneous fluid state. Aside from any biological implications of my research, this project provides the opportunity to study the interesting physical phenomena

that occur during solid-liquid phase separation in a quasi-two-dimensional system.

1.1 Thesis Layout

Chapter 2 of my thesis gives some background on the physical chemistry of lipids. This starts by addressing the question *'what is a lipid?'* and an explanation of lipid nomenclature. This is followed by a discussion of the self-assembly of lipids into aggregates of various structures when in aqueous solution and a detailed analysis of the structure and phases of lipid bilayers. The chapter ends with a brief discussion of some of the wider interests and possible applications of my research beyond the physics, including cell membranes and drug delivery. More theoretical background material is contained in chapter 3. This chapter begins with an overview of the mechanical properties of membranes, which includes the area compression modulus, the bending rigidity and the interactions between membranes. The second half of chapter 3 focuses upon the topology and properties of equilibrium phase diagrams.

The experimental methods used in my research are described in chapter 4. The technique of electroformation was used to produce the GUVs; this, along with the formation chambers that I had built for this project, are described at the beginning of the chapter. The phenomenon of fluorescence and the fluorophores used is covered in the next part followed by a generic description of optical microscopy. The chapter culminates in descriptions of confocal fluorescence microscopy and multiphoton fluorescence microscopy, which were used to obtain digital images of the vesicles. Chapter 5 then concentrates on the analysis of these digital images in order to gain quantitative data for the vesicles. The digital images represent a two-dimensional projection of a three dimensional vesicle hemisphere. Methods to calculate area fractions, distances and angles on the surface of the vesicle are explained in this chapter where programs to extract this data from the images were written using the Interactive Data Language (IDL).

Results to compare the fraction of gel phase on a vesicle as the temperature is slowly cooled are presented in chapter 6. This is done for varying compositions of DPPC/DPPE vesicles. The gel fraction against temperature data is compared with equilibrium expectations using the lever rule on published phase diagrams for the system. A mechanism of non-equilibrium growth, which

we name 'tree ring' growth, is proposed which provides a much better fit to our observations. The 'tree ring' model is discussed with respect to the diffusion constant in lipid gel phases and I look at its implications on the attainment of equilibrium phase diagrams for binary lipid systems.

I analyse the behaviour and morphology of the gel phase domains in chapter 7. Firstly I discuss DPPC/DPPE binary lipid vesicles. The movement, interaction and shape of the domains is addressed as well as the curvature of the gel domains. Secondly I present images of DPPC/DPPS GUVs where my analysis concentrates on the morphology of the observed domains. I also briefly review work done by other researchers in the group on binary lipid mixtures with the same head group but different lengths of hydrophobic tails where the gel phase formed is known as the ripple phase or rippled gel. I draw this chapter to a close by pointing out a one-to-one correlation between the gel phase formed by a system and the basic morphology of observed domains. I explain how this correlation can be understood from the molecular structure of the gel phases.

Chapter 8 draws together some results and observations that I have not previously discussed but still deserve mention within the framework of my thesis. Attempts to explain the phenomena reported in this chapter should be treated as speculative. The first section shows results of single component GUVs as they are cooled through their main transition temperature. This is followed by observations of domain formation in DPPC/DPPA vesicles and a brief consideration of why attempts to form DPPG/DPPE GUVs failed. I finally cover two subjects which caused much hindrance in obtaining results for this thesis, vesicle adhesion and lysis.

The conclusions to my work are finally summarised in chapter 9. Included in this chapter are suggestions for further work to advance upon the findings of this thesis and to investigate other observed phenomena. After the main body of my thesis, appendix A contains the code for the IDL programs written to analyse the digital images I obtained from my experiments. This is followed by a bibliography of references that are referred to in the main text of this thesis. Finally there is a list of figures and a list of tables.

Chapter 2

Background

In this chapter we will review the physical chemistry of lipids and lipid structures as well as outline some of the practical uses of lipids and their biological relevance. The chapter starts with an explanation of what a lipid is and a guide to the chemical structure of a particular class of lipids, the phospholipids. This is followed by a discussion of the various structures lipids can form in aqueous solution, concentrating on the molecular configurations and organisation within one of these structures: the bilayer. Finally, this chapter concludes with a guide to the wider interests of lipid research beyond physics.

2.1 What is a Lipid?

Despite a long search, I have still not come across what I feel is a satisfactory definition of a lipid. Lipids are naturally occurring molecules that appear to be categorised by their physical properties rather than their chemical structure. Lipids are natural, water insoluble molecules that can be extracted by non-polar solvents. They are the major constituent of biological cell membranes and can be fats, fatty acids or their derivatives. Classes of lipids include sphingolipids, glycolipids, lipoproteins and steroids such as cholesterol but this thesis concentrates on the *phospholipids*.

All lipids are amphiphiles, having hydrophilic (water loving) and hydrophobic (water hating) parts to the molecules. They therefore self-assemble in aqueous solution to form structures

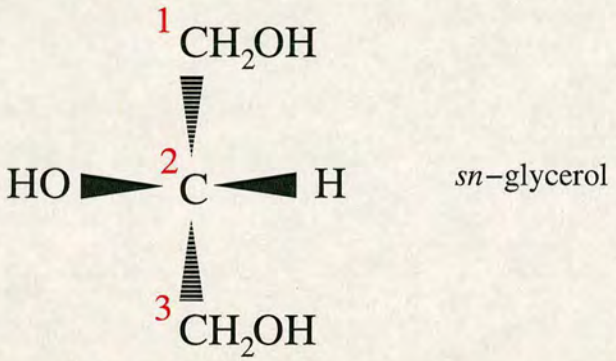

Figure 2.1: The structure of glycerol, the carbon atoms are labelled 1-3 using the stereospecific numbering (*sn*) system [14].

which 'hide' the hydrophobic parts from the water whilst exposing their hydrophilic parts to the aqueous environment. This will be discussed in detail in section 2.2.

2.1.1 Phospholipid Nomenclature

This section is a guide to the structure of many types of lipids and the conventions for naming them. I will concentrate on the phospholipids and in particular those phospholipids which are relevant to this thesis but references will be given for resources which explain the standard protocol for nomination of other lipid types. This section will start with an explanation of the lipid backbone, in this case glycerol, before explaining the acyl chains. Finally there will be an explanation of the lipid head groups.

The formal system of lipid nomenclature is proposed by the IUPAC-IUB Commission on Biochemical Nomenclature (CBN) [13]. Other shorthand methods of naming common lipids are also used in the literature and will be briefly covered here too.

All the phospholipids used in this thesis have a glycerol backbone[1]. Glycerol is a symmetric molecule but it becomes chiral about the central carbon if the outer two carbons (1 and 3 in Figure 1) are substituted differently. This chirality which is present in phospholipids means that the chemical structure of these compounds is described using stereospecific numbering,

[1]The other common backbone of natural lipids is a *N*-acylated sphingoid base, which will not be discussed at all within this thesis.

		Shorthand designations		
Systematic name	Common name	IUPAC-IUB	Δ-system	n-system
Dodecanoyl	Lauroyl	Lau	12:0	12:0
Tetradecanoyl	Myristoyl	Myr	14:0	14:0
Hexadecanoyl	Palmitoyl	Pam	16:0	16:0
Octadecanoyl	Stearoyl	Ste	18:0	18:0
cis-9-Octadecenoyl	Oleoyl	Ole	$18{:}1c\Delta^9$	18:1(n-9)

Table 2.1: Conventions for naming lipid acyl chains [14].

shown as *sn*-glycerol in figure 2.1. The glycerol backbone has two acyl[2] chains attached. In all lipids relevant to this thesis, the two chains are associated with the number one and two carbons. If these chains are symmetric, it leads to a name of the lipid being of the form 1,2 diacyl-*sn*-glycero-3-phospho-[*headgroup*] where the hydrophilic head group is associated with the number 3 carbon of the glycerol backbone.

The acyl chains are fatty acids which are substituted onto the glycerol backbone. The '-oic acid' part of their name is replaced by '-oyl' when it is attached to another molecule, for example (formally using the standard IUPAC system) hexadecanoyl or (using the common name) palmitoyl. I will use the common names for acyl chains within the framework of this thesis. If the acyl chains are asymmetric, for example a palmitoyl and an oleoyl tail, then the phospholipid is named 1-palmitoyl-2-oleoyl-*sn*-glycero-3-phospho-[*headgroup*]. Other shorthand methods for describing the acyl chains exist. The Δ-system tells you the number of carbon atoms in the acyl chain, followed by a colon and then the number of double bonds (C=C) i.e. the degree of unsaturation. For unsaturated chains, this is also followed by a 'c' or 't' for each double bond denoting whether it is 'cis-' or 'trans-' and a Δ with superscripts numbering the carbons where the double bonds are located (an explanation of the cis and trans conformations in hydrocarbon chains is in figure 2.2). In this case the numbering of the carbon atoms starts at the glycerol end of the chain. The n-system is similar to the Δ-system in its reference to the number of carbon atoms and the degree of unsaturation. This is then followed by (n-x),

[2]Acyl refers to a radical derived from an organic acid by the removal of the carboxylic hydroxyl group; it has the general formula RCO where R is an organic group. Alkyl and alkenyl chains also occur in phospholipids but will not be discussed here as all the phospholipids used in experiments and described in discussions have acyl chains

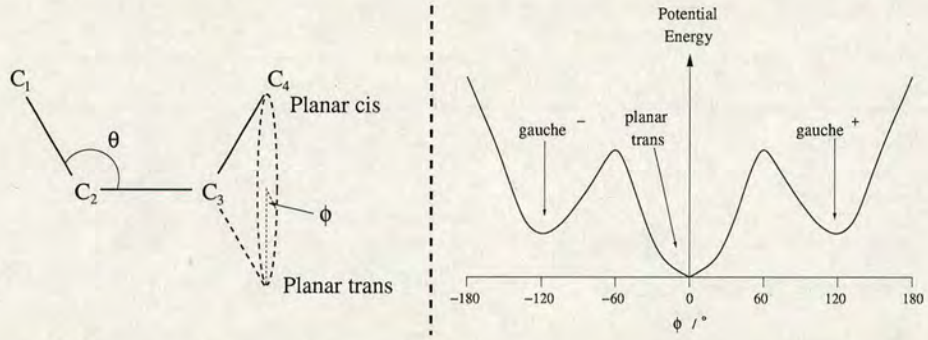

Figure 2.2: Diagram illustrating cis and trans bond conformations for a hydrocarbon chain. The C-C bond angles (θ) are fixed at around 120 ° but there can be rotation about the bond through an angle ϕ. The schematic graph (not real data) shows the potential energy as a function of ϕ: there is a global energy minimum in the trans conformation ($\phi = 0$) with two local minima at $\phi = \pm 120$ °known as the gauche$^+$ and gauche$^-$ conformations.

where x is the position of the first double bond encountered when numbering from the methyl terminus of the acyl chain. Formal, common and shorthand names for acyl chains which will be referred to in this thesis are shown in table 2.1.

The hydrophilic headgroup, attached to the number 3 carbon of the *sn*-glycerol, begins with a PO_3 group which is in turn attached to an alcohol. The alcohols are described by their common names unless they are a rare or unnatural compound. An example is ethanolamine which is used instead of the more formal 2-aminoethanol. The headgroups relevant to this thesis are shown in table 2.2. A standard shorthand 'phosphatidyl' is used to denote a 1,2-diacyl-*sn*-glycero-3-phospho- moiety, eg. phosphatidylcholine. For the case of a glycerol headgroup which is neither symmetrically nor stereospecifically substituted, i.e. the PG headgroup, the prefix '*rac*' is used, as in phospho-*rac*-(1-glycerol). A diagrammatic explanation of the nomenclature of 1,2-dipalmitoyl-*sn*-glycero-3-phosphocholine with respect to its molecular structure is shown in figure 2.3.

Further shorthand, which is common to much of the literature, is used to describe the phospholipids within this text. Four letter acronyms are employed with the first two letters describing the hydrophobic tails and the last two letters describing the hydrophilic headgroup (see table 2.2). For symmetric acyl chains, the first letter of the shorthand name is '**D**' to denote the **D**iacyl nature, followed by the first letter of the common name of the acyl chain, for example

Headgroup	Shorthand
Phosphocholine	PC
Phosphoethanolamine	PE
Phospho-L-serine	PS
Phosphate (Phosphatic Acid)	PA
Phospho-*rac*-(1-glycerol)	PG

Table 2.2: Lipid hydrophilic headgroups and their shorthand abbreviations which are used in this thesis and most of the published literature.

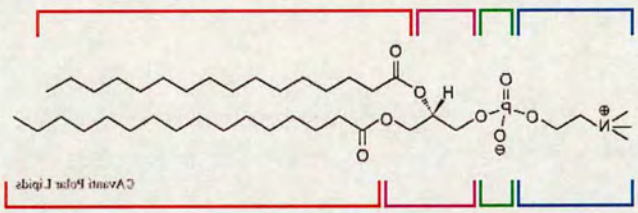

Figure 2.3: Schematic explanation for the nomenclature of 1,2-dipalmitoyl-*sn*-glycero-3-phosphocholine (DPPC) with respect to its molecular structure. Descriptions of the nomenclature of the acyl chains (red), glycerol (magenta) and phosphate (green) backbone and alcohol headgroup (blue) are explained in the text. Note that the phosphorous and nitrogen are 'back-to-front' as I have taken a mirror image of the structure on the Avanti website [15].

'**DP**' refers to **DiP**almitoyl. Hence the shorthand DPPC refers to 1,2-dipalmitoyl-*sn*-glycero-3-phosphocholine. If the lipid has asymmetric acyl chains then the first letter of each common name of the acyl chain is used in order of the acyl chain attached to the number one carbon of the *sn*-glycerol followed by the acyl chain attached to the number two carbon. This means that the shorthand POPC refers to 1-**P**almitoyl-2-**O**leoyl-*sn*-glycero-3-**P**hospho**C**holine. The molecular structures of the lipids used in the experimental work for this thesis are shown in figure 2.4.

DPPC

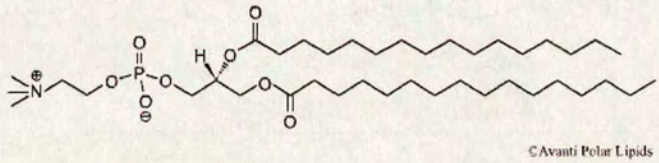

DPPE

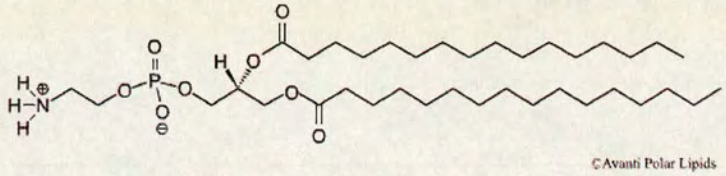

DPPS

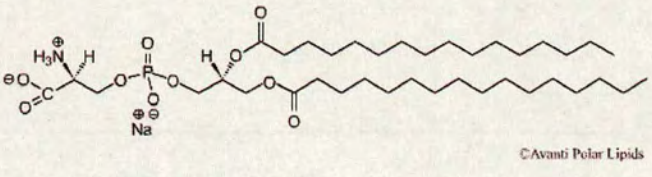

DPPA

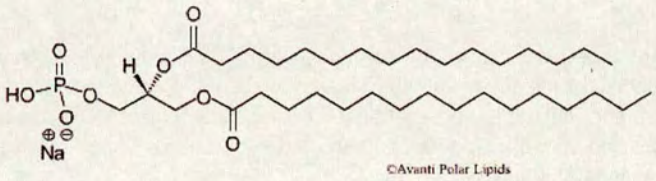

DPPG

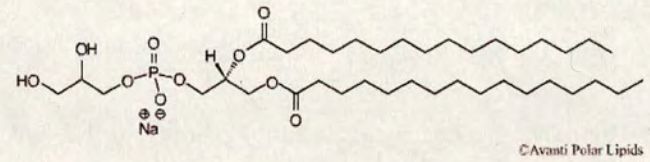

Figure 2.4: Molecular structures of the five lipids purchased from Avanti Polar Lipids, Inc. [15]. From top to bottom, they are DPPC, DPPE, DPPS, DPPA & DPPG.

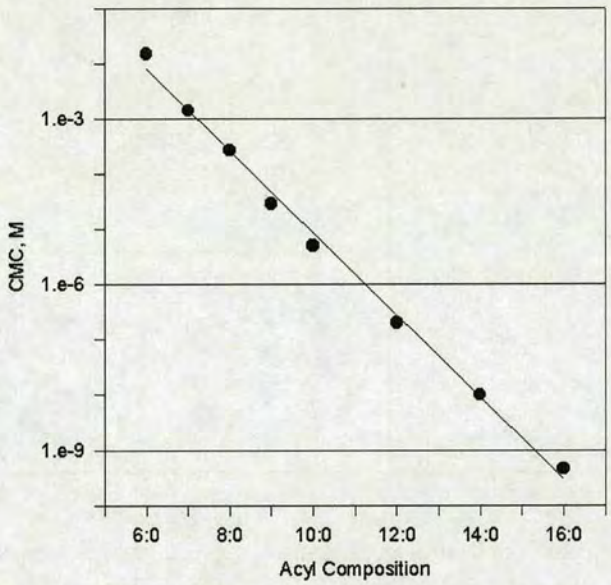

Figure 2.5: Critical micellar concentration (cmc) against acyl chain length for phosphatidylcholines [15].

2.2 Self-Assembly

As mentioned earlier, lipids are amphiphilic in nature causing them to self-assemble into structures in aqueous solution. At very low amphiphile concentration, amphiphilic molecules cluster at the air-water interface with their hydrophobic chains sticking into the air and their hydrophilic head groups surrounded by water. These surface amphiphiles are in a dynamic equilibrium with a few monomeric amphiphiles in the bulk aqueous solution. Above a certain concentration of amphiphiles, there is no more space for extra amphiphiles to gather at the air-water interface and so spontaneously self-assemble into structures in the aqueous solution. This is known as the critical micellar concentration (cmc). Lipids are very insoluble and hence have a very low cmc: this is of order nano-molar concentrations for DPPC (see figure 2.5).

The hydrophobic, hydrocarbon cores to these self-assembled structures have a similar density to that of fluid hydrocarbons. The self-assembled structures formed by amphiphiles depend on their molecular geometry, which affects the possible packing of the molecules in the aggregate. The important molecular parameters to consider are the optimal area per headgroup (a_0), the

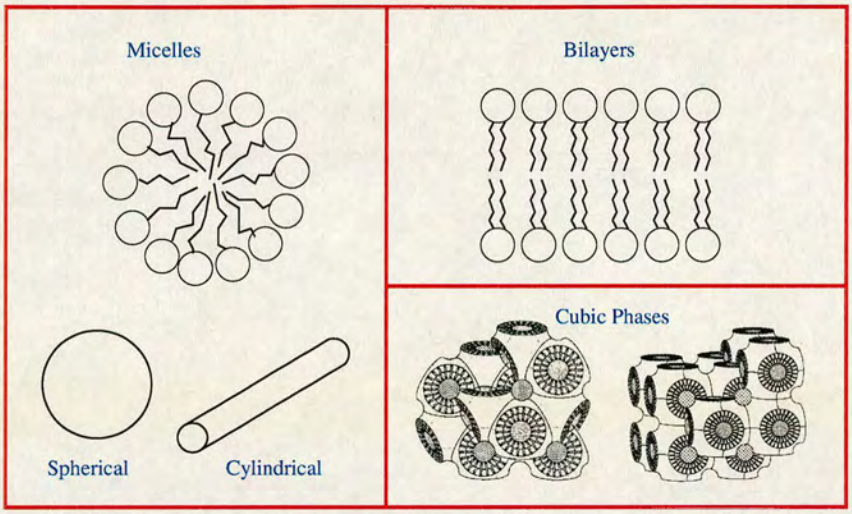

Figure 2.6: Possible self-assembled structures. These are micelles (both cylindrical and spherical), bilayers and cubic phases [16]. The inverted hexagonal phase is not shown.

volume of hydrophobic moiety (v) and the maximum length of the hydrophobic chains (l_0). The possible self-assembled structures of amphiphiles are shown in figure 2.6.

If we consider a spherical micelle of radius R with aggregation number N (number of amphiphiles in the micelle), the total volume of the micelle must correspond to the total volume of its constituent amphiphiles:

$$Nv = \frac{4}{3}\pi R^3 \,, \tag{2.1}$$

and the total surface area must correspond to the exposed surface area, i.e. headgroup areas, of its constituent amphiphiles:

$$Na_0 = 4\pi R^2 \,. \tag{2.2}$$

If we divide equation 2.1 by equation 2.2, we get

$$\frac{v}{a_0} = \frac{R}{3} \,. \tag{2.3}$$

The radius of the micelle can be no greater than the maximum length of the amphiphile ($R \leq l_0$), giving us a constraint on a packing parameter, P, for spherical micelles of

$$\frac{v}{a_0 l_0} = P \leq \frac{1}{3} . \tag{2.4}$$

For cylindrical micelles of radius R and length L, we can use the same model to get the following equations for the volume and surface areas:

$$Nv = \pi R^2 L \quad ; \quad Na_0 = 2\pi RL . \tag{2.5}$$

We again have the constraint that $R \leq l_0$, so dividing the volume and area equations by each other and rearranging gives us a constraint on the packing parameter for cylindrical micelles of

$$\frac{1}{3} < P \leq \frac{1}{2} \tag{2.6}$$

since for $P \leq \frac{1}{3}$ we get spherical micelles as it is entropically more favourable to have a greater number of aggregates in solution. This condition is satisfied by having the minimum number of amphiphiles per aggregate.

If we now consider a bilayer of thickness D and area A, using the same model, the equations for the volume and area due to the number of amphiphiles in the bilayer are

$$Nv = AD \quad \text{and} \quad Na_0 = 2A . \tag{2.7}$$

For a bilayer, the constraint on its thickness is that it can be no greater than the maximum length of two amphiphiles, $D \leq 2l_0$. These equations can be rearranged as before to give us our constraint for the molecular packing parameter for a bilayer of

$$\frac{1}{2} < P \leq 1 \tag{2.8}$$

as it was previously shown that cylindrical micelles occur for $P \leq \frac{1}{2}$, this is entropically more favourable than bilayers due to the greater number of aggregates in solution for a given

Packing Parameter	Amphiphile Aggregate
$P \leq \frac{1}{3}$	Spherical Micelles
$\frac{1}{3} < P \leq \frac{1}{2}$	Cylindrical Micelles
$\frac{1}{2} < P \leq 1$	Bilayers
$P \geq 1$	Inverted Structures (eg. Inverted Hexagonal Phase)

Table 2.3: Aggregates formed by amphiphilic molecules with a packing parameter P in aqueous solutions at concentrations above their cmc. The packing parameter is expressed in terms of the molecular dimensions of the amphiphile (*see text*), $P = v/(a_0 l_0)$.

number of amphiphiles. If an amphiphile has a molecular packing parameter greater than one then inverted structures such as inverted hexagonal phases preferentially form. The amphiphile aggregates with respect to the molecular packing parameter are summarised in table 2.3.

Under conditions of excess aqueous phase and at the temperatures investigated in my experiments, all the phospholipids studied in this thesis form bilayer phases. A model for the maximum length of a saturated hydrocarbon chain containing n carbons is [17]:

$$l_0 \approx (0.154 + 0.1265n)\text{nm} \,, \tag{2.9}$$

and the volume of the hydrophobic moiety is:

$$v \approx (27.4 + 26.9n) \times 10^{-3}\text{nm}^3 \,. \tag{2.10}$$

If we have a lipid with two 16 carbon acyl chains, this model gives us a maximum chain length of l_0 =2.178 nm and a hydrophobic volume of v =0.888 nm^3 where n =16 has been used to calculate the chain length and n =32 has been used to calculate the volume as this takes into account the two acyl chains. The area per hydrophilic head group for DPPC in the fluid phase, a_0, is 0.65 nm^2 [14]. Calculating the packing parameter, P, for DPPC in the fluid phase, we get a value of 0.63 which, as can be seen in table 2.3, is within the range for bilayers in our model of amphiphile structures.

Bilayers can have a rich phase behaviour of their own; these phases will be discussed in section 2.3. The bilayers of interest in this thesis are those which close round to form spherical sheets

called vesicles. Bilayers which form a structure of this geometry ensure that the ends of a bilayer sheet are not exposed to the aqueous solution which is very energetically unfavourable. In effect the bilayer, in the form of a vesicle, has periodic boundary conditions.

2.3 Bilayer Structure & Phases

Lipids in lamellar bilayers can be in more than one phase. This section aims to give a brief overview of the structure of these phases for lipid bilayers in an environment of excess water, i.e. the lipids are fully hydrated. Different lipids exhibit different phases and phase transitions, so it may seem impossible to describe a generic phase behaviour for all single component lipid membranes. Therefore I will firstly give an overview of the general phases observed in these lipid membranes before reviewing the phase behaviour of the single component bilayers of lipids relevant to this thesis. Finally I will summarise these lipid phases at the end of this section and attempt to provide a rough, generic model of the phase behaviour of these phospholipids.

2.3.1 Generic Bilayer Phases

The Fluid Phase

The fluid phase (L_α) is the high temperature state of lipid bilayers. The acyl chains are in a conformationally disordered state with a mixture of gauche$^+$, gauche$^-$ and trans bonds between the carbons of the hydrocarbon chains (see figure 2.2 for an explanation of bond conformations in hydrocarbon chains). The head groups also adopt a disordered arrangement. The fluid nature of the bilayer means that lipids are free to diffuse in a two dimensional fluid matrix. A schematic of the bilayer structure in the fluid phase is shown in figure 2.7. A comprehensive review on the structure of lipid bilayers in the fluid phase has been published [18]. The fluid phase is the phase which is considered to be closest to the state of real cell membranes in living systems and so has received the most interest and investigation out of all the lipid bilayer phases.

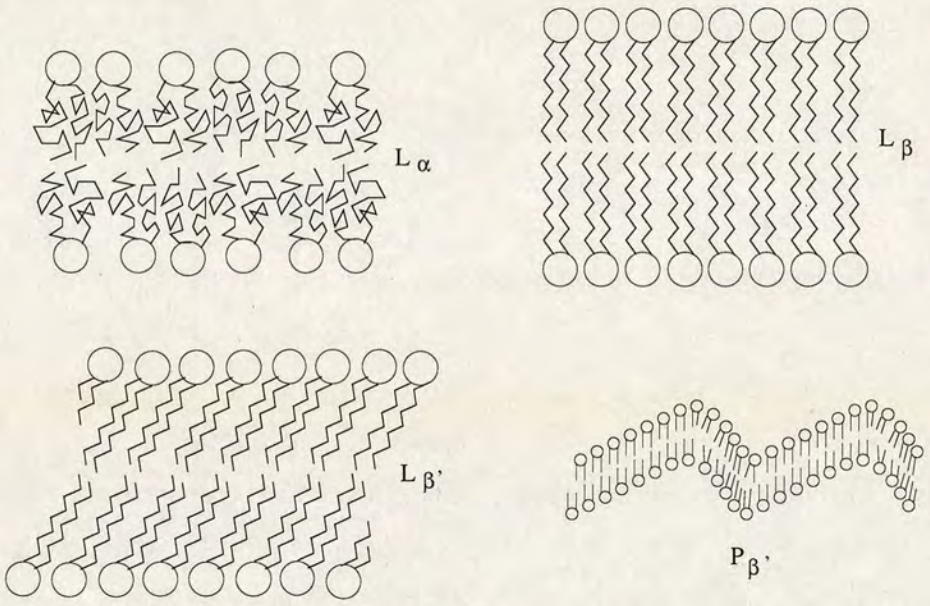

Figure 2.7: Schematics of lipid bilayer phases: [*top left*] the fluid phase (L_α); [*top right*] the lamellar gel phase with untilted chains (L_β); [*bottom left*] the lamellar gel phase with tilted chains ($L_{\beta'}$), the diagram shows a 30 ° tilt to the bilayer normal in the tails; [*bottom right*] the rippled gel phase ($P_{\beta'}$), the rippling is asymmetric and has a fixed wavelength.

Gel Phases

At lower temperatures than the fluid phase in the phase diagram are one or more gel phases. Schematic diagrams of the structure of lipid bilayers in the gel phases discussed in this section are shown in figure 2.7. Much of the literature refers to 'the gel phase' without considering which gel phase a particular lipid has under the given conditions and in the case of binary lipid phase diagram, very few authors give any consideration to what affect different single component lipid gel phases will have on the structure of the gel phase of the mixture. This apparent lack of interest by much of the lipid community in carefully considering gel phases probably stems from the fact that the fluid phase is the lipid state which is considered to be the one of biological relevance as mentioned above.

The fluid-gel transition is a chain ordering transition. In gel phases, most of the C-C bonds in the acyl chains are in the trans conformation and so the chains are stretched out to near their maximum length. Therefore the fluid-gel transition results in an increase in bilayer thick-

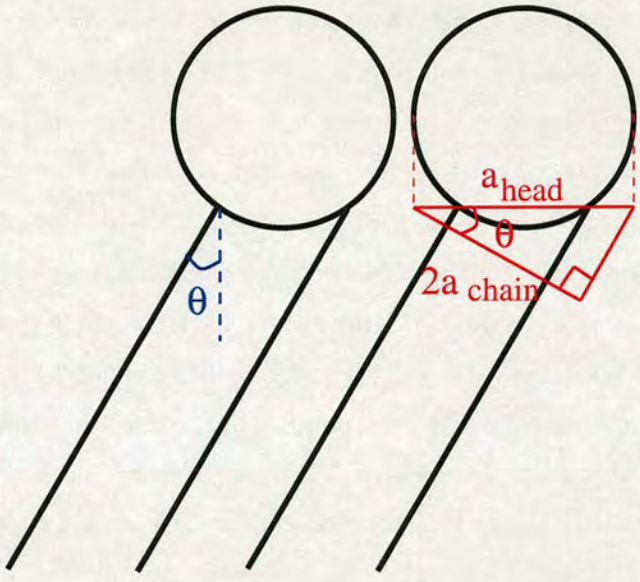

Figure 2.8: Diagram to prove equation 2.11. This is a two dimensional representation of the three dimensional situation. The area of the headgroup in the bilayer plane (a_{head}) must be matched by the area of the two acyl chains below it ($2a_{\mathrm{chain}}$) so that no empty space is left. In this cartoon with reduced dimensionality, areas are represented by lengths and the angle of tilt of the acyl chains to the bilayer normal (θ_{tilt} in the text) is represented by θ. It can be seen by geometric derivation that $\cos\theta = 2a_{\mathrm{chain}}/a_{\mathrm{head}}$, which can be rearranged to give equation 2.11.

ness and correspondingly, a decrease in area per lipid headgroup in the membrane. The lipid headgroups in the gel phase are packed in a near-hexagonal lattice [18].

The different gel phases that have been reported for diacyl phospholipids are L_{β}, $\mathrm{L}_{\beta'}$ and $\mathrm{P}_{\beta'}$. The 'L' denotes a lamellar phase and the 'P' a rippled phase. The 'β' represents the fact that the bilayer is in a gel phase and the primed denotes a tilting of the acyl chains with respect to the bilayer normal. This tilt in the acyl chains is a geometric consideration when comparing the area per headgroup (a_{head}) and the cross-sectional area per acyl chain (a_{chain}). The tilt angle to the bilayer normal (θ_{tilt}), can be calculated as [14]:

$$\theta_{\mathrm{tilt}} = \arccos\left(\frac{2a_{\mathrm{chain}}}{a_{\mathrm{head}}}\right) . \tag{2.11}$$

A proof of this equation is given in figure 2.8. The chains in each monolayer of the bilayer are known to be parallel to each other in the lamellar gel phases [18].

The rippled gel ($P_{\beta'}$) phase only seems to have been reported in systems where it occurs between the L_α and $L_{\beta'}$ phase, so acyl chain tilt may be important in its occurrence. On transition from the $L_{\beta'}$ to the $P_{\beta'}$ phase, there is an increase in lipid rotation about its long axis and an increase in area per headgroup due to the bilayer attaining a rippled structure. It is thought that the headgroups wish to attain some fluidity whilst the acyl chains wish to remain ordered, resulting in the asymmetric rippling of the bilayer with a set periodic wavelength [14]. Kirchner and Cevc [19] suggest that as temperature is increased in the $L_{\beta'}$ phase, θ_{tilt} decreases coinciding with a corresponding decrease in area per headgroup (see equation 2.11). This decrease in headgroup area is in competition with the hydrophilic head of the lipid wishing to increase its area on increasing temperature to increase its hydration. The pretransition is therefore seen in this model as the natural response to these opposing effects. Other work has considered the ripple phase as a gel-fluid coexistence [18].

Very recent molecular dynamics simulations of DPPC bilayer stacks show a transition to a rippled bilayer when the bilayers are cooled from the fluid phase [20]. The simulations show the ripples are asymmetric with the long arm of the ripple being a splayed gel and the other arm being an interdigitated gel[3]; the concave region (the 'kink') between these two domains consists of lipids with disordered acyl chains. The results of these simulations still need to be verified by experiment.

Subgel Phases

Subgel phases appear at lower temperatures than the gel phase(s) in the phase diagram. The low temperature equilibrium phase of phospholipid bilayers, L_c (where 'c' denotes crystalline), has a greater lipid ordering in an orthorhombic lattice than the gel phases as well as dehydration of the headgroups so that they lie in the plane of the bilayer.

Transition to the equilibrium L_c phase can be a slow process which can take between minutes and months, or longer, to occur. This transition time to the L_c phase increases with increasing acyl chain length [14]. This leads to long-lived metastability of gel, and even fluid, phases of

[3]This is a gel where the acyl chains of the lipids of opposing leaflets of the bilayer lie side-by-side rather than end-to-end. An interdigitated gel phase is commonly denoted $L_{\beta I}$.

phospholipids. There are often one or more metastable intermediates in the transition to the L_c phase such as a sub-subgel phase which has increased lipid ordering where it appears that in general the chain packing becomes orthorhombic from the hexagonally packed gel phase, before dehydration of the headgroups occurs.

Some publications have made a distinction in the subgel phases between an L_c and an $L_{c'}$ phase. Again the primed here denotes a tilting of the acyl chains with respect to the bilayer normal as was the case in the gel phase notation. This notation does not appear to be widespread throughout the literature and, seeing as the subgel phase is not of direct significance to the results within this thesis, I will not concern myself with differentiating between these phases.

2.3.2 Phases of Specific Lipids

As stated at the beginning of this section, the phases and phase transitions of a single component lipid bilayer is dependent on the lipid itself. Below is a review of the phases and phase transitions of single component membranes of the lipids used in this thesis. Extensive details are given of the phase behaviours of DPPC and DPPE bilayers compared to those of DPPS, DPPA and DPPG membranes. This reflects the volume of literature available on the respective lipids. The vast majority of the data is obtained from multilamellar vesicles (MLVs) rather than unilamellar vesicles to obtain a greater signal to noise ratio in their experiments due to the greater number density of lipids per unit volume attainable in solution using MLVs. Nagle and Tristram-Nagle show that the interactions between fully hydrated membranes of MLVs has a negligible effect on the phase behaviour of the lipid bilayers [18].

DPPC

A review of phases and phase transitions of phosphatidylcholines is available in the literature [21]. After low temperature equilibration (below 8 °C), DPPC membranes are in the subgel (L_c) phase with chains tilted to the bilayer normal and the headgroups bent over parallel to the bilayer. On increasing temperature the lipids undergo a phase transition to an $L_{\beta'}$ gel, the so called sub-transition, at 18.8 ± 3.1 °C where the uncertainty is due to averaging over the

results of many published values. Nagle *et al.* claim that this value is too high due to fast scan rates in Differential Scanning Calorimetry (DSC) giving non-equilibrium results; they claim that the sub-transition temperature is 14.5 °C [18]. The $L_{\beta'}$ phase has reduced chain tilt and increased headgroup hydration, i.e. the headgroup is no longer parallel to the bilayer but at an angle to it. On further increase in temperature, there is a pre-transition where a change in gel phase to the rippled gel ($P_{\beta'}$) occurs at 34.4 ± 2.5 °C. Again, increasing the temperature further, there is another phase transition (the main transition) to the fluid (L_α) phase at 41.3 ± 1.8 °C ($P_{\beta'} - L_\alpha$). This is sometimes also referred to as the melting transition where the C-C bonds of the hydrocarbon tails, which are in the *trans* conformation in the gel phase, can now access more conformational degrees of freedom. It has been shown that this transition is highly cooperative with no detectable coexistence of $P_{\beta'}$ and L_α phases. The $P_{\beta'} \rightarrow L_\alpha$ transition for DPPC has a slow relaxation time of 260 s and a half-width of 0.067 °C.

On cooling, the L_α phase forms a long-lived, metastable $P_{\beta'}^{mst}$ phase which has a different ripple structure to the original $P_{\beta'}$ phase. The $P_{\beta'}^{mst}$ phase has two ripple structures, one with wavelength 13 nm as is seen in the $P_{\beta'}$ phase, and a second with double the wavelength of ripple structure at 26 nm [22]. The $L_{\beta'}$ phase is restored on further cooling as the $L_{\beta'} - P_{\beta'}$ transition is reversible. The $L_{\beta'}$ phase is metastable below the $L_c - L_{\beta'}$ transition temperature. The $L_{\beta'}$ phase needs to be cooled below 8 °C for a few hours for the L_c phase to nucleate, after which the temperature can be raised to any point below the $L_c - L_{\beta'}$ transition temperature and the L_c phase will continue to form [18]. The $L_{\beta'}$ phase, which has hexagonal packing, converts to the L_c phase via an intermediate sub-subgel phase (SGII) where the tilted acyl chains become more ordered in a lattice with orthorhombic packing. The second step of the transition, SGII $- L_c$, is thought to involve the dehydration of the headgroups and can have one or more intermediate metastable states. Full conversion from SGII to L_c takes more than 10 days for DPPC.

For clarity, the phase transitions of DPPC and their temperatures are summarised in table 2.4. Large DPPC vesicles with diameters greater than 70 nm have been shown to have phase transition temperatures independent of vesicle diameter: 70 nm in diameter is well below the size range of giant vesicles. Effects on DPPC phase transition temperatures have also not been seen for salt concentrations less than 0.1 M and a pH greater than 3.

DPPE

The phases and phase transitions of phosphatidylethanolamines have been reviewed in the literature [23]. At low temperatures, DPPE membranes are in the subgel, L_c, phase. On increasing temperature, the L_c phase converts irreversibly to the fluid, L_α, phase at 66.36 ± 1.00 °C. On further heating, the L_α DPPE membranes can undergo a phase transition to the non-lamellar inverted hexagonal phase (H_{II}) at 120.57 ± 3.58 °C. This transition temperature is much higher than any that will be studied in my experiments so I will not consider this phase relevant to my results.

On cooling from the L_α phase, DPPE membranes do not undergo a transition directly back to the L_c phase but instead have a reversible phase transition to a lamellar gel, L_β, phase at a temperature of 62.28 ± 4.99 °C (a rather unsatisfactorily large error in temperature), lower than the $L_c \rightarrow L_\alpha$ transition temperature. The DPPE L_β phase is metastable across its entire temperature range: it slowly converts to the L_c phase over a time scale of several months. The L_α phase is also metastable in the temperature range between the $L_\beta - L_\alpha$ and $L_c \rightarrow L_\alpha$ transitions. The metastable L_α phase converts to the L_c phase at a faster rate than the metastable L_β phase. This is 15 hours for the complete DLPE[4] metastable fluid to subgel transition as opposed to several days for the metastable gel to subgel transition. The conversion times from metastable phases to the subgel phase increase with increasing acyl chain length, so conversion to the L_c phase of DPPE will not be considered to be relevant on the time scale of my experiments (a few hours).

A sub-subtransition analogous to the SGII $- L_{\beta'}$ transition of DPPC has been reported for DPPE [24]. This new metastable phase, denoted L_{R1}, occurs via a reversible transition at 9.0 °C. The acyl chains in the L_{R1} phase are still perpendicular to the bilayer plane but the packing of the acyl chains becomes orthorhombic from the hexagonal packing of the L_β phase. The orthorhombic lattice of the L_{R1} phase is also different in structure to the orthorhombic packing of the SGII phase of DPPC.

The $L_c \rightarrow L_\alpha$ transition is thought to involve two steps, hydration of the headgroup as well as disordering of the acyl chains whereas the $L_\beta - L_\alpha$ transition is a chain order/disorder transition. It was once thought that DPPE had a pretransition similar to the $L_{\beta'} - P_{\beta'}$ transition of

[4]Two 12 carbon acyl chains.

DPPC. Experiments show that DPPE undergoes a single chain melting transition when heating from the L_β phase but a complex transition is seen on cooling from the L_α to the L_β phase[5] which possibly accounts for some of the error in the main transition temperature.

The phase transitions of DPPE and their temperatures are summarised in table 2.4. The temperatures are an average of those obtained between a pH of 5 and 8 and a salt concentration less than 0.2 M since phase transition temperatures of DPPE do not seem to vary noticeably within these ranges.

DPPS

After low temperature equilibration, DPPS has been seen to have a subgel phase, L_c, which, on heating, undergoes a phase transition to a gel phase at 32.2 °C [25]. The gel phase of DPPS was thought to be $L_{\beta'}$ by Hauser *et al.* [26], as Luna and McConnell had previously guessed [27], although they were not conclusive in this assertion. More recent work by Petrache *et al.* [28] shows that the gel phase structure of DMPS is a hexagonally packed L_β phase. The hexagonal lattice of the gel phase is also reported by Hauser *et al.* [26]. Seeing as chain tilt in gel phase structure appears to be a geometric consideration due to the steric size of the headgroup compared to the area of the two acyl chains, it is fair to assume that DPPS has the same gel phase structure as DMPS. This gel phase invariance over wide ranges of acyl chain length is seen for the diacyl PC and PE lipids. The L_β phase in DPPS is an equilibrium phase unlike the metastable L_β phase of DPPE. The main transition of DPPS ($L_\beta - L_\alpha$) is reversible and, taking an average over several published values, is at a temperature of around 52.5 °C [15, 25–27, 29, 30].

Lewis and McElhaney claim that the L_c phase formed by shorter chain diacyl PS lipids is more ordered but structurally similar to the L_c phase of the longer chain PS lipids [25]. One possibility is that the diacyl PS lipids undergo a chain ordering transition to a metastable sub-subgel phase (analogous to the L_{R1} phase of DPPE) as an intermediate state in the conversion of L_β to L_c. The dehydration of the headgroups from the sub-subgel phase to the subgel phase of PC and PE lipids takes much longer with increasing length of the diacyl chains [21, 23], so

[5] This is from calorimetry and time-resolved x-ray diffraction experiments.

this could account for the observation of the ordering in the L_c phase of PS phospholipids, i.e. the shorter chain PS lipids had fully hydrated to the L_c but the longer chain PS lipids were still predominantly in the sub-subgel phase and so appeared to be less ordered. No direct detection of a sub-subgel phase has been reported but literature on PS bilayers is sparse in comparison to PC and PE headgroups. The phase transitions of DPPS are summarised in table 2.4.

DPPA

The main transition temperature of DPPA is about 67.2 °C; this is an average over several published values [15, 30–33]. Both Jacobson and Papahadjopoulos [32] and Blume [31] report pretransitions for other lipids but do not observe one in DPPA membranes, so it can be presumed that the $L_{\beta'} - P_{\beta'}$ transition is not present in the case of DPPA close to neutral pH[6]. DPPA has a reported $L_\alpha - H_{II}$ transition at a pH of 4.6 [33] although this transition could not be detected at a pH 7. Inverted structures such as the H_{II} phase require the packing parameter, P, to be greater than one as discussed in section 2.2 which is analogous to saying that the optimal headgroup area for the lipid is less than the cross-sectional area of the two acyl chains. Seeing as the tilting of the acyl chains in the $L_{\beta'}$ phase is related to the geometric constraint of the cross-sectional areas of the two acyl chains being less than that of the optimal headgroup area of the lipid, then it seems very unlikely that the chains are tilted in the gel phase of DPPA. This also seems likely when considering the molecular structure of DPPA (see figure 2.4): its small hydrophilic headgroup lends further support, without having found X-ray or neutron scattering data to support it, to DPPA's gel phase being L_β. No data on the L_c phase of DPPA was found in the literature, so it is not possible to infer whether the L_β phase of DPPA is metastable as in the case of DPPE, or an equilibrium phase as it is for DPPS. The known phase transition of DPPA is also included in the summary of phase transitions of dipalmitoylated phospholipids in table 2.4.

[6] As with all the phospholipids, their charge per headgroup is pH dependent as is their phase behaviour. The phase transition data for all the phospholipids reviewed in this chapter is taken at neutral pH and minimal ionic strength (less than 50 mM, except where stated) or a pH close to neutral where the behaviour of that particular lipid has not been seen to deviate from the neutral pH behaviour.

	Phase Transition Temperatures / °C								
	Tilted-Chain Gel Phases				Untilted-Chain Gel Phases				
	$L_c \rightarrow L_{\beta'}$	SGII $- L_{\beta'}$	$L_{\beta'} - P_{\beta'}$	$P_{\beta'} - L_\alpha$	$L_c \rightarrow L_\beta$	$L_c \rightarrow L_\alpha$	$L_{R1} - L_\beta$	$L_\beta - L_\alpha$	$L_\alpha - H_{II}$
DPPC	18.8 ± 3.1 [a]	7.1 ± 0.6	34.4 ± 2.5	41.3 ± 1.8					
DPPE						66.36 ± 1.00	9.0[b]	62.28 ± 4.99	120.57 ± 3.58
DPPS					32.2			52.5	
DPPA								67.2	
DPPG	24.8		35 ± 1	41.3					

[a] Nagle *et al.* claim that this value is too high, with 14.5 °C being a more accurate determination of the transition temperature [18].
[b] Data from Tenchov *et al.* [24].

Table 2.4: Summary of phase transition temperatures for the dipalmitoyl phospholipids used in experiments. An '→' between phases denotes an irreversible transition, while reversible transitions are expressed with a dash ('–') between phases. Except where noted the phase transition temperatures for DPPC are taken from Koynova and Caffrey's 1998 review [21] and the transition temperatures for DPPE are taken from Koynova and Caffrey's 1994 review [23]. The references for the phase transitions of the other phospholipids can be found in the text. Phase transition temperatures for all lipids are taken from data which is valid for neutral pH, low ionic strength and in excess water, i.e. the bilayers are fully hydrated. The main transition temperature for each lipid is underlined and highlighted in red.

DPPG

Wilkinson and McIntosh report a subtransition ($L_c \rightarrow L_{\beta'}$) in DPPG at pH 7.0 and an ionic strength of 5 mM at 24.8 °C [34]. A pretransition ($L_{\beta'} - P_{\beta'}$) has also been reported at 35 ± 1 °C [32]. Taking an average over several references, the main transition ($P_{\beta'} - L_\alpha$) temperature for DPPG is 41.3 °C [15, 30, 32]. These values are all taken for close to neutral pH as the charge per headgroup of PG, and its phase behaviour, is dependent on the pH. None of the papers I looked at mentioned a sub-subtransition but none of the authors studied the relaxation of the $L_{\beta'}$ phase to the L_c phase so this is not indicative of the absence of a sub-subgel phase such as the SGII phase seen in DPPC. The phase transitions of DPPG are summarised in table 2.4.

2.3.3 Summary

The phases of fully hydrated single component phospholipid membranes appear complicated with each species exhibiting different behaviour. It does appear though that a simple model of phospholipid phase transitions can explain much of the behaviour. If we consider the gel phases of the phospholipids, they appear to either prefer tilted or untilted chains, dependent on the headgroup area compared to the cross-sectional area of the acyl chains. Splitting the phospholipids into two categories of tilted-chain gel phases (DPPC and DPPG) and untilted-chain gel phases (DPPE, DPPS and DPPA) we can draw the phase transition schematics shown in figure 2.9. The two graphs roughly represent the phase behaviours of DPPE and DPPC but these can also be used to think about the other phospholipids.

If we assume that the phase boundaries of these two diagrams can shift relative to each other, we can describe the major phase behaviour of many other lipids. Some phospholipids exhibit a direct $L_{\beta'} - L_\alpha$ transition without a pretransition to $P_{\beta'}$. If we look at the pre- and main transition temperatures of phosphatidylcholines of different acyl chain lengths in figure 2.10a, the transition temperatures get closer together until there is only a single $L_{\beta'} - L_\alpha$ transition for PCs with diacyl chains greater than 22 carbons in length. This is analogous to the $L_{\beta'} - P_{\beta'}$ shifting closer to the $P_{\beta'} - L_\alpha$ transition in figure 2.9 until the $L_{\beta'} - P_{\beta'}$ transition disappears altogether.

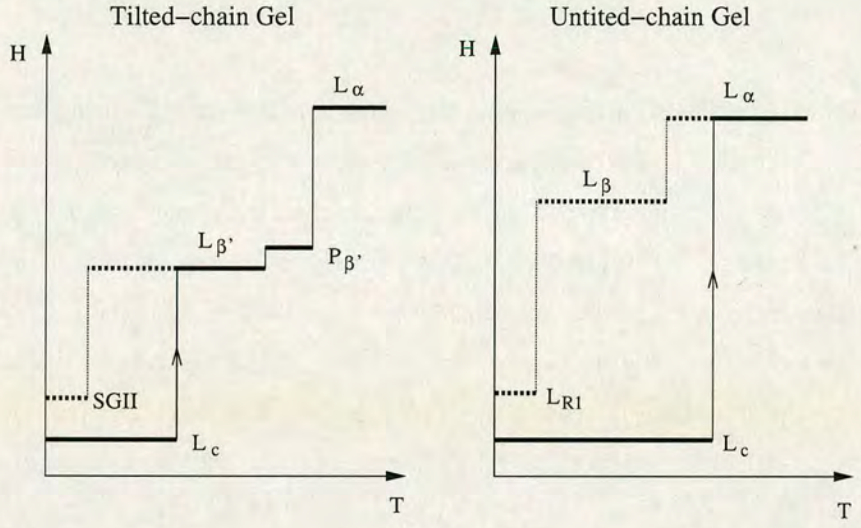

Figure 2.9: Generic phase transitions for phospholipids which prefer to have gel phases with tilted (DPPC-like) or untilted (DPPE-like) acyl chains with respect to the bilayer normal. Equilibrium phases are shown by unbroken lines and metastable phases are shown by the dashed lines. The graphs are of temperature (T) against enthalpy (H); no attempt is made to show accurate enthalpy differences (in terms of scaling on the enthalpy axis) between different lipid phases. Arrows are shown on phase transitions which are not reversible to indicate the direction in which the transition occurs. These diagrams are based on the schematics by Cevc [35].

Similarly for DPPS, we have an equilibrium L_β phase rather than the the metastable L_β of DPPE. This is due to the $L_\beta - L_\alpha$ transition shifting above the $L_c \rightarrow L_\alpha$ transition in figure 2.9. Looking at the phase transition temperatures of the phosphatidylethanolamines as a function of acyl chain length in figure 2.10b, the L_β phase of PEs becomes an equilibrium phase for 19 carbons per acyl chain and greater. Also the transition temperature of the $L_\alpha - H_{II}$ transition is seen to decrease until the L_α phase disappears for PEs with 22 carbon acyl chains, with a direct $L_\beta - H_{II}$ transition. For PS lipids with 12 carbon acyl chains, the L_β phase is metastable as the $L_\beta - L_\alpha$ transition temperature shifts below the $L_c \rightarrow L_\alpha$ transition [25].

For conditions of near-neutral pH and low ionic strength DPPE, DPPS and DPPA come under the category of untilted-chain gels and DPPC and DPPG come under the tilted-chain gel category. This is not a perennial label for these lipids under all conditions. PA and PE both exhibit a pretransition to a phase with a ripple structure at pH 12 [33] and also in DPPS at pH 13 [29]. At these higher pHs, these lipids have an extra negative charge per headgroup. An explanation

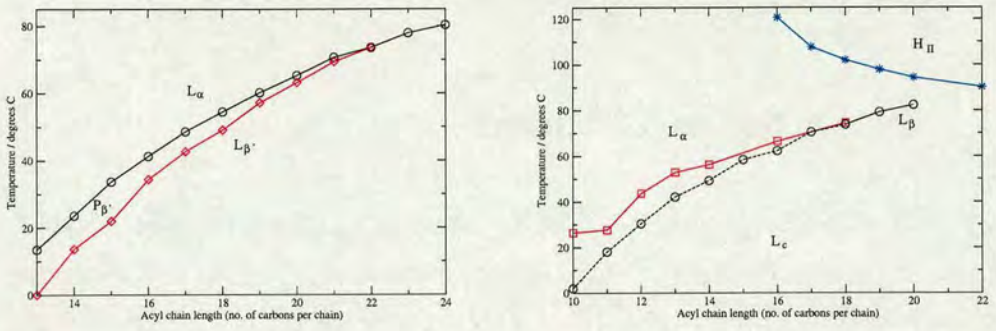

Figure 2.10: (a) [*left*] Graph of the pre- and main transition temperatures of phosphatidylcholines as a function of acyl chain length. Data is taken from Koynova and Caffrey [21]. Circles represent the main transition and diamonds represent the pretransition; (b) [*right*] Graph of the phase transition temperatures of phosphatidylethanolamines as a function of acyl chain length. Data is taken from Koynova and Caffrey [23]. Squares represent the $L_c \rightarrow L_\alpha$ transition, circles represent the $L_\alpha - L_\beta$ transition and stars represent the transition to the H_{II} phase. Phase boundaries which are solid lines represent equilibrium phase boundaries whereas dashed lines represent metastable phase boundaries.

of these observed phenomena would be that the increased charge per headgroup increases the electrostatic repulsion between headgroups. This leads to a greater area per headgroup to the point where the acyl chains have to become tilted due to geometric packing considerations. These lipids should then be considered using the tilted-chain gel phase schematic where an $L_{\beta'} - P_{\beta'}$ pretransition is possible. Also, at a lower pH of 3, PS has been seen to display an H_{II} phase which is expected for amphiphiles with a packing parameter, P, greater than one.

It appears that the two schematics of generic phase behaviour in figure 2.9 can supply a good estimate to the phase behaviour of many phospholipids, providing a good source for deducing a first guess of the gel phase structures. These diagrams though are not able to provide a comprehensive guide to the phase behaviour as, for example, they do not predict the L_x phase that has been observed in DLPC [21]. A three-dimensional phase space that included temperature, acyl chain length and another parameter which encapsulated the headgroup interaction (i.e. the preferred area per headgroup in a given phase compared to the cross-sectional area of the acyl chains) may be able to provide a single phase-space for phospholipids with regions of tilted and untilted gel phases as well as, perhaps, inverted non-bilayer phases such as H_{II}. A guide to

the phase transitions of the lipids used in this thesis is shown in table 2.4; the main transition temperature for each lipid is highlighted in red.

2.4 Lipids in Nature & Medicine

This section addresses the occurrence of lipids in nature as well as medical science in an attempt to convey some of the wider interests and motivations of biophysical lipid, membrane and vesicle research. Firstly I will describe the current understanding of the structure of cell membranes including a brief guide to the major scientific question which currently surrounds cell membrane structure, the existence and nature of *lipid rafts*. The next section gives a brief description of the uses of lipids and vesicles in medicine, particularly concentrating on one aspect, drug delivery. Finally, I will address one of the most profound scientific questions of all: the origins of life. Have I really gone too far in proposing that my research could have any relevance to this issue?

Lipids also have uses in technology and have been utilised in the paint, cosmetics and food industries [14]. Despite their many applications in biology, medicine and industry, one should bear in mind that the main motivation for this project is interesting physics. Binary lipid vesicles provide an opportunity to investigate phase separation in quasi-two-dimensional systems. Biological molecules such as lipids have developed over billions of years by evolutionary processes resulting in highly sophisticated molecules which exhibit rich, fascinating physical phenomena.

2.4.1 Cell Membranes

The human body contains of order 10^{14} cells, although there are only around 200 different cell types [36]. All cells are surrounded by a membrane which defines their external boundary. This boundary controls the passage of material into and out of the cell interior, isolating cell contents and giving the cell structural stability.

Lipids are the main constituents of biological cell membranes. There are currently thought to be around 800 to 1000 different lipid species in a single cell membrane; these lipids include

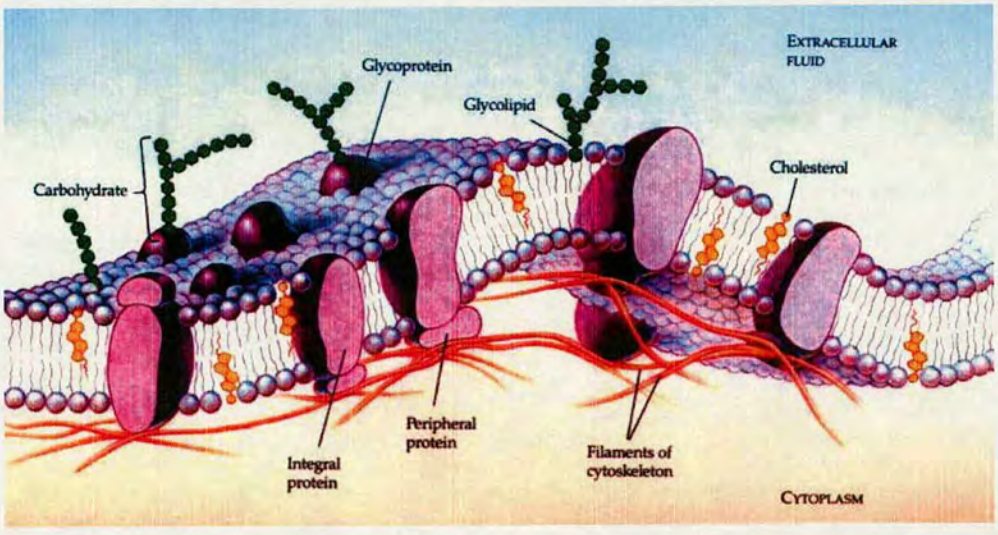

Figure 2.11: A cartoon of a portion of a biological cell membrane [37].

phospholipids, glycolipids and cholesterol. Membranes also contain proteins which have large hydrophobic parts to their exterior structure. These proteins 'hide' their exterior hydrophobic portions in the hydrophobic core of the lipid bilayer membrane, either spanning the whole membrane (integral proteins) or just a single leaflet of the bilayer, sometimes via a lipid 'anchor' (peripheral proteins).

The model of the cell membrane which has been used, without improvements, until recent times is the *fluid mosaic model*. This was proposed by Singer and Nicolson in 1972 [1]; their model addresses the molecular organisation of the membrane. The membrane is described as a fluid lipid bilayer acting as a 2D solvent for membrane proteins, which have rotational and lateral diffusion (see figure 2.11). The fluid mosaic model also predicts that there is no long range ordering (distances greater than a few hundred nm) within the membrane but does not discount the presence of short range order, for example a small fraction of the lipid being tightly coupled to a particular membrane protein, differentiating it from the bulk lipid.

More recently the structure and organisation of cell membranes has become a hot topic of research with the hypothesis that the membrane constituents are not randomly distributed, but instead are confined into domains termed '*rafts*' [38–49]. Several types of membrane hetero-

geneities are thought to exist: caveolae, confined diffusion due to actin networks and lipid rafts [38].

Caveolae are flask-shaped membrane invaginations which are about 60 nm in diameter. The main constituent of caveolae is the protein caveolin which binds cholesterol. Caveolae are thought to be important in the cellular processes of endocytosis, cholesterol transport and signal transduction (the movement of signals from outside to inside the cell) [43,48]. The second form of membrane heterogeneity mentioned above is due to the network of actin, which are shown in figure 2.11 as the filaments of cytoskeleton. Actin is a protein which is found under the cell membrane and provides structure to the cell, thus helping to maintain its shape. The diffusion of membrane proteins is hindered by the mesh-work of the cytoskeleton, resulting in transient confinement zones (TCZs) being detected by single particle tracking experiments. These TCZs have been found to be of order 300-600 nm in diameter with confinement times of around 3-30 s [50]. This confinement due to the mesh size of the actin network has led to the 'membrane skeleton fence' model [51] and the 'anchored protein picket' model [52] where membrane components can hop between compartments due to thermal fluctuations of the membrane.

The most elusive and controversial form of membrane heterogeneity are lipid rafts[7]. Lipid rafts are considered to be small liquid-ordered domains which have high cholesterol content and lipids, such as sphingolipids, with saturated acyl chains. Some membrane proteins, for example those with glycosylphosphatidylinositol (GPI) anchors, are thought to preferentially partition into lipid rafts. These 'raft' domains are considered to be surrounded by liquid-disordered membrane which has a faster molecular diffusion constant. Lipid rafts are considered to be the detergent resistant membranes (DRM[8]), the parts of the membrane which are insoluble in non-ionic detergents[9]. Caveolin is also found in the DRM fraction but caveolae should be considered as distinct structures separate from lipid rafts [38].

[7]Some biologists take the existence of lipid rafts as a proven fact whereas others dispute that they exist at all.

[8]Other acronyms used in the literature include DIGs (detergent insoluble glycolipid-enriched membrane domains), TIFFs (Triton-insoluble floating fractions) and GEMs (GSL (glycosphingolipid)-enriched membranes) [40].

[9]Experiments have shown that the addition of non-ionic detergent to a homogeneous membrane can cause DRM portions to be left in patches which resemble domains [53]. This hints at the possibility that DRM fractions do not suggest that the membrane, in vivo, has a heterogeneous structure corresponding to 'raft' domains of similar composition.

Lipid rafts have been implicated in membrane sorting and trafficking as well as signal transduction. Unlike the liquid-ordered/liquid disordered phase separation seen in simple cholesterol containing model membranes [6, 7, 9–12, 54, 55], lipid rafts are considered to be short-lived, dynamic structures which hints that they are not equilibrium structures [39]. One may expect that if these rafts were equilibrium structures then they would coalesce to form larger domains thereby reducing the interfacial line tension with the liquid-disordered phase as has been seen in artificial systems [9][10].

At the time of writing, lipid rafts have still not been unambiguously detected in vivo. The techniques that have been used in an attempt to probe these membrane domains yield contradictory results. These techniques include single-particle tracking [56], fluorescence techniques [40] and photonic force microscopy [57]. Experiments have also been carried out on model membrane systems containing natural lipid mixtures [6]. Predictions of raft diameter range from less than 5 nm with no more than four GPI-anchored proteins in a cluster [58] to micron sized domains [59]. These domains are seen to have lifetimes between 0.1 s and 10 minutes with an abundance of between 13% and 80% of the cell surface [38]. Differences in experimental techniques, conditions and cell types used could be responsible for these large variations in data with more than one type of lipid raft existing in a particular cell. A full review of current biophysical results of in vivo membrane hetrogeneities has been published by Lommerse et al. [38].

My experiments using binary lipid mixtures have no direct relationship to lipid raft structures as the domains formed are of solid-like gel phases, although an improved understanding of the behaviour of simple lipid mixtures is a stepping stone on the way to a better comprehension of the vastly more complicated systems of biological membranes. There is a thought published in a review by Edidin that lipid-protein interactions will be shown to be more important than lipid-lipid interactions in the structural organisation in membranes [49]. The fluidity of membranes has been shown to affect protein function, for example the amount and specific activity of the transmembrane proteins ToxR and ToxS found in the *Vibrio cholerae* bacterium were found to be altered by increasing pressure. This is because the increased pressure reduces the membrane fluidity [60].

[10] It should be noted that any biological system which reaches equilibrium would, in layman's terms, be dead!

Although gel phase domains are generally not considered to form in the plasma membrane of biological cells, there is evidence for their existence in a few specialist cells. Gel phase domains have been implicated in the membrane structures of the *stratum corneum* of mammalian skin [61], the axon myelin sheaths of the central nervous system [62] and sperm [63, 64].

The vast majority of papers published on the properties of phospholipids are of phospholipids with an even number of carbon atoms per acyl chain. This reflects the situation in nature: the anabolism and catabolism of fatty acids involves the two carbon units of acetyl Coenzyme A [21]. A small amount of lipids with fatty acid chains containing an odd number of carbon atoms are found in terrestrial organisms, although a greater abundance is found in marine life. The most common lipid head group used in phospholipid research is phosphatidylcholine, the most abundant in eukaryotic cells. This is followed by phosphoethanolamine which is generally the second most abundant head-group found in natural membranes [14, 65]. The most common acyl chains in the research literature are dipalmitoyl (two saturated 16 carbon chains) followed by dimyristoyl (two saturated 14 carbon chains). Other common acyl chains are stearoyl (saturated 18 carbon chain), lauroyl (saturated 12 carbon chain) and oleoyl (mono-unsaturated 18 carbon chain) [65]. The lipid compositions of membranes vary between different cell types, different organisms and different membranes within a cell [14] but membrane biology has a large influence on which lipids are preferentially studied by chemists and physicists.

2.4.2 Drug Delivery

Drug delivery systems (DDS) are ways of encapsulating drugs so that they can be transported in vivo to their target site before being released. Many DDS have already been given regulatory approval for medical use whilst others are in the stages or clinical trials [66]. One method of encapsulation is by use of lipid liposomes: hydrophobic drugs can be transported in the hydrophobic region of the lipids' hydrophobic tails and hydrophilic drugs can be transported in the aqueous interior of the liposomes. There are many advantages of using DDS over administering the unadulterated drug. Poor solubility and aggregation of hydrophobic drugs can be prevented by transportation in the hydrophobic environment of liposomes, drugs which are rapidly broken down in vivo can be protected in the DDS until reaching the target site reducing

the required dosage and damage caused to healthy tissues by distribution of the drug throughout the body is reduced by site-specific targeting of the DDS. Scientists are currently working on ligand-specific targeting of DDS as well as improving the control over the time and rate of drug release.

Another challenge for medicine is to get the drug across the cell membrane to the interior of the cell. The cell membrane is a semi-permeable barrier only letting specific molecules enter into the cell. So far, drugs which have managed to cross this barrier have been produced by good fortune rather than a good scientific understanding of how this is achieved [67]. A better understanding of lipid membranes will help produce more sophisticated DDS and aid our comprehension of the structure and function of the cell membrane leading to the development of techniques to transport drugs into the cell interior.

Phospholipids and liposomes have many other uses in medicine. They have applications in diagnosis (eg. immunoassays), artificial lung surfactants and artificial blood [14].

2.4.3 Origins of Life?

One of the big questions for science is, 'where, when and how did life[11] begin?'. The very first life-form would need to have a well-defined external boundary to differentiate it from its environment. The simplest such boundary that can be seen in modern day organisms is the cell membrane of single-cell organisms. The first cell would have been a comparatively simple organism, unlike any of the complex lifeforms that exist on Earth today. It's expected that the external membrane of the primitive cell would not have had all the complicated mechanisms of its neoteric descendant as described in section 2.4.1. The purpose of the primeval membrane would be to be impermeable to (i.e. trap) the primitive biochemical materials, probably some form of mixture of self-replicating nucleic acids, whilst being permeable to any materials needed to provide energy (i.e. fuel or feed) to the biomechanisms that were taking place inside [68]. This semi-permeable membrane would also need to be able to undergo fission, dividing into two, new identical lifeforms. Such a primitive entity born from the 'primordial

[11] I will make no attempt to define the properties that make something 'living'. There is no single definition of life that is agreed on by all biologists and although this point may be of importance in a full discussion of the origins of life, it is not essential to the brief discussion in this thesis.

soup would then evolve over billions of years, perhaps initially at least by copying errors in its nucleic acid sequence, into the array of different forms of life currently in existence [69].

One question that may be asked is, 'what gave rise to the presence of amphiphilic molecules in the primordial soup?'. A possible answer to this is that it came from outer space. This may sound like science fiction but research by NASA on a realistic model mixture of interstellar ice containing water, methanol, ammonia and carbon monoxide shows this to be a possibility [70]. Low temperature UV photolysis of this mixture produced amphiphilic molecules which self-assembled into vesicles in aqueous solution. This suggests that the molecular building blocks of primitive membranes could have been delivered to Earth by the bombardment of comets and meteorites which are made up from these interstellar ices.

Any biomimetic properties exhibited by simple model membranes investigated by biophysicists may hint at some of the properties and requirements of the original primitive cell membranes before evolution increased their complexity. The majority of scientific work written about the origins of life is highly speculative; for an excellent introduction to the topic read *The Fifth Miracle*, a popular science account of this subject area by astrophysicist Paul Davies [69].

Chapter 3

Theoretical Aspects

This chapter reviews some of the theoretical factors that are going to be relevant to this thesis. Firstly, much of the existing literature on the morphology of domains in lipid vesicles concentrates on the bending mechanics of membranes [71–78]. The mechanical parameters of membranes will be the subject of the first part of this chapter. The second part will discuss the kinds of topologies that we may predict for the equilibrium phase diagrams of binary systems as well as the compositions of these phases in equilibrium.

3.1 Membranes

The aspects of the theoretical treatment of membranes which I briefly review in this section follow the arguments of Boal in his book *Mechanics of the Cell* [36]. I will begin with a discussion of the area compression modulus, which is linked to the elasticity of bilayers and in turn can be related to the bending energy of membranes, which is the subject of the second part of this section. The bending energy is then compared to the edge tension to explain why bilayers form vesicles rather than flat sheets; my main motivation for introducing the concept of edge tension is for a discussion on vesicle lysis in chapter 8.5. Finally there is a brief overview of the interactions between lipid bilayers as I will compare these interactions to the bilayer bending rigidity when discussing vesicle adhesion in chapter 8.4.

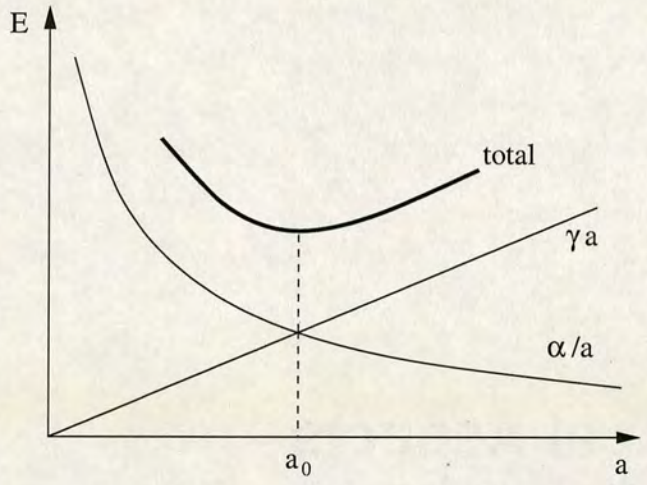

Figure 3.1: Diagram illustrating the interaction energy (E) between lipids in one layer of a bilayer as a function of the mean area per headgroup (a). The total interaction energy is equal to $\alpha a^{-1} + \gamma a$ and has a minimum at the equilibrium area per headgroup (a_0) [36].

3.1.1 Area Compression Modulus

The interaction between lipids in one layer of a bilayer in aqueous solution is the sum of the repulsion between the lipids, due to stretching of the hydrocarbon chains and steric interactions between lipids, and the attraction due to the surface tension at the lipid-water interface. The attraction occurs due to the energetic unfavourability of contacting the hydrophobic tails with the water and will be modelled as γa where a is the mean area per lipid headgroup and γ is the surface tension. The repulsion will be modelled as being proportional to a^{-1} for small deviations from the equilibrium area per headgroup, ignoring higher order terms in a^{-1}. This gives an interfacial energy per lipid of $E = \frac{\alpha}{a} + \gamma a$ where α is a constant. This energy as a function of a is illustrated in figure 3.1.

The equilibrium area per headgroup (a_0) can be found for this simple model by finding the minimum of the energy curve ($\frac{dE}{da} = 0$), giving $a_0 = \sqrt{\frac{\alpha}{\gamma}}$. We can use this to eliminate α from the energy equation, giving

$$E = 2\gamma a_0 + \frac{\gamma}{a}(a - a_0)^2 \,. \tag{3.1}$$

The first term is a constant so the change in energy, ΔE, when the area per headgroup changes from its equilibrium value is $\frac{\gamma}{a}(a - a_0)^2$. Dividing by a_0 and approximating $a \sim a_0$, we get an elastic energy density for the monolayer of $\gamma \left(\frac{a-a_0}{a_0}\right)^2$. The elastic energy density can also be written in terms of the area compression modulus as $\frac{1}{2}K_A(\Delta A)^2$ where ΔA is the relative change in area per headgroup, $\frac{a-a_0}{a_0}$. Comparison of these expressions for the elastic energy density gives, for a monolayer, $K_A = 2\gamma$ and hence for a bilayer, our simple model predicts an area compression modulus of

$$K_A = 4\gamma \,. \tag{3.2}$$

Typical values for the surface tension, γ, at a water-amphiphile interface[1] are around $0.02 - 0.05$ Jm^{-2} which leads to a prediction of K_A in the range $0.08 - 0.2$ Jm^{-2} [36]. Values for K_A have been measured experimentally by the aspiration of lipid vesicles; many of the results lie in the range $0.1 - 0.2$ Jm^{-2} [36].

3.1.2 Bending Rigidity

The bending of a flat bilayer involves the compression of the inner monolayer and the expansion of the outer monolayer, displacing the mean area per headgroup from its equilibrium value. As was seen in the previous section, this requires energy.

First we define the radius of curvature (C) for a surface as the rate of change of the unit vector tangential to the surface along a particular direction. The simplest example of a sphere of radius R has a curvature $C = \frac{1}{R}$. In general however, it is not possible to describe a surface by a single curvature, two curvatures are needed in mutually orthogonal directions along the surface. The two curvatures (C_i) are defined by their radii of curvature (R_i) such that $C_i \equiv \frac{1}{R_i}$ where $i = 1, 2$.

The energy per unit area ($\mathcal{E}$) to bend a flat surface can be described in terms of the squared mean curvature $(\frac{C_1+C_2}{2})^2 = \frac{1}{4}\left(\frac{1}{R_1} + \frac{1}{R_2}\right)^2$ and the Gaussian curvature $C_1C_2 = \frac{1}{R_1R_2}$. The

[1] This is crudely estimated by the water/hydrocarbon surface tension.

energy density is then written as[2]

$$\mathcal{E} = \frac{\kappa_b}{2}\left(\frac{1}{R_1} + \frac{1}{R_2}\right)^2 + \frac{\kappa_G}{R_1 R_2}\,, \tag{3.3}$$

where κ_b is the bending rigidity and κ_G is the Gaussian bending rigidity. The energy (E_{sp}) required to bend a flat bilayer into a sphere where $C_1 = C_2 = \frac{1}{R}$ can hence be calculated. The energy per unit area, $\mathcal{E} = \frac{E_{sp}}{4\pi R^2}$ can be inserted into equation 3.3 to give

$$E_{sp} = 4\pi(2\kappa_b + \kappa_G)\,, \tag{3.4}$$

which is independent of the radius of the sphere. Most measurements in the literature are of the bending rigidity κ_b; few measurements of κ_G have been made.

The bending rigidity of lipid bilayers has been measured by analysing the thermal fluctuations of vesicles [79, 80] and also using vesicle aspiration techniques [81]. The measured values are around 10^{-19} J or $\sim 10 - 20\ k_B T$ where k_B is Boltzmann's constant and T is the temperature, i.e. $k_B T$ is a measure of the thermal energy.

As stated at the beginning of this section, the bending of a bilayer involves the compression of the inner leaflet and expansion of the outer leaflet. Hence, we should be able to model the bending rigidity in terms of the area compression modulus. Several attempts at this have been made, where the polymer brush model [82] appears to be the most successful giving the expression [36]

$$\kappa_b = \frac{K_A d_{bl}^2}{24}\,. \tag{3.5}$$

Here d_{bl} is the bilayer thickness.

[2]Equation 3.3 assumes a symmetrical bilayer, i.e. both monolayers are identical and hence the natural curvature of the membrane would be to be flat. If there was an asymmetry between monolayers that led to a preferred curvature of the bilayer then the mean squared curvature of the bilayer can be modified to $\left(\frac{C_1+C_2-C_0}{2}\right)^2$, where C_0 is the spontaneous curvature of the bilayer. For our case of the symmetrical bilayer, $C_0 = \frac{1}{R_0}$ where the spontaneous (natural) radius of curvature, R_0, is infinite due to the bilayer's preference to be flat. Hence $C_0 \to 0$ and can be removed from our equation for the bending energy of symmetrical membranes.

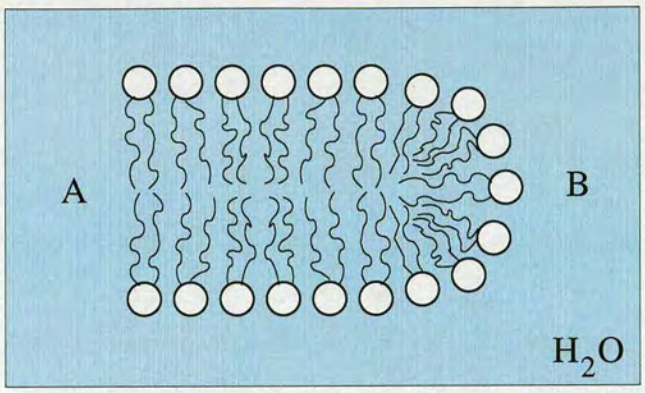

Figure 3.2: Illustration of two possibilities of how the edges of a flat may look: (A) the bilayer terminates exposing the hydrophobic tails of the edge lipids to the water, or (B) there is an end cap of high curvature where the lipid heads still shield the hydrophobic tails from the aqueous environment.

3.1.3 Edge Tension: why bilayers form vesicles

In chapter 2.2 I showed that phospholipids preferred to self-assemble into bilayers but so far I have not discussed why these bilayers close up to form vesicles. If we had a flat lipid bilayer then the edges of the bilayer would be exposed to the aqueous environment in one of two ways as shown in figure 3.2. Situation A has an associate energy cost due to the hydrophobic chains at the edge of the bilayer being exposed to the water. Similarly, situation B also costs energy since, as was shown in section 2.2, phospholipids have a packing parameter which favours bilayers rather than the high curvature of a micelle which would be needed to create such an end cap.

We will model this energy cost by an edge tension (λ), as an energy per unit length. We will assume that λ does not depend on the curvature of the boundary at the bilayer edge. If we consider a spherical vesicle of radius R_v and a flat bilayer disc of the same area, hence a radius $2R_v$, the energy cost of the the disc boundary, E_{disc}, is

$$E_{disc} = 4\pi R_v \lambda \,. \tag{3.6}$$

This can be compared to the energy cost in bending a flat bilayer into a sphere (E_{sp}) from equation 3.4. If we assume zero temperature and hence ignore any entropic contribution then

this results in a critical radius

$$R_v^* = \frac{2\kappa_b + \kappa_G}{\lambda} \tag{3.7}$$

above which vesicles are energetically preferential to flat bilayer discs and will form as long as the energy barrier for vesicle formation can be overcome. Experiments give $\lambda \sim 10^{-11}$ Jm^{-1} which corresponds to a minimum vesicle radius of $R_v^* \sim 15$ nm (taking $\kappa_b \sim \kappa_G \sim 10\ k_BT$) [36]. This critical radius for vesicle formation is three orders of magnitude less than the radii of the GUVs studied in my experiments, which had radii in the range of around $5 - 80\ \mu$m. If we now model the energy barrier to vesicle formation by considering a bowl of constant radius of curvature R and surface area $4\pi R_v^2$. The perimeter of the bowl (p) can be calculated by [36,83]

$$p = 4\pi R_v \left(1 - \frac{R_v^2}{R^2}\right)^{\frac{1}{2}} . \tag{3.8}$$

Combining the edge energy and the bending energy, this gives a total energy of

$$E = 4\pi\lambda R_v \left(1 - R_v^2 C^2\right)^{\frac{1}{2}} + 4\pi R_v^2 C^2 \left(2\kappa_b + \kappa_G\right) , \tag{3.9}$$

where the curvature C is equal to $1/R$. If we substitute R_v for R_v^* as defined in equation 3.7 and minimise the total energy E with respect to the curvature C, we can find the the radius of curvature where the energy is a maximum. Substituting this back into the total energy in equation 3.9 to find the maximum energy E_{max} and dividing by the energy needed to bend a flat membrane into a sphere, E_{sp} (from equation 3.4), we obtain that

$$\frac{E_{max}}{E_{sp}} = \frac{5}{4} . \tag{3.10}$$

This means that there is an energy barrier to vesicle formation for $R_v = R_v^*$ and so energy must be put into the system to form vesicles of this radius. A more detailed discussion of vesicle formation can be found in the literature [84].

3.1.4 Interaction Between Membranes

Here I will give a brief overview of the interaction between lipid membranes. The vesicles in my experiments are adjacent to other vesicles which are in turn attached to an electrode. The inter-membrane interactions will become relevant to my discussion of vesicle adhesion in chapter 8.4. Interactions between membranes are extremely complex and still an active area of research. A full treatment of this subject is beyond the scope of this thesis, so for further reading see Israelachvili [17], Safran [85] or Leckband and Israelachvili [86].

The interaction between membranes have contributions from:

- Van der Waals attraction of induced, fluctuating and permanent dipoles;
- Electrostatic repulsion of charged membranes;
- Steric repulsion from membrane undulations;
- Repulsive hydration forces.

The **van der Waals** potential for a molecule has a long-range attractive term due to fluctuating dipoles which decays as r^{-6} and a short range repulsion originating from the overlap of electron clouds which decays as r^{-12}, where r is the distance between the molecules. The attractive van der Waals interaction energy can be shown to decay less rapidly for geometries other than intermolecular interactions: relevant to membranes is the interaction between two rigid thin sheets, where the separation (D) is greater than the sheet thickness, which decays as D^{-4}. When the separation of the sheets becomes considerably less than the sheet thickness then the attraction decays as D^{-2} [17, 36]. The van der Waals interaction is screened by ions in the aqueous solution between the membranes. This screening is not completely exponential and the screening length is half the Debye length (l_D) which will be explained in the discussion of electrostatics below.

The dimensionless electrostatic potential (Ψ) at a distance z from a charged plate in an electrolyte is given by $\Psi(z) = \Psi_0 \exp\left(-\frac{z}{l_D}\right)$ where Ψ_0 is the potential at the charged plate and l_D is the Debye screening length mentioned above. The dimensionless electrostatic potential can also be written as $\Psi(z) \equiv \frac{q\psi(z)}{k_B T}$ where ψ is the electrostatic potential, q is the charge on

an ion, k_B is Boltzmann's constant and T is the temperature. The Debye length can be defined as $l_D^{-2} \equiv 8\pi l_B \rho_s$ where ρ_s is the number density of monovalent ions in the bulk solution and l_B is the Bjerrum length. The Bjerrum length is defined as $l_B \equiv \frac{q^2}{4\pi\varepsilon k_B T}$ where ε is the permitivity of the medium in which the ions are dissolved (water), in other words, it is the distance at which two charges of magnitude q in a medium of dielectric constant ε have energy equal to $k_B T$. The Debye length is a length scale over which electrostatic potentials are screened; for pure water, $l_D \sim 1.0$ μm at room temperature (due to auto-dissociation of water). Two identically charged plates which approach each other in a monovalent[3] electrolyte experience an **electrostatic repulsion**. The repulsive pressure (P) from the screened electrostatics between the plates decays exponentially with distance between the plates (D) and can be written as [36]:

$$P \cong 64\rho_s k_B T \tanh^2\left(\frac{\Psi_0}{4}\right) \exp\left(-\frac{D}{l_D}\right) . \tag{3.11}$$

At low ψ_0 (the electrostatic potential at the plates), this can be simplified to

$$P = \left(\frac{2\sigma_s^2}{\varepsilon}\right) \exp\left(-\frac{D}{l_D}\right) , \tag{3.12}$$

where σ_s is the charge density on the plates.

Electrostatic and van der Waals interactions can be combined using the DLVO (Derjaguin, Landau, Verwey and Overbeek) theory. For interactions between membranes in an electrolyte, van der Waals interactions dominate at short distances. In low ionic strength solutions, electrostatics dominates at longer distances. If the ionic strength is high then it is possible that, due to a short Debye length, electrostatics quickly become screened out so that they only dominate at intermediate distances with van der Waals interactions dominating both at short and long ranges [36].

Lipid bilayers exhibit thermal fluctuations which exert an entropic repulsion between membranes. This **steric repulsion** results in a pressure which decays as D^{-3}, where D is the inter-membrane separation. A review of membrane undulations can be found in chapter 6 of Boal [36].

[3] In an electrolyte with higher charges, correlation effects can sometimes induce an attraction [17].

The lipid headgroups of a membrane wish to be hydrated, i.e. they desire to be in contact with water. This means that energy is required to remove water from between two bilayers as they approach each other and hence there is a repulsive interaction known as the **hydration force** between the membranes. This is a very short range interaction (of order a few tens of angstroms) which only becomes important when the hydration layers of the membranes begin to overlap. A model of two flat plates approaching each other in a solvent predicts an interaction which oscillates between attractive and repulsive on the molecular length scale of the solvent but due to the roughness of the membrane surface on the length scale of a water molecule, the interaction due to hydration is seen to be monotonically repulsive. The repulsive energy per unit area due to the hydration of the membranes has been modelled to decay as $\exp\left(-\frac{D}{\lambda_h}\right)$, where the length scale λ_h is of order 2 Å [87]. For a review on hydration forces between phospholipid bilayers see Rand and Parsegian [88].

3.2 Equilibrium Phase Diagrams

In this section I discuss the topology of equilibrium phase diagrams for binary mixtures and the information which can be extracted from them. Phase diagrams offer pictorial representations of what is known about the equilibrium states of materials under a range of thermodynamic conditions. In this section I will concentrate on temperature-composition phase diagrams as this is the type commonly found in the literature for binary lipid mixtures.

3.2.1 General Properties

For a binary system, the equilibrium state under given conditions can consist of up to four (number of components plus two degrees of freedom for temperature and pressure, using the *Gibbs phase rule*) coexisting phases. The equilibrium state of a system is the state of minimum free energy, hence it can be shown that the pressures and chemical potentials of coexisting phases must be equal in equilibrium.

Let us consider a system that has three phases (1-3). The system has total mass M, total volume V and internal energy U, conservation of these three quantities allows us to write down the

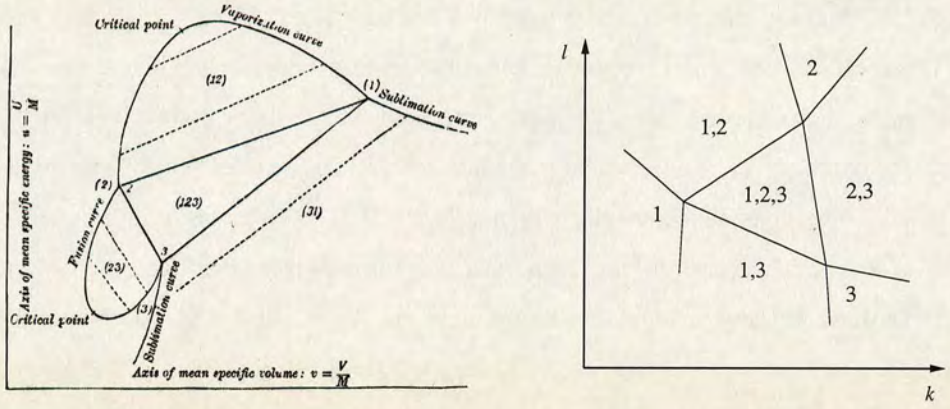

Figure 3.3: (a) [*left*] Phase diagram sketched by Planck of specific energy u against specific volume v for a three phase (1-3) system where $v_1 < v_3 < v_2$ and $u_1 < u_2 < u_3$ [89]. (b) [*right*] Generic topology for a region of three phase coexistence (1, 2 and 3) in a phase diagram with two thermodynamic variables, k and l.

following equations:

$$M_1 + M_2 + M_3 = M \,, \tag{3.13}$$

$$M_1 v_1 + M_2 v_2 + M_3 v_3 = V \,, \tag{3.14}$$

$$M_1 u_1 + M_2 u_2 + M_3 u_3 = U \,. \tag{3.15}$$

M_i represents the mass of phase i, v_i represents the specific[4] volume of phase i and u_i represents the specific energy of phase i. Further conditions of $M_i, v_i, u_i \geq 0$ are applied so that these terms have physical meaning. Planck used these conditions to work out topological constraints for a phase diagram in the $v - u$ plane ($v = \frac{V}{M}$, $u = \frac{U}{M}$) for $v_1 < v_3 < v_2$ and $u_1 < u_2 < u_3$, i.e. a substance like water where 1 = gas, 2 = liquid and 3 = crystal [89]. The phase diagram that Planck sketched using these constraints is shown in figure 3.3a[5]. A phase diagram for u against v can be scaled to temperature against inverse mass density, so is comparable to the temperature against composition phase diagrams of lipids if mass density is considered analogous to composition.

[4] per unit mass

[5] It should be noted that Planck got one thing wrong: there is no critical point along the fusion curve since liquid and crystal phases have fundamentally different symmetries, and hence cannot be linked by a critical point.

For a phase i to exist in a region of the phase diagram, then M_i must be greater than zero under the relevant conditions u and v that define the region of the phase diagram where phase i exists. Planck shows that a three phase region must have a triangular topology where each side is bounded by a two phase region whose boundaries pass through the vertices of the three phase triangle. The two phase region may or may not have a critical point. The two phase regions are, in turn, bound by single phase regions where each single phase represents a vertex of the three phase triangle. A generic phase diagram topology for a region three phase coexistence in terms of two random thermodynamic variables k against l is shown in figure 3.3b. The two phase regions may or may not come together at a critical point, but no critical points are shown on the diagram.

3.2.2 Complete Solid Phase Miscibility

If we consider a binary mixture of two components, A and B, which are completely miscible in both the solid and fluid phases forming ideal mixtures, then the two solid phases of components A and B must have identical symmetry. This would also require the two components to be chemically similar so that one could directly substitute molecules of component A for molecules of component B in the solid phase. If we follow the arguments of Lee [90], then we can derive the expected phase diagram topology.

At equilibrium, the chemical potentials for the components in the liquid and solid phases must be equal:

$$\mu_A^{(s)} = \mu_A^{(l)} , \tag{3.16}$$

$$\mu_B^{(s)} = \mu_B^{(l)} . \tag{3.17}$$

Here $\mu_i^{(s)}$ represents the chemical potential of component i in the solid phase and $\mu_i^{(l)}$ represents the chemical potential of component i in the liquid phase. If we now just consider component A, we can write the chemical potentials for one mole as

$$\mu_A^{(l)} = \mu_A^{(l)\circ} + RT \ln x_A^{(l)} , \tag{3.18}$$

$$\mu_A^{(s)} = \mu_A^{(s)\circ} + RT \ln x_A^{(s)} \,, \tag{3.19}$$

where $\mu_A^{(l)\circ}$ and $\mu_A^{(s)\circ}$ are constants, $x_A^{(l)}$ and $x_A^{(s)}$ are the mole fractions of component A in the liquid and solid phases respectively, T is the temperature, and R is the molar gas constant. Substituting equations 3.18 and 3.19 into equation 3.16, we get

$$\ln \frac{x_A^{(l)}}{x_A^{(s)}} = \frac{-\mu_A^{(l)\circ} + \mu_A^{(s)\circ}}{RT} \,. \tag{3.20}$$

We can now write[6]

$$\frac{\partial \ln(x_A^{(l)}/x_A^{(s)})}{\partial T} = \frac{H_A^{(l)\circ} - H_A^{(s)\circ}}{RT^2} \,, \tag{3.21}$$

where $H_A^{(l)\circ}$ and $H_A^{(s)\circ}$ are molar enthalpies of component A in pure liquid and solid phases. If we define $(\Delta H_A)_T = H_A^{(l)\circ} - H_A^{(s)\circ}$ as the heat of melting of pure component A at temperature T, this can be related to the latent heat of melting at the melting temperature, T_A, by

$$(\Delta H_A)_T = (\Delta H_A)_{T_A} + \int_{T_A}^{T} \Delta C_p \, \mathrm{d}T \,, \tag{3.22}$$

where ΔC_p is the difference in specific heats of the liquid and solid phase of component A. Integrating gives $(\Delta H_A)_T = (\Delta H_A)_{T_A} + \Delta C_p(T - T_A)$. Assuming $\Delta C_p = 0$ which is considered to be reasonable over a small range of temperature close to T_A, equation 3.21 can be integrated as follows:

$$\ln \frac{x_A^{(l)}}{x_A^{(s)}} = \int_{T_A}^{T} \frac{(\Delta H_A)_{T_A}}{RT^2} \, \mathrm{d}T \,. \tag{3.23}$$

[6]The change from chemical potential difference to enthalpy difference can be justified by considering that $\mu = \frac{G}{N}$ where G is the Gibbs free energy and N is the number of molecules. We can write $G = U - TS + pV$ and enthalpy, $H = U + pV$ where U is internal energy, S is entropy, p is pressure and V is volume. Hence $G = H - TS$, which when substituted into the equation for μ gives $\mu = h - Ts$ where h is the molar enthalpy and s is the molar entropy. If we now add superscripts l and s to denote the liquid and solid phases, $\mu^l - \mu^s = h^l - h^s - T(s^l - s^s)$. The Clausius-Clapeyron equation tells us that $\frac{\mathrm{d}p}{\mathrm{d}T} = \frac{\Delta s}{\Delta v}$ where v is the molar volume. We now have $\mu^l - \mu^s = h^l - h^s - T\frac{\mathrm{d}p}{\mathrm{d}T}\Delta v$, which if we assume fixed pressure reduces to $\mu^l - \mu^s = h^l - h^s$ as required.

Solving this integral and exponentiating each side of the equation gives

$$\frac{x_A^{(l)}}{x_A^{(s)}} = \exp\left[-\frac{(\Delta H_A)_{T_A}}{R}\left(\frac{1}{T} - \frac{1}{T_A}\right)\right] = \mathrm{e}^{-A} . \tag{3.24}$$

A similar argument for component B gives

$$\frac{x_B^{(l)}}{x_B^{(s)}} = \exp\left[-\frac{(\Delta H_B)_{T_B}}{R}\left(\frac{1}{T} - \frac{1}{T_B}\right)\right] = \mathrm{e}^{-B} . \tag{3.25}$$

In equations 3.24 and 3.25, the last equality in each case serves to define the quantities A and B respectively. Using the equations $x_A^{(l)} + x_B^{(l)} = 1$ and $x_A^{(s)} + x_B^{(s)} = 1$ with equations 3.24 and 3.25, we have four equations for the four unknown parameters $x_A^{(l)}$, $x_B^{(l)}$, $x_A^{(s)}$ and $x_B^{(s)}$. Solving these, we get for the liquidus curve

$$x_A^{(l)} = \frac{\mathrm{e}^{-A}(\mathrm{e}^{-B} - 1)}{\mathrm{e}^{-B} - \mathrm{e}^{-A}} , \qquad x_B^{(l)} = \frac{\mathrm{e}^{-B}(\mathrm{e}^{-A} - 1)}{\mathrm{e}^{-A} - \mathrm{e}^{-B}} , \tag{3.26}$$

and for the solidus curve

$$x_A^{(s)} = \frac{\mathrm{e}^{-B} - 1}{\mathrm{e}^{-B} - \mathrm{e}^{-A}} , \qquad x_B^{(s)} = \frac{\mathrm{e}^{-A} - 1}{\mathrm{e}^{-A} - \mathrm{e}^{-B}} . \tag{3.27}$$

These equations can be used to draw a theoretical phase diagram for a binary system with complete solid phase miscibility. Such a phase diagram would look similar to the phase diagram in figure 3.4 where between the single phase regions of liquid and solid is a region of two phase coexistence between liquid and solid phases.

3.2.3 Regular Solutions

We will again follow the arguments of Lee to investigate the effects of non-ideal mixing in binary solutions [90]. In the previous section we assumed that the fluid and solid phases were ideal solutions so, in a mixture, component A had a chemical potential $\mu_A = \mu_A^\circ + RT \ln x_A$ and component B had a chemical potential $\mu_B = \mu_B^\circ + RT \ln(1 - x_A)$. The molar Gibbs free energy ($G = \frac{\mu}{N_A}$) is therefore

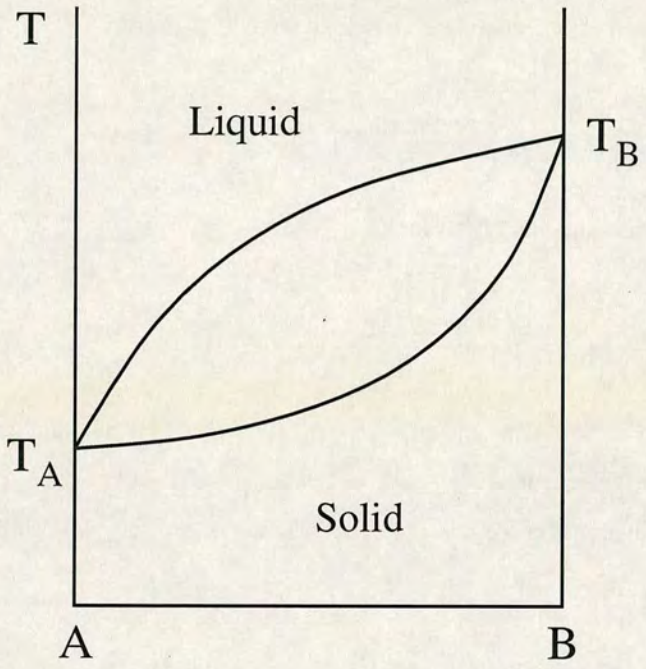

Figure 3.4: Phase diagram of a binary system, components A and B, with temperature (T) on the vertical axis and composition on the horizontal axis. The phase diagram is for a system which shows complete miscibility in the solid and liquid phases. The solid and liquid phases are assumed to be ideal mixtures. The phase transition temperature of pure component A is T_A and the phase transition temperature of pure component B is T_B. Between the single phase regions of the liquid phase and the solid phase is a region of two phase coexistence between liquid and solid phases.

$$G = x_A\mu_A^\circ + (1 - x_A)\mu_B^\circ + RT(x_A \ln x_A + (1 - x_A)\ln(1 - x_A)) \; . \tag{3.28}$$

The energy of mixing (ΔG_m) is the difference between this free energy and the free energy of a mechanical mixture of A and B, $x_A\mu_A^\circ + (1 - x_A)\mu_B^\circ$. Thus

$$\Delta G_m = RT(x_A \ln x_A + (1 - x_A)\ln(1 - x_A)) \tag{3.29}$$

and the entropy of mixing (ΔS_m) can be obtained by differentiating this with respect to the temperature

$$\Delta S_m = R(x_A \ln x_A + (1 - x_A)\ln(1 - x_A)) \; . \tag{3.30}$$

From the relationship

$$\Delta G_m = \Delta H_m - T\Delta S_m \,, \tag{3.31}$$

where ΔH_m is the enthalpy of mixing, it can be seen that for an ideal solution $\Delta H_m = 0$. Now for a non-ideal solution, the molar chemical potential for component A can be written as

$$\mu_A = \mu_A^\circ + RT \ln x_A j_A \,, \tag{3.32}$$

where j_A is known as the activity coefficient of component A. This gives an excess chemical potential (μ_A^e), or deviation from ideality, of $\mu_A^e = RT \ln j_A$ and an excess free energy for the mixture of $G^e = x_A \mu_A^e + x_B \mu_B^e$. The regular solutions model[7] for non-ideal mixing assumes that the entropy of mixing tends to the value obtained for ideal solutions but the enthalpy of mixing is now

$$\Delta H_m = \rho_\circ x_A x_B \,, \tag{3.33}$$

where $\rho_\circ$ is a constant related to the pair interaction energies between components:

$$\rho_\circ = Z(2U_{AB} - U_{AA} - U_{BB}) \,. \tag{3.34}$$

In the above equation, Z is the coordination number, i.e. the number of adjacent molecules in the packing structure, and U_{ij} is the pair interaction energy between component i and component j. Physically, $\rho_\circ$ is the simplest way of modelling whether components A and B want to stay close or separate from each other depending on the sign of equation 3.34. We can now work backwards from the enthalpy of mixing to obtain expressions for the excess chemical potentials of the components. As ΔS_m is defined to be the same as for ideal solutions (equation 3.30), from equation 3.31, the excess free energy must be equal to the enthalpy of mixing:

[7] This is equivalent to the Bragg-Williams model originally developed to account for order-disorder transitions in metallic alloys (such as Brass = copper + zinc).

$$x_A\mu_A^e + x_B\mu_B^e = \rho_\circ x_A x_B \ . \tag{3.35}$$

The functional forms μ_A^e and μ_B^e must be similar, giving the same solution if the subscripts A and B are switched. Multiplying the right hand side of equation 3.35 by $(x_A + x_B)$, which is equal to unity, we obtain by inspection

$$\mu_A^e = \rho_\circ x_B^2 \ , \qquad \mu_B^e = \rho_\circ x_A^2 \ . \tag{3.36}$$

If we now return to the problem of two components A and B which show complete miscibility in the liquid and solid phases but this time assume that these mixtures are no longer ideal but instead are regular solutions then the chemical potentials for each in component in the solid and liquid phases can be written as:

$$\mu_A^{(s)} = \mu_A^{(s)\circ} + RT\ln x_A^{(s)} + \rho_\circ^{(s)}(1 - x_A^{(s)})^2 \ , \tag{3.37}$$

$$\mu_B^{(s)} = \mu_B^{(s)\circ} + RT\ln(1 - x_A^{(s)}) + \rho_\circ^{(s)}(x_A^{(s)})^2 \ , \tag{3.38}$$

$$\mu_A^{(l)} = \mu_A^{(l)\circ} + RT\ln x_A^{(l)} + \rho_\circ^{(l)}(1 - x_A^{(l)})^2 \ , \tag{3.39}$$

$$\mu_B^{(l)} = \mu_B^{(l)\circ} + RT\ln(1 - x_A^{(l)}) + \rho_\circ^{(l)}(x_A^{(l)})^2 \ , \tag{3.40}$$

The conditions for equilibrium are $\mu_A^{(s)} = \mu_A^{(l)}$ and $\mu_B^{(s)} = \mu_B^{(l)}$. Following a similar argument to that in section 3.2.2, the simultaneous equations

$$\ln\frac{x_A^{(l)}}{x_A^{(s)}} + \frac{\rho_\circ^{(l)}(1 - x_A^{(l)})^2 - \rho_\circ^{(s)}(1 - x_A^{(s)})^2}{RT} = -\frac{(\Delta H_A)_{T_A}}{R}\left(\frac{1}{T} - \frac{1}{T_A}\right) \ , \tag{3.41}$$

$$\ln\frac{1 - x_A^{(l)}}{1 - x_A^{(s)}} + \frac{\rho_\circ^{(l)}(x_A^{(l)})^2 - \rho_\circ^{(s)}(x_A^{(s)})^2}{RT} = -\frac{(\Delta H_B)_{T_B}}{R}\left(\frac{1}{T} - \frac{1}{T_B}\right) \ , \tag{3.42}$$

are obtained [90]. These cannot be solved analytically and hence numerical methods need to be used. Many of the binary lipid phase diagrams in the literature are modelled using this method as will be seen in chapter 6, where whether such a model for binary lipid mixtures is suitable will also be discussed.

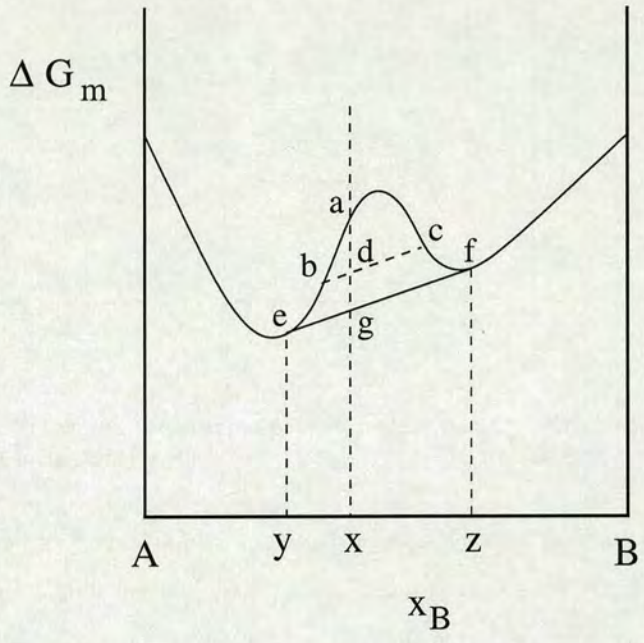

Figure 3.5: Free energy of mixing (ΔG_m) against composition (x_B) for a temperature at which an immiscibility gap is possible.

Free Energy Landscapes

Now we will consider the free energy landscape of a mixture with a miscibility gap. The free energy of mixing is given by equation 3.31. If the enthalpy of mixing is positive then this function can, over a certain range of temperatures, have a local maximum point as shown in figure 3.5. If we have a sample with total composition x, the free energy of the homogeneous solution is a. If we demix the sample into two phases along the line b-c then the free energy of the solution is now d, which is lower than a. In equilibrium, the sample minimises its free energy. This condition is met by phase separating into two solutions of compositions y and z which are defined by the common tangent to the free energy of mixing curve. The minimum free energy of the sample of composition x is therefore at point g. At this temperature, the equilibrium state of a sample of composition $0 \leq x_B \leq y$ or $z \leq x_B \leq 1$ will be a homogeneous solution but for $y \leq x_B \leq z$, the equilibrium state will be a solution of composition y coexisting with a solution of composition z.

Similarly, if we consider figure 3.6, the free energy landscapes as a function of composition

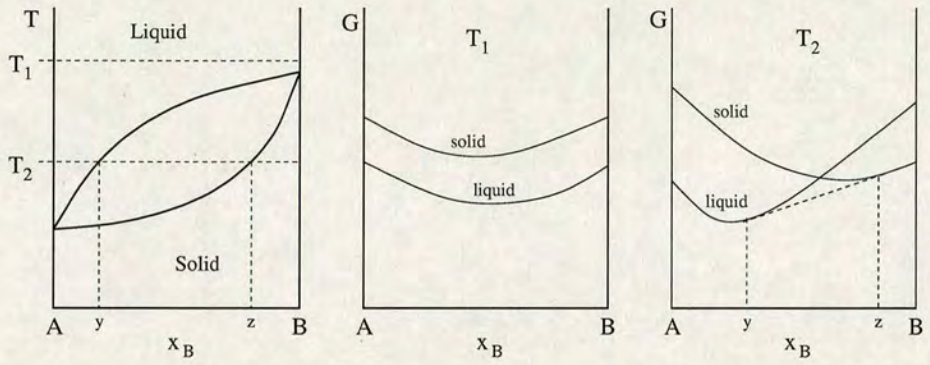

Figure 3.6: [*left*] Phase diagram for a binary system showing two temperature cuts, T_1 and T_2. [*centre*] Free energy landscape at temperature T_1. [*right*] Free energy landscape at temperature T_2.

are plotted for temperatures T_1 and T_2. At temperature T_1 the free energy of the liquid phase is always lower than that of the solid phase and hence the equilibrium state is always a single component liquid. At temperature T_2, the liquid phase is of lowest free energy for some compositions and the solid phase has the lowest free energy for other compositions: for $0 \leq x_B \leq y$ the equilibrium phase is a liquid of composition x_B, for $z \leq x_B \leq 1$ the equilibrium phase is a solid of composition x_B and for $y \leq x_B \leq z$ the equilibrium state is a coexistence of a liquid phase of composition y and a solid phase of composition z. The phase diagram for a system can be evaluated by investigating the family of free energy curves as the temperature is varied.

3.2.4 Other Categories

Regular solution theory can be extended in an attempt to model more complicated deviations from non-ideality. One such method is to add an extra constant (ρ_{o1}) to the enthalpy of mixing so that it is now of the form [90]

$$\Delta H_m = x_A x_B(\rho_o + \rho_{o1} x_B) \, . \tag{3.43}$$

If this form of the enthalpy of mixing provides a suitable fit to the experimental data then the mixture is know as a *sub-regular solution*. Other similar methods are in the literature [91]. It should be noted though that the addition of further constants to fit experimental data can

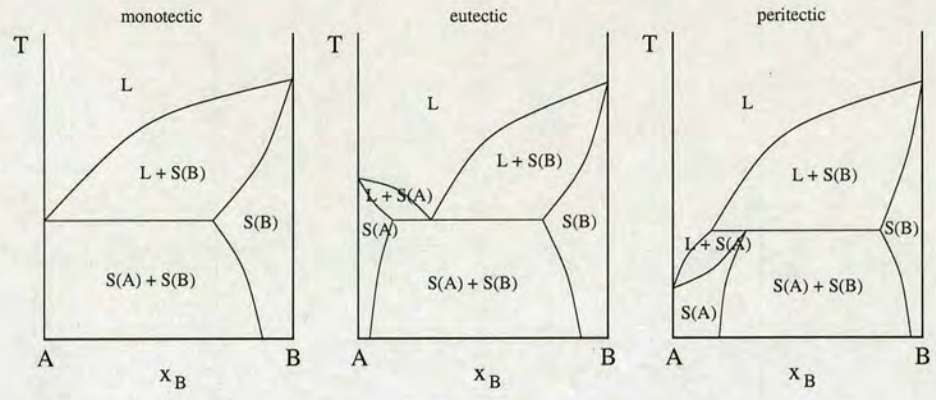

Figure 3.7: Phase diagrams showing solid phase immiscibility: [*left*] monotectic, [*centre*] eutectic, [*right*] peritectic. L denotes the liquid phase, $S(A)$ represents the solid phase of pure component A and $S(B)$ represents the solid phase of pure component B.

soon become just an exercise of curve fitting where the extra constants provide no real physical insight into the system. There is no physical meaning for ρ_{o1}, this is just a first step in just fitting the data.

If the two components, A and B, have different solid phase structures then they are likely to exhibit regions of solid phase immiscibility in the phase diagram. Some examples of equilibrium binary phase diagrams which exhibit solid phase immiscibility and are possibilities for binary phospholipid mixtures are shown in figure 3.7 [91]. Phase diagrams similar to the peritectic phase diagram shown will be encountered in chapter 6.

3.2.5 The Lever Rule

When in a region of two phase coexistence in the phase diagram, it would be desirable to be able to calculate a predicted equilibrium mole fraction of each phase. A temperature-composition binary phase diagram is shown in figure 3.8 with a region of two phase coexistence. The composition axis runs from zero to one representing the mole fraction of a component B in a sample containing another component, A. We start with a sample of total composition x_t in the high temperature, single phase region and cool it into the two phase region to a temperature T_1. Once the sample has equilibrated, the sample phase separates into a phase of composition x_a coexisting with a second phase of composition x_b along an isothermal tie-line as shown in

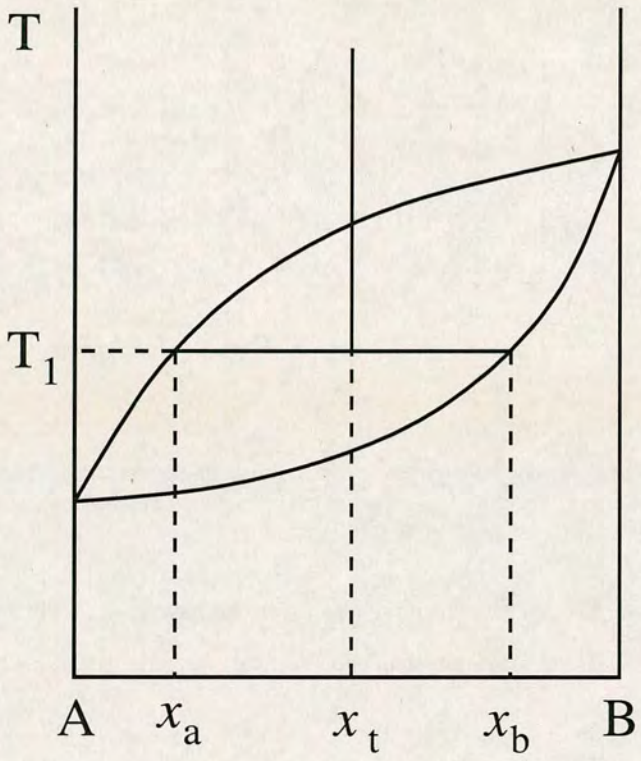

Figure 3.8: Schematic of a binary phase diagram for components A and B. The vertical axis represents the temperature of the system and the horizontal axis represents the mole fraction of component B in the sample with component A. The phase diagram has a region of two phase coexistence. If a sample of overall composition x_t is cooled to temperature T_1 then the sample, in equilibrium, phase separates into two phases of composition x_a and x_b. The mole fractions of each phase (ϕ_a and ϕ_b) can be calculated using the Lever Rule (*see text*).

figure 3.8. This phase coexistence represents the condition of minimising the free energy of the system as discussed earlier.

To calculate the mole fractions, ϕ_i, of each phase of composition x_i (where $i = a, b$), we can use the condition of conservation of number of molecules of each component, A and B. Initially, the total mole fraction of component B is x_t and of component A is $1-x_t$. After phase separation, these total mole fractions must be conserved as we are not adding or subtracting molecules from the system. This results in the conservation equations

$$(1 - x_t) = \phi_a(1 - x_a) + \phi_b(1 - x_b) \,, \tag{3.44}$$

$$x_t = \phi_a x_a + \phi_b x_b \, . \tag{3.45}$$

Rearranging for ϕ_a in equation 3.45 and substituting into equation 3.44, we obtaining after rearranging for ϕ_b and simplifying:

$$\phi_b = \frac{x_t - x_a}{x_b - x_a} \, . \tag{3.46}$$

Similarly, for ϕ_a we obtain

$$\phi_a = \frac{x_b - x_t}{x_b - x_a} \, . \tag{3.47}$$

Equations 3.46 and 3.47 are known as the lever rule and can be used to predict, using the phase diagram for the system, the equilibrium mole fractions of each phase at a given temperature and total sample composition in a region of two phase coexistence. It should also be noted that ϕ_a and ϕ_b are connected by the equation

$$\phi_a + \phi_b = 1 \tag{3.48}$$

since the sum of the mole fractions of all coexisting phases for any sample must be unity.

Chapter 4

Methods

In this chapter I will explain the experimental techniques used in my work. Firstly, I will explain how giant vesicles are made by the process of electroformation (section 4.2). This section also contains a description of the formation cells produced for the imaging of the vesicles (section 4.2.1). Then I will review the technique of fluorescence microscopy (section 4.3), culminating in multi-photon microscopy, which was the main technique I used for data collection. These sections briefly explain the physical principles behind how these techniques work as well as how the experiments were carried out.

4.1 Materials

The lipids 1,2-dipalmitoyl-*sn*-glycero-3-phosphocholine (DPPC), 1,2-dipalmitoyl-*sn*-glycero-3-phosphoethanolamine (DPPE), 1,2-dipalmitoyl-*sn*-glycero-3-[phospho-L-serine] (sodium salt) (DPPS), 1,2-dipalmitoyl-*sn*-glycero-3-phosphate (monosodium salt) (DPPA) and 1,2-dipalmitoyl-*sn*-glycero-3-[phospho-*rac*-(1-glycerol)] (sodium salt) (DPPG) were purchased from Avanti Polar Lipids, Inc. either in powder form or already dissolved in chloroform and were used without further purification. Lipids bought in powder form were made up into concentrated stock solutions in chloroform from which the desired lipid/fluorophore mixtures could be made. An explanation of the lipid structure and nomenclature is in section 2.1.1 along with diagrams of the chemical structures of the lipids used in figure 2.4.

The fluorophores Lissamine^{TM} rhodamine B 1,2-dipalmitoyl-*sn*-glycero-3-phosphoethanolamine (triethylammonium salt) (Rh-DPPE), 6-dodecanoyl-2-dimethylaminonaphthalene (Laurdan) and 1,1'-dioctadecyl-3,3,3',3'-tetramethylindocarbocyanine perchlorate (DiIC$_{18}$(3)) were purchased from Molecular Probes in powder form and used without further purification. Concentrated stock solutions of the fluorophores in chloroform were made up for storage. Lipids and fluorophores were stored in the freezer (approximately -15 °C) in glass vials with parafilm around the lids to prevent solvent evaporation. Analytic reagent grade chloroform, analytic reagent grade methanol and laboratory reagent grade acetone were all purchased from Fisher Scientific.

4.2 Electroformation

There are many methods of producing lipid GUVs in the laboratory. All of these methods need to be carried out above the main transition temperature of the lipids present in the mixture i.e. the lipids must be in the fluid phase (L_α). These methods include the *'gentle hydration method'* where the dried lipid film is exposed to an aqueous solution for periods of up to 36 hours [92, 93], the *'solvent evaporation method'* where aqueous solution is added to an organic lipid solution in a rotary evaporator under reduced pressure [94] and the *'electroformation method'* which will be discussed in detail below. Bagatolli et al. [4] carried out a study of the effectiveness of these three preparation methods. They found that the *'solvent evaporation method'* and the *'gentle hydration method'* show high heterogeneity in "size, shape, shell thickness and internal structure of the different lipid vesicles" [4]. This study concluded that no more than 10% of the vesicles produced by these two techniques were unilamellar, with lipid tubes or tethers frequently observed in these samples. In comparison, the *'electroformation method'* produced a yield of unilamellar vesicles which was greater than 95% with a more homogeneous size distribution than vesicles formed using the alternative preparation methods. The unilamellarity of electroformed vesicles has also been proven by measurements of bending elasticity [80] and by electron microscopy [95]. When the *'electroformation method'* was used, observations of tubes, tethers and small vesicles inside larger ones were rare in comparison with the other techniques. Giant vesicles have also been formed by dialysis [96], freeze-thaw [97]

and titration techniques [98]. No study was available which compared the quality and yield of GUVs using these latter three techniques so due to the research reported above, all the vesicles studied in my experiments were prepared by electroformation.

The electroformation protocol I used was as follows: lipid solutions of between 0.2 mg/ml and 1.0 mg/ml of lipid in chloroform, with the lipids in the desired molar ratio, were made up. The desired fluorophores were added to these solutions in appropriate amounts; Rh-DPPE was used at no more than 0.5 mol.%, Laurdan at no more than 1.0 mol.% and $DiIC_{18}(3)$ was also used at less than 1.0 mol.%. Approximately 4 μl of lipid solution (usually between 0.2 and ~0.7 mg/ml (1.0 mM)) was pipetted dropwise onto the two platinum wires taking care not to drop any onto the glass coverslip below (this sometimes seemed to affect the electroformation process). In the case of ITO plates, 10 μl of lipid solution (between ~0.7 (1.0 mM) and 1.0 mg/ml) was pipetted onto the middle of the bottom plate and spread evenly over approximately 1 cm^2. This lipid in chloroform solution was then dried on the electrodes (platinum wires or Indium-Tin-Oxide-coated (ITO) plates) under a nitrogen atmosphere for 2 hours to remove all traces of solvent. The inert nitrogen atmosphere prevents oxidation of the lipids.

The formation cell was then placed onto the microscope so that it could remain in situ for the entire experiment without unnecessary agitation. Excessive disturbance of the formation cell during or after the electroformation process affected the quality and yield of vesicles produced. The electroformation chamber was then filled with deionised water of resistivity 18 MΩ.cm, being careful to avoid air bubbles which inhibited electroformation, and the temperature raised above the melting temperature of the highest melting component lipid so that all lipids were in the fluid phase. The electrodes were attached to a Thandar TG501 5 MHz function generator and a sinusoidal AC field with a frequency of 10 Hz and an amplitude of approximately 6 V peak-to-peak was applied. The applied electric field was monitored using a Farnell 20 MHz oscilloscope DTV 20. The field was switched off after approximately 90 minutes; during this period the water level was occasionally topped up with deionised water using a dropping pipette. This was done slowly and carefully so not to disturb the forming vesicles and to make sure the temperature did not drop by more than a degree or so.

The formation temperatures used were a minimum of 70 °C when the highest melting compo-

nent was DPPE, 65 °C when the highest melting component was DPPS, and 75 °C when the highest melting component was DPPA. The actual temperatures used were up to 5 °C greater than the minimum temperatures that I have listed.

After the electroformation process, the range of vesicle sizes observed in my samples was usually 10−60 μm in diameter with vesicles occasionally reaching sizes of up to 80 μm in diameter. Changes in the AC field used for formation (such as using 3 V peak-to-peak amplitude) did not seem to have a noticeable effect on the size and yield of vesicles formed as has been suggested in some of the literature [68, 99]. The AC frequency of 10 Hz appears to be used throughout the literature. Although a careful study was not carried out, I did not find that the properties of the GUVs formed could be controlled by altering the AC regime.

It appears that there is still no clear understanding as to how the process of electroformation actually works even though the technique has been widely used since its first publication by Angelova and Dimitrov in 1986 [100]. It is seen as up to each individual scientist to find the electroformation protocol which works for their particular system with no real consensus on which experimental parameters affect which vesicle properties for a given lipid mixture and formation medium [68]. There has been much speculation as to possible mechanisms but the electroformation method would almost be considered as black magic by many who work with giant vesicles. This technique has predominantly been used with lipids with a phosphocholine (PC) headgroup. It has been found that not all lipids or lipid mixtures will form GUVs using an electroformation protocol [68] and that an aqueous medium of too high an ionic strength inhibits formation with Ca^{2+} particularly effective at impeding GUV formation [99]. It has also been found that AC or DC fields can be used to form vesicles.

What does appear to be agreed upon is that the mechanism involves the separation and bending of individual hydrated bilayers. Certain lipids when dried onto a substrate and exposed to an aqueous environment can form giant vesicles as has already been mentioned with the *gentle hydration method* above. Electrostatic interactions between adjacent membranes and hydration forces are thought to separate the bilayers of lipids which are on the substrate. Bending instabilities may be caused by surface tension and line tension caused by defects in the bilayers which expose hydrophobic parts of the lipids to the aqueous environment. Hence it is thought

that fluid membranes are of low enough viscosity to be able to bend and eventually close off into vesicles [101]. Membranes in the gel phase have a bending rigidity approximately an order of magnitude higher than the bending rigidity of fluid membranes [102]. The energy needed to bend gel phases membranes into spherical vesicles is probably too great for the electroformation process to work[1]. The role of the electric field has been seen to improve this mechanism but also, in some cases, prevent it. When DC fields are used with charged lipid mixtures, vesicle formation for, say, negatively charged lipid mixtures is increased on the cathode but suppressed on the anode. The opposite effect is seen for positively charged lipid mixtures, the formation of vesicles being enhanced on the anode [103].

The electric field is thought to provide direct electrostatic interactions between the electrode and the bilayers as well as redistribution of counter ions between the membranes. Electroosmotically induced mechanical stresses are also thought to play a part as well as the electric field affecting membrane surface and line tensions [103]. Other speculations include the involvement of electrochemical reactions, injection of charges from the electrode and the reorientation and lateral redistribution of lipids (inverse flexoelectric effect) [68]. Electric fields can be used to produce temporary holes or pores in vesicle membranes, a process known as electroporation [104–106]. This may cause defects which aid smaller vesicles to fuse with each other, forming larger vesicles. The mechanism of electroformation could involve a complicated mix of several of the above processes or, indeed, a mechanism that has so far not been proposed in the literature.

The formation of vesicles by electroformation is sensitive to many parameters. These variables include the types of lipid and the thickness of the lipid film which is dried onto the electrodes, the concentration and nature of various solutes in the aqueous solution, the nature of the substrate/electrodes, the frequency and amplitude of the electric field, and the temperature. The uncertainty in the understanding of the underlying mechanisms of electroformation is highlighted by Angelova and Dimitrov's acknowledgement that some of their experimental and theoretical results "might be wrong" [100] and their concepts are "hypotheses which need further experimental and theoretical work" [101].

[1]Using equation 3.7, the critical vesicle radius for gel phase membranes would be $R_v^* \sim 300$ nm (assuming $\kappa_b \sim \kappa_G \sim 10^{-18}$ J [102]). At this critical radius the energy barrier to vesicle formation (using equation 3.10) would be $\sim 2200\, k_B T$.

4.2.1 Formation Cells

I designed two different electroformation chambers which were made for fluorescence imaging of multicomponent lipid vesicles. These chambers were built for in situ formation on the microscope due to the high formation temperatures needed. In one of these cells the vesicles were formed on platinum wires and in the other the vesicles were formed on an ITO plate. These cells are described in detail in the sections below.

Both cells were cleaned after experiments by first washing in chloroform, then washing in a 2:1 chloroform:methanol mixture and then washing in acetone.

Platinum Wire Cell

The electroformation cell with platinum wire electrodes was heated resistively. Diagrams of the cell are shown in figure 4.1. It consists of a stainless steel 316 body ($80 \times 38 \times 13$ mm^3) surrounded by a pale blue TUFSET, rigid polyurethane (purchased from RS) casing. The cell also has an insulating pyrophylite top.

The stainless steel body had two cylindrical wells of 29 mm diameter with a small channel connecting them. One of the wells had the two parallel 0.5 mm diameter platinum electrodes (purchased from Aldrich), 3 mm apart and less than 2.0 mm above a 15×10 mm^2 observation window in the bottom of the well. The gap needed to be less than 2.0 mm so that the vesicles which formed on the wires could be viewed using an inverted microscope, i.e. the vesicles needed to be within the working distance of the objective lens positioned below the observation window. The observation window was made from coverglass purchased from Agar Scientific (L4239-1): the coverglass dimensions were 35×64 mm^2 and was between 0.130 and 0.160 mm thick. The coverglass was glued in place using the Norland Optical Adhesive 61 UV-curing glue purchased from Norland Products Inc, which can withstand temperatures up to 125 °C. The electrodes went through the sides of the body with pale blue TUFSET used to electrically insulate them from the stainless steel. Dow Corning was used to secure the electrodes in place. The electrodes ended in nylon and brass terminal blocks. These terminal blocks were kept electrically isolated from each other by placing insulating strips of plastic between them.

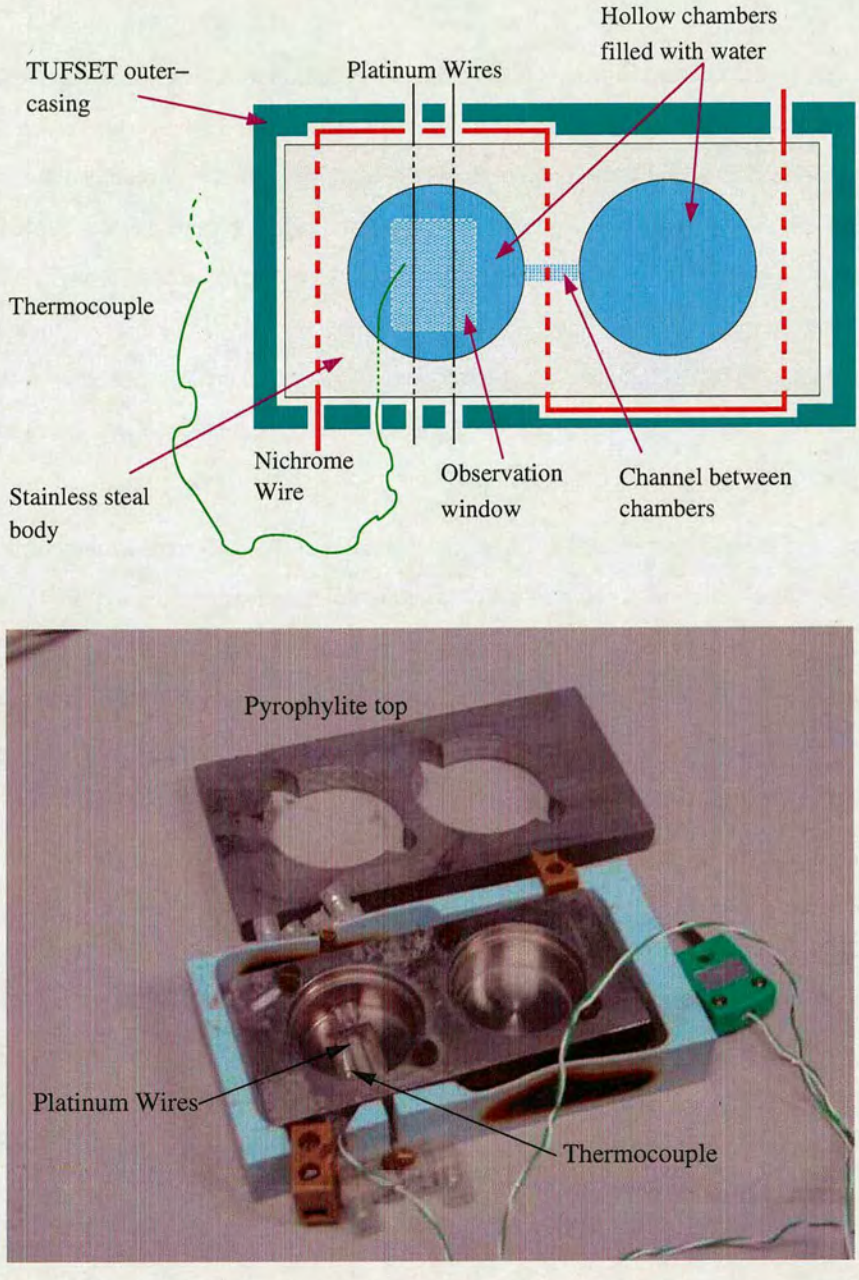

Figure 4.1: [*top*] A schematic diagram of the platinum wire electroformation cell. [*bottom*] A photograph of the platinum wire electroformation cell. The burn mark on the casing is from the aluminium oxide beads which touch the TUFSET at this point.

The terminal blocks were connected to the function generator by attaching crocodile clips to their screws.

Nichrome wire, with a resistance of 1.6 Ω, surrounded by aluminium oxide beads was used for heating; this passed through and around the stainless steel body as shown in figure 4.1. The nichrome wire ended in ceramic and brass terminal blocks. These blocks were the connectors for the wires from the Griffin low tension variable voltage supply. A K-type thermocouple with moulded plug was inserted through the side of the cell, close to the electrodes; it was secured in place using Dow Corning 732 silicone sealant. The temperature from the thermocouple was read using a Fluke 52II thermometer. The thermocouple was positioned as close to the wires as possible (within a couple of mm) to ensure that the temperature measurement was as close to that of the vesicles being imaged as possible.

The purpose of the second well and connecting channel was for the replacement of water which had evaporated from the formation cell. Dropping deionised water directly into the well containing the electrodes caused a hydrodynamic disturbance which disturbed the vesicle formation during the electroformation process. The replenishment of water into the neighbouring well meant that water passed through the connecting channel with the minimum of disturbance to the vesicles on the electrodes.

Indium Tin Oxide (ITO) Plate Cell

The electroformation cell where vesicles were formed on an ITO plate can be seen in figure 4.2. ITO is a transparent, conducting compound that can be deposited onto glass surfaces. This cell was heated using Peltier effect heaters. The central body of the cell is made from stainless steel (45×45 mm^2 $\times$ 23 mm, with walls $\sim$ 3 mm thick) and has thin plastic strips glued to the bottom to thermally insulate the body of the cell from the microscope stand. It has a 25 mm diameter circular hole in the bottom for viewing using an inverted microscope. This hole is covered by a $0.130 - 0.160$ mm thick coverslip which is cut down to fit inside the cell from an L4239-1 Agar Scientific coverglass as mentioned above. The coverslip is glued in place using Norland Optical Adhesive 61 UV-curing glue. This coverslip has a 20×20 mm^2 coating of ITO in its centre with a strip of ITO running to the edge of the coverslip from this central

square section (see figure 4.2). A wire is attached to the ITO, which runs to the edge of the coverslip, using a silver loaded epoxy adhesive purchased from RS Components. This wire plugs into a Printed Circuit Board (PCB) edge connector in the side of the central stainless steel compartment which in turn has another wire passing to the outside of the cell which can be connected via a crocodile clip to the external function generator.

Two L-shaped spacers, made from pale blue TUFSET, are attached to the coverslip using the UV-curing glue. The spacers are used to position another ITO plate ~ 2 mm above the bottom coverslip. This second ITO plate is 30×30 mm cut from an Agar Scientific L4222 76×39 mm^2 plain microscope slide which is $1.0 - 1.2$ mm thick. A 20×20 mm^2 ITO-coating is in the centre of the plate, again with a strip of ITO running to one of the sides. This strip was a wire attached to it using the silver loaded epoxy adhesive. The ITO-coating on the plates had resistances in the range $0.5 - 2$ kΩ. When the second ITO plate is placed onto the spacers (with the ITO-coated side facing downwards), the attached wire plugs into a second PCB edge connector in the opposite corner of the stainless steel body to the first PCB edge connector. Again, this edge connector has a wire leading outside of the cell from which the function generator can be attached using a crocodile clip.

Lipid is dried onto the bottom ITO plate of the cell under nitrogen with the upper ITO plate removed. The upper ITO plate is then positioned using plastic tweezers and its wire plugged into the PCB edge connector. This ensures no grease from fingers gets inside the clean formation cell. Deionised water is then gently added into the cell ensuring that there are no air bubbles between the two plates. Addition of further water replacing that which is lost to evaporation can be done directly into this chamber without disturbing the forming vesicles: the top plate shields the lipids from the excess hydrodynamic disturbances of adding more water to the formation chamber.

The temperature control for the cell comes from four thermoelectric modules: Marlow DT-3-8-01LS DuraTEC high power heat pumps purchased from Farnell. These had a 17 W capacity and could withstand a maximum current of 7.4 A and a maximum potential difference of 3.6 V. The dimensions of each component was 20×24.5 mm^2 and were 3.63 mm thick. These modules are semiconductor devices which either heat or cool depending on which direction the

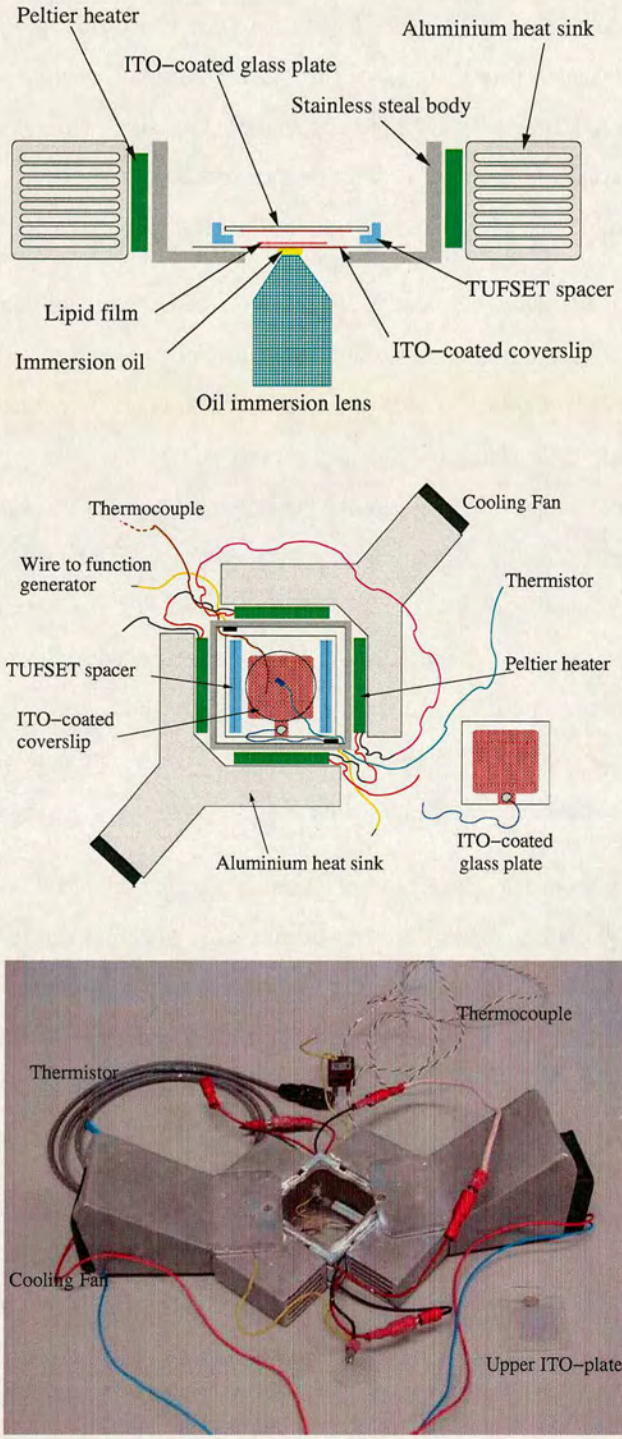

Figure 4.2: Schematic diagrams of the ITO plate formation cell: [*top*] side cross-section including positioning of the lens using an inverted microscope; [*middle*] overhead view including ITO-coated glass plate shown outside of the formation cell; [*bottom*] a photograph showing the ITO plate formation cell.

electric current flows through them. The Peltier devices were sealed against condensation and moisture.

The peltiers were fitted to the four sides of the stainless steel body using Electrolube HTS silicone heat transfer compound (purchased from Farnell) and connected in series. Aluminium heat sinks were then attached to the other side of the peltiers using the Electrolube as shown in figure 4.2. Two miniature 12 V, 1.6 W cooling fans (Papst Plc 40 × 40 × 20 mm^3 fans purchased from RS components) were used to assist heat dissipation. The fans had an air flow rate of 13.5 m^3h^{-1}. They were either screwed onto the heat sinks or attached to the microscope stand using blu-tack. The heat sinks were shaped in such a way as to channel the air through the slots in the heat sink, maximising the surface area for heat exchange with the environment. The heat sinks were screwed into corners of the stainless steel main body with thin plastic insulation thermally isolating the body from the heat sinks. Pale blue TUFSET corner pieces were made to improve thermal isolation of the stainless steel body from the heat sinks.

A T-type thermocouple with moulded plug, purchased from RS Components, and a TS67-170 thermistor, purchased from Oven Industries, Inc., were fitted though the side of the stainless steel body and secured in place using Dow Corning 732 silicone sealant. The thermistor was given a thin coating of Dow Corning to make it waterproof. A model 5C7-362 thermoelectric temperature controller, purchased from Oven Industries, Inc., was used to provide proportional (P), integral (I) and derivative (D) temperature control within the cell to a resolution of 0.05 °C. The temperature controller was regulated via computer software on the PC attached to the confocal microscope. The software communicated with the temperature controller through the computer's RS232 communications port. The temperature controller monitored the temperature in the formation cell via the TS67 series thermistor. An ASTEC LPS254 power supply was used; this was boxed with the 5C7-362 controller to provide a composite unit to be used in experiments. The maximum output of the power supply is 16.7 A but this was reduced to below the 7.4 A maximum load of the Peltier modules. The voltage output could be set to between 12 and 24 V but was set at just below 14.4 V, the maximum for the four peltiers connected in series.

The following procedures were used to set the PID parameters for the temperature controller.

Temp. / °C	**P** / °C	**I** / repeats/min.	**D** / cycles/min.
70.0	11.0	0.24	0.024
65.0	12.8	0.22	0.022
60.0	16.0	0.21	0.021
55.0	18.9	0.19	0.019
50.0	20.0	0.18	0.018
45.0	21.6	0.16	0.016
40.0	22.1	0.15	0.015
35.0	22.8	0.14	0.014

Table 4.1: PID parameters for the ITO plate electroformation cell for a range of temperatures.

The PID parameters were set for a range of temperatures over which the cell would be used. The formation cell was filled with deionised water. Initially the integral and derivative values of the controller were set to zero. The proportional bandwidth, which is the temperature range around the desired set value where the power to the Peltiers is modulated from 100 % down to zero at the desired temperature, is set to a value where the system comes to a steady temperature near to the setpoint without over-shooting. If the bandwidth is too small then the temperature will oscillate about the setpoint without ever settling to this desired value. The proportional bandwidth is then decreased until the temperature just begins to oscillate. This bandwidth is recorded along with the period of oscillation, τ_p (in minutes). The proportional bandwidth for this particular temperature is then calculated as 1.5 times the noted bandwidth for the onset of oscillations.

The period of oscillation recorded above is used to obtain a value for the integral reset. The integral reset monitors the difference between the actual and desired temperatures (ΔT), slowly changing the power output to the Peltiers until the set temperature is reached. This is done by integrating the error signal, ΔT, at fixed intervals which are expressed in repeats per minute. The integral reset value for a given temperature in repeats/minute is then set as $\frac{1}{2\tau_p}$. Finally the derivative rate, in cycles per minute, is set as one tenth the value of the integral reset. This parameter allows the controller to anticipate the power needed by sensing the rate of change of

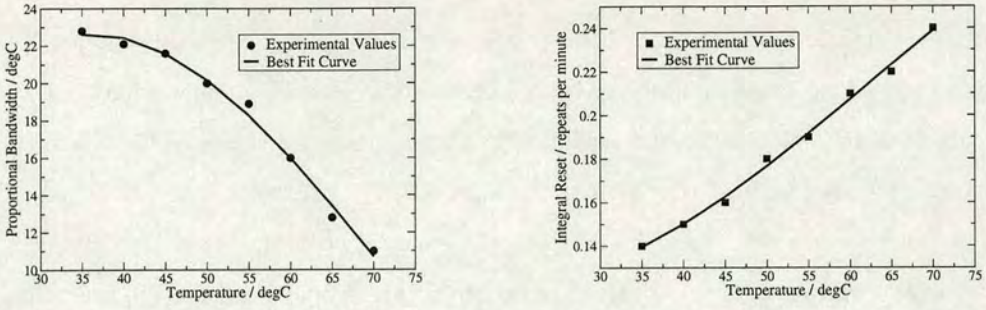

Figure 4.3: PID control parameters for the ITO plate formation cell: [*left*] Graph of proportional bandwidth against temperature, and [*right*] graph of integral reset against temperature.

the temperature.

The PID parameters for the formation cell over a range of temperatures are shown in table 4.1. These parameters are put into graphical form with curves of best fit in figure 4.3 with the exception of the derivative rate which just varies from the integral reset by a constant of proportionality.

4.3 Fluorescence Microscopy

4.3.1 Fluorescence

Fluorescence is a category of the more general phenomenon of luminescence. Luminescence is the emission of light by a substance from an electronically excited state, i.e. a process that is not incandescence (where light is emitted by an object due to its temperature). The two categories of luminescence are fluorescence, which we are interested in here, and phosphorescence, the difference being derived from the nature of the excited state. The ground state of a fluorescent molecule is a singlet state and, in general, fluorescence emission is due to de-excitation of an electron from a singlet excited state (an allowed transition), whereas phosphorescence is an electronic transition from a triplet state (a forbidden transition) and hence has a much longer

lifetime than fluorescence excitation. The term forbidden transition refers only to the lowest order dipolar transition; higher order transitions are allowed but have much longer lifetimes.

Fluorescence emission with wavelengths at or beyond the near ultraviolet usually occurs in highly conjugated molecules (molecules with long chains of alternate single and double bonds), including aromatic molecules (cyclic conjugates). The electronic transitions of fluorescence emission are usually described using a Jabłoński diagram [107]. An example is shown in figure 4.4. In equilibrium, the electrons are in the S_0 singlet ground state of the fluorescent molecule (fluorophore). The vibrational energy levels of each molecular orbital are denoted 0, 1, 2,... in the diagram. Since thermal energy is not sufficient for the electrons to significantly populate excited vibrational states, the fluorophores are excited by the absorption of the energy from an incident photon. The electron is usually excited to a higher vibrational level of either the S_1 or S_2 singlet states. This transition takes about 10^{-15} s, too quickly for nuclear rearrangements and so the energy level structure of the fluorophore in this excited state is the same as that in the ground state (the *Franck-Condon principle*), i.e. the absorption spectra of the fluorophore gives information on the energy levels of the ground state (with vibrational fine structure) of the fluorophore. From here a rapid rearrangement, without the emission of a photon, known as internal conversion, takes place where the electron relaxes to the lowest vibrational state of the S_1 orbital ($\sim 10^{-12}$ s). The excited electron is paired to the second electron, of opposite spin, in the ground state orbital and rapidly returns to an excited vibrational state of the S_0 orbital with the emission of a photon ($\sim 10^{-8}$ s). The electron quickly reaches thermal equilibrium in the lowest vibrational state of the S_0 orbital.

Phosphorescence occurs when there is intersystem crossing; a molecule in the singlet S_1 state undergoes a spin conversion to the T_1 triplet state of lower energy. The transition from the T_1 state to the ground state is forbidden (to lowest dipolar order) and so has a much longer lifetime of milliseconds to seconds. Much longer lifetimes are possible as used in glow-in-the dark toys. Phosphorescence is not usually seen in fluid solutions due to other de-excitation processes such as quenching or non-radiative decay which dominate over the radiative phosphorescence emission.

The common and fashionable example is that of the fluorophore quinine. Quinine fluorescence

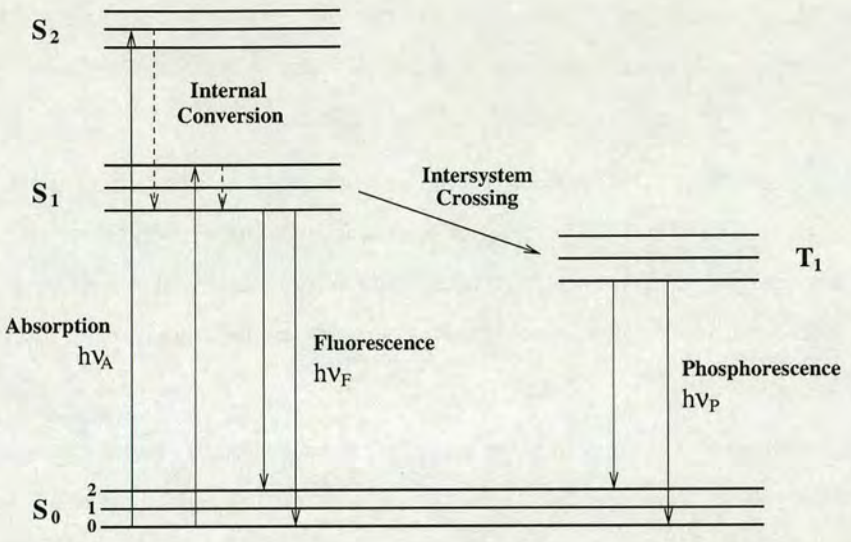

Figure 4.4: An example of a Jabłoński diagram taken from chapter 1 of *Principles of Fluorescence Spectroscopy* [107].

was first reported by Sir John Frederick William Herschel as long ago as 1845 [108]. Quinine is found naturally in tonic water. It is excited in the UV part of the electromagnetic spectrum; a faint blue glow can be seen on the surface of a glass of tonic water when exposed to sunlight, an emission wavelength of around 450 nm. The brightness of quinine fluorescence is dependent on solvent polarity and so is a probe of its neighbouring environment. Hence when a polar solvent (such as alcohol) is added to tonic water, reducing the dielectric constant, the blue fluorescent glow becomes brighter and more apparent. Many may be familiar to this popular experiment when drinking gin and tonic under UV disco lights.

It can be seen from figure 4.4 that the energy of absorption is greater than that of fluorescence emission, i.e. the fluorescence emission is at lower frequencies or, equivalently, longer wavelengths. This was first noticed by Sir G. G. Stokes in 1852 [109] and is now referred to as the *Stokes' shift*. This occurs because the electron is excited from the lowest vibrational state of the S_0 orbital to an excited vibrational state of the S_1 or S_2 orbital before losing energy by internal conversion as it rapidly relaxes to the lowest vibrational state of the S_1 orbital. Further energy is lost in the emitted photon as the electron usually only de-excites to a higher vibrational state of S_0 orbital rather than the lowest vibrational state from whence it came. Stokes' shift means

that it is possible to discriminate between photons emitted by an excitation source (such as a laser) and those emitted by the fluorophores. Figure 4.4 also shows that phosphorescence emission is typically at longer wavelengths than fluorescence emission.

Another general property of fluorescence is that the emission spectrum is independent of excitation wavelength (*Kasha's rule*) [110]. Irrespective of which electronic or vibrational state the fluorophore is excited into there is a rapid relaxation to the lowest vibrational state of the S_1 orbital, which takes about 10^{-12} s, from where the fluorescence emission takes place. Exceptions do occur but are rare [107].

Important characteristics of fluorophores are their fluorescence lifetimes and their quantum yields. For some types of fluorescence experiments such as resonance energy transfer, anisotropy and fluorophores whose emission is sensitive to their surroundings, the lifetime is the time in which the fluorophore has to interact with its environment. The details of its environment are then given in its emission. The quantum yield, Q, of a fluorophore is a measure of the number of emitted photons compared to the number of absorbed photons. This affects the brightness of the fluorophore's emission. If we consider the rate of emission of a fluorophore (Γ) and its rate of non-radiative decay to the ground state (k_{nr}), then we can write down the following expression for the quantum yield:

$$Q = \frac{\Gamma}{\Gamma + k_{nr}} \,. \tag{4.1}$$

For some fluorophores, such as rhodamine, $k_{nr} \ll \Gamma$ and hence have quantum yields approaching unity [107]. The fluorescence lifetime (τ) can be written as

$$\tau = \frac{1}{\Gamma + k_{nr}} \tag{4.2}$$

although it should be noted that this is only a measure of the average time a fluorophore spends in the excited state since the emission is a random process.

Photobleaching, although a poorly understood phenomenon, is thought to be caused by a transition into a long-lived excited triplet state which gives a longer time for chemical reactions to occur such as covalent modification, causing permanent photochemical damage and the molecule

loses its fluorescence [111]. A given fluorophore can only be excited a certain average number of times before photobleaching takes place causing an intensity loss in the fluorescence emission signal. This cannot be prevented by reducing the intensity of light used to excite the fluorophore, but the rate of photobleaching will be reduced.

Fluorophores

Some biological macromolecules have their own natural fluorescence. One example of this is in proteins where the indole group of tryptophan is fluorescent. Membranes, however, do not have their own intrinsic fluorescence and so extrinsic fluorophores need to be added for fluorescent labelling. Fluorescent membrane probes tend to have large hydrophobic parts to their molecules which preferentially partition into the membrane's hydrophobic core. The properties of the fluorophores used in these experiments are described below and summarised in table 4.2:

Rh-DPPE

The fluorophore Rh-DPPE is a headgroup modified fluorescent lipid with molecular formula $C_{70}H_{117}N_4O_{14}PS_2$ and has a molecular weight of 1333.81 Da [112]. It has an excitation wavelength peak at 560 nm and an emission peak at 581 nm in methanol solution. Its molar extinction coefficient has been measured to be around 75000 $cm^{-1}M^{-1}$. The extinction coefficient is a measure of the fraction of light absorbed or scattered per unit distance into the medium at the excitation wavelength of the fluorophore. Figure 4.5 shows how Rh-DPPE sits in the membrane with its dipole tangential to the membrane surface. It has been shown that Rh-DPPE does not readily transfer between separated bilayers [113].

In my experiments, Rh-DPPE is excited by two photons at 780 nm (see section 4.3.2). This is an effective single photon excitation of 390 nm, a much shorter wavelength than the characteristic excitation wavelength of 560 nm given on the Molecular Probes website [112]. This means that the Rh-DPPE is being excited to a molecular orbital of higher energy although the emission is still seen to be around 581 nm, from the S_1 orbital (*Kasha's Rule*).

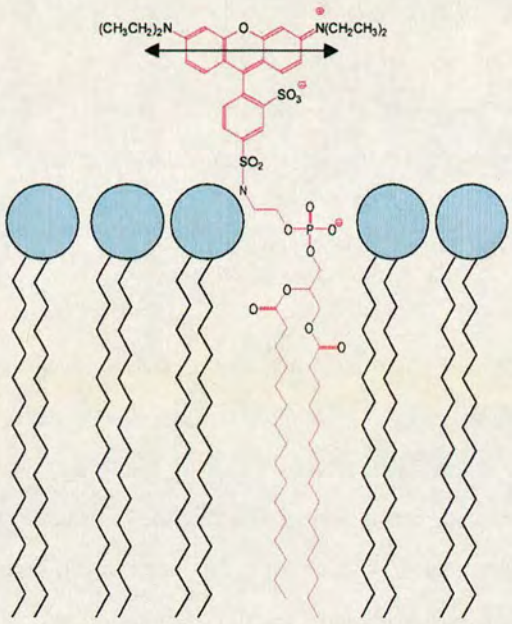

Figure 4.5: Fluorophore Lissamine Rhodamine B 1,2-dipalmitoyl-*sn*-glycero-3-phosphoethanolamine (Rh-DPPE) in a lipid membrane [3]. The fluorophore dipole sits tangentially to the membrane.

The Rh-DPPE fluorophore partitions strongly into the more disordered fluid phase. It is thought that the large headgroup of Rh-DPPE disturbs the lipid packing in the gel phase making it energetically unfavourable to remain there and hence it is expelled into the fluid phase.

Laurdan

Laurdan has a molecular formula $C_{24}H_{35}NO$ and a molecular weight of 353.55 Da [112]. In methanol it has a peak excitation wavelength of 364 nm and a peak emission wavelength of 497 nm with an extinction coefficient of around 20000 $cm^{-1}M^{-1}$. In fact the emission spectra of Laurdan is highly solvent-dependent. This property can be used to probe the fluidity of lipid membranes as Laurdan emission is sensitive to the number of water molecules which surrounds it [3, 5, 114]. I do not use this property of Laurdan in my experiments as the necessary dichroic mirror needed to collect this data in a simultaneous scan was not available and it was decided that performing sequential scans would not provide reliable data (more on this later).

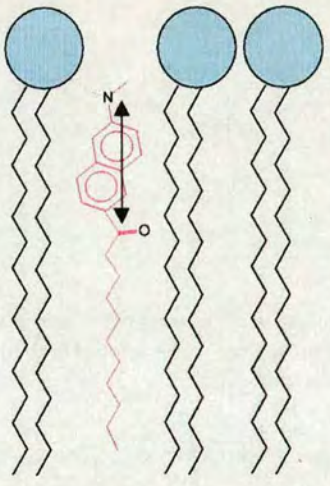

Figure 4.6: Fluorophore 6-dodecanoyl-2-dimethylaminonaphthalene (Laurdan) in a lipid membrane [3]. The fluorophore dipole sits parallel to the bilayer normal.

The property of Laurdan of most interest in my experiments was that it partitioned equally between gel and fluid membrane phases as opposed to Rh-DPPE which just labelled the fluid phase. This meant that the whole membrane was visible by fluorescence.

The position of Laurdan in the lipid bilayer can be seen in figure 4.6. The dipole of the fluorophore is parallel to the bilayer normal. Laurdan is also excited at 780 nm by two photons, an effective single photon excitation of 390 nm. This is longer than the wavelength of 364 nm as stated on the Molecular Probes website [112] but as excitation spectra are broad distributions centred on a particular wavelength, this wavelength is sufficient to excite the fluorophore.

DiIC$_{18}$(3)

DiIC$_{18}$(3) is weakly fluorescent in water but highly fluorescent and quite photostable in lipid membranes; transfer of this probe between intact membranes is negligible. It's a long-chain dialkylcarbocyanine with a high extinction coefficient (148000 cm^{-1}M^{-1}), moderate quantum yield and short excited state lifetime in lipid systems (1 ns) [112]. It has a molecular weight of 933.88 Da and molecular formula $C_{59}H_{97}ClN_2O_4$; its molecular structure can be seen in figure 4.7a. In methanol, its excitation and emission spectra have peaks at 549 nm and 565 nm

Fluorophore	Molecular Formula	Molecular Weight / Da	Wavelengths / nm		Ext. coeff. / $cm^{-1}M^{-1}$
			Absorption	Emission	
Rh-DPPE	$C_{70}H_{117}N_4O_{14}PS_2$	1333.81	560	581	75000
Laurdan	$C_{24}H_{35}NO$	353.55	364	497	20000
$DiIC_{18}(3)$	$C_{59}H_{97}ClN_2O_4$	933.88	549	565	148000

Table 4.2: Properties of the fluorophores used in experiments. The information used is from Molecular Probes [112]. Absorption and emission wavelengths are quoted for fluorophores in methanol solution. Ext. Coeff. is an abbreviation of extinction coefficient.

respectively [112]. Its excitation and emission spectra are shown in figure 4.7b.

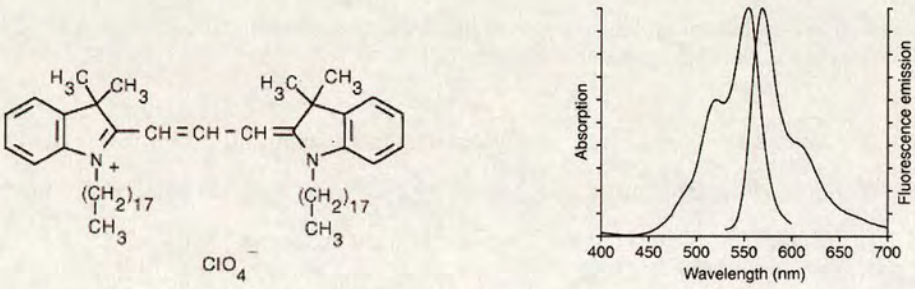

Figure 4.7: (a) [*left*] Molecular structure of $DiIC_{18}(3)$ [112], and (b) [*right*] excitation and emission spectra of $DiIC_{18}(3)$ [112].

The $DiIC_{18}(3)$ probe could be excited at 488 nm and 514 nm using single photon excitation. This fluorophore, as with the Rh-DPPE, preferentially partitioned into the more disordered fluid phase of the lipid membranes.

There is no information in the literature as to how the excitation dipole sits with respect to the membrane. Figure 4.8 shows an image section close to the equator of a uniformly fluid vesicle labelled with the $DiIC_{18}(3)$ probe. The light used to excite the fluorophore is linearly polarised in the direction shown. The section of membrane at the right side of the vesicle is much brighter than the bottom portion of membrane. From this it can be assumed that most of the excitation dipoles of fluorophores at the bottom of the vesicle are perpendicular to the direction of polarisation of light whereas a higher proportion of excitation dipoles can be excited at the

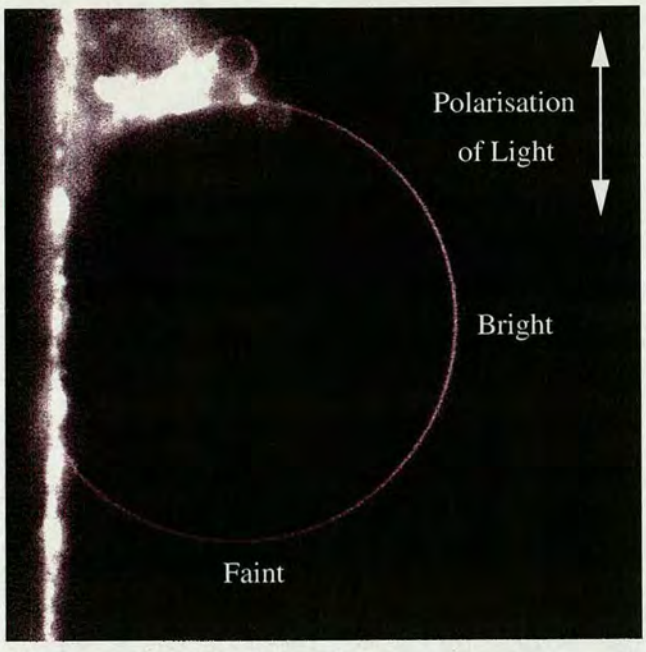

Figure 4.8: An image slice near the middle of a 1:1 DPPC:DPPE vesicle, containing the $DiIC_{18}(3)$ fluorophore, in a uniform fluid phase. The light which excites the fluorophore is linearly polarised in the direction shown. The membrane is brighter at the side compared to the bottom of the vesicle; this indicates that the excitation dipole of the fluorophore (roughly) sits tangentially to the bilayer plane similarly to the Rh-DPPE fluorophore in figure 4.5.

side of the vesicle. This indicates that the excitation dipole sits approximately tangential to the bilayer as shown in figure 4.5 for the Rh-DPPE probe.

4.3.2 Microscopy

Optical microscopy is thought to have been around since as early as 1590, providing high angular magnification below the resolution of the human eye. Since its original invention there have been many improvements in microscopy techniques which have lead up to the highly sophisticated imaging systems available today. A schematic ray diagram of a simple compound microscope is shown in figure 4.9.

The objective lens forms a real, magnified, inverted image of the specimen in the plane of the field stop of the eyepiece. This image then acts as an object for the eyepiece lens which acts like a magnifying glass producing an inverted virtual image of the original specimen for the eye to

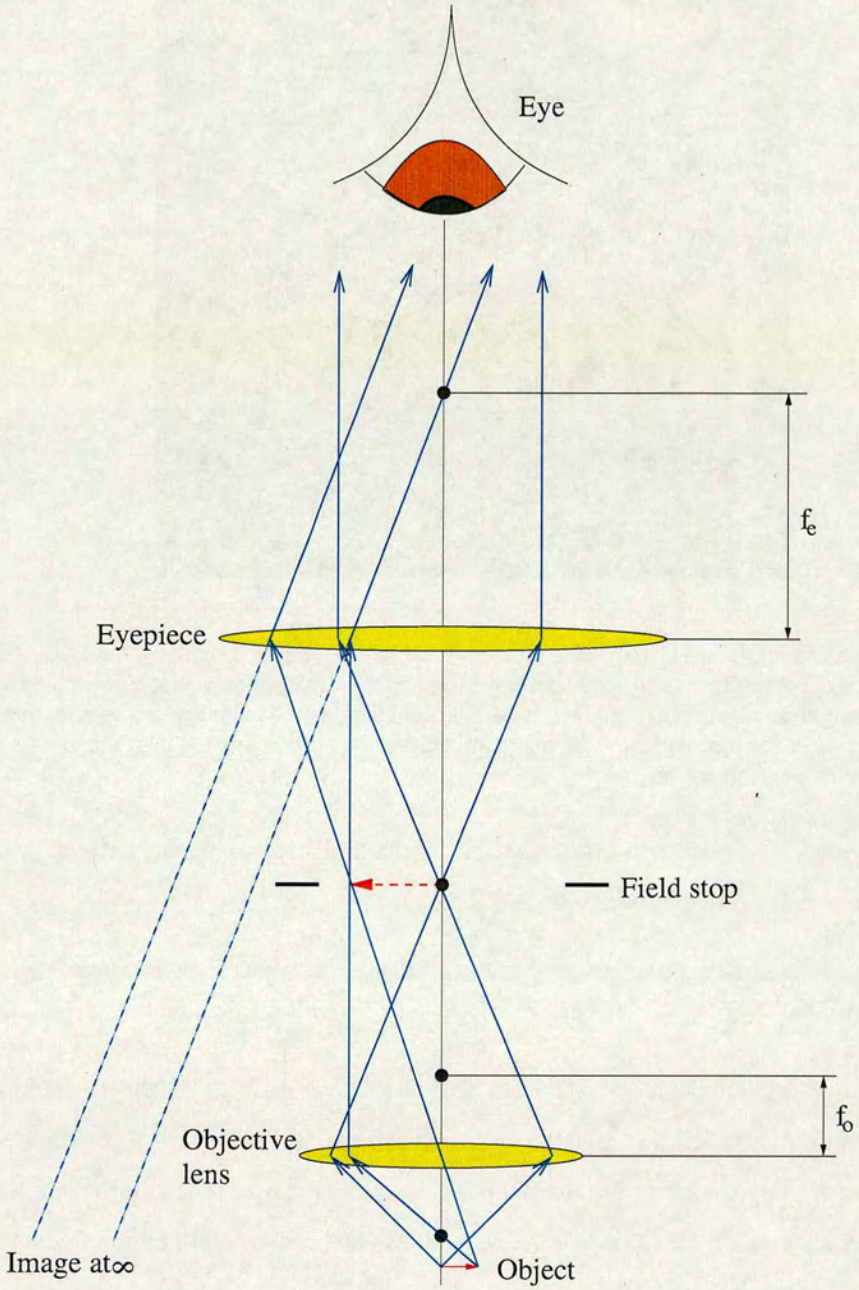

Figure 4.9: Ray diagram for a simple compound microscope.

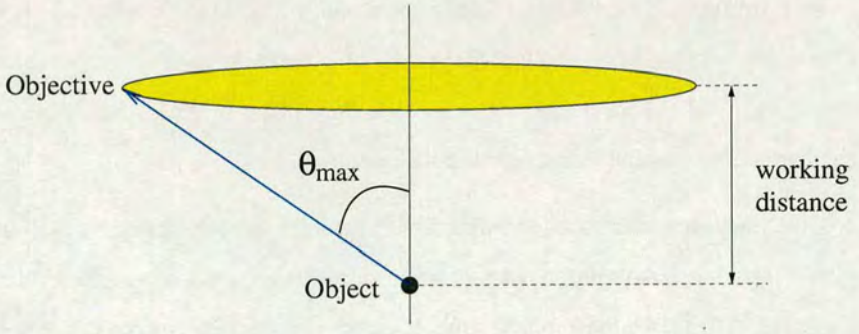

Figure 4.10: The maximum cone of light that can be collected by an objective has half angle θ_{max} when the lens is at its working distance from the object.

see. The total angular magnification of the lens $M = M_o \times M_e$, where M_o is the magnification of the objective and M_e is the angular magnification of the eyepiece.

Modern laboratory microscopes have more complicated optics than the single lens objective and single lens eyepiece that is shown in figure 4.9. Objectives and eyepieces are a sophisticated combination of lenses which reduce chromatic and spherical aberrations resulting in high quality images. The brightness of the image is partly dependent on the amount of light collected by the objective lens. The numerical aperture ($N.A.$) is a parameter which can describe this. For an objective lens

$$N.A. = n_i \sin\theta_{max} \,, \tag{4.3}$$

where n_i is the refractive index of the medium directly next to the objective lens and θ_{max} is the half angle of the maximum cone of light that can be collected by the objective (see figure 4.10). The medium directly next to the lens is not necessarily air; immersion objectives are available where the medium between the objective and the sample is, for example, oil or water. This means that lenses with $N.A.$ greater than 1.0 are possible due to the higher refractive indexes or these media. The image intensity is in fact proportional to $(N.A.)^4$ and inversely proportion to M^2 [115], so a small increase in numerical aperture at a given magnification has a significant effect on the brightness of the image.

The maximum resolution of a microscope is also dependent on the $N.A.$ of the objective lens.

Ernst Abbe, who came up with the concept of the numerical aperture whilst working at the Carl Zeiss microscope laboratory, discovered that the resolving power was directly proportional to the wavelength of light, λ, and inversely proportional to $N.A.$. The origin of this is the wave nature of light, and its consequent diffraction at finite apertures.

The aperture of the imaging system causes diffraction of the light passing through it even if the image is free of aberrations. A point object will not result in a point image and therefore the resolution of the image is diffraction-limited. The blur spot or diffraction pattern which results is known as the point spread function (PSF) and in an imaging system of circular geometry will, in the image plane, produce an intensity pattern known as the Airy discs (figure 4.11a). The amplitude PSF for a spherical lens in the image plane, $h(r)$, can be shown to be

$$h(r) = \frac{2J_1(\nu)}{\nu}\,, \tag{4.4}$$

where $J_1(\nu)$ is the first order Bessel function of the first kind and the normalised, dimensionless distance from the optical axis, $\nu = krn_i \sin\theta_{max} = kr(N.A.)$ with the wavenumber, $k = \frac{2\pi}{\lambda}$. Therefore the observed intensity of the perfect point object, $I(r) = |h(r)|^2$. The radial PSFs for amplitude and intensity of the light in the image plane are shown in figure 4.11b. It can be seen that the central maximum of the intensity PSF is narrower than that of the amplitude PSF and the peripheral lobes of the intensity PSF are a lesser proportion of its central maximum than is the case for the amplitude PSF.

The light source for a standard laboratory light microscope is spatially incoherent and so the intensities of two neighbouring points are added in the final image as opposed to their amplitudes which would be the case if the light source was spatially coherent, for example a laser. This point is important when considering other forms of microscopy such as *phase contrast*. It can be seen that the image formation in these two cases is different by considering the inequality:

$$|h(r_1)|^2 + |h(r_2)|^2 \neq |h(r_1) + h(r_2)|^2\,. \tag{4.5}$$

Here, the left-hand side of the inequality corresponds to the addition of intensities (incoherent illumination) and the right-hand side corresponds to the addition of amplitudes (coherent illu-

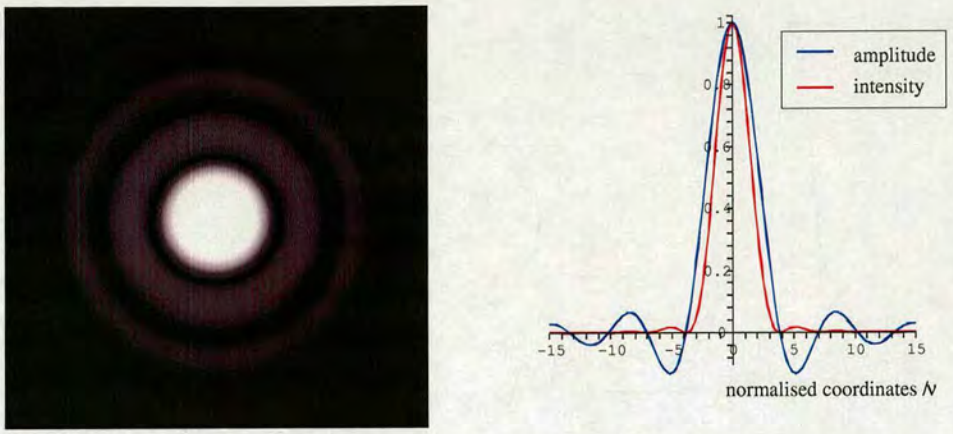

Figure 4.11: (a) [*left*] Airy disc pattern of the intensity in the image plane of a point source through a spherical lens; (b) [*right*] The amplitude and intensity PSFs with respect to the normalised coordinate, ν, from the optical axis.

mination). It should be noted that in both cases the detector responds to the intensity of the signal.

To calculate a theoretical optimal resolution for our image we need to consider how far apart two neighbouring points on our object will have to be for us to be able to distinguish their PSFs. This will be dependent on whether our illumination source is coherent or incoherent as this affects whether we need to sum the amplitude or intensity fields to create the final image and, as discussed above, the amplitude PSF is broader than that of the intensity PSF. The broader amplitude PSFs will need to have a greater separation in the image plane to be distinguished from each other so the resolution will be lower for coherent illumination.

The most commonly used postulate is the *Rayleigh Criterion*. This states that for two points of equal brightness to be resolved, the central maximum of the first PSF must be no closer to the central maximum of the second PSF than its first minimum (see figure 4.12a). It can be shown that this corresponds to a drop in intensity of 26.5 % between the maxima of the combined intensity PSFs. It can be shown that, for an incoherent light source, this corresponds to

$$d_s = \frac{0.61\lambda}{N.A.}, \tag{4.6}$$

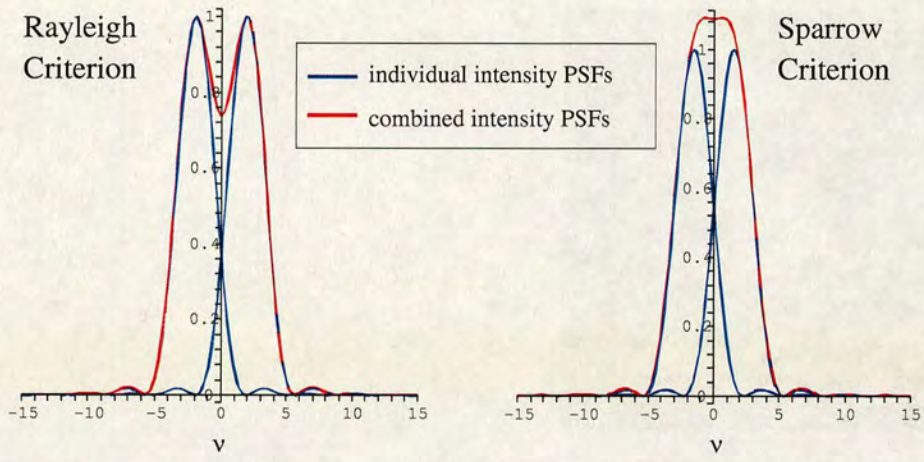

Figure 4.12: Comparison of the optimal resolution of two point objects. Graphs show the intensity PSFs for (a) [*left*] the *Rayleigh Criterion*, and (b) [*right*] the *Sparrow Criterion*.

where d_s is the separation of the two point sources. This is an arbitrary choice of definition for the optimal resolution and another definition, which has been shown to be more realistic [116], is the *Sparrow Criterion*. This is the limit where the intensity at the midway points is equal to that at the points or, more clearly (perhaps!), the drop in intensities between the two peaks of the intensity PSFs becomes zero, i.e. there is a long flat ridge between the two summits where the second spatial derivative of the combined intensity PSFs is zero (figure 4.12b). This is seen as a more general definition, and for incoherent illumination we now get

$$d_s = \frac{0.51\lambda}{N.A.}\,, \tag{4.7}$$

with the value for coherent illumination being a factor of 1.5 times greater [115].

Phase Contrast Microscopy

Instead of viewing the amplitude of transmitted or reflected light from a sample, it is possible to view an image of the phase of the light. Membranes and water have similar transmittance of light so vesicles are difficult or impossible to see when viewing the transmitted light intensity.

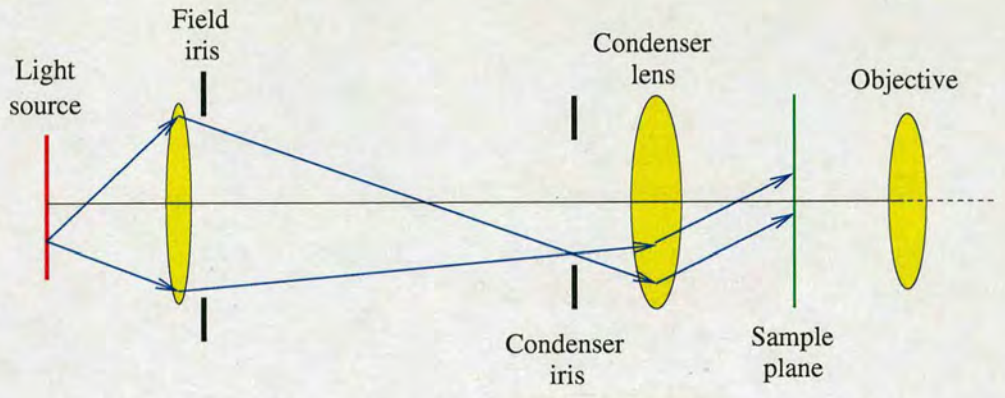

Figure 4.13: Köhler illumination in a standard light microscope. This provides uniform illumination of the sample from an incoherent light source.

Due to the difference in refractive index of water and membranes though, it is possible to view vesicles using phase contrast microscopy. Phase contrast microscopy was first developed by Fritz Zernike in 1935, an innovation for which he was awarded the Nobel prize in 1953.

Firstly, we need to set up Köhler illumination for the sample using an incoherent light source. This provides uniform illumination for the whole sample as shown in figure 4.13. The objective lens is positioned such that the sample is in focus. Then the field iris aperture is reduced so that its edges can be seen in the field of view. The condenser lens is used to obtain a sharp image of the edge of the field iris. Now the image of the field iris is centred in the field of view using the condenser centring knobs. Then the field iris is opened so that its edges are just beyond the field of view. The image contrast can now be controlled using the condenser iris and the light intensity is varied by increasing or decreasing the power to the light source.

When light passes through an object of different refractive index, it is diffracted and there is a phase shift. It is only possible for the human eye to see differences in intensity of incident light as we are not sensitive to differences in phase so to view these objects we need to convert the phase modulation into an amplitude modulation. If we examine the straight forward explanation in reference [116]: the light passing through the object is considered to consist of a direct, undiffracted beam ($E_i = E_0 \sin \omega t$) and a small diffracted beam (E_d) with a phase shift $\phi(x, y)$ dependent on where it passes through the x-y object plane, then the phase modulated field (E_{PM}) in the image plane would be

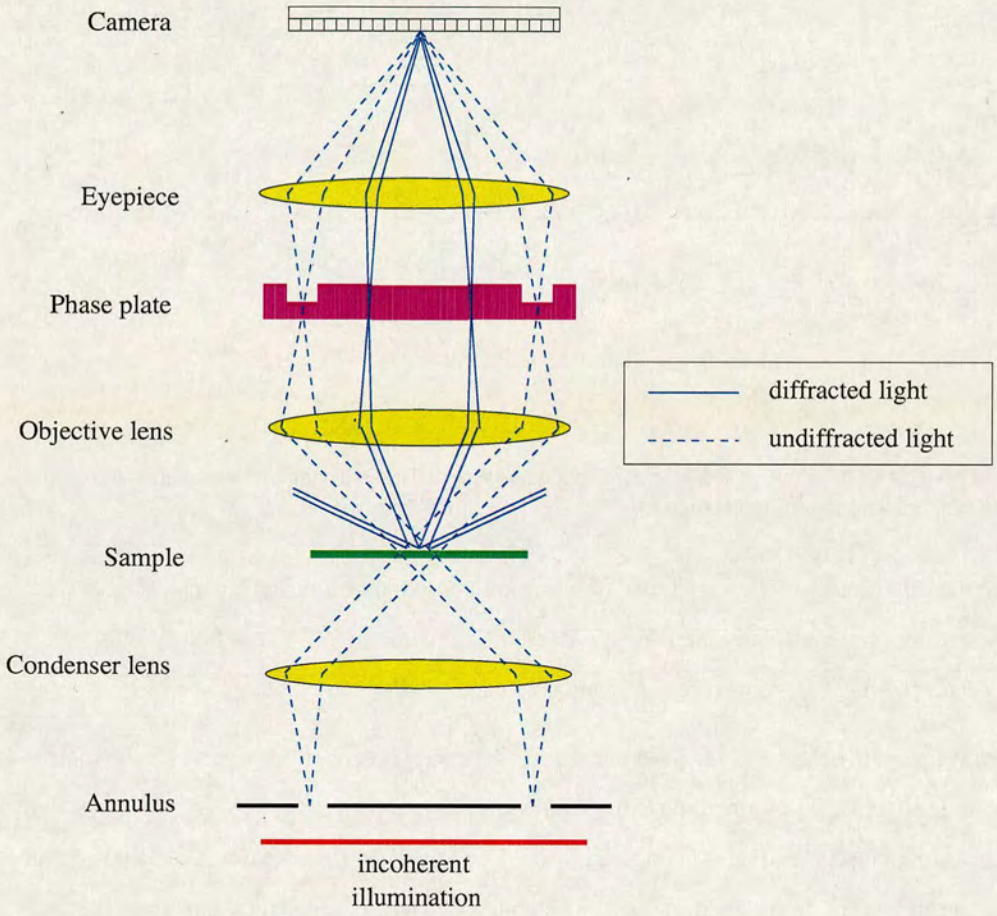

Figure 4.14: Schematic ray diagram of the setup of a phase contrast microscope.

$$E_{PM}(x, y, t) = E_0 \sin[\omega t + \phi(x, y)] \, . \tag{4.8}$$

This wave would have constant amplitude and so the object would not show up as an intensity variation in our image. If we write the above equation as

$$E_{PM}(x, y, t) = E_0 \sin \omega t \cos \phi + E_0 \cos \omega t \sin \phi \, , \tag{4.9}$$

and assume that the phase shift, ϕ, caused by the object is small, then

$$E_{PM}(x, y, t) = E_0 \sin \omega t + E_0 \phi(x, y) \cos \omega t \, . \tag{4.10}$$

If the relative phases of the direct and diffracted waves are changed by $\frac{\pi}{2}$, then the cosine becomes a sine or vice versa in the above equation. The observed field in the image plane now becomes

$$E_{AM}(x, y, t) = E_0[1 + \phi(x, y)] \sin \omega t \, , \tag{4.11}$$

where $E_{AM}(x, y, t)$ is now an amplitude modulated field and hence can be detected as intensity variations in the image. The phase contrast microscope does this by introducing a phase plate to the back focal plane of the object as shown in figure 4.14. The undiffracted light passes through a thinner ring which retards its phase by $\frac{\pi}{2}$. The diffracted light passes through the phase plate without incurring a phase shift. To ensure all the undiffracted light passes through the ring of the phase plate, an annulus is placed in the back focal plane of the condenser lens.

The phase ring is usually darkened or covered by a thin metallic film to attenuate the undiffracted light. This is because the direct beam dominates over the diffracted beam and so reducing its intensity improves the contrast in the image. Different phase contrast objectives and condensers are available commercially with different diameter annuli and phase rings. These are called Ph1, Ph2, etc. It is important that the correct phase contrast objectives and condensers are used with each other as the annulus and phase ring must be aligned for phase contrast imaging to work.

One property of phase contrast microscopy that is often seen as a disadvantage is the formation of halos around the image. This is because the side lobes of the PSF of the light passing through the phase ring are larger in amplitude than the PSFs of light passing through the centre of the phase plate. This weak halo surrounding the image is in fact seen as a slight advantage when viewing giant vesicles since, with membranes of order 50 Å in thickness, they can be difficult to see. The halo makes the vesicles more obvious to spot under the microscope; phase contrast images of POPC vesicles, formed by electroformation on platinum electrodes, can be seen in figure 4.15. POPC is a phospholipid which readily forms giant vesicles by electroformation at room temperature.

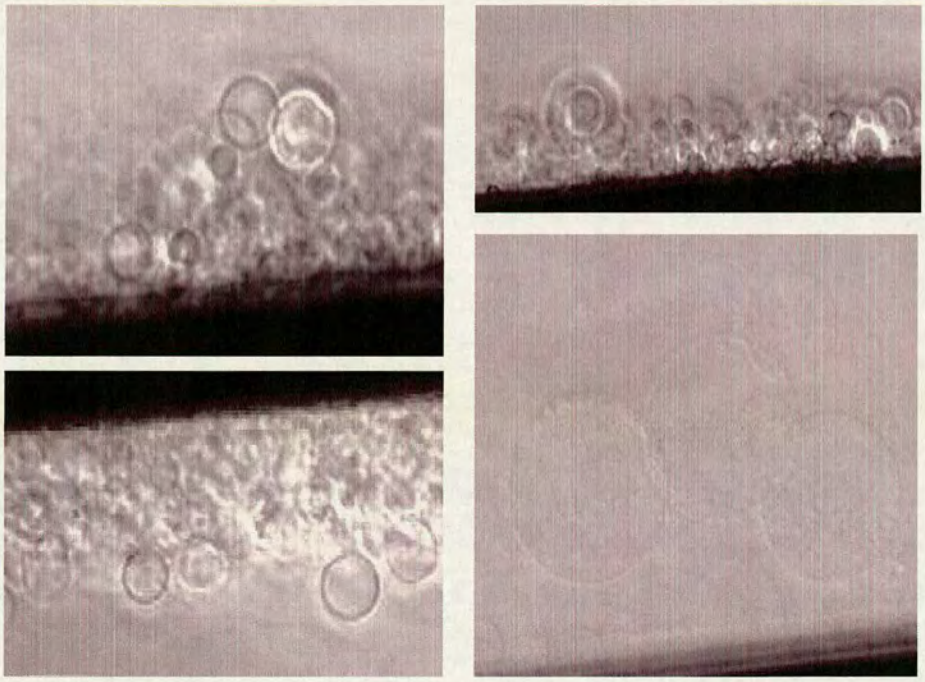

Figure 4.15: Phase contrast images of POPC GUVs formed on platinum wires captured using a CCD camera.

Confocal Microscopy

In confocal microscopy, light from out of focus planes is omitted from the image. This allows for clear, sharp images of the object of interest without light from blurred objects masking the details of the sample.

Out of focus light from the sample is omitted by using pinholes as shown in figure 4.16. The illuminating light is focused to a diffraction-limited spot by the objective, onto the sample. Light reflected from this point can then pass back through the objective lens and through the pinhole to the detector. Any light which does not come from this point will not pass through the detector pinhole and so will not be observed. The use of a two pinhole system as shown in figure 4.16c prevents light reflected from the diaphragm of the illuminating pinhole from getting into the detector.

As the sample is viewed point by point, the image of the object must be viewed by scanning the

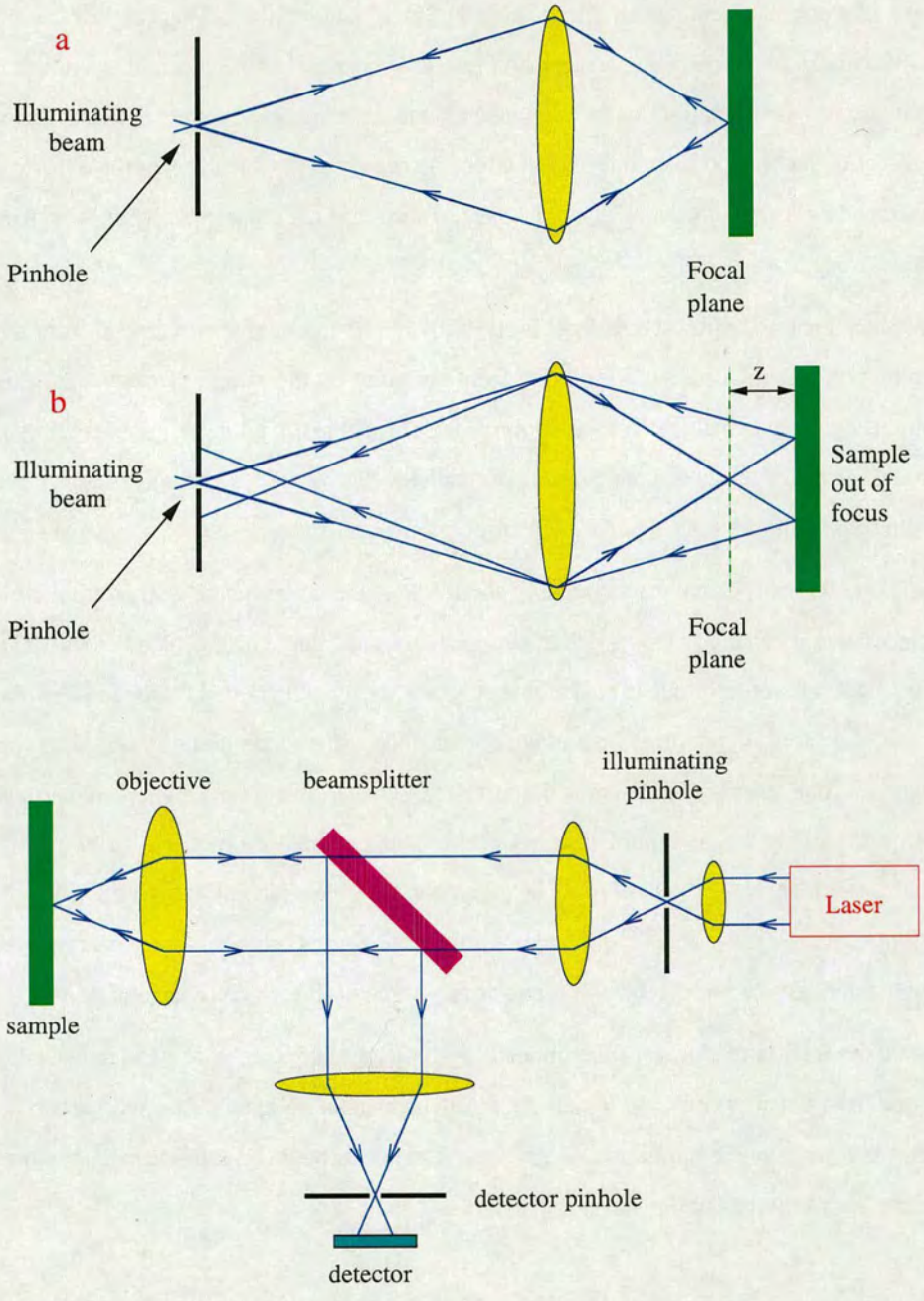

Figure 4.16: Diagrams showing the basic principle of operation of a confocal microscope. (a) [*top*] The object is in focus in the focal plane of the objective lens; light from the object passes through the pinhole and can be observed. (b) [*middle*] The object has moved a distance z out of the focal plane; the sample is no longer in focus and light reflected from the object does not pass through the pinhole and so is not observed in the image. (c) [*bottom*] A schematic showing a two pinhole set-up as is most commonly used in laboratory confocal scanning laser microscopes.

focal plane in a raster pattern so that the image is built up pixel by pixel. This can be done by moving the sample or the objective but, most commonly, beam scanning techniques are used. One technique of beam scanning is the use galvanometer mirrors: one to scan the laser beam in the x direction and one to scan in the y direction. A focus motor, which moves the objective lens towards or away from the sample, can be used to scan through the sample by known steps in the z direction.

In fluorescence confocal microscopy, light used to illuminate the sample is removed from the image so that only the fluorescence emission from the point on the sample is observed. This is done by using emission filters. As the fluorescence emission is at a longer wavelength than the excitation wavelength due to the Stokes' shift, filters can be used which allow the longer wavelength to pass through but remove the shorter wavelength signal.

In conventional fluorescence microscopy, only about 5 % of the fluorescence emitted from each resolvable volume is detected. This is due to the size of the solid angle from which the objective can collect light, loss of light due to reflections at lenses, beamsplitters and filters and also the efficiency of detectors. In confocal fluorescence microscopy, due to the pinholes, the situation is even worse with a less than 0.2 % collection efficiency [117]. This means that attention must be paid to maximising the amount of light collected. This can be done by using good quality lenses with as high an $N.A.$ as possible, as few filters as possible which have high transmittion for the desired wavelengths and fluorophores with a large Stokes' shift so that the excitation wavelength can easily be removed without also losing some of the fluorescence emission.

To calculate the section thickness of the image in a confocal microscope, we need to consider the distance from the focal plane at which the blurred image is no longer detected. It can be shown that the variation in amplitude of the light passing through an infinitesimal pinhole, $V(z)$, where $Z = 0$ in the focal plane of the objective can be written as [115]:

$$V(z) = \frac{sin\left(\frac{u}{2}\right)}{\left(\frac{u}{2}\right)}, \qquad u = 2n_i kz(1 - \cos\theta_{max}) . \tag{4.12}$$

The axial intensity, $I(z) = |V(z)|^2$, is plotted in figure 4.17 with respect to the normalised axial distance, u. The depth resolution of the confocal microscope is defined to be the width at half height of the intensity distribution. This can be approximated as

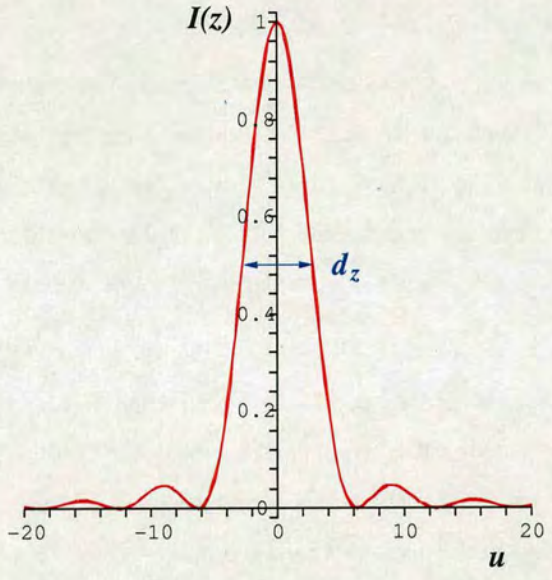

Figure 4.17: The depth response of a confocal microscope. The detected light intensity, $I(z)$, is plotted as a function of the normalised axial coordinate, u, where $u = 0$ corresponds to the focal plane. The depth resolution, d_z, is defined to be the width of the distribution at half intensity.

$$d_z = \frac{0.45\lambda}{n_i(1 - \cos\theta_{max})} . \tag{4.13}$$

In a real confocal microscope, aberrations will cause a broadening of the depth resolution. For an emission wavelength, λ, of 565 nm ($DiIC_{18}(3)$) using a 1.0 $N.A.$ water immersion lens, this gives an approximate depth resolution, d_z, of 0.56 μm.

The lateral, or transverse, resolution of a confocal microscopy is slightly different to that of an ordinary light microscope, which was discussed earlier. A confocal image is created point by point. A point source is focused onto the sample by the objective lens, illuminating an area of the sample with an Airy pattern, $h(r)$ (see equation 4.4), due to the PSF of the lens. This is now imaged by the objective lens into a point detector giving an amplitude PSF for that point on the sample as $h^2(r)$. This means that, in a confocal microscope, the image intensity of a point is

$$I_C(r) = |h^2(r)|^2 \,. \tag{4.14}$$

The two point resolution of the confocal microscope is found to be 8 % better than that of the ordinary microscope if we use the Rayleigh Criterion but using the Sparrow Criterion, the resolutions of standard and confocal microscopes are found to be the same [115]. A very detailed discussion of the depth and transverse resolution of the confocal microscope can be found in chapter 3 of *Confocal Scaning Optical Microscopy and Related Imaging Systems* [115].

We will assume that the Sparrow Criterion, as stated in equation 4.7, is our best estimate to the resolution of images in a confocal microscope. This means that for laser excitation of the $\mathrm{DiIC}_{18}(3)$ fluorophore, which emits at 565 nm, observed using a 1.0 $N.A.$ lens, the theoretical optimal resolution, $d_s = 288$ nm. This is using the formula for incoherent illumination since although the fluorophore is excited by coherent light, its observed fluorescence emission is incoherent. The true resolution of the imaging system will not, in fact, be as good as this theoretical limit since aberrations will lower the resolution but this acts as a good estimate. For optimal imaging, only a few pixels should correspond to this limit, d_s, since any further magnification will not generate more information.

Confocal microscopy experiments were carried out in the COSMIC research facility[2]. The system used was a BIORAD Radiance 2100 laser scanning system mounted on a Nikon Eclipse TE300 microscope. All the equipment was on an optical bench to minimise vibrations. The confocal system was controlled by a computer using the BIORAD LaserSharp 2000 software. A BIORAD motorised focus unit could be used to quantitatively control the depth within the sample (z) which was being imaged when taking 3D data sets.

Vesicle samples containing the $\mathrm{DiIC}_{18}(3)$ fluorophore could be excited using the 488 nm or 514 nm line of the argon laser or the 543 nm line of the green helium-neon laser contained in the BIORAD confocal system. A $HQ590/70$ emission filter was used to observe the fluorescence

[2]COSMIC is a collaborative research facility between physicists, chemists and biologists at the University of Edinburgh. It has equipment for the analysis and manipulation of samples by optical techniques as well as facilities for the processing of the data produced. COSMIC is an acronym for Collaborative Optical Spectroscopy Micromanipulation & Imaging Centre. For more details on COSMIC and its current research programs visit the website: *http://www.cosmic.ed.ac.uk.*

emission whilst blocking any light at the excitation wavelength which was reflected by the sample. The $HQ590/70$ is a bandpass filter; any light of wavelength within a 70 nm band centred at 590 nm can pass through the filter. This means that light below 555 nm is not transmitted by the filter, so all excitation wavelengths are removed whereas the fluorescence emission wavelength of $DiIC_{18}(3)$ (565 nm) is within the 555 nm - 625 nm bandpass of the filter and so passes into the detector.

A quarter wave-plate was placed into the microscope in the path of the incident illumination. This is because the laser source for the confocal microscope is linearly polarised. The effect of the quarter wave-plate is to circularly polarise the light. This is desired because of the way the fluorophore excitation dipoles sit with respect to the vesicle membrane[3]. Circularly polarised light ensures that all fluorophores can be excited no matter what their orientation is in the x-y plane. It is not possible to excite a fluorophore whose dipole sits directly in the z direction of the incident radiation. The use of a quarter wave-plate means that the fluorescent signal from the membranes is maximised and that all areas of the membrane with comparable dye concentrations are seen to fluoresce with the same intensity.

The objective lenses used were as follows: for the platinum wire cell the vesicles were imaged using a Nikon 1.0 $N.A.$ 60× Fluor[4] water immersion lens which had a working distance of 2.0 mm. When the ITO plate cell was used, it was possible to use a lens with a shorter working distance. The lens used was a Nikon 1.4 $N.A.$ 60× Plan Apo[5] oil immersion lens with a working distance of 0.21 mm.

The LaserSharp software was used to display the images of the vesicles. The software sets the size of the confocal pinhole to its optimum value for the objective lens that was in use. Images were scanned in the x-y plane to give a 512×512 array of pixels. The scan rate used to obtain images of an acceptable quality was 500 lines per second. The scan rate was set at the fastest possible speed where the image clarity was good enough for detailed image analysis (see chapter 5). A laser power of around 30 % maximum, with a gain on the detected signal of

[3] see the discussions of the individual fluorophores in section 4.3.1

[4] The Nikon Plan Fluor series have high ultraviolet transmittance rates and low autofluorescence allowing high contrast fluorescence images to be obtained.

[5] The Nikon Plan Apochromat series have red, blue and violet chromatic aberrations corrected to cover the full visible spectrum. These lenses have high numerical apertures and ideal corrections of aberrations all the way to the edges of the field of view.

around 30.0 was usually used to gain[6] a good image from the $DiIC_{18}(3)$ fluorophore which was bright and had good contrast; these values were found empirically whilst imaging the samples. Image stacks through vesicles were gained by zooming in on the vesicle so that most of its diameter covered the 512×512 image and then taking x-y image slices through the vesicle at 0.5 μm intervals in the z direction. For smaller vesicles it was not necessary to zoom in too far since the resolution limits the detail available; no more information is available from the sample than having the maximum resolution of the image covering a few pixels. The choice of the distance in depth between scans was so that each image slice was approximately half the section thickness of the confocal sectioning effect below the previous image slice. See the next chapter for a detailed discussion on how these images were analysed.

Multiphoton Microscopy

Even though we are only imaging the focal plane in confocal fluorescence microscopy, fluorophores in other planes above and below the region of interest are excited. Although the illumination is not as strong in the out of focus planes, it is for longer and integrates over time to a constant intensity [117]. Therefore the unwanted phenomenon of fluorophore photobleaching occurs evenly through the sample.

If, instead, the technique of multiphoton fluorescence microscopy is used, then only fluorophores in the vicinity of the focal region are excited and so fluorophores throughout the sample are not photo-damaged, only those close to the focal plane being excited. This optical sectioning effect happens because in multiphoton microscopy two photons have to arrive at the fluorophore in a short enough time span that, to the fluorophore, they effectively arrive simultaneously. This provides enough energy to promote the electron to an excited state because the wavelength of the illumination is approximately twice that which is necessary to stimulate the fluorophore by single photon excitation (as used in conventional confocal microscopy) and so only provides half the energy necessary for the electronic transition. In multiphoton microscopy, only those fluorophores close to the focal point of the objective receive a high

[6]The gain on the signal amplifies both the fluorophore emission and the random noise in the image. The laser power has to be large enough to produce a signal to noise ratio which provides good contrast in the image collected before the signal is amplified to cover a large range of pixel intensities (the maximum range of pixel intensities is 0 to 255 for 8 bit images).

enough photon flux to have a high probability of being excited and so a sectioning effect is attained similar to that of confocal microscopy but without the use of pinholes.

Due to the simultaneous absorption of two photons, the fluorescence emission depends on the square of the illumination intensity. This provides a tightly confined region around the focal point where fluorescence excitation takes place with the probably of a fluorophore being excited outside of this region decreasing rapidly with distance.

To provide a large enough photon flux for excitation, pulsed lasers are used as power densities of order TW/cm^2 are required [115]. The two photon signal, at constant average power, is proportional to the reciprocal of the duty cycle, $\frac{t_p}{T_p}$ [117]. Here t_p is the pulse duration (of order 100 fs) and T_p is the repetition time. It is possible to attain peak excitation intensities 10^6 times greater than the laser illumination used in typical confocal microscopy, so a low duty cycle of order 10^{-5} is used in order that the average power is low enough to allow heat dissipation in the sample [115].

Increasing the repetition time at constant average power and pulse duration increases the pulse intensity. It is not desirable to increase the pulse intensity above the point where excitation of the fluorophores in the focal volume saturates, also it is necessary for T_p to be longer than the fluorescence lifetime as it is desirable to give time for fluorescence emission. Trying to excite the fluorophores with a second pulse before emission has taken place will reduce the available fluorescence signal from the second pulse.

Image resolution and optical section thickness in multiphoton microscopy is comparable to but not better than those attained in regular confocal microscopy. A detailed treatment of this can be found in *Principles of Three-Dimensional Imaging in Confocal Microscopes* [118].

Multiphoton microscopy was also undertaken in COSMIC. The same Nikon microscope, BIO-RAD laser scanning system and software were used as described for confocal microscopy above. A Coherent Verdi-V10 Ti:Sapphire laser was used as the pumping source at a power of 10 W. The laser light first passed through a Coherent Mira 900 laser cavity which was used to tune and mode-lock the laser. The laser could be tuned between 700 nm and 1000 nm; for all my experiments a wavelength of 780 nm was used. The laser was mode-locked to provide a pulsed illumination source as discussed above as opposed to continuous wave radiation. An

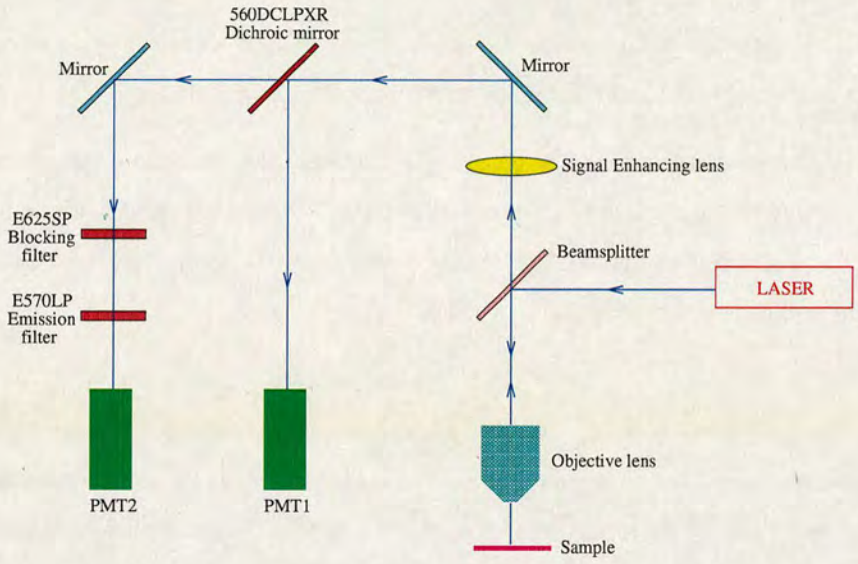

Figure 4.18: Simplified schematic of the optical detection system for dual wavelength experiments where the Rh-DPPE and Laurdan dyes are used. Laurdan fluorescence is detected in PMT 1; Rh-DPPE fluorescence is detected in PMT 2.

Ist-rees laser spectrum analyser was used to monitor the laser light along with two oscilloscopes (Hitachi V-212 and Tektronix 465) which monitored the waveform of the laser pulses and the intensity as a function of wavelength. Coherent solid state temperature control was used to keep the laser at a constant 18 °C. This ensured that changes in temperature did not make the laser drift out of being mode-locked and also ensured a constant laser power during experiments.

The pulsed light source passed from the laser cavity into a BIORAD Radiance 2100 MP beam conditioning unit before reaching the laser scanning system as was used in the confocal microscopy experiments. A prism mounted in place of the objective lens was used to check the alignment of the laser. The beam conditioning unit was used to alter the path of the laser light so that it struck the centre of the prism and hence would fully illuminate the back of the objective lens giving a maximum possible illumination intensity. The LaserSharp software was used to fully open the confocal iris as this was not needed to provide the sectioning effect for multiphoton microscopy.

The fluorophores used to probe the vesicles using multiphoton microscopy were Laurdan and

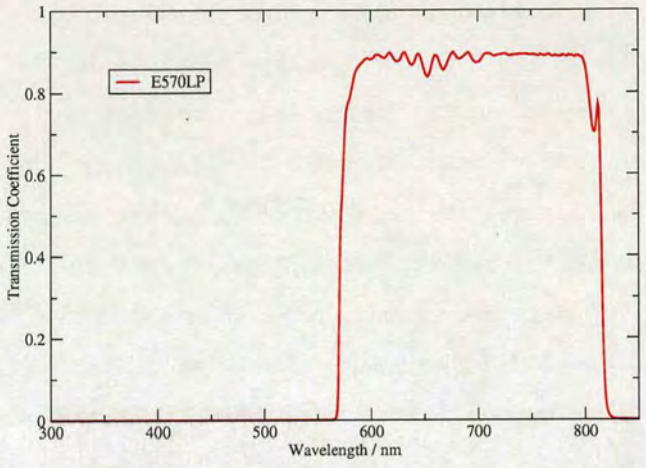

Figure 4.19: Graph of transmission coefficient against wavelength of incident light for the $E570LP$ filter. The transmission coefficient is the proportion of light which passes through the filter at a particular wavelength; 0 corresponds to no transmission and 1 corresponds to full transmission. Data was taken from the Chroma website [120].

Rh-DPPE. When Rh-DPPE was the only fluorophore in use, an $E625SP$ filter was used. This is a short pass filter which allows light of wavelengths below 625 nm to pass through but blocks all light with a wavelength greater than this value. Therefore, with the fluorescence emission of Rh-DPPE being 581 nm, the fluorescent signal from the sample passed through the blocking filter. Conversely, the excitation wavelength was 780 nm so all the illuminating light that was reflected by the sample was blocked by the filter. Consequently only the fluorescent signal of Rh-DPPE was detected by the photomultiplier tube (PMT) at the detector. The signal from the fluorophores was also improved by using a signal enhancing lens. The signal enhancing lens increases the diameter of the detector iris (by up to 24 times for high N.A. objectives) above that for optimum confocal function so that more light is collected and thereby increasing the brightness of the image without increasing the laser power [119].

When Laurdan was used together with Rh-DPPE, it was essential to have optics which could distinguish between the emissions of the two fluorophores. A simplified schematic of the optical detection set up for this particular combination of dyes is shown in figure 4.18. Two PMTs were used for detection, one for each fluorophore. The reflected light was again passed through a signal enhancing lens to improve the strength of the signal before encountering a

$560DCLPXR$ dichroic mirror which was used to split the emissions of the two fluorophores. The dichroic mirror reflected light with a wavelength below 560 nm towards PMT 1, which collected the emission from the Laurdan fluorescence. As Laurdan fluoresces at around 497 nm, it was reflected by the dichroic mirror whereas the Rh-DPPE emission (581 nm) and the excitation wavelength of 780 nm were transmitted towards PMT 2, which was used to collect the Rh-DPPE emission. An $E625SP$ blocking filter (see above) and an $E570LP$ filter was used before reaching PMT 2. This ensured that no reflections of the light used to excite the fluorophores was detected. The $E570LP$ filter is a long pass filter which allows light to pass which has a wavelength of 570 nm or longer. This was used because Laurdan's emission wavelength is sensitive to its environment (see the discussion of Laurdan in section 4.3.1); it was an added precaution so that no signal from the Laurdan was detected in the second PMT, improving the image contrast. The transmission coefficient of the $E570LP$ filter as a function of incident wavelength is shown in figure 4.19. This graph demonstrates that the filters do not have a completely sharp 'on/off' effect on the transmission of light at their stated wavelengths although the transition between blocked and transmitted wavelengths is steep. It also shows that some of the fluorescence emission is lost when passing through the filter, the transmission of this particular filter being around 90 % for wavelengths above 570 nm.

The same objective lenses were used for the respective formation cells as was the case for confocal microscopy experiments. A quarter wave-plate was also used to circularly polarise the incident radiation. The technique for using the LaserSharp software was the same as for the discussion under the confocal microscopy section with the exception that the confocal pinholes were fully opened and slightly different illumination power and gain on the fluorescence signal were used. It was found empirically that an illumination of between 5% and 10% maximum transmitted laser power and a gain of between 10.0 and 20.0 provided bright images with good contrast for the fluorophores used.

Chapter 5

Image Analysis

This chapter describes the techniques I used to obtain quantitative data from images of vesicles obtained by confocal and multiphoton microscopy experiments. This includes the measurement of areas and angles as well as the movement of structures on a spherical surface.

The BIORAD confocal software produces 8 bit digital images, *i.e.* pixel intensities of integer values between 0 and 255, which are saved in BIORAD's own *.pic* format. The 3D image stacks were 512 × 512 pixels in the x and y directions taken in numerous sections through the z direction with constant step size.

These images were first viewed using BIORAD's LaserVox software for 3D rendering of confocal images. Image sections of half a spherical vesicle were stacked on top of each other to form 2D projections of the lower and then upper hemispheres of the vesicle. These 2D images were saved as *.tif* format image files which retain all data in the byte array. The software package IrfanView was then used to batch convert all the *.tif* files to Portable Grey Maps (*.pgm*), again without loss of data, for analysis using the IDL software package.

The LaserVox software also contained a measurement tool which was used to measure vesicle diameters as an average of several measurements. An estimation of the pixel which defined the centre of the vesicle (in 2 dimensions) was also obtained along with the size in microns represented by a single pixel (i.e. a 'scale bar').

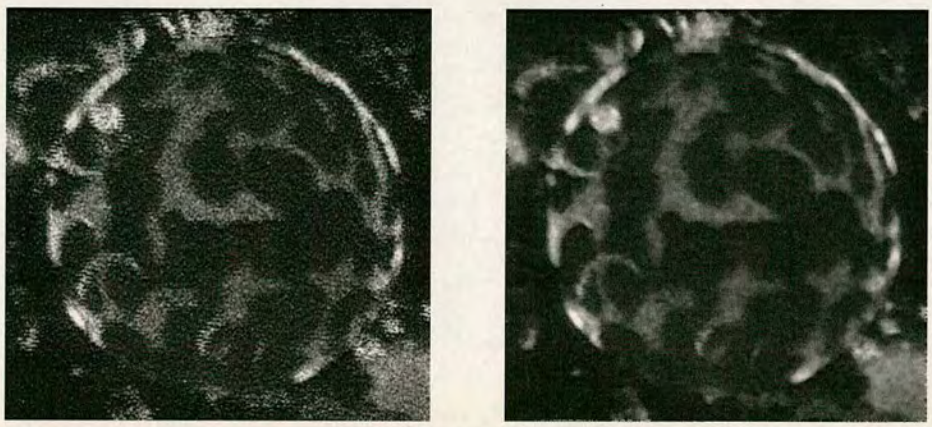

Figure 5.1: Unfiltered image projection of a phase separated GUV (left); the same image after filtering with a 5×5 median filter (right).

5.1 Image Filtering

A median image filter is used in the IDL programs to remove single pixel (*'salt & pepper'*) noise. The median filter is very effective at removing large, spike-like intensity variations from the pixel array. An $M \times M$ median filter removes features of size below $M^2/2-1$, smoothing the image whilst retaining edge sharpness. A 5×5 box is centred on each pixel. The image intensity for that pixel is then replaced with the median value of the pixel intensities in its 5×5 neighbourhood. This is a non-linear, spatial domain filter with the property that it preserved edges and does not move edges by more than the box size used. An example of a vesicle image before and after median filtering is in figure 5.1:

5.2 Intensity Histograms

To decide on a suitable threshold intensity between the bright fluid phase and dark gel phase, it is necessary to look at the intensity histogram for the projected image. The histogram of pixel intensity against frequency of a hemispherical projection of a vesicle can be viewed using the IDL program *histdatafit2.pro* (appendix A.1). This only considers pixels within 95% of the radius from the centre of the vesicle; the reason for this choice will become clear in section 5.3.

5.2.1 Image Thresholding

This histogram can be used to select a sensible value for a threshold pixel intensity between fluid (bright) and gel (dark) phases. The area of membrane represented by each pixel varies depending on the portion of vesicle being imaged (see section 5.3).

The laser light which excites the fluorophore is (near) circularly polarised (see chapter 4) and so can excite fluorophores whose dipole is oriented at any angle in the x-y plane. At positions on the vesicle hemisphere further away from the vesicle centre, despite each pixel representing a greater area of the membrane, the fluorophore dipole could have a greater component in the z-direction and reduce the chances of it being excited by the laser light. A complicated thresholding as a function of distance from the centre of the vesicle could be constructed but this was found to be unnecessary as the separate phases could be picked out from the raw image data by a single threshold value.

5.2.2 Curve fitting the histogram

IDL's *curvefit* function can be used to fit the intensity histogram to the sum of two Gaussian curves. The width at half height (w), maximum height (A) and centre value of each Gaussian (μ) need to be estimated as an input for the *curvefit* function to work from. The dual-Gaussian function, $F(I)$, where I is the intensity, is

$$F(I) = A_1 \exp\left(-\ln 2\left(\frac{\mu_1 - I}{w_1/2}\right)^2\right) + A_2 \exp\left(-\ln 2\left(\frac{\mu_2 - I}{w_2/2}\right)^2\right). \qquad (5.1)$$

5.2.3 Example

The intensity histogram for the image in figure 5.1 and curve fitting for the unfiltered and filtered image can be seen in figure 5.2. A bin size of 2 is used for fitting the data to help smooth the intensity histogram since the curve fitting routine is sensitive to rapid changes in gradient. Each individual Gaussian curve is shown by a dashed blue line and these are summed to an overall curve fitting function shown by the solid red line. The fitting parameters for each of these curves are shown in table 5.1.

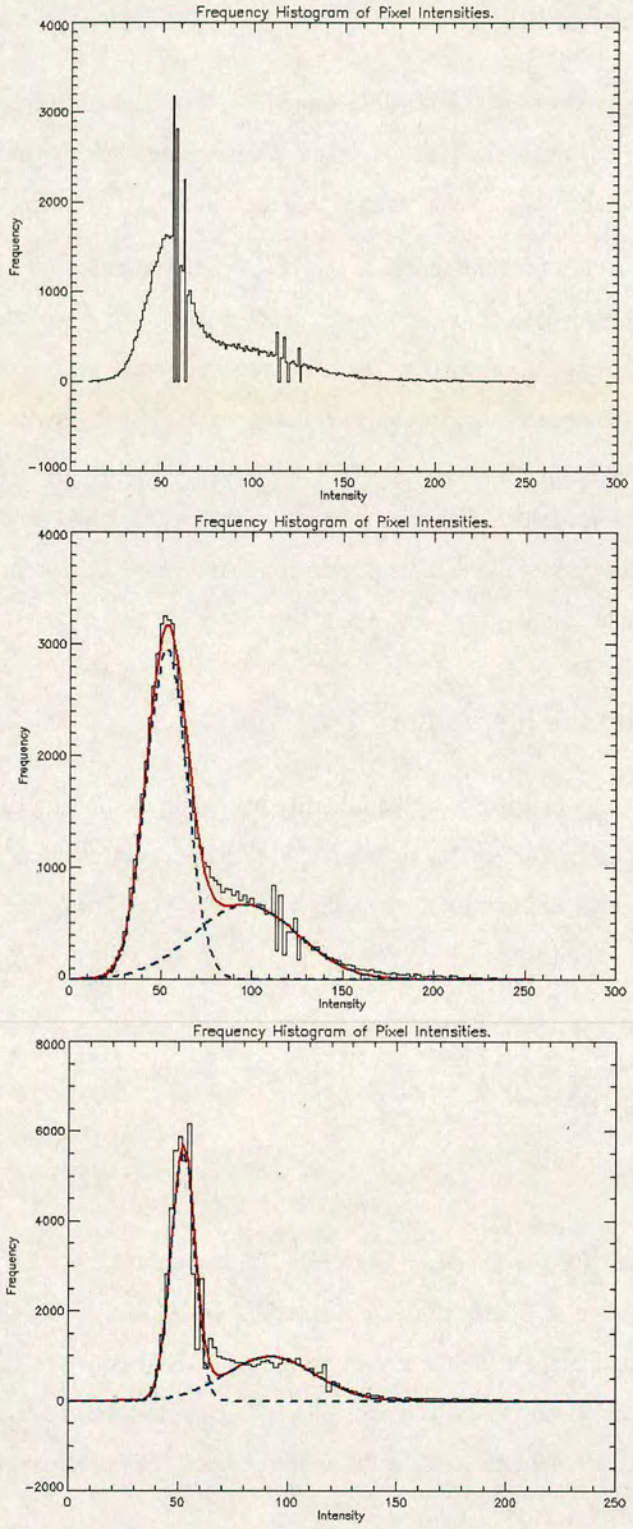

Figure 5.2: Intensity histogram of the unfiltered image in figure 5.1 (top); histogram of the unfiltered image with a bin size of 2 fit to the sum of two Gaussian curves (centre); histogram of the median filtered image, also with a bin size of 2 and fit to the sum of two Gaussians (bottom). The red line is the overall fitted curve and the blue dashed lines are the individual Gaussian curves.

		Unfiltered Image	Filtered Image
Gaussian 1	A_1	2958.1972	5560.1972
	μ_1	53.223299	52.445177
	w_1	26.0656693	12.843289
Gaussian 2	A_2	667.31104	984.61335
	μ_2	96.788166	92.463055
	w_2	67.547327	48.400168

Table 5.1: Curve fitting parameters for unfiltered and filtered vesicle image in figure 5.2 centre & bottom respectively.

The fitting parameters in table 5.1 show that the median filter causes the two Gaussian curves to become narrower with a greater maximum amplitude whilst keeping the centres of the distribution approximately the same. Also, the Gaussian distributions for the fluid (bright) phase are much broader than the low intensity gel phase. The histogram in the bottom of figure 5.2 shows that the Gaussian curves which model the gel and fluid phases of the filtered image cross at a pixel intensity close to 70. This will be the threshold intensity used in section 5.3.1.

5.3 Measuring Area Fractions

To convert the area of the total amount of light and dark pixels on the raw images to the total amounts of fluid and gel phases is not straightforward, because the image is a projection of a hemisphere. In this section I explain how I measure phase area fractions from the raw data and then convert these into mole fractions of each phase. The associated IDL programs (*raft_areas2.pro, raft_areas4.pro, ArcLength.pro*) can be found in appendix A.2.

The area of a single pixel of the 2D projection has a value which depends on its location on the sphere. To gain correct area fractions of the different phases (light & dark areas), it is necessary to integrate over each pixel to find the area it represents.

The following derivation is summarised from section 9.5.1 of *Mathematical Methods for Physics and Engineering* [121] and then expanded upon to the problem of interest. A surface S has a

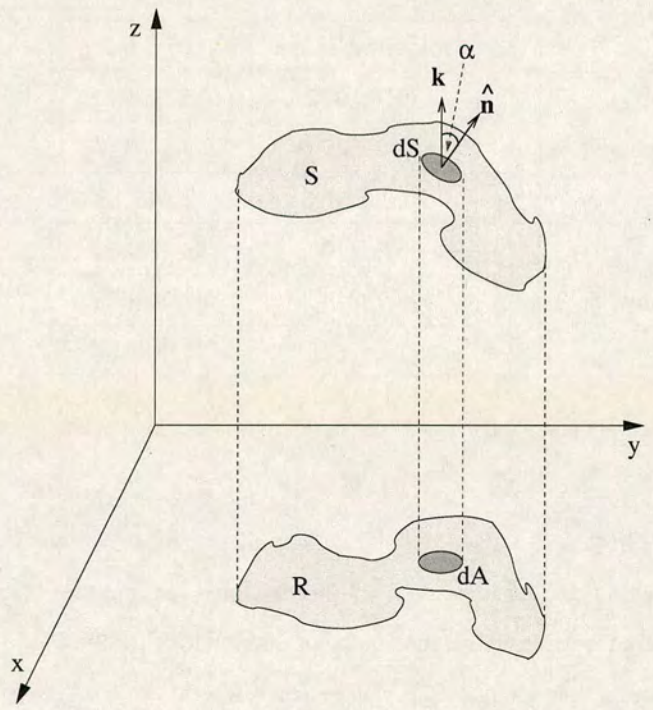

Figure 5.3: A surface, S, projected onto a region, R, in the x-y plane. The surface element $\mathrm{d}S$ projects onto the area element $\mathrm{d}A$. The surface normal unit vector, $\hat{\mathbf{n}}$, is at angle α to the unit vector in the z-direction, $\mathbf{k}$.

projection to a region R in the x-y plane such that a surface element $\mathrm{d}S$ projects onto the area element $\mathrm{d}A$ (see figure 5.3). By geometry, it is seen that $\mathrm{d}A = |\cos\alpha|\mathrm{d}S$, where α is the angle between the surface normal, $\hat{\mathbf{n}}$ and the unit vector, $\mathbf{k}$, in the z direction. Hence,

$$\mathrm{d}S = \frac{\mathrm{d}A}{|\hat{\mathbf{n}} \cdot \mathbf{k}|} \,. \tag{5.2}$$

For a surface defined by $f(x, y, z) = 0$, ∇f is a normal vector and so $\hat{\mathbf{n}} = \nabla f / |\nabla f|$ is a unit normal. Also, using the equality

$$\hat{\mathbf{a}} \cdot \nabla = a_x \frac{\partial}{\partial x} + a_y \frac{\partial}{\partial y} + a_z \frac{\partial}{\partial z} \,, \tag{5.3}$$

where $\hat{\mathbf{a}}$ is a unit vector and inserting $\hat{\mathbf{a}} = \mathbf{k} = (0, 0, 1)$, we are left with:

$$\mathrm{d}S = \frac{|\nabla f|\mathrm{d}A}{\partial f/\partial z} \,. \tag{5.4}$$

For a hemisphere, $f(x,y,z) = x^2+y^2+z^2-a^2 = 0$, where a is the radius of the hemisphere and $z \geq 0$. With $\nabla f = 2x\mathbf{i} + 2y\mathbf{j} + 2z\mathbf{k} = 2\mathbf{r}$ where $\mathbf{r}$ is the radial vector, thus giving $|\nabla f| = 2|\mathbf{r}| = 2a$. Also, $\partial f/\partial z = 2z = 2\sqrt{a^2-x^2-y^2}$. Putting all this together gives us

$$\mathrm{d}S = \frac{a}{\sqrt{a^2-x^2-y^2}}\mathrm{d}x\mathrm{d}y \,, \tag{5.5}$$

where $\mathrm{d}A$ has become $\mathrm{d}x\mathrm{d}y$. We can now integrate over a pixel area by defining the centre pixel of the vesicle, which is an input to the program, as our origin. The vesicle diameter and pixel size, which we will call p, in microns are also inputs to our program. The above equation is symmetrical in x and y, so we will choose arbitrarily to integrate firstly with respect to y over a pixel, and then x. If the units of x and y are also in microns, our integral becomes with change of variables $x \to x'$ and $y \to y'$;

$$A_p = \int_{x-p/2}^{x+p/2}\int_{y-p/2}^{y+p/2} \frac{a}{\sqrt{a^2-x'^2-y'^2}}\mathrm{d}y'\mathrm{d}x' \,, \tag{5.6}$$

where A_p is the surface area of the vesicle projected into the pixel at position (x,y). The integral $\mathrm{d}y'$ can be analytically solved by inspection with the substitution $b^2 = a^2 - x'^2$:

$$A_p = a\int_{x-p/2}^{x+p/2}\int_{y-p/2}^{y+p/2} \frac{1}{\sqrt{b^2-y'^2}}\mathrm{d}y'\mathrm{d}x' \tag{5.7}$$

leaving,

$$A_p = a\int_{x-p/2}^{x+p/2}\left[\arcsin\left(\frac{y+p/2}{\sqrt{a^2-x'^2}}\right) - \arcsin\left(\frac{y-p/2}{\sqrt{a^2-x'^2}}\right)\right]\mathrm{d}x' \,. \tag{5.8}$$

The integral in equation 5.8 is evaluated numerically using the Romberg algorithm contained within the IDL package. The integrand is contained in a separate function file, *ArcLength.pro* contained in appendix A.2. Details of the Romberg method can be found in *Numerical Recipes in C: the art of scientific computing* [122].

The *raft_areas2.pro* program calculates the areas of each pixel within 95% of the radius of the vesicle. Outside of this constraint, the integral diverges rapidly for pixels close to the vesicle equator. Also, at these extremities, any detail in domain structure cannot be resolved as the area represented by a single pixel becomes very large.

Whether a pixel represents fluid or gel phases (light or dark) is determined by intensity thresholding (see section 5.2.1). The areas of pixels in each phase are summed to give a total fluid phase area and a total gel phase area. To find the mole fraction of each phase, the molecular area per head group for the gel and fluid phases needs to be taken into account. A full discussion of the choice of values for these is found in chapter 6. The number of molecules in the gel phase, $N_g = A_g/a_g$, where A_g is the total area of gel phase on the vesicle and a_g is the area per headgroup of lipids in the gel phase. Similarly, the number of molecules in the fluid phase, $N_l = A_l/a_l$, where A_l is the total area of fluid phase on the vesicle and a_l is the area per headgroup of lipids in the fluid phase. Hence, the molar fraction of gel phase on the vesicle, ϕ_g, is found by:

$$\phi_g = \frac{N_g}{N_g + N_l} = \frac{1}{1 + N_l/N_g} \,. \tag{5.9}$$

Defining the ratio of molecular headgroup areas, $\gamma = a_g/a_l$ and the ratio of total areas of the two phases, $\mathcal{A} = A_g/A_l$, we get:

$$\phi_g = \frac{1}{1 + \gamma/\mathcal{A}} \,. \tag{5.10}$$

Similarly the mole fraction of fluid phase on the vesicle is given by:

$$\phi_l = \frac{1}{1 + \mathcal{A}/\gamma} \,. \tag{5.11}$$

Finally, we need to calculate the area of that portion of the hemisphere included when we integrate up to 95% of its radius, A_s. Using figure 5.4, it can be seen that $\sin\beta = \chi a/a = \chi$, so $\beta = \arcsin\chi$. Thus:

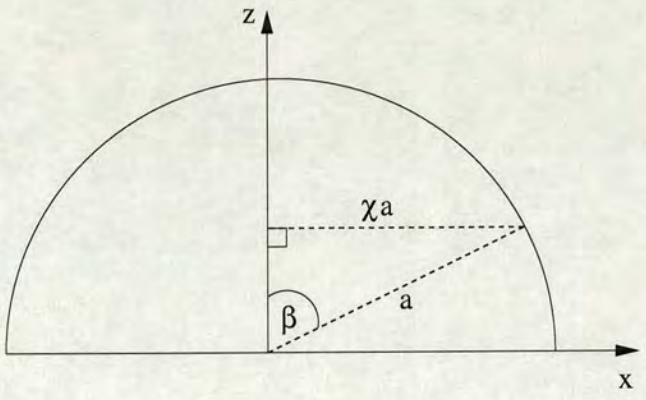

Figure 5.4: Schematic of a 2D slice of a hemisphere in the x-z plane. χ represents the fraction of the radius over which image stacks of a vesicle hemisphere are integrated.

$$A_s = \int_0^{2\pi} \int_0^{\arcsin\chi} a^2 \sin\theta \mathrm{d}\theta \mathrm{d}\phi = 2\pi a^2 (1 - \cos(\arcsin\chi)) \,. \tag{5.12}$$

As the area of a hemisphere is equal to $2\pi a^2$, the fractional area of a hemisphere considered when integrating out to a proportion χ of the radius is equal to $1 - \cos(\arcsin\chi)$ and is independent of the hemisphere radius, a. The percentage error between the total calculated area by integration over pixels, $A_g + A_l$, and the expected area, A_s, is calculated to check that the error is small. It is expected that there would be some small error as we are measuring the area of a section of a hemisphere by summing the areas of square projections on a 2D plane. This error will tend to zero as the ratio $p/a \to 0$.

5.3.1 Example

An example of *raft_areas2.pro* being used on an image of a vesicle is shown below:

The area fractions of the gel and fluid phases of the vesicle in figure 5.1 are measured. The 2D image projection has already been cropped to 362×354 pixels. The vesicle is $33.5\mu m$ in diameter, the centre pixel is $(187, 177)$ and the pixel size is $0.10837\mu m$ in both the x and y directions. An intensity threshold of 70 is used (see figure 5.2).

The centre pixel of the vesicle was found firstly by approximating the centre pixel by placing the mouse over the pixel which visually appeared to be roughly in the central to the vesicle

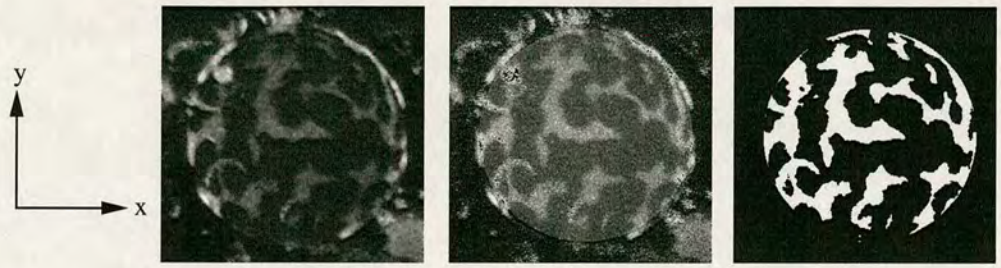

Figure 5.5: The median filtered image (left); the original vesicle image with the area of interest shaded lighter (centre); bi-level image showing which regions of the area of interest the program has picked out to be fluid (bright) and gel (dark) (right).

Molar fraction of gel phase :	0.64766113
Molar fraction of fluid phase :	0.35233887
Area of gel phase measured :	$708.96561\mu m^2$
Area of fluid phase measured :	$503.75776\mu m^2$
Total area measured :	$1212.7234\mu m^2$
Area of hemisphere of radius a :	$1762.8262\mu m^2$
Area proportion considered :	0.68775006
Total area measured should be :	$1212.3838\mu m^2$
Error in total area measured :	0.028007091%

Table 5.2: Data from *raft_areas2.pro* for the vesicle in figure 5.5. Note that these numbers represent those returned by the program and not the accuracy of the measurements.

when the image was viewed using*IrfanView* and noting the pixel coordinates reported by the software. The centre pixel was then found more accurately by using trial and error to make sure that the circular shaded area outputted by *raft_areas2.pro* was centrally positioned over the vesicle (see the centre image of figure 5.5).

Image output from the *raft_areas2.pro* program are shown in figure 5.5. These are used to check that the program is producing results that are in agreement with what the eye can pick out from the original image. The data output from the program is shown in table 5.2.

This data tells us that when measuring the surface area to 0.95 of the vesicle radius, we are only measuring approximately 69 % of the surface area of the hemisphere. It can also be seen that

the error in total measured area by our numerical integration over pixels is less than 0.03 % and is hence considered negligible. The dominant error in the measurement of the mole fractions of the two phases is that only $\sim$ 69 % of the hemsiphere is analysed and hence $\sim$ 34 % of the area of the whole vesicle. The distribution of gel domains appears random on the surface of the vesicle (see images in section 7) and so the mole fractions of phases on the portion of membrane analysed are not necessarily the mole fractions of the phases on the whole vesicle. This error in the measurement of the mole fractions of the phases will be represented by the scatter in my data in chapter 6.

5.3.2 Partly obscured vesicles

If part of a vesicle is masked by other vesicles or lipid junk then the code can be altered by the addition of one or more conditional statements so that only visible areas of vesicles are considered when calculating fractions of the two phases. Examples are $x > 0, y < 0, x > y$ but more complicated conditions can be added if required. These conditions are commented out in the *raft_areas2.pro* code in appendix A.2.

5.3.3 Moving Domains

In the case of moving domains, a composite projection of the vesicle hemisphere does not show any domains as the same part of a membrane is excited several times during a single image acquisition. Some sections of the membrane will have a dark gel phase in one instance but be a bright fluid phase in the next. To measure mole fractions of the two phases, we now need to consider each image section individually. The program *raft_areas4.pro* (appendix A.2) allows the integration of a section of the hemisphere between two inputed radii representing a single 2D image section. Sections near the poles of the vesicle are considered, as sections near the equator of the vesicle represent very narrow differences in radii and contain less lateral resolution of the membrane per pixel. The gel mole fraction is then estimated by averaging over a number of sections:

$$\phi_g = \frac{\sum_i A_i \phi_i}{\sum_i A_i}, \tag{5.13}$$

where A_i is the total area considered in the i^{th} section and ϕ_i is the molar gel fraction in the i^{th} section.

To consider whether a domain moves significantly during the acquisition of a single image, and hence how accurately I can locate and find the area of moving domains, it is necessary to separate the domain velocity into an x-component (left-right) and a y-component (up-down) since the 512 $\times$ 512 pixel image is scanned at 500 lines per second from top to bottom. Firstly, considering the component of the domain velocity in the x-direction (v_x), a single line of the image takes 2 ms to be acquired. If the scale of the image is 0.15 μm/pixel, then for the domain to move by a single pixel whilst the line is scanned it would need to have $v_x > 75$ μm/s. This is far in excess of any experimentally observed domain velocity: see section 7.1 for a full discussion on the observed domain speeds in my experiments. Now considering the component of the domain velocity in the y-direction (v_y), a large domain of, say, 7 μm in diameter moving at a large velocity with $v_y \sim 6$ μm/s would span over $\sim$ 47 lines of an image with a scale of 0.15 μm/pixel. The time taken to scan 47 lines of the image would be $\sim$ 94 ms during which time the domain would have moved up or down by $\sim$ 560 nm or $\sim$ 3 pixels (compare with the theoretical optimum resolution of $\sim$ 300 nm). This however would only introduce a small error in the size of the observed domain and this example is of the extreme of a large domain travelling with a high velocity. The same calculation for a 4 μm domain moving with $v_y \sim 2$ μm/s shows that this domain will move by less than the pixel size whilst being imaged.

5.4 Defining Separate Domains

The program *domain_finder2.pro* reproduced in appendix A.3 is used to isolate independent domains. All the pixels in the image with intensities below the stated threshold value are set to 255 and those above the threshold set to zero. The *label_region* function in IDL, which is for use on bi-level integer arrays, is then used to define the separate domains. Pixels from the original

vesicle image below the threshold intensity are considered to be part of the same domain as any of their 4 neighbouring (above, below, left and right) pixels which also have intensities below the threshold value. An output is created with the independent domains labelled by different indices. The area (in μm^2) and number of pixels of each domain is then printed to the screen.

5.4.1 Movement of Domains

Using *domain_finder3.pro* (appendix A.3), in a similar way to *raft_areas4.pro*, separate domains can be defined in single image slices when the domains are moving.

The centre of masses of these domains in the x-y plane of each domain can be found by taking moments about the x and y axes. With $A_p(x_i, y_i)$ representing the area on the hemisphere of the pixel at coordinate (x_i, y_i) and c_x & c_y corresponding to the x and y coordinates of the centre of mass respectively, we get:

$$c_x = \frac{\sum_i A_p(x_i, y_i) x_i}{\sum_i A_p(x_i, y_i)} , \qquad c_y = \frac{\sum_i A_p(x_i, y_i) y_i}{\sum_i A_p(x_i, y_i)} . \tag{5.14}$$

Now, if we find the 2D centre of mass coordinates (c_x, c_y) of the same domain in two successive image sections, we can find the arc length by which the centre of mass has moved (in μm) using *distance.pro* (appendix A.4). The 3D centre of mass coordinates in frames 1 & 2 can be calculated by Pythagoras' theorem since we know the length of these radial vectors is equal to the radius of the vesicle, a.

$$\mathbf{c_1} = (c_{x,1}, c_{y,1}, c_{z,1}) , \qquad \mathbf{c_2} = (c_{x,2}, c_{y,2}, c_{z,2}) \tag{5.15}$$

where

$$c_{z,1} = \sqrt{a^2 - c_{x,1}^2 - c_{y,1}^2} , \qquad c_{z,2} = \sqrt{a^2 - c_{x,2}^2 - c_{y,2}^2} . \tag{5.16}$$

The angle (θ) between the two radial vectors can be found from the vector dot product:

$$\theta = \arccos\left(\frac{\mathbf{c_1} \cdot \mathbf{c_2}}{a^2}\right) . \tag{5.17}$$

Hence the arc length travelled by the centre of mass of the domain between image sections, $a\theta$, is calculated. Knowing the scanning time between confocal sections, we can then calculate an average velocity of the domain between image slices.

5.5 Measuring Angles on a Sphere

This section explains how the IDL program *sphere_angle.pro* works[1]. The code for this program can be found in appendix A.4.

If we have a spherical vesicle of radius a and wish to find the angle of an apex of a feature on the vesicle surface as viewed on the two dimensional hemispherical projection, we can define three points on the projection: the apex A and two other points, B and C, such that the angle BAC is that which we wish to measure. If we define the centre of the vesicle as the origin, O of our three dimensional coordinate system, then $\mathbf{A} = (x_a, y_a, z_a)$, $\mathbf{B} = (x_b, y_b, z_b)$ and $\mathbf{C} = (x_c, y_c, z_c)$ are radial vectors where the z components can be calculated using Pythagoras: $z = \sqrt{a^2 - x^2 - y^2}$ where the relevant subscripts for each coordinate should be added (see figure 5.6a).

To calculate the angle at point A, we need to find the angle between the two tangents to the sphere at point A which lie in the OAB and OAC planes. The generic equation for a plane in Cartesian coordinates is:

$$kx + ly + mz + n = 0 . \tag{5.18}$$

If we just consider the OAB plane to begin with, the constants k, l, m and n can be found by substitution of the points in the plane O, A and B. Substituting 0 into equation 5.18 simply gives us $n = 0$, whilst substituting points A and B gives us

[1]There may be a simpler and more elegant technique for finding angles on a sphere but this method works with negligible computation time so is more than adequate for the task.

$$kx_a + ly_a + mz_a = 0 \,, \tag{5.19}$$

and

$$kx_b + ly_b + mz_b = 0 \,. \tag{5.20}$$

We have two equations and three unknowns but we can arbitrarily substitute in a value for one of the unknowns as the other two constants will scale with this. I will use $k = 1$ but will, for now, keep k in the equations without substituting this value in. Rearranging equation 5.19 for l gives

$$l = \frac{-(kx_a + mz_a)}{y_a} \,, \tag{5.21}$$

which can be substituted into equation 5.20 and, rearranging for m, leaves

$$m = \frac{k(x_a b_y - x_b y_a)}{z_b y_a - z_a y_b} \,. \tag{5.22}$$

We can now calculate m by substitution of k into equation 5.22 and l by substitution of k and m into equation 5.21. Now that we have the equation of the plane OAB, we need the vector tangential to radial vector $\mathbf{A}$ in the OAB plane, $\mathbf{t_b}$. Vectors $\mathbf{A}$ and $\mathbf{t_b}$ are perpendicular to each other, hence

$$\mathbf{t_b} \cdot \mathbf{A} = 0 \,. \tag{5.23}$$

Defining a point $\mathbf{T} = (x_t, y_t, z_t)$ which lies on the tangent such that we can define our tangential vector as

$$\mathbf{t_b} = \mathbf{T} - \mathbf{A} \,, \tag{5.24}$$

then substitution into equation 5.23 gives $(\mathbf{T} - \mathbf{A}) \cdot \mathbf{A} = 0$. Since $\mathbf{A}$ is the radial vector, then $\mathbf{A}) \cdot \mathbf{A} = a^2$ and so $\mathbf{T} \cdot \mathbf{A} = a^2$. Substituting in coordinates we get

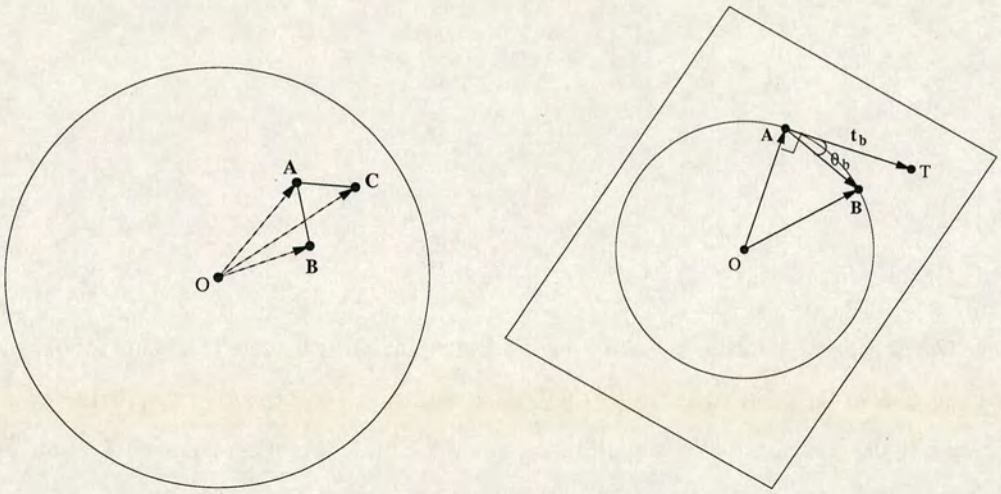

Figure 5.6: (a) [*left*] Schematic of a projection of a spherical vesicle. We wish to find the angle at which the arc AB and arc AC meet. (b) [*right*] Diagram of the OAB plane. The tangent to the sphere, $\mathbf{t_b}$, and point $\mathbf{T}$ are illustrated as well as the acute angle θ_b between vectors $\mathbf{t_b}$ and $\mathbf{AB}$.

$$x_t x_a + y_t y_a + z_t z_a = a^2 \,, \tag{5.25}$$

and since $\mathbf{T}$ also lies in the OAB plane we can write

$$kx_t + ly_t + mz_t = 0 \,. \tag{5.26}$$

Equations 5.25 and 5.26 give us two equations with three unknowns. We can again arbitrarily set, say, $x_t = 1$ since y_t and z_t scale with this. Rearranging equation 5.25 for y_t gives

$$y_t = \frac{a^2 - x_t x_a - z_t z_a}{y_a} \,, \tag{5.27}$$

and substituting this into equation 5.26, rearranging for z_t, leaves

$$z_t = \frac{l(x_t x_a - a^2) - k x_t y_a}{m y_a - l z_a} \,. \tag{5.28}$$

It is now possible to calculate the coordinates of $\mathbf{T}$ for $x_t = 1$ using equations 5.27 and 5.28, and hence $\mathbf{t_b}$ from equation 5.24. Using the arbitrary substitution for x_t means that $\mathbf{t_b}$ could

have a component in the same direction as the vector $\mathbf{AB} = \mathbf{B} - \mathbf{A}$ or in the opposite direction. We desire the former of these two possibilities. To ensure this we can calculate the angle, θ_b between $\mathbf{t_b}$ and $\mathbf{AB}$ by

$$\theta_b = \arccos\left(\frac{\mathbf{t_b} \cdot \mathbf{AB}}{|\mathbf{t_b}||\mathbf{AB}|}\right) , \tag{5.29}$$

where we want θ_b to be acute. If θ_b comes out to be an obtuse angle then $\mathbf{t_b}$ is modified by multiplying this vector by minus one.

A similar calculation is used to obtain the tangential vector in the OAC plane, $\mathbf{t_c}$ and hence the angle on the sphere at point A, θ_A, is

$$\theta_A = \arccos\left(\frac{\mathbf{t_b} \cdot \mathbf{t_c}}{|\mathbf{t_b}||\mathbf{t_c}|}\right) . \tag{5.30}$$

Figure 5.6b illustrates point $\mathbf{T}$ and vector $\mathbf{t_b}$ in the OAB plane.

Chapter 6

Domain Growth

This chapter looks at the growth of gel phase domains in DPPC/DPPE vesicles. Firstly I will review the phase diagrams available in the literature for this system. Based on these phase diagrams, the lever rule can be used to predict the fraction of gel phase. If the system is in equilibrium, the observed fractions should agree with these predicted values. The observed gel fractions observed on slow cooling for three lipid compositions are discussed. I will then introduce a model of non-equilibrium domain growth which provides a better fit to my data than the equilibrium predictions of the lever rule. This non-equilibrium model of growth will then be discussed in terms of published measurements of the diffusion constant of lipids in a gel phase.

6.1 DPPC/DPPE Phase Diagrams

Many phase diagrams for the DPPC/DPPE system have been published [35, 123–138]. These phase diagrams were found in the literature by searching catalogues/databases of lipid phase diagrams [139, 140]. These phase diagrams have been obtained by various different experimental techniques. Most phase diagrams were obtained by differential scanning calorimetry (DSC) although the other techniques that have been used are fluorescence [125], Raman spectroscopy [126], DSC with the addition of optical detection (transmitted light through crossed polarisers due to changes in birefringence at phase transitions) [128], DSC along with freeze

fracture electron microscopy [136], nuclear magnetic resonance (NMR) [127, 129], electron spin resonance [123] and time-resolved X-ray diffraction [133].

The DPPC/DPPE phase diagrams have different topologies and there are considerable differences between the shapes and quantitative position of the phase boundaries. Therefore I will review the phase diagrams available for this system. Phase diagrams shown in figure 6.1 do not consider the effects of the structures of the gel phases of DPPC and DPPE; these phase diagrams show a homogeneous fluid phase at high temperatures and a homogeneous solid or gel phase (the terminology varying from author to author) at low temperatures, with these single phase regions separated by a region of gel-fluid coexistence.

Recall the discussion of the single component phase behaviour of DPPC and DPPE in section 2.3. These two lipids have different structures in the gel phase and hence when in a mixture may not be expected to be miscible in the solid phase over the whole range of compositions. DPPC is in a $P_{\beta'}$ phase and DPPE is in a L_{β} phase below their main transition temperatures; also, DPPC has a pre-transition between solid phases ($L_{\beta'} - P_{\beta'}$) at $\sim 34\,^{\circ}C$. The pre-transition of DPPC and the possible immiscibility of the different solid phases is not considered in the phase diagrams collected in figure 6.1.

Phase diagrams that have taken the different gel phase structures into account are shown in figure 6.2. This type of phase diagram was first published in 1982 [129] but phase diagrams which assume complete miscibility in the 'solid' phase despite the different preferred gel phase structures of the individual components are still published long after this date as shown in figure 6.1[1]. Figures 6.2a,c,d have the same basic topology with figure 6.2b in close enough agreement for me to believe that these phase diagrams at least give a good qualitative representation of the phase behaviour of the system. Quantitatively it can be seen that all the phase diagrams in figures 6.1 and 6.2 have reasonably acceptable agreement in the shape and position of the liquidus curve but there is considerable disagreement in the solidus curve bounding the L_{α}-gel coexistence region. The shape of the fluid-gel coexistence region varies from a thin 'cigar' shape, for example 6.1a,b,c and 6.2d, to a much broader region with a long flat boundary

[1]The earliest binary lipid phase diagrams I have found which take into consideration the different gel phase structures is by Luna and McConnell in 1977 for the DPPC/DPPS system [27], i.e. prior to many of the other phase diagrams in figure 6.1 which fail to take this into consideration.

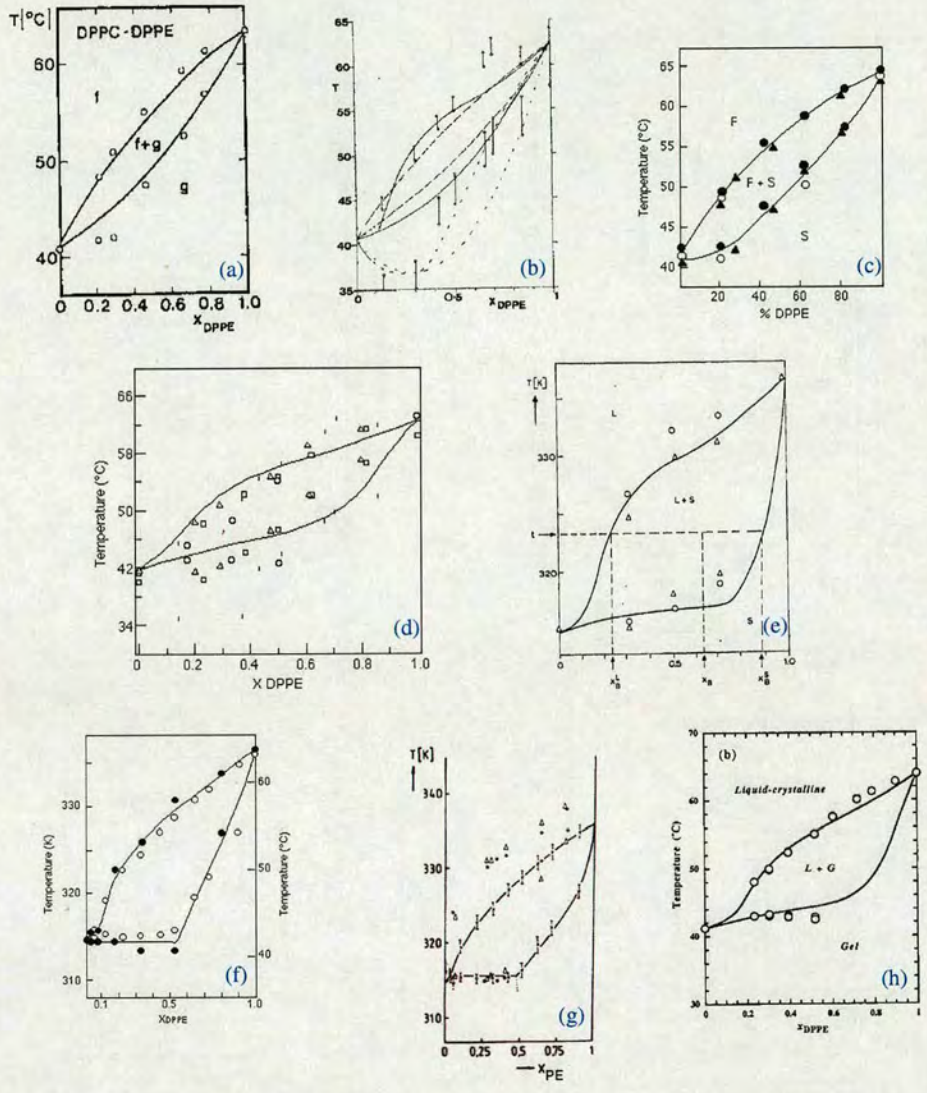

Figure 6.1: Phase diagrams for the DPPC/DPPE system which do not consider the effect of the structures of gel phases on the phase diagram topology: (a) Ipsen and Mouritsen 1988 [135] constructed a phase diagram using the data of Shimshick and McConnell 1973 [123] adding theoretically calculated phase boundaries; (b) Lee 1977 [90] produced using the data of Blume and Ackermann 1974 [124] with the addition of theoretically calculated phase boundaries. This phase diagram is also reproduced by Tenchov *et al.* 1984 [130] with different theoretically calculated model phase boundaries; (c) Sklar *et al.* 1977 [125]; (d) Mendelsohn and Koch 1980 [126]; (e) Arnold *et. al.* 1981 [127]; (f) Petrov *et al.* 1982 [128]; (g) Dörfler *et al.* 1990 [136], also printed in the later publication Dörfler 2000 [138]; (h) Inoue and Nibu 1999 [137].

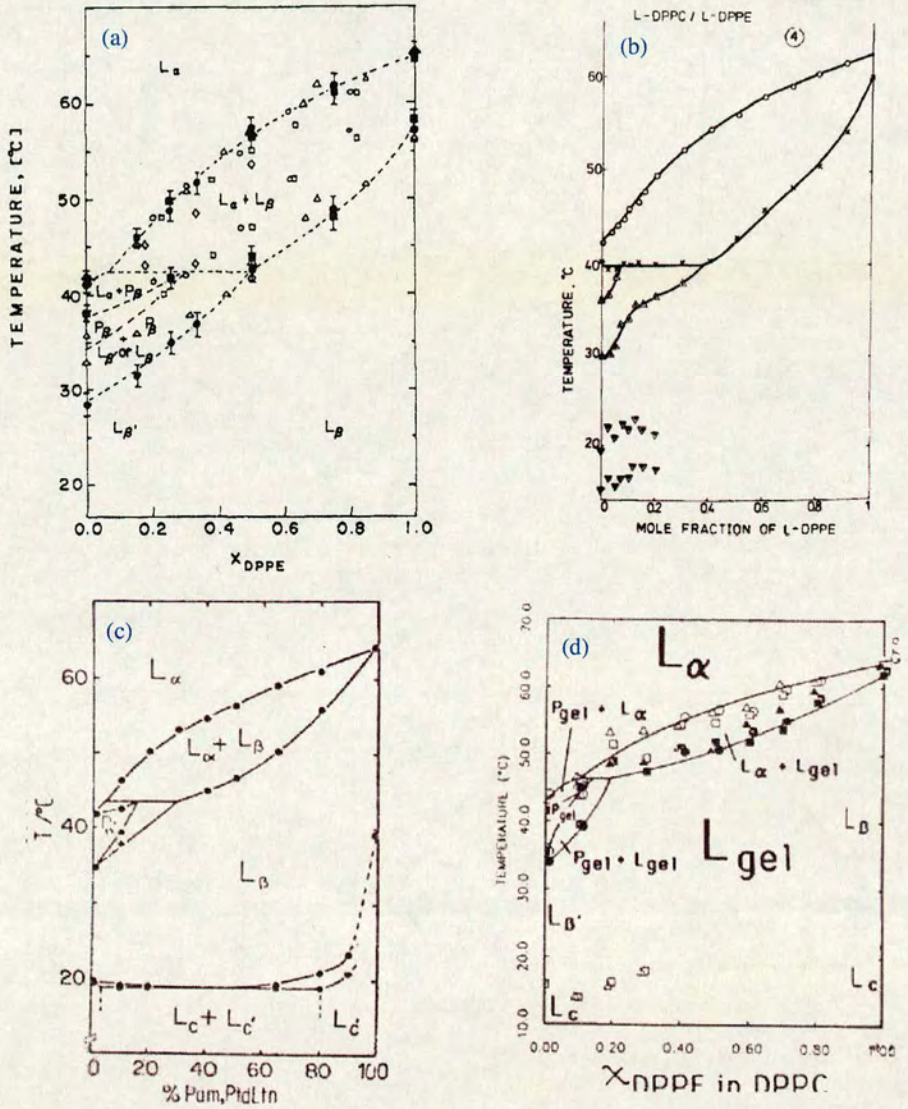

Figure 6.2: Phase diagrams for the DPPC/DPPE system which do consider the effect of the structures of gel phases on the phase diagram topology: (a) Blume *et al.* 1982 [129]; (b) Boyanov *et al.* 1986 [131]; (c) Cevc 1991 [35] reprinted from the original publication by Silvius 1986 [132]; (d) Caffrey and Hing 1987 [133] which is later reprinted in Caffrey and Bywater 1988 [134].

parallel to the composition axis for low DPPE concentrations, for example 6.1f,g and 6.2a,b.

The size and shape of the fluid-gel coexistence region is of most concern when comparing the observed mole fraction of gel phase to that predicted by the equilibrium phase diagram using the lever rule (see section 3.2.5). The gel fraction data I have collected is compared to two phase diagrams with these two different shapes of coexistence region: the 'cigar' shape of Blume and Ackermann (figure 6.1b) [124], and the broader 'sail' shape of Petrov *et al.* (figure 6.1f) [128]. The reason for these choices is partly a historical artefact in that the Blume and Ackermann phase diagram was the first one that I discovered in the literature and hence was the one I initially used to compare my data to. The Blume and Ackermann phase diagram is also of the extreme of the 'cigar' shaped two gel-fluid coexistence region. The Petrov *et al.* phase diagram was later chosen as a second phase diagram to compare my results to as it was of the opposite extreme of the 'sail' shaped gel-fluid coexistence region. These two phase diagrams therefore cover the extremes of the shapes of the gel-fluid coexistence regions of the phase diagrams found in the literature.

It can be seen in the phase diagrams of figure 6.2 that there is no first order phase transition marked on the phase diagram between the $L_{\beta'}$ phase of the DPPC axis and the L_{β} phase of the DPPE axis. Luna and McConnell discuss the possibility of second order phase transitions between gel phase structures as the composition is varied in binary membranes [27]. Blume *et al.* suggest using their NMR data that the gradual transition from $L_{\beta'}$ to L_{β} on increasing DPPE composition is complete at 40-50 % DPPE [129]. This would imply that the gel phase structure of all accessible compositions of the solidus curve of the fluid-gel coexistence region of their phase diagram (figure 6.2a) are in the L_{β} phase prefered by DPPE. This then implies that it is not necessary to consider a change in gel phase structure during cooling through the fluid-gel coexistence region and what effect this might have on my results.

6.2 Observed Fractions of Gel Phase

This section of the chapter discusses the results obtained for the observed gel fractions on slow cooling at a rate between $\sim$ 0.1 and 0.2 °C/min. Vesicles of different compositions were

studied: 1:1 DPPC:DPPE, 3:1 DPPC:DPPE and 1:3 DPPC:DPPE. The images were obtained by multiphoton microscopy and analysed using the methods described for gel fraction analysis in chapter 5. The area per headgroups for the DPPC-rich fluid phase and DPPE-rich gel phase were taken to be 0.65 nm^2 and 0.42 nm^2 respectively [14]. These values are for a single component DPPC fluid and a single component DPPE gel since no data is available in the literature for areas per headgroup in phases consisting of a mixture of these lipids. The value used for the DPPC-rich fluid is in close agreement with the data of Nagle and Tristram-Nagle for the DPPC fluid phase of 0.64 nm^2 [18]. The gel fractions that are measured are compared with the predictions of the lever rule (section 3.2.5) using the phase diagrams in figure 6.1b and 6.1f.

6.2.1 1:1 DPPC:DPPE

A graph of gel fraction against temperature for the slow cooling of 1:1 DPPC:DPPE vesicles is shown in figure 6.3. The red circles and blue squares represent vesicles where the gel domains were moving within the membrane. The black triangles represent the data with static domains. All data are for vesicles labelled with the Rh-DPPE fluorophore with the exception of the blue squares which are for vesicles labelled with $DiIC_{18}(3)$. The observed gel fraction appears to be independent of the fluorophore used and so it would be fair to assume that the observed gel fraction is not significantly affected by the small fluorophore composition of the vesicles.

On cooling, moving domains are first detected at $\sim$ 55 °C. The measured gel fraction increases on decreasing temperature until the domains become static below 45 °C at a vesicle gel fraction between $\sim$ 0.4 and 0.6. The observed gel fractions fall well below the equilibrium predictions of DPPC/DPPE phase diagrams published by Blume and Ackermann [124] (green dashed line) and Petrov *et al.* [128] (purple continuous line). The error in the data points is roughly equal to the scatter in the data.

6.2.2 3:1 DPPC:DPPE

Data for the vesicle gel fraction against temperature for 3:1 DPPC:DPPE vesicles are shown in figure 6.4; the symbols have identical meaning to those for 1:1 DPPC:DPPE as previously

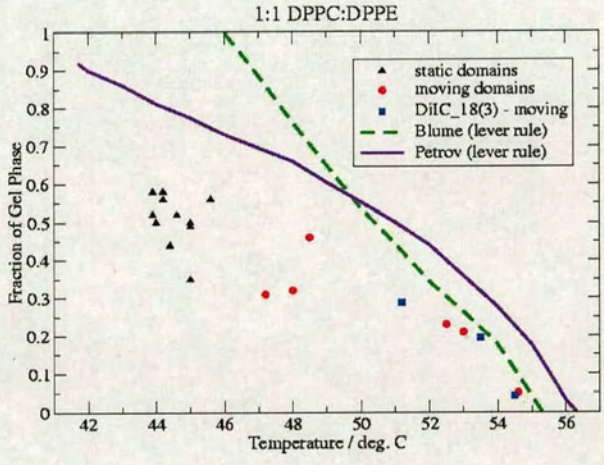

Figure 6.3: Graph of gel fraction against temperature for 1:1 DPPC:DPPE vesicles. The data points represent experimental data and the lines are theoretical predictions using the lever rule for DPPC/DPPE phase diagrams in the literature. The black triangles represent data from vesicles with static domains, the red circles represent data from vesicles with moving domains and the blue squares represent data from moving domains in vesicles with a different fluorophore ($DiIC_{18}(3)$). The green dashed line represents lever rule predictions from the phase diagram of Blume and Ackermann [124] and the indigo unbroken line represents lever rule predictions from the phase diagram of Petrov *et al.* [128].

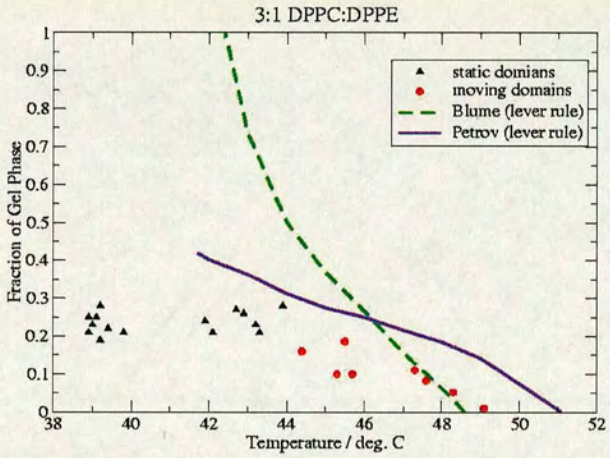

Figure 6.4: Graph of gel fraction against temperature for 3:1 DPPC:DPPE vesicles. The data points represent experimental data and the lines are theoretical predictions using the lever rule for DPPC/DPPE phase diagrams in the literature. The black triangles represent data from vesicles with static domains and the red circles represent data from vesicles with moving domains. The green dashed line represents lever rule predictions from the phase diagram of Blume and Ackermann [124] and the indigo unbroken line represents lever rule predictions from the phase diagram of Petrov *et al.* [128].

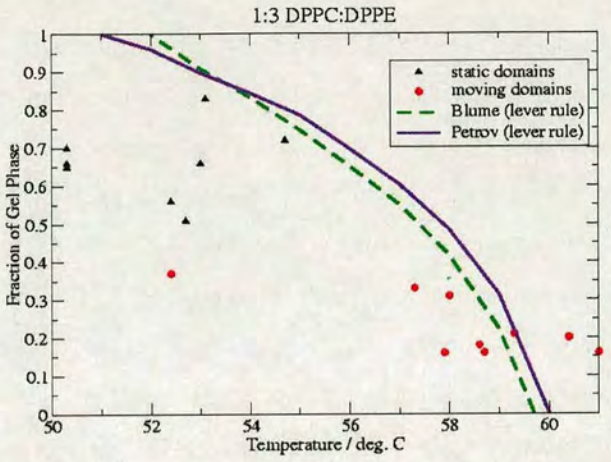

Figure 6.5: Graph of gel fraction against temperature for 1:3 DPPC:DPPE vesicles. The data points represent experimental data and the lines are theoretical predictions using the lever rule for DPPC/DPPE phase diagrams in the literature. The black triangles represent data from vesicles with static domains and the red circles represent data from vesicles with moving domains. The green dashed line represents lever rule predictions from the phase diagram of Blume and Ackermann [124] and the indigo unbroken line represents lever rule predictions from the phase diagram of Petrov *et al.* [128].

discussed for figure 6.3. Moving gel domains first appear in the membrane at $\sim$ 49 °C, between the temperatures predicted by the two phase diagrams that I compare my data against. The fraction of gel phase increases on further cooling with gel domains appearing static below $\sim$ 44 °C, a temperature above that of the solidus curve, possibly suggesting that there is a considerable increase in fluid phase viscosity as the solidus curve is approached. On further cooling to temperatures well below the solidus curve, no noticeable increase in dark domains is observed[2] as the fluorophore appears to be kinetically trapped in what was the fluid phase.

Again my data falls well below the equilibrium predictions of Blume and Ackermann [124] as well as considerably below the predictions of Petrov *et al.*.

6.2.3 1:3 DPPC:DPPE

Gel fraction against temperature data for 1:3 DPPC:DPPE vesicles are displayed in the graph in figure 6.5 where the same symbols are used as figures 6.3 and 6.4 as discussed above. Moving gel domains are first observed at $\sim$ 61 °C, slightly above the temperatures predicted by the phase diagrams with which I am comparing my data. Gel fraction increases on decreasing temperature as expected with domains becoming static below $\sim$ 55 – 56 °C, although there is an out-lier point where moving domains were observed at $\sim$ 52.5 °C with a gel fraction lower than 0.4. There is a large scatter in my data points for 1:3 DPPC:DPPE vesicles but for temperatures well below the fluidus curve my data points are all below the equilibrium predictions of Blume and Ackermann [124] and Petrov *et al.* [128],which both forecast very similar area fractions. The 1:3 DPPC:DPPE vesicles never reached a gel fraction of 1.0 below the solidus curve as predicted by the equilibrium phase diagrams.

6.3 Model of 'Tree Ring' Growth

Despite considerable data scatter, the data in figures 6.3-6.5 consistently show that the observed gel fractions observed in the membranes do not reach the equilibrium composition as predicted by the lever rule. Therefore a new model of non-equilibrium domain growth is needed to explain my results. I would like to acknowledge and thank Dr. Peter Olmsted for providing the intellectual insight into the proposed non-equilibrium growth mechanism.

Lipid gel phases are solid-like with a high degree of lateral packing and ordered acyl chains (see section 2.3). This results in a slow diffusion constant within gel phases; the experimentally measured diffusion constants for lipid gel phases will be reviewed in section 6.4 to quantify this claim. As the vesicle is slowly cooled through the fluid-gel coexistence region, the composition of gel phase domains has to change as shown in figure 6.6. If lipid diffusion in the gel domains is not fast enough to alter the composition of the domain to the equilibrium composition for the current temperature then the system will drop out of equilibrium, resulting in non-equilibrium domain growth.

[2]Note that I do not use the term gel fraction here since below the solidus curve the whole vesicle will be in gel phase(s).

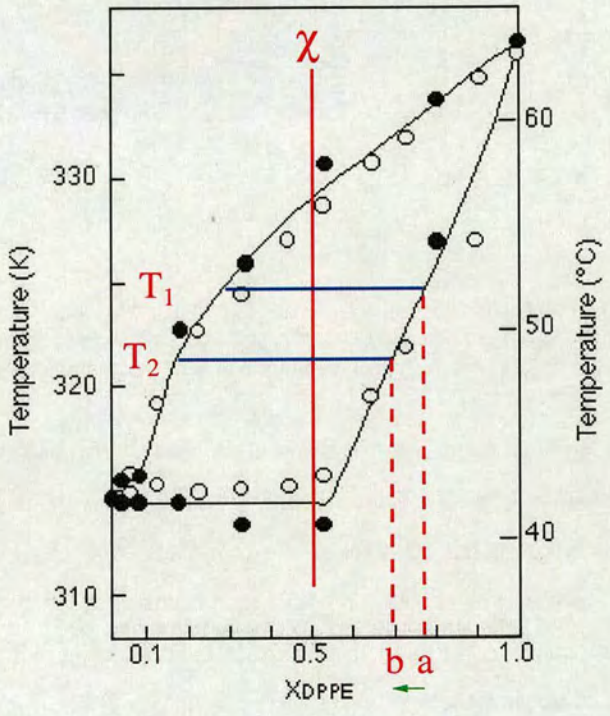

Figure 6.6: On cooling a vesicle of total composition χ, in equilibrium at temperature T_1 the gel phase will have composition a. On cooling to temperature T_2, for the vesicle to remain in equilibrium the gel phase will have to alter its composition to b. If the diffusion constant in the gel phase is too slow such that it cannot change its composition quickly enough then the system will become out of equilibrium resulting in non-equilibrium growth of the gel domain. The phase diagram used in this figure is that of Petrov *et al.* [128].

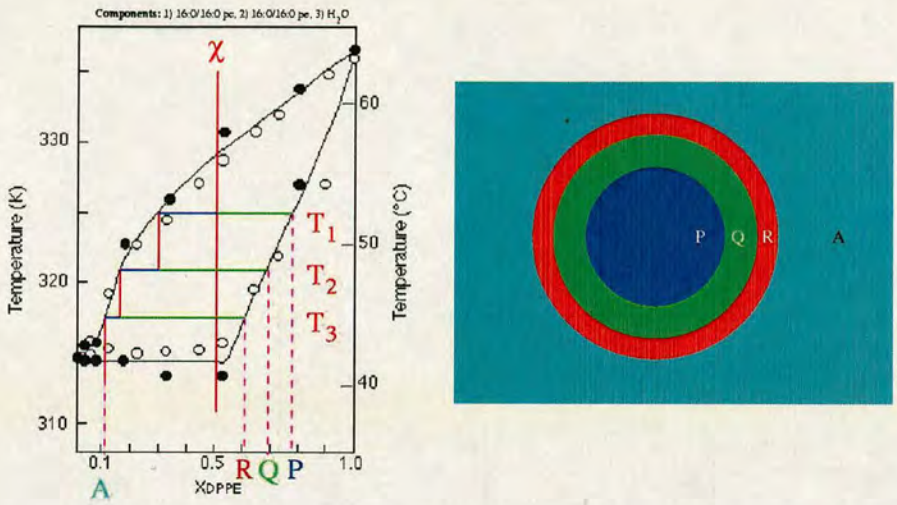

Figure 6.7: [*left*] Phase diagram to explain the non-equilibrium 'tree ring' growth of gel phase domains in a membrane of total composition χ. The phase diagram using is that of Petrov *et al.* [128]. [*right*] Cartoon of the 'tree ring' growth of a gel domain in a section of membrane as depicted in the phase diagram (*left*).

If the gel domains become out of equilibrium with the fluid phase, then the fluid phase will behave as an isolated system and phase separate according to the lever rule, depositing a gel phase of a different composition on the gel domains which already exist. As the temperature is cooled further, the fluid phase again cannot remain in equilibrium with the gel phase and so acts as an isolated system, phase separating by the lever rule and depositing more gel phase on the existing domains of a composition which is different again in composition.

This non-equilibrium 'tree ring' growth is explained by the cartoon in figure 6.7: if the vesicle starts off with a composition χ and is cooled to a temperature T_1, it will phase separate, according to the lever rule, into a gel of composition P and a fluid of a composition determined by where the tie-line intersects the liquidus curve. When the system is cooled further to temperature T_2, the gel phase cannot rearrange its composition quickly enough to remain in equilibrium with the fluid phase, so the fluid phase behaves like an isolated system and phase separates according to the lever rule into a gel of composition Q and a fluid of composition determined by the liquidus curve at that temperature. On further cooling to temperature T_3, again due to the gel phase being unable to remain in equilibrium with the fluid phase, the fluid phase phase separates according to the lever rule into a gel of composition R and a fluid of

composition A. The right of figure 6.7 shows a cartoon of the membrane at this point where a gel domain with composition P at its centre surrounded by a ring of gel of composition Q which in turn is surrounded by a ring of gel of composition R. This gel domain is surrounded by a fluid of composition A. This ring structure of the gel phase is reminiscent of the ring structure seen in the cross-section of tree trunks which can be used to determine the age of the tree, hence I refer to this non-equilibrium mechanism of domain growth as 'tree ring' growth.

The rationale for using symmetric (circular) growth of domain in the cartoon in figure 6.7 should become clear in chapter 7 where the morphology of gel domains is discussed in detail. Also, the size of temperature steps indicated in figure 6.7 should not be taken literally,since in the slow cooling regime of my results, the temperature steps down the phase diagram would be expected to be very small; this diagram is only meant as schematic explanation of the mechanism of 'tree ring' growth. The lever rule for each step of 'tree ring' growth down the phase diagram can be used to predict the gel composition of a vesicle for a given temperature. I will now compare prediction of the 'tree ring' model with my gel fraction data.

Predictions of the lever rule and 'tree ring' growth for the phase diagrams of Petrov *et al.* [128] and Blume and Ackermann [124] were compared. Figure 6.8a shows the final gel composition when exiting the two-phase region for the phase diagram of Petrov *et al.* as a function of the number of 'tree ring' steps (N_s) taken through the two-phase region. Each step was an equal drop in temperature with the exception of the 24 steps for 1:3 DPPC:DPPE: this was where the first 8 steps of the 16-step calculation were halved with the final 8 steps remaining the same[3]. It can be seen that the final gel fraction drops quickly and then levels out, so it is assumed that the number of steps used (the largest number of steps shown in the graph for each composition) reflects the 'tree ring' growth in the limit of a large N_s. The large N_s limit represents the amount of gel phase, at the compositions determined by the solidus curve, that needs to grow to shift the fluid phase composition down the liquidus curve.

Figures 6.8b and 6.8c show comparisons of gel fraction against temperature for the relevant compositions for the lever rule and 'tree ring' growth for the phase diagrams of Petrov *et al.*

[3]This was because the first 8 steps were having the most significant effect on the final gel fraction whilst the final 8 steps couldn't be sensibly halved due to the steep gradient of the fluidus curve making measurement errors significant in the result.

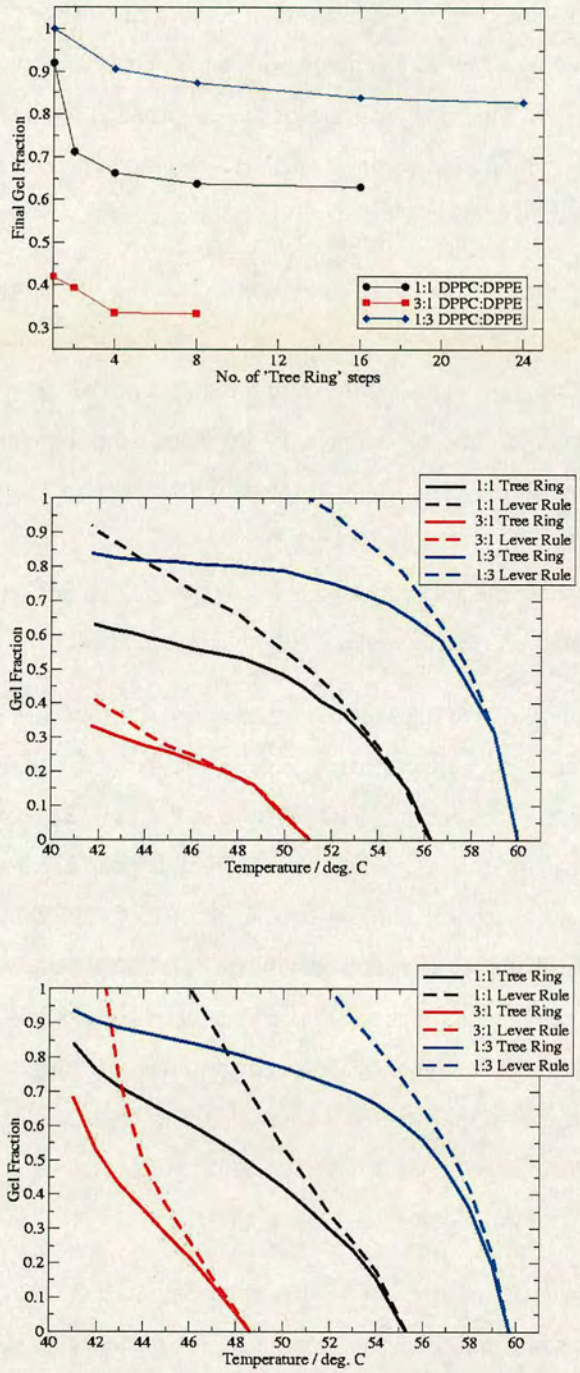

Figure 6.8: (a) [*top*] Final gel phase fraction as a function of the number of 'tree ring' steps (N_s) taken through the two-phase region of the phase diagram by Petrov *et al.* [128] for the three compositions. (b) [*middle*] Comparison of lever rule and 'tree ring' predictions of gel fraction against temperature for the three compositions using the phase diagram of Petrov *et al.* [128]. (c) [*bottom*] Comparison of lever rule and 'tree ring' predictions of gel fraction against temperature for the three compositions using the phase diagram of Blume and Ackermann [124].

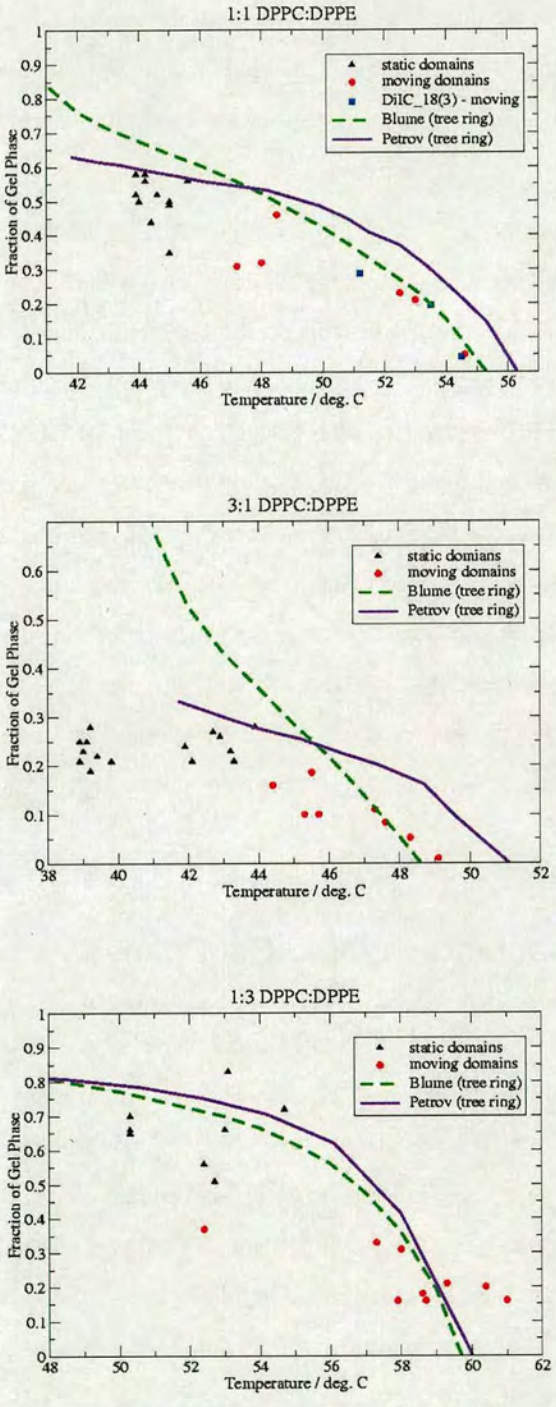

Figure 6.9: Gel fraction against temperature data plotted on the same graph as predictions by the 'tree ring' model using phase diagrams from the literature. (a) [*top*] 1:1 DPPC:DPPE; (b) [*middle*] 3:1 DPPC:DPPE; (c) [*bottom*] 1:3 DPPC:DPPE. The black triangles represent data from vesicles with static domains, the red circles represent data from vesicles with moving domains and the blue squares represent data from moving domains in vesicles with a different fluorophore ($DiIC_{18}(3)$). The green dashed line represents 'tree ring' model predictions from the phase diagram of Blume and Ackermann [124] and the indigo unbroken line represents 'tree ring' model predictions from the phase diagram of Petrov *et al.* [128].

and Blume and Ackermann respectively. In both cases the 'tree ring' predictions are assumed to represent the behaviour in the limit of a large N_s through the two-phase region. In all cases 'tree ring' growth predicts a lower gel fraction than equilibrium lever rule predictions because the inner part of the domains have higher than equilibrium concentrations of the high melting temperature lipid.

My data for the three compositions of 1:1, 3:1 and 1:3 DPPC:DPPE are again shown in figure 6.9 but this time the tree ring predictions for large N_s are plotted with the data. The 'tree ring' predictions are a much closer fit to my data than the equilibrium predictions with the predictions of the phase diagram of Petrov *et al.* [128] providing the closest fit. The fluidus curve at 0.5 and 0.25 composition of DPPE, as predicted by my data for 1:1 and 3:1 DPPC:DPPE, is below that reported by Petrov *et al.* and my data is consistently below the 'tree ring' prediction but the data follows a similar shape to the Petrov *et al.* 'tree ring' curve shifted to slightly lower temperatures. This suggests that a phase diagram with the same qualitative 'sail' shape to that of Petrov *et al.* but slightly different quantitative positioning of the solidus and liquidus curves would provide an excellent fit to my data. In view that the quantitative positions of the liquidus and, in particular, the solidus curves of the phase diagrams in figures 6.1 and 6.2 vary considerably, then it can be argued that the 'tree ring' model provides a good fit for my experimental data.

6.4 Diffusion Constants in Lipid Gel Phases

Are the measured diffusion constants for lipids in a gel phase slow enough to allow non-equilibrium tree ring growth of gel domains? Here I will review the measured diffusion constants in the published literature for lipids in a gel phase. Many review articles exist on diffusion in lipid membranes [141–148]. These articles, however, concentrate on the diffusion of lipids and proteins in fluid membranes with only fleeting reference to the gel phase if it is mentioned at all. This represents the vast literature on diffusion in fluid bilayers whilst comparatively few researchers have published results on diffusion in a lipid gel phase.

Many different techniques are used to measure lipid diffusion constants. These techniques include fluorescence recovery after photobleaching (FRAP) [149–153], fluorescence correlation

spectroscopy (FCS) [154, 155], single particle tracking (SPT) [156], nuclear magnetic resonance (NMR) [157–159] and neutron scattering [160]. Fluorescence techniques, particularly FRAP, are most commonly used particularly for the determination of diffusion constants in a gel phase.

Most researchers seem to be in agreement that the diffusion constant (D) of a lipid in the fluid phase is around 4×10^{-8} cm^2s^{-1} [155]. Although results exist in the range $10^{-6} - 10^{-9}$ cm^2s^{-1}, the faster diffusion constants are obtained by neutron scattering which is sensitive to picosecond timescales and so these results are interpreted to be the 'short time' diffusion constant for a 'caged' lipid in a potential defined by its neighbouring lipids [161].

There appears to be far less clarity on the diffusion constant for a lipid in a gel phase. Hac *et al.* claim the range of values in the literature to be $10^{-16} - 10^{-9}$ cm^2s^{-1} [155] and Almeida and Vaz claim a range of $10^{-16} - 10^{-11}$ cm^2s^{-1} [146]. Other authors prefer simply to state a maximum value, for example $D \lesssim 10^{-11}$ cm^2s^{-1} [162]. Saxton claims that diffusion in a gel phase is 'along defects and grain boundaries' with $D \leq 10^{-10}$ cm^2s^{-1} [148]. I have found values to vary from $D \leq 3 \times 10^{-17}$ cm^2s^{-1} for DMPC at 13 °C [150] to $D = 2.1 \times 10^{-6}$ cm^2s^{-1} for DPPC in the $L_{\beta'}$ phase at 45 °C [145] although I would consider DPPC to be in the fluid L_α phase at this temperature (see table 2.4). A high activation energy of $30 - 40$ kcal/mol has also been reported for the diffusion of lipids in the gel phase [143].

The vast majority of the experiments to find D in a gel phase have been done by FRAP where a section of membrane is photobleached and the diffusion constant is determined from the rate at which the membrane regains its fluorescence intensity. This technique measures the diffusion of a fluorescent probe in a lipid gel phase and this diffusion constant is then inferred to represent the diffusion constant of the lipids in their gel state despite the probe having a different chemical structure to the lipid. This assumption may be flawed for an ordered gel state since, assuming the statement of Saxton to be correct that diffusion in a gel phase occurs due to defects and grain boundaries, inserting a chemically different species into an ordered structure would be expected to create a defect within the packing structure of the gel phase. Hence the diffusion constant of a fluorophore would be observed to be greater than that of the lipids in their gel phase since the fluorophore would create a defect that would enhance

its diffusion. Similar arguments criticising the insertion of probe molecules to determine the diffusion constant of lipid membranes have been made [145].

Vaz *et al.* [141] take the argument for probes reporting incorrect diffusion constants in the gel phase further. They argue that the probes could be 'squeezed out' of the ordered gel phase domains into clusters which would be rich in the probe and more fluid-like than the surrounding gel phase and hence the probe diffusion would be much higher than that of the gel phase. They argue a mechanism by which the probe clusters can diffuse within the gel phase at a rate similar to that of the perturbing probe. This mechanism is not unreasonable as experiments to study the diffusion constant in the gel phase are done on single component vesicles where the membrane is completely gel. In my experience, with the exception of Laurdan, all the probes I have used have preferentially partitioned into the fluid phase of a bilayer in fluid-gel coexistence. As a vesicle undergoes a transition from the fluid to gel phases, it is reasonable to think that probes which do not favour being in the gel phase would cluster together into more disordered regions when the membrane undergoes a fluid to gel transition. A further argument by Vaz *et al.* [141] for the measurement of anomalously high diffusion constants in the gel phase is for experiments when vesicles with diameter 300 nm or less are used. They argue that due to the higher curvature of the smaller vesicles, the packing isn't able to be as tight in the gel phase and hence lipid diffusion constants are faster than lipids in a gel phase in larger liposomes.

Many researchers do not differentiate between the different gel phases which the membrane could be in ($P_{\beta'}$, L_{β}, $L_{\beta'}$) when discussing the diffusion constant for lipids in a gel state. All the data I have found for diffusion constants in a gel phase have been for DMPC or DPPC and the majority of these are for the $P_{\beta'}$ phase. Schneider *et al.* [150] report anomalously large diffusion along line defects of $D \sim 4 \times 10^{-11}$ cm^{2}s^{-1} in the $P_{\beta'}$ phase of DMPC at 16 °C whereas the diffusion coefficient in the 'ordered material' is $D \leq 10^{-16}$ cm^{2}s^{-1}; these line defects are considered by the authors to be due the corrugations of the $P_{\beta'}$ (ripple) phase.

I was unable to find any data in the literature on the diffusion constant in the L_{β} phase of DPPE. Hydrogen bonding occurs between PE headgroups [163]; this additional attraction between PE headgroups may possibly reduce their diffusion constant compared to lipids with a PC headgroup. In light of the above discussion, it seems only possible at present to put an upper

limit on D for a lipid gel phase, with perhaps $D \lesssim 10^{-11}$ cm^{2}s^{-1} a reasonable upper bound for lamellar gel phases (L_β and $L_{\beta'}$). Due to a lack of a definitive diffusion constant for a DPPE rich L_β phase, it would be reasonable to consider 'what is the upper bound on D for the gel phase that would be implied by 'tree ring' growth of domains?'

The mean square distance ($< x^2 >$) that a lipid with diffusion constant D would diffuse in a time t is given by

$$< x^2 >= 4Dt \, . \tag{6.1}$$

This implies that the mean time taken for a lipid to diffuse a distance of 2 μm (an estimate of the diameter of a small gel domain) would be 100 s for $D \sim 10^{-10}$ cm^{2}s^{-1}, 1000 s (16 mins 40 s) for $D \sim 10^{-11}$ cm^{2}s^{-1} and 10^8 s (3.18 yrs!) for $D \sim 10^{-16}$ cm^{2}s^{-1}. The slow diffusion of DPPC at room temperature, i.e. in the $L_{\beta'}$ phase, has been shown by Scherfeld *et al.* by photobleaching a 5×5 μm^2 patch of a giant DPPC vesicle labelled with DiIC$_{18}$(3); fluorescence recovery was not observed within hours [10].

Rough measurements of domain growth rate were taken using time series of domain formation observing the top of the vesicle. Initial growth rates where the majority of domains were still circular[4] showed an approximate increase of domain radius of $\sim 0.01 - 0.03$ μm/s. At $D \sim 10^{-11}$ cm^{2}s^{-1}, the lipid lateral diffusion is[5] ~ 0.002 μm/s and hence lipid diffusion cannot keep up with the growth of the domain boundary as it is approximately an order of magnitude slower. This implies that it would not be possible for the composition of the gel phase to remain in equilibrium with the fluid phase, resulting in 'tree ring' growth of the domains. Even if one were to believe that the lipid diffusion constant was as fast as $D \sim 10^{-10}$ cm^{2}s^{-1}, lipid diffusion (~ 0.02 μm/s) would be at approximately the same rate as the growth of the domain front and so the lipid composition at the centre of the domain certainly would not be able to remain in equilibrium with the fluid phase, again resulting in 'tree ring' growth of domains. A discussion of domain interactions in terms of the viscoelasticity of the gel phase in

[4] See section 7.1 for a full discussion of the growth and morphology of domains in DPPC/DPPE vesicles.

[5] This is on the assumption of the time taken to travel micron length-scales being the important consideration; the 'diffusion velocity' is dependent on the length-scale, or time, over which the lipid motion is considered since $v = \mathrm{d}\sqrt{< x^2 >}/\mathrm{d}t = \sqrt{D/t} = 2D/\sqrt{< x^2 >}$.

section 7.1 suggests that the diffusion constant is less than 10^{-11} cm^{2}s^{-1} but is not as slow as 10^{-16} cm^{2}s^{-1}.

6.5 Implications for Equilibrium Phase Diagrams

If the gel domains I've observed are growing by a non-equilibrium mechanism whilst in a cooling regime of $\sim 0.1 - 0.2$ °C/min., does this have any implications for the equilibrium phase diagrams obtained for the DPPC/DPPE system? Are the measurements made by DSC and other methods in equilibrium?

Heating and cooling rates for DSC are similar to, or faster than, the regime in which I observe my samples [124, 128, 131, 132, 136–138] and so we may expect the domain growth in these systems to be out of equilibrium. In DSC the samples used are multilamellar vesicles (MLVs) rather than GUVs so that the mole fraction of lipid in water is large enough to get a resolvable signal for the transition enthalpy. The GUVs I observe are around ~ 30 μm in diameter and an estimate of the diameter of the vesicles in the MLVs would be 300 nm (~ 100 times smaller). If in turn we estimate that the average domain size is also a factor of ~ 100 less than the domains observed in the GUVs[6], we should estimate the time it takes for a lipid to diffuse 20 nm. For $D \sim 10^{-11}$ cm^{2}s^{-1} this would be 0.1 s and for $D \sim 10^{-16}$ cm^{2}s^{-1} this would be 2 hrs 47 mins. Therefore for the faster of our estimates for the lipid diffusion constant in the gel phase, where the lipid diffusion is ~ 0.2 μm/s over a distance of 20 nm for $D \sim 10^{-11}$ cm^{2}s^{-1}, the system should be able to comfortably remain in equilibrium at the experimental heating rates[7] but 'tree ring' growth would probably still occur for our slowest estimate of D.

Non-equilibrium growth of gel phase domains may be an explanation for the variation in the quantitative position and shape of the solidus curve seen in the DPPC/DPPE diagrams in the literature (as discussed in section 6.1), i.e. the observed phase behaviour is sensitive to sample

[6]This is similar to assuming that the same number of domains nucleate in both systems. This may not be the case but due to the much smaller system size for MLVs, the domains must be smaller than for GUVs simply because a 2 μm diameter domain cannot physically exist on a vesicle of diameter 300 nm. I will assume the difference in domain size to be roughly proportional to the difference in system size.

[7]The slow diffusion constant of the gel phase would still be an issue on heating vesicles since the gel phase would still have to change its composition in agreement with the solidus curve as the temperature increased through the gel-fluid coexistence region.

preparation and kinetics. Even though 'tree ring' growth of domains predicts gel-fluid coexistence down to $\sim$ 42 °C for all compositions, it can be seen for 1:3 DPPC:DPPE in figure 6.8b that the gradient of the gel fraction against temperature curve becomes relatively flat as the temperature decreases below $\sim 50 - 51$ °C. This implies that very little gel phase is added below this temperature and hence the enthalpy of this transition may not be resolvable by DSC, leaving the experimenter to predict the phase boundary to lie around this temperature for 1:3 composition as is shown by the lever rule prediction for 1:3 DPPC:DPPE in the same figure. A similar effect could occur for other samples with high DPPE content.

6.6 Summary

Gel fractions were measured for vesicles of compositions of 1:1, 3:1 and 1:3 DPPC:DPPE on slow cooling through the gel-fluid coexistence region of the phase diagram. Observed gel fractions did not agree with equilibrium predictions of the lever rule using published phase diagrams for the system. A non-equilibrium, 'tree ring' model of domain growth provided a much better fit to the data. Domains were observed to grow radially at rates which were at least an order of magnitude faster than the diffusion within the gel domains. Therefore the gel domains were unable to alter their composition to the equilibrium value required by the solidus curve as the temperature was reduced. The gel phase was unable to remain in equilibrium with the fluid phase and so the fluid phase behaved as an isolated system, phase separating so that gel of differing composition was deposited on the existent gel domains on cooling, leading to a structure of the gel domains analogous to the rings through the cross section of a tree trunk which increase in number as the tree ages.

Chapter 7

Domain Morphology

In this chapter I will discuss the morphology of gel phase domains observed in my experiments. I will also discuss the movement and interaction of the domains. This will begin with DPPC/DPPE vesicles, the system which was studied in the greatest detail and will be followed by a discussion of DPPC/DPPS vesicles. I will also summarise results from other workers in our research group on lipid systems where the gel phase formed is rich in lipids with a PC headgroup, and hence is the $P_{\beta'}$ gel phase. Finally I will draw together the observed morphologies of all these systems to explain these results in terms of the structure of the gel phase that is formed.

7.1 DPPC/DPPE vesicles

GUVs of composition 1:3, 1:1 and 3:1 DPPC:DPPE were formed at 70 °C, i.e. in the fluid phase, and observed while the sample was slowly cooled through a region of two phase coexistence of the fluid (L_α) and gel (L_β) phases. These vesicles contained less than 0.5 mol.% Rh-DPPE which preferentially partitioned into the fluid phase which therefore appears to be bright. The gel phase can be observed as dark areas on the membrane where the fluorophore has been excluded.

When the temperature is reduced below the liquidus curve (for a discussion of the phase diagram of this system see section 6.1), small dark domains were observed to be moving in the

bright membrane. As the temperature was further reduced, these domains were observed to grow larger and could be seen to have a circular morphology. Circular domains are the expected morphology of an isotropic phase since this gives the minimal interfacial energy cost between phases: the L_β phase of DPPE is isotropic as will be discussed further in section 7.4.

All domains that were observed spanned both leaflets of the bilayer, as has been noted previously in the literature for this system and other binary lipid mixtures [2, 3, 5]. This can be deduced from my data since I only ever observed a bright fluid phase of similar fluorescence intensity to the membrane in the homogeneous single fluid phase region or a dark domain with very low fluorescent signal where the fluorophore had been expelled from both leaflets of the bilayer. No intermediate fluorescence intensities were observed where only one leaflet of the bilayer was in the gel phase whereas the opposing monolayer was in the fluid phase. Lipowsky and Dimova [76] speculate that this correlation between the two monolayers is due to conservation of the hydrocarbon density across the interface between the two monolayers. If both monolayers were in the same phase then the hydrocarbon density would not change across this 'buried' interface; but if one monolayer was in a gel phase and the other in a fluid phase then the hydrocarbon density would change across the interface between monolayers. This would cause an increased tension across the interface between each lipid monolayer for monolayer domains, hence domains which span the bilayer (bilayer domains) are favoured.

All domains in any one vesicle appeared to move coherently around the vesicle as shown in figure 7.1. This was possibly due to convection currents in the fluid membrane caused by small temperature differences within the sample.

The domains were moving with a drift velocity in the region of $1-8$ μm/s. Graphs showing the average speed of moving domains for various domain sizes, vesicle diameters and temperatures are shown in figure 7.2. The average speed of the domains were calculated by determining the distance moved by the centre of mass of a domain between successive frames of a time series using the IDL programs *domain_finder2.pro* and *distance.pro* (see sections 5.4 and 5.4.1). Knowing the time between successive frames means that the average velocity for that time step can be estimated. As the domains are moving in a common direction in the membrane, the velocity ($\mathbf{v}^i(\mathbf{r}, t)$) of a domain i at a position $\mathbf{r}$ in the membrane at time t can be modelled as

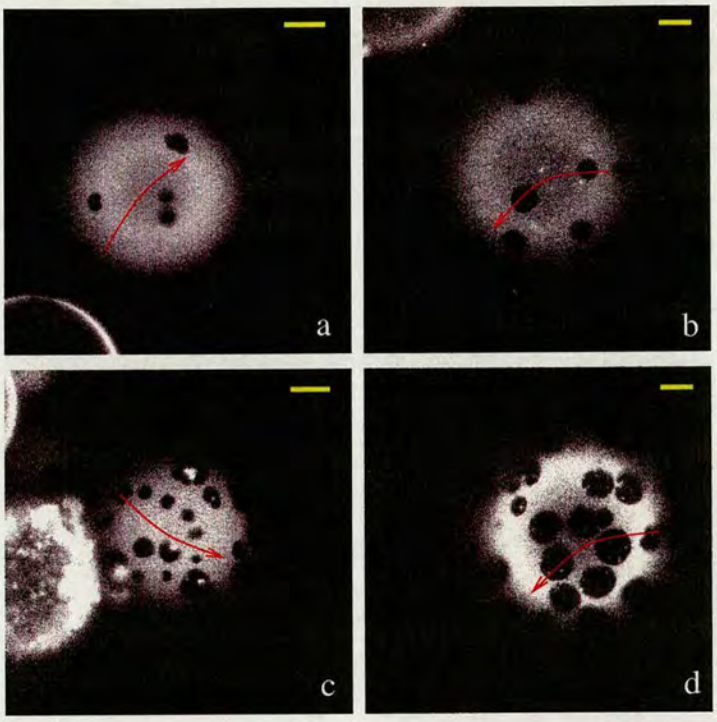

Figure 7.1: Single image sections showing moving domains in the fluid membrane. All domains are moving in the direction of the arrows. Vesicle compositions are all 1:1 DPPC:DPPE. Domain movement was imaged by focusing near a pole of the vesicle and taking successive images without changing the focus depth. (a) 54.6 °C; (b) 54.3 °C; (c) 51.1 °C; (d) 49.5 °C. Scale bars represent 10 μm.

$$\mathbf{v}^i(\mathbf{r},t) = \mathbf{v}^i_d(\mathbf{r},t) + \mathbf{v}^i_b(t)\ , \tag{7.1}$$

where $\mathbf{v}^i_d(\mathbf{r},t)$ is the drift velocity of domain i at position $\mathbf{r}$ in the membrane at time t due to the convective flow field in the fluid phase and $\mathbf{v}^i_b(t)$ is the velocity due to the random diffusion, or Brownian motion, of domain i at time t. The observed motion of the moving domains suggests that the drift velocity due to the convective flow dominates over the Brownian motion ($\mathbf{v}^i_d(\mathbf{r},t) >> \mathbf{v}^i_b(t)$), therefore calculating the mean magnitude of the velocity between several successive time-steps (ranging between 3 time steps for faster domains and 17 time steps for slower domains in figure 7.2) for a given domain will give a rough estimate of the magnitude of the average drift velocity of the domain due to convective flow in the fluid membrane. The error in this velocity is simply estimated by calculating the standard error of the mean.

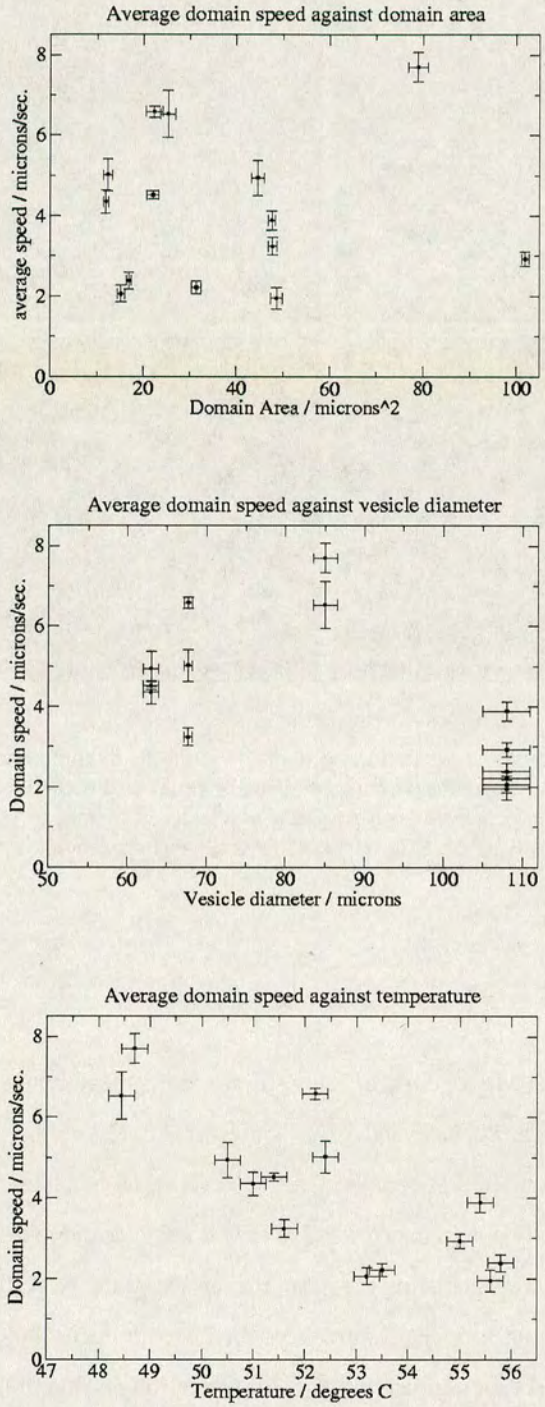

Figure 7.2: (a) [*top*] Graph of average domain speed against domain area; (b) [*middle*] Graph of average domain speed against vesicle diameter; (c) [*bottom*] Graph of average domain speed against temperature. All data is for vesicles at a composition of 1:1 DPPC:DPPE.

The graphs in figure 7.2 are for circular domains on four different vesicles where data was collected on two separate days. 7.2a shows the domain speed against the domain area; there appears to be no correlation between domain area and domain speed (even for domains at different times on the same vesicle). 7.2b displays domain speed against vesicle diameter; again there appears to be no correlation between these parameters and domain speeds vary by up to a factor of two for the same vesicle. Finally, 7.2c is a graph of domain speed against temperature; despite there appearing to be a trend for slower domain speeds at higher temperatures, I believe this to be an artefact of the low statistics of only having looked at the domains on four vesicles since I have not visually noticed a significant increase in domain speed with decreasing temperature over the larger statistics of all my experiments (a factor of ~ 4 increase in domain speed as shown in figure 7.2c should be noticeable by eye). Each vesicle is only observed over a small range of temperature before photobleaching or vesicle lysis (see section 8.5) occurred. Two of these vesicles were observed within the range $\sim 51 - 53.5$ °C where a large range of domain speeds were observed. The data in figures 7.2a and 7.2b are for domains over a range of temperatures under the assumption that domain speed is independent of temperature. It appears that the observed speed of the circular moving domains is independent of the domain area, vesicle diameter and the temperature but instead is determined by the convective flow in the fluid phase driven by small temperature differences within the sample. In agreement with this, moving domains of different sizes visually appear to be moving at the same speed as each other at the same point in time in the same vesicle.

When two circular domains 'stuck' to one another then the resulting domain had a dumbbell shape as seen in figure 7.3. To minimise the fluid-gel line tension, these two domains should coalesce into a larger circular domain. This does not occur. As the sample cools further, additional gel phase grows on top of the dumbbell shape; this domain adhesion and growth on top of the new domain shape without rearrangement in the shape of the domain to reduce the interfacial tension between phases means that at lower temperatures many domains look non-circular although their building blocks and preferred morphology is a circular structure: see figures 7.7 - 7.10 later in the chapter. This is probably due to the high viscosity (low lipid diffusion constant) in the gel phase[1]; the lipids cannot diffuse fast enough for the domain to

[1]See section 6.4 for a discussion on the diffusion constant in lipid gel phases

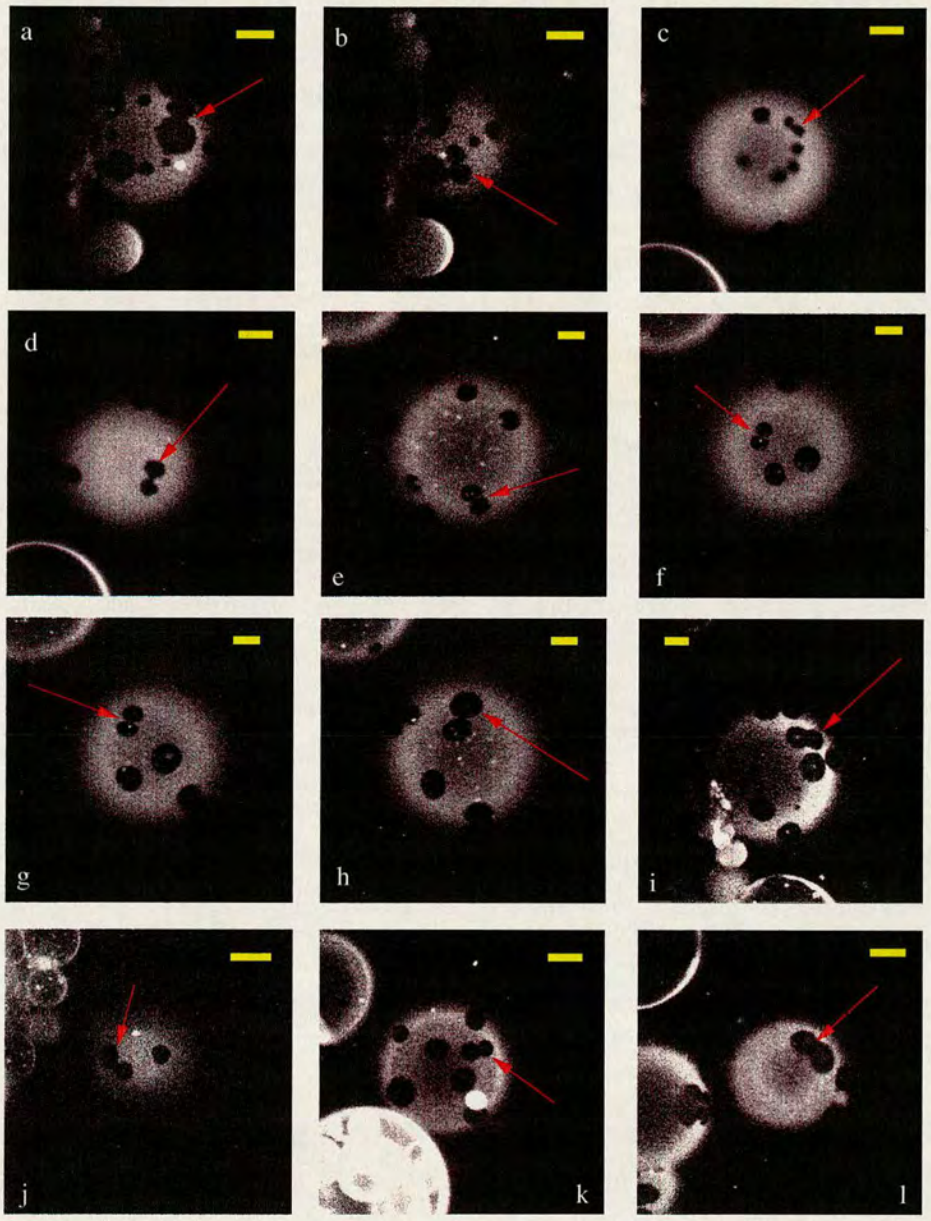

Figure 7.3: Image sections through the poles of vesicles where dark, 'dumbbell' shape, gel domains can be seen moving in the bilayer. These domains are highlighted in the images by red arrows. (a) 1:3 DPPC:DPPE, 58.7 °C; (b) 1:3 DPPC:DPPE, 58.2 °C; (c) 1:1 DPPC:DPPE, 55.4 °C; (d) 1:1 DPPC:DPPE, 54.9 °C; (e) 1:1 DPPC:DPPE, 55.2 °C; (f) 1:1 DPPC:DPPE, 55.0 °C; (g) 1:1 DPPC:DPPE, 54.5 °C; (h) 1:1 DPPC:DPPE, 54.3 °C; (i) 1:3 DPPC:DPPE, 58.6 °C; (j) 1:1 DPPC:DPPE, 54.7 °C; (k) 1:3 DPPC:DPPE, 59.8 °C; (l) 1:3 DPPC:DPPE, 57.9 °C. Scale bars represent 10 μm.

rearrange its shape. This also implies that all circular domains observed in the membrane had grown by the addition of monomers from the fluid phase rather than the coalescence of smaller gel domains.

Gel domains did not always stick to one another when they came into contact, domains sometimes bounced off one another too. This is reminiscent of the '*moving droplet phase*' reported by Hajime Tanaka for viscoelastic phase separation in polymer solutions [164]. The dynamic asymmetry required for viscoelastic phase separation could be provided by the difference in diffusion constants between the fluid and gel phase of a lipid bilayer. The important time scales are the characteristic time of collision between two domains (τ_c) and the characteristic rheological time of the gel phase (τ_t). Domains will behave as elastic bodies, bouncing off each other, for $\tau_t > \tau_c$ and for $\tau_t < \tau_c$ domains can coalesce with each other. However, for $\tau_t \sim \tau_c$ domains will sometimes coalesce and sometimes bounce apart. An estimate of the collision time can be taken as a characteristic domain size, say 4 μm, divided by a characteristic ballistic speed of the domains, say 4 μms^{-1}, giving $\tau_c \sim 1$ s (see figure 7.2c). In this time, taking the diffusion constant in the gel phase to be $D \leq 10^{-11}$ cm^{2}s^{-1} (see section 6.4), a lipid can diffuse a maximum distance of 63 nm. Taking the diameter of a lipid headgroup to be ~ 7 Å, then a lipid can diffuse a distance of ~ 90 lipids during the collision time τ_c. This however is an upper limit since the diffusion constant could be up to several orders of magnitude slower than our estimate making it conceivable that the moving gel domains observed in my experiments are in the $\tau_t \sim \tau_c$ viscoelastic regime. A lower limit of this regime would be that a lipid diffuses less than the diameter of a lipid headgroup during the collision time; in this case it would be expected that the domains would behave like elastic solids and bounce off each other, i.e. this would be the $\tau_t > \tau_c$ regime. Therefore a diffusion constant as low as $D \sim 10^{-16}$ cm^{2}s^{-1} seems unlikely since this would only allow a lipid to diffuse ~ 0.3 lipid diameters during the collision time[2].

Gel domains have been seen to reach a certain size limit. Figure 7.4 shows image sections through a vesicle where, on cooling, the gel domains grow to a certain size (*top*) and then, on further cooling, new, small gel domains nucleate which coexist with the larger domains. The larger gel domains do not appear to grow as the sample is cooled further, with the smaller

[2]See section 6.4 for a full discussion of diffusion constants in lipid gel phases.

domains growing instead. The explanation for the size limit of these domains is unknown; possible explanations are:

- Size limited domains have been observed in lipid monolayers at the air-water interface due to electrostatic repulsion [165–170]. Electrostatic interactions have been thought to be insignificant in lipid bilayers due to the high dielectric constant of water; the electrostatic interaction is mediated through the air for lipid monolayers. Molecular dynamics simulations however have shown that repulsive interactions dominate the interaction energy between lipid dipoles at large distances [171]. These simulations were done for DPPC in the L_α phase. The components of the headgroup dipole in the plane of the membrane provided an attractive interaction which decayed as r^{-6} (where r is the in-plane distance from the dipole) and was screened by a dielectric permitivity ~ 80; the components of the dipole perpendicular to the membrane resulted in a repulsive interaction energy which decayed as r^{-3} and was screened by a dielectric permitivity ~ 10. The condensation in area per headgroup in the gel phase, i.e. more headgroup dipoles per unit area, could result in a long-range repulsive interaction between gel domains. This is analogous to charge-limited clusters that have been observed in colloidal suspensions which have short-range attraction and long-range repulsive interactions [172–174]. However, the 'clusters' in my system are domains in quasi-two dimensions as opposed to three and the repulsion is due to electric dipoles rather than point charges.

- Formation of a rigid gel phase on the spherical geometry of a vesicle may become increasingly energetically unfavourable as the domain becomes larger. The energy cost of bending a large gel domain to the curvature of the spherical vesicle may become increasingly large until a point where the energy cost due to the interfacial tension of nucleation and growth of new gel domains becomes less than further growth of the existing gel domains.

- Due to the 'tree ring' growth of gel domains (see chapter 6), there would be interfacial tension within gel domains between each ring of the 'tree ring' structure. This internal tension could result in the energy cost due to the interfacial tension of nucleation and growth of new gel domains becoming less than further growth of the existing gel

domains. As the composition of the gel phase changes, a second order phase transition between L_β and $L_{\beta'}$ is expected. This gradual change in acyl chain tilt will add to the interfacial tension between 'rings of the tree' on top of that due to the change in composition.

The observed size limit of the gel domains could result from none, one, or a combination of several of the above reasons. Further experimental investigation is needed to pin down the cause of this phenomenon. Initial observations looking at images in figures 7.7-7.10, scale bars seem to show that domains reach a similar size on most vesicles irrespective of the radius of curvature of the vesicle. Most of the outliers to this are from vesicles imaged using the ITO-plate formation cell as opposed to the platinum wire cell: figures 7.7h and 7.8a,c,e,h,i,j,k,p,q. I cannot control the tension in the vesicles produced by electroformation and so it is likely that the vesicle tension is different for the two different formation geometries of platinum wires and ITO plates; this may be related to the origin of the difference in length scales of these domains. However, I would still not fully rule out, at this point, a role for bending energy in limiting the size of the gel domains. Preliminary data on the size limit of domains as a function of vesicle diameter for one afternoon's results did show a trend of increasing domain size with increasing vesicle diameter (data not shown) but data from experiments on other days did not map onto this trend. Further studies are needed before a definitive statement on the effect of the radius of curvature on domain size can be made.

At higher temperatures, moving gel domains were seen to sometimes 'stick' to one another as was discussed above with the formation of 'dumbbell'-shaped domains. However, at lower temperatures gel domains moving in the fluid membrane were seen to repel each other far more frequently. The domains still want to try to coalesce to reduce the line tension but the repulsion between the domains has increased with decreasing temperature. This repulsion was observed most apparently at temperatures below those where new domains nucleated after the larger domains stopped growing. If these domains are not able to grow further by the addition of further monomers from the fluid phase then it seems likely they'd be unable to grow by sticking to another gel phase domain, therefore repulsion between the domains is observed.

If more than two moving domains 'stick' together then more complicated domain shapes than

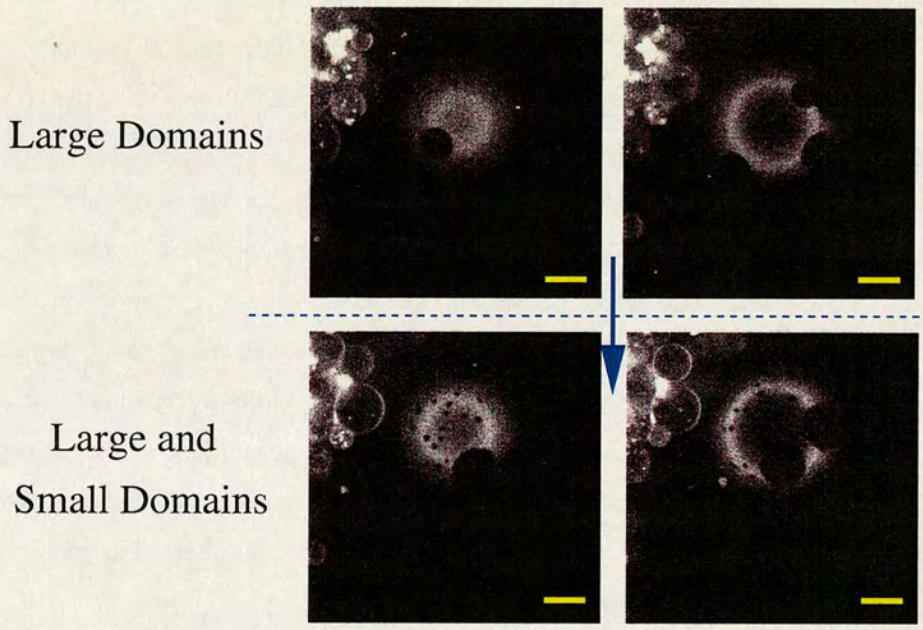

Figure 7.4: Single image sections through the same vesicle of composition 1:1 DPPC:DPPE. [*top*] Two image sections showing large gel domains in the fluid membrane, 53.4 °C. [*bottom*] Two image sections through the same vesicle as above taken $\sim$ 5 minutes later and $\sim$ 0.5 °C cooler in temperature; small gel domains are now seen to coexist with the large gel domains. Scale bars represent 10 μm.

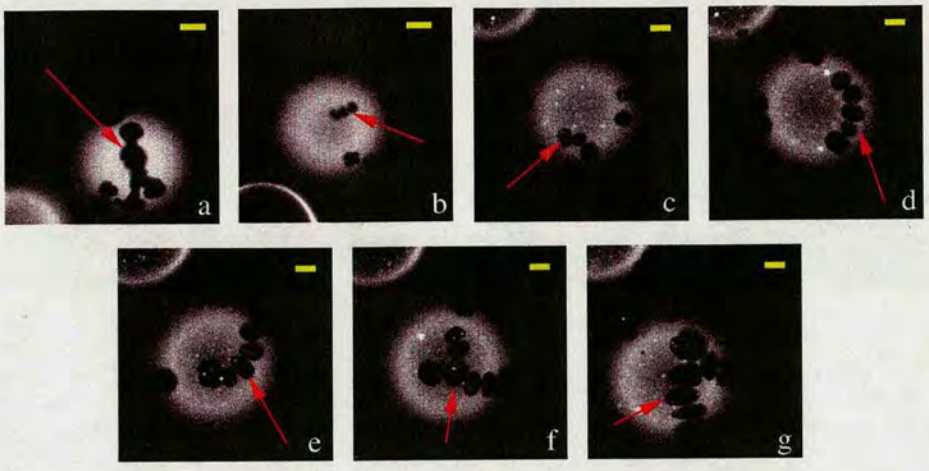

Figure 7.5: When more than two circular domains 'stick' together then these domains appear to form long 'bead-like' chains which can form branches (as seen in a,f,g). Vesicle compositions are all 1:1 DPPC:DPPE. (a) 52.9 °C; (b) 55.5 °C; (c) 55.3 °C; (d) 54.7 degrees C; (e) 54.4 °C; (f) 53.0 degrees C; (g) 51.9 °C. Scale bars represent 10 μm.

'dumbbells' are formed. Domains were seen to bead in long chains which could also form branches as shown in figure 7.5. I can offer no explanation of this phenomenon.

In gel-fluid coexistence, where moving gel domains were observed, static domains were also seen at points on the membrane where the vesicle was adhering to other membranes[3], as shown in figure 7.6. Domains which appear to be preferentially located at points of adhesion between vesicles can also be seen in figures 7.7c,d,i,p,s,t, 7.9a,b,d,e and 7.10g. It is not clear if these domains nucleate and grow at the points of adhesion on the membrane, remaining static due to inter-membrane interactions, or whether they were diffusing in the free membrane before becoming 'stuck' at the point of adhesion between two vesicles. A domain may become stuck at this location due to the change in curvature of the membrane caused by adhesion. Gel phase domains are much more rigid than the fluid membrane and so may not be able to bend to compensate for this change in curvature and hence become 'stuck'.

As the solidus curve is approached (on cooling), the area fraction of the gel phases can lead to a large connectivity between domains which causes the domains to become static. The morphology of the gel domains is always static below the solidus curve, whilst what was the

[3]see section 8.4 for a discussion on vesicle adhesion

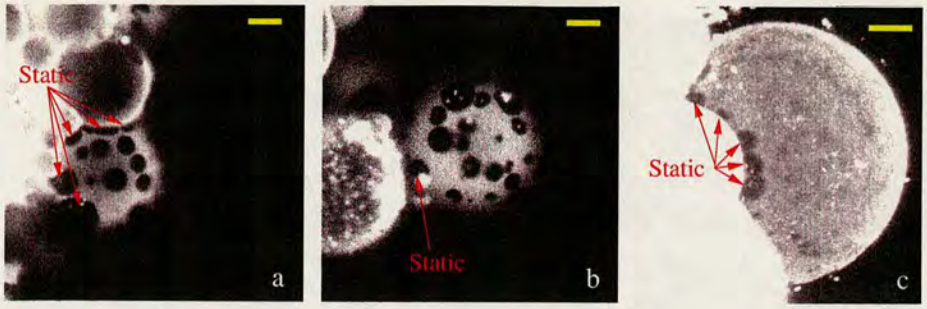

Figure 7.6: Domains are static at points on the membrane where two vesicles adhere to each other. (a,b) Image sections through 1:1 DPPC:DPPE vesicles. Static domains are marked by arrows; the other domains are moving in the fluid membrane. (b) Image stack of a hemisphere of a 1:3 DPPC:DPPE vesicle. The static domains where the vesicle adheres to other membranes are marked. The moving domains cannot be seen in the free membrane as the same region of membrane is excited several times during the z-stack acquisition; sometimes the membrane at a given point can be fluid and other times it can be gel. (a) 49.6 °C; (b) 52.3 °C; (c) 59.1 °C. Scale bars represent 10 μm.

fluid membrane becomes a gel phase with the fluorophore kinetically trapped in it. Images of z-stacks of vesicle hemispheres with static domains of 1:1 DPPC:DPPE vesicles are shown in figures 7.7, 7.8; 3:1 DPPC:DPPE vesicles are shown in figure 7.9; 1:3 DPPC:DPPE vesicles are shown in figure 7.10. The morphology of all these vesicles comes from the aggregation of circular domains and further growth of the gel phase on top of the new aggregate shape. Circular domains can still be observed in some of the images (for example figures 7.7a, 7.8d, 7.9c, 7.10e). All these domain morphologies are non-equilibrium in nature since it would be expected that the true equilibrium morphology would be a single gel domain with a circular boundary with the fluid phase, thereby minimising the interfacial line tension between phases. The vesicles in my images do not evolve to this state on the timescale of my experiments due to the slow diffusion constant of the gel phase.

Lipowsky and Dimova [76] predict that gel phase domains would create flat facets on a spherical vesicle due to the rigidity of the phase. The Rh-DPPE probe partitions into the fluid phase, leaving the gel phases dark in the images collected; this means that we cannot infer anything about the curvature of the gel phase membrane using the Rh-DPPE fluorophore.

Laurdan is a membrane probe which partitions equally between fluid and gel phases[4] (see

[4]The common use of the Laurdan probe is to study the fluidity of the membrane by its emission [3, 5, 114, 175]. Although Laurdan partitions equally between fluid and gel phases, its emission wavelength changes. The emission

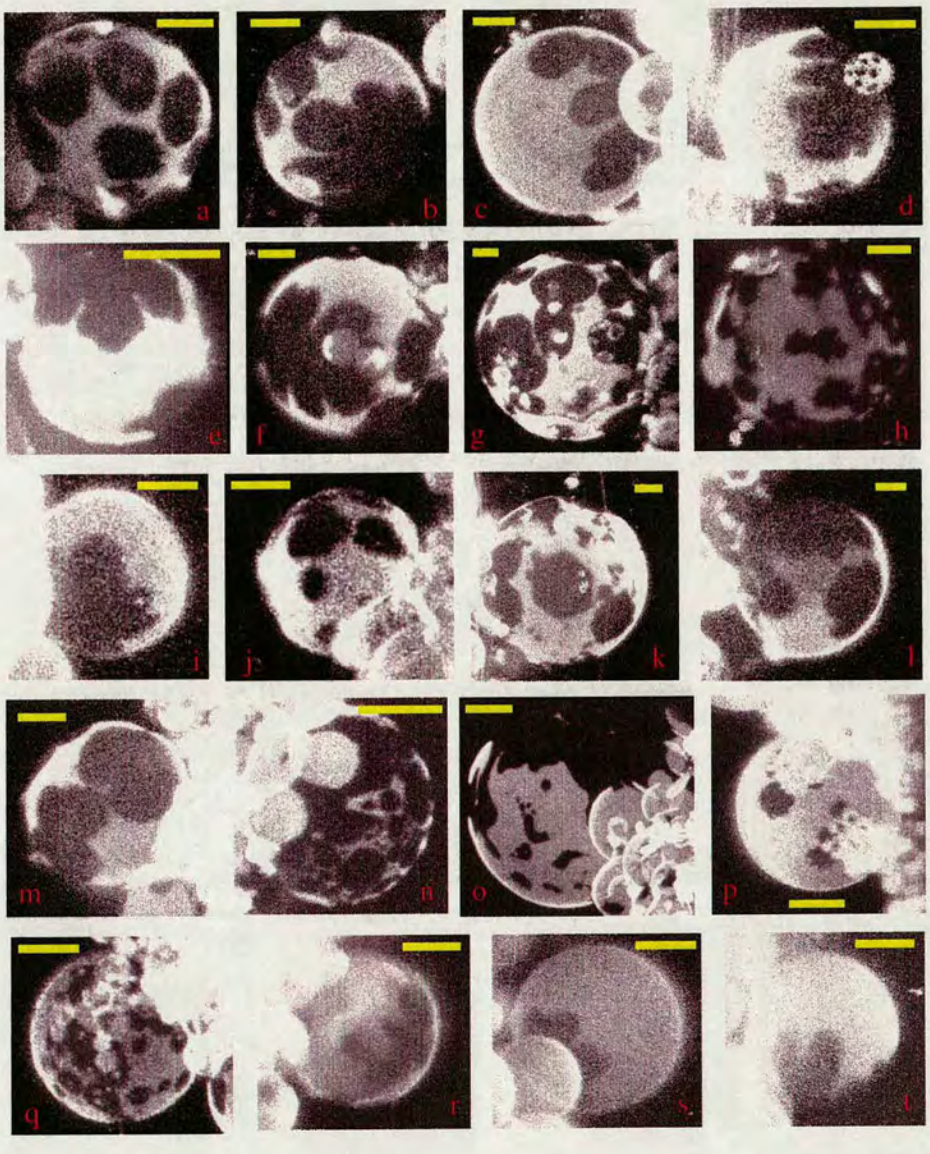

Figure 7.7: Static domains on 1:1 DPPC:DPPE vesicles. (a) 45.5 °C; (b) 44.6 °C; (c) 49.3 °C; (d) 44.3 °C; (e) 47.0 °C; (f) 43.9 °C; (g) 44.2 °C; (h) 25.1 °C; (i) 48.3 °C; (j) 49.3 °C; (k) 46.8 °C; (l) 43.6 °C; (m) 42.5 °C; (n) 41.7 °C; (o) 43.0 °C; (p) 48.4 °C; (q) 48.4 °C; (r) 46.5 °C; (s) 52.5 °C; (t) 52.2 °C. Scale bars represent 10 μm.

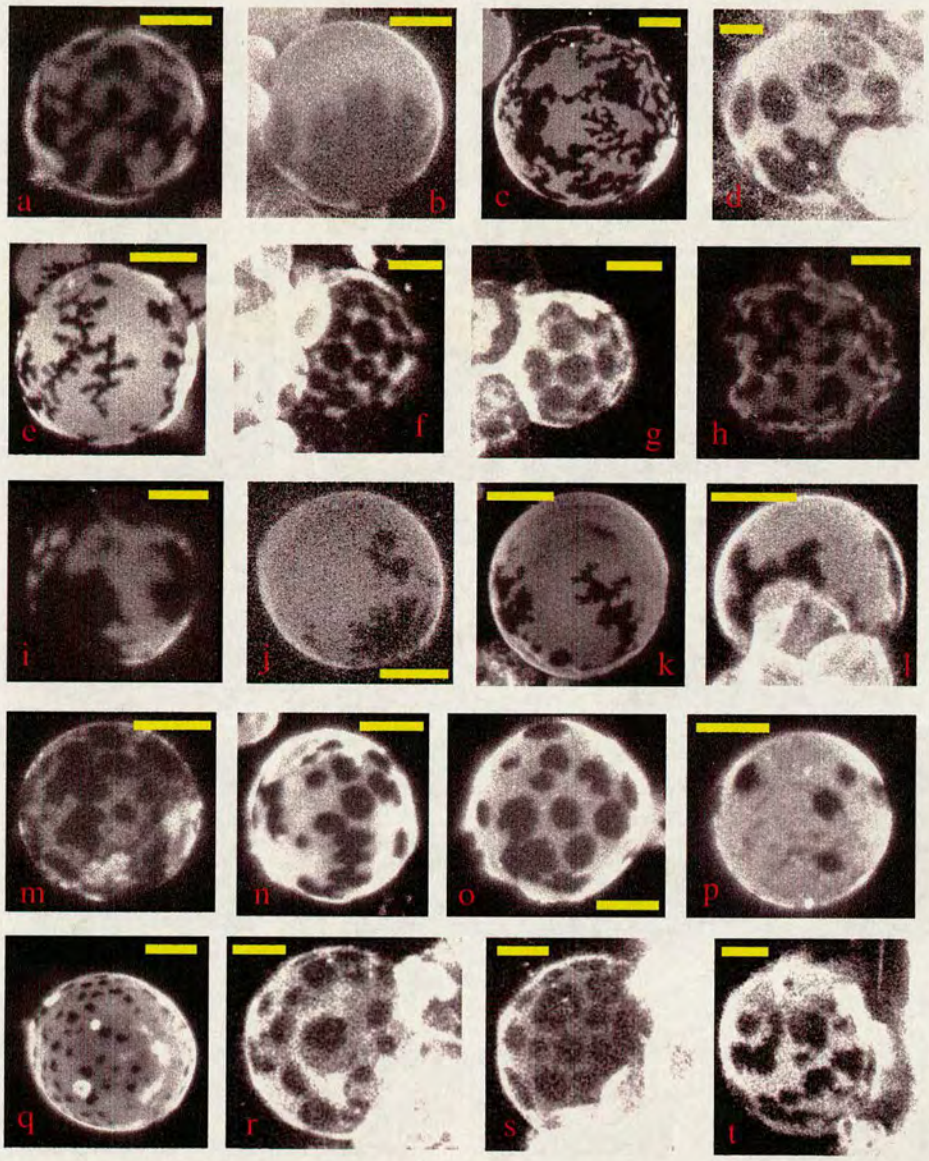

Figure 7.8: Static domains on 1:1 DPPC:DPPE vesicles. (a) 25.9 °C; (b) 48.0 °C; (c) 46.5 °C; (d) 47.9 °C; (e) 51.0 °C; (f) 45.6 °C; (g) 45.7 °C; (h) 24.7 °C; (i) 24.6 °C; (j) 53.0 °C; (k) 51.0 °C; (l) 47.0 °C; (m) 44.5 °C; (n) 33.8 °C; (o) 45.0 °C; (p) 44.7 °C; (q) 49.7 °C; (r) 46.1 °C; (s) 46.1 °C; (t) 50.1 °C. Scale bars represent 10 μm.

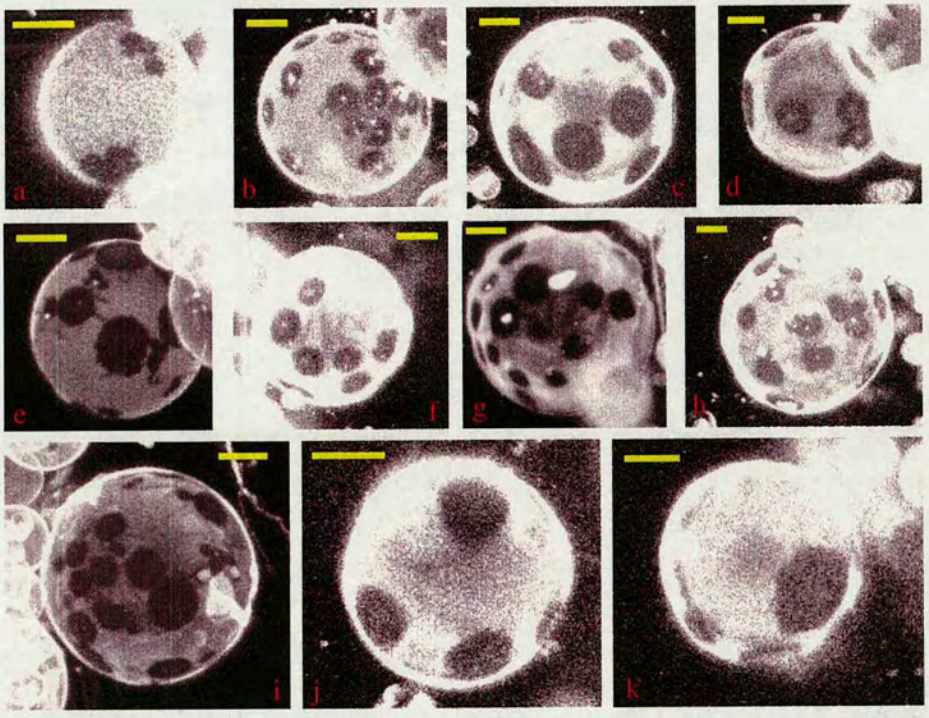

Figure 7.9: Static domains on 3:1 DPPC:DPPE vesicles. (a) 44.9 °C; (b) 43.1 °C; (c) 39.2 °C; (d) 39.1 °C; (e) 43.9 °C; (f) 44.2 °C; (g) 41.9 °C; (h) 38.9 °C; (i) 41.7 °C; (j) 42.8 °C; (k) 39.4 °C. Scale bars represent 10 μm.

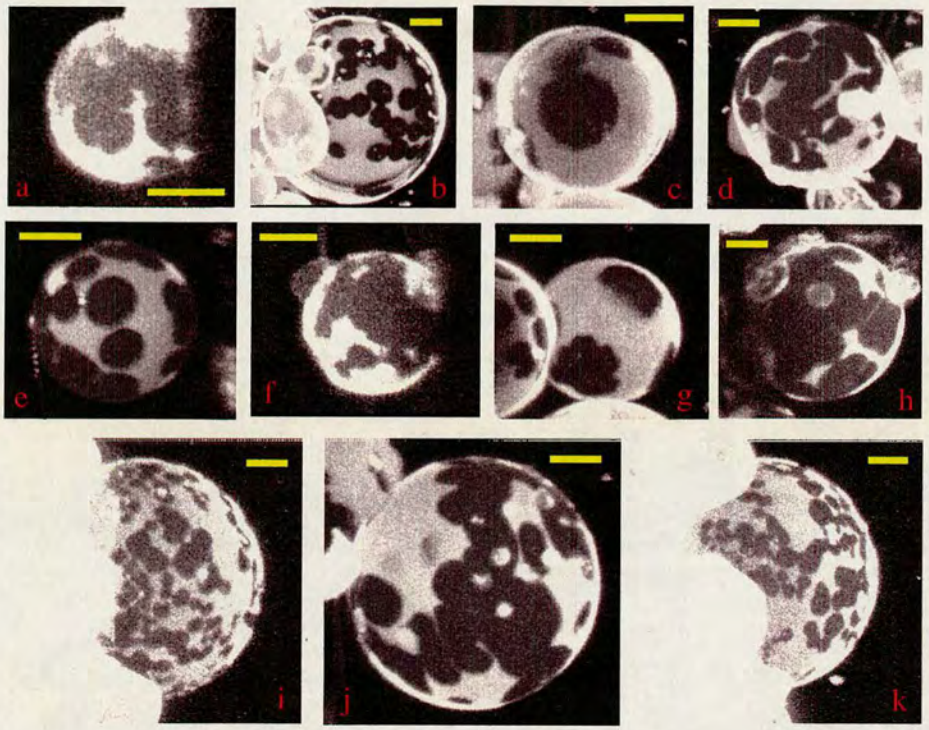

Figure 7.10: Static domains on 1:3 DPPC:DPPE vesicles. (a) 49.7 °C; (b) 52.6 °C; (c) 52.4 °C; (d) 52.7 °C; (e) 53.0 °C; (f) 49.7 °C; (g) 52.4 °C; (h) 53.1 °C; (i) 57.4 °C; (j) 52.4 °C; (k) 56.7 °C. Scale bars represent 10 μm.

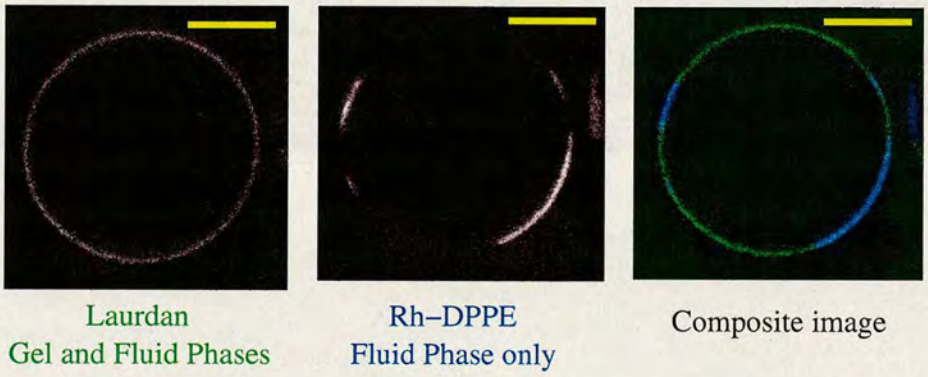

Figure 7.11: Curvature of the gel phase. [*left*] Image section through the equator of a vesicle at 44.5 °C using Laurdan fluorescence emission. Laurdan partitions equally between gel and fluid phases and hence labels the whole membrane. [*centre*] The same image section of the same vesicle as labelled by Rh-DPPE. This fluorophore preferentially partitions into the fluid phase. [*right*] Composite image with the Laurdan emission in green and the Rh-DPPE emission in blue. The gel phase is seen to have the same curvature of the vesicle. Scale bars represent 10 μm.

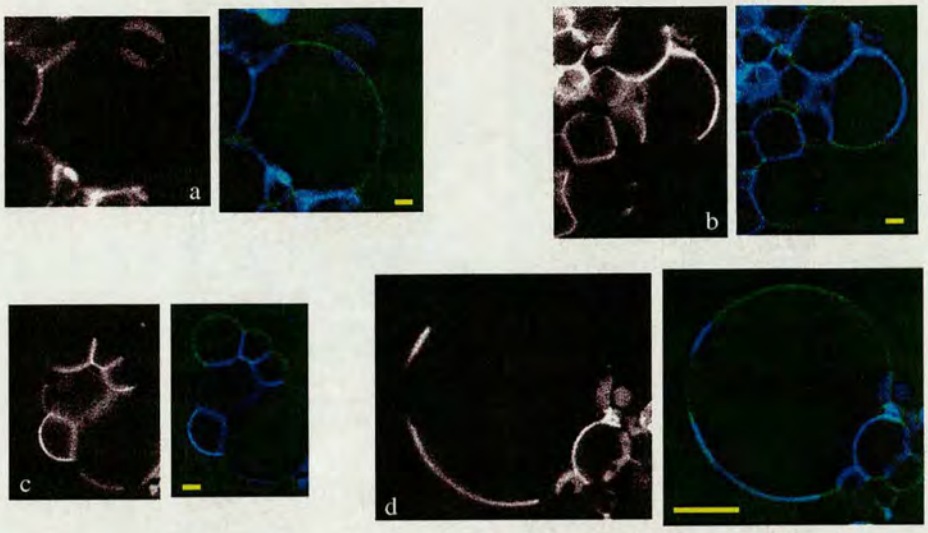

Figure 7.12: (a-d) More image sections through vesicles labelled with Laurdan and Rh-DPPE probes. The black and white image on the left of each pair is the Rh-DPPE fluorescence (fluid phase) and the right-hand image is the composite image with the same colour coding as figure 7.11. The gel phase membrane follows the native curvature of the vesicle. (a) 43.7 °C; (b) 42.8 °C; (c) 44.1 °C; (d) 43.3 °C. Scale bars represent 10 μm.

section 4.3.1). 1:1 DPPC:DPPE vesicles containing the Rh-DPPE and Laurdan dyes were cooled slowly and imaged close to the solidus curve of the gel-fluid coexistence region of the phase diagram so that there were large gel phase domains coexisting with the fluid phase. Image sections, obtained by multiphoton excitation, through the equators of these vesicles could be used to analyse whether the gel domains formed flat facets or followed the natural curvature of the spherical vesicle as shown in figures 7.11 and 7.12.

---

wavelength of Laurdan is sensitive to the number of water molecules that surround it. The emission intensities at 440 nm and 490 nm are collected and a generalised polarisation function (GP) is calculated:

$$\mathrm{GP} = \frac{I_{440} - I_{490}}{I_{440} + I_{490}}, \tag{7.2}$$

where I_n is the emitted intensity at a wavelength of n nm. The GP varies between -1 and 1. The GP values for the fluid phase of the DPPC/DPPE system have been found to lie in a distribution centred at $\sim$ 0.0 and, for the gel phase, values in a distribution centred at 0.56 [3]. There was no dichroic available in the BIORAD confocal system in COSMIC that could split the emission spectra between wavelengths 440 nm and 490 nm; there was also no 50/50 beam splitter available. The dichroics in the BIORAD system were fixed and so could not be changed by the user, hence the GP for Laurdan emission could not be calculated from simultaneously collected intensities. The alternative would be to collect the intensities at 440 nm and 490 nm using sequential scans. For this method to be valid the membrane would have to be in the same state for each scan; this would not be the case when there are moving gel domains in the membrane and hence the data collected by this method would be meaningless. Therefore it was not possible to use Laurdan to detect the different membrane phases using the confocal equipment in COSMIC.

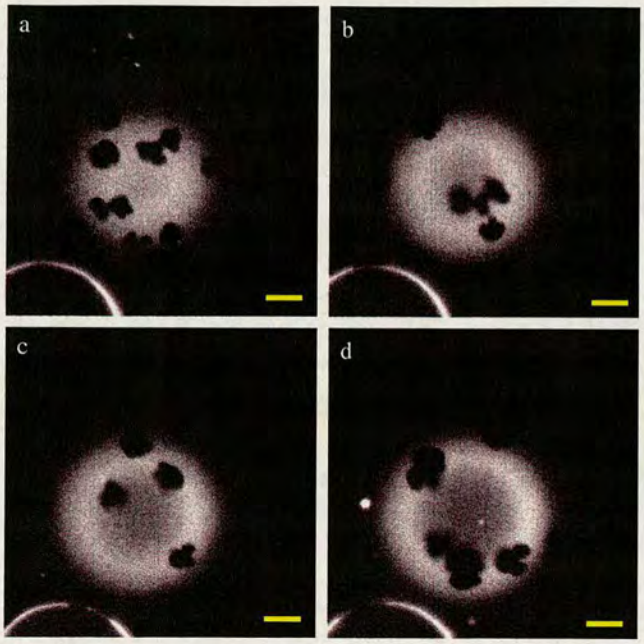

Figure 7.13: Image sections through a vesicle under conditions of fast cooling. (a) 53.3 °C; (b) 53. 1 °C; (c) 52.6 °C; (d) 53.0 °C. Scale bars represent 10 μm.

It can be seen from all of my data that the gel domains are not flat but instead have the native curvature of the vesicle. To the best of my knowledge this is the first time that experimental data on the curvature of the gel phase domains on giant vesicles has been reported. Lipowsky and Dimova's argument is based around bending flat, rigid, incompressible sheets onto the spherical geometry of a vesicle [76]. This reasoning probably does not hold since the gel phase phase domains nucleate and grow on a spherical geometry rather than starting out as flat sheets.

One final comment on the morphology of domains in DPPC/DPPE vesicles concerns cooling rate. I did not study faster cooling rates systematically. Nevertheless, cooling rates faster than $0.1 - 0.2$ °C/min. were accessed unintentionally when the cooling failed to be controlled for whatever reason. When the cooling rate was $\gtrsim 0.4$ °C/min. (a temperature drop of a couple of degrees in a few minutes), the domains observed were non-circular but were still rounded as shown in figure 7.13. This could be due to uneven growth of the domains under faster cooling rates, i.e. rapid domain growth causes them to appear 'knobbly'. Diffusion limited fractal domain growth has been seen under a rapid increase of lateral pressure for phospholipid

monolayers [176, 177] although the observed domain morphologies in these experiments differ from those in figure 7.13.

7.2 DPPC/DPPS vesicles

The DPPC/DPPS system was studied in order to see what the morphology of gel phase domains would be: changing the higher melting component lipid brings the possibility of a different gel phase structure and also DPPS is has a net charge at neutral pH whereas DPPE is neutral. It is conceivable that both these effects could change the observed domain morphology, particular the former effect of gel phase structure since I already had a clue to this from experiments on phosphatidylcholine mixtures in our research group which I will briefly review in section 7.3. A phase diagram taken from the literature for the DPPC/DPPS system is shown in figure 7.14. This phase diagram takes into account the different structures of gel phases formed and was obtained by electron spin resonance (ESR) and freeze-fracture electron microscopy [27]. This binary lipid phase diagram, published in 1977, is the earliest I have seen that considers the effect on the phase diagram topology of the different gel phase structures.

DPPS is a charged lipid at neutral pH as can be seen in figure 7.15. It can be seen that phosphatidylserine has a charge of -1e per headgroup at a pH of 7 in 0.1 M NaCl. My experiments are in deionised water, so the magnitude of the charge per headgroup could be slightly lower than this as the pH close to the bilayer will be decreased by hydrogen ions (instead of sodium ions) being attracted to the negative headgroups to form the electric double layer.

Vesicles were formed at 3:1 DPPC:DPPS. No GUVs could be formed by electroformation at 1:1 composition. This reflects the difficulties widely encountered in the literature of electroforming vesicles with charged lipids, the origins of these difficulties are obscure. When the 3:1 DPPC:DPPS vesicles were cooled slowly from the fluid phase into the gel-fluid coexistence region, small, dark, moving domains, which expelled the Rh-DPPE fluorophore, formed in the membrane. These domains were too small to make any definite statements about their morphology. The movement and interaction of the domains was not studied as the main interest of these experiments was observation of the domain morphology.

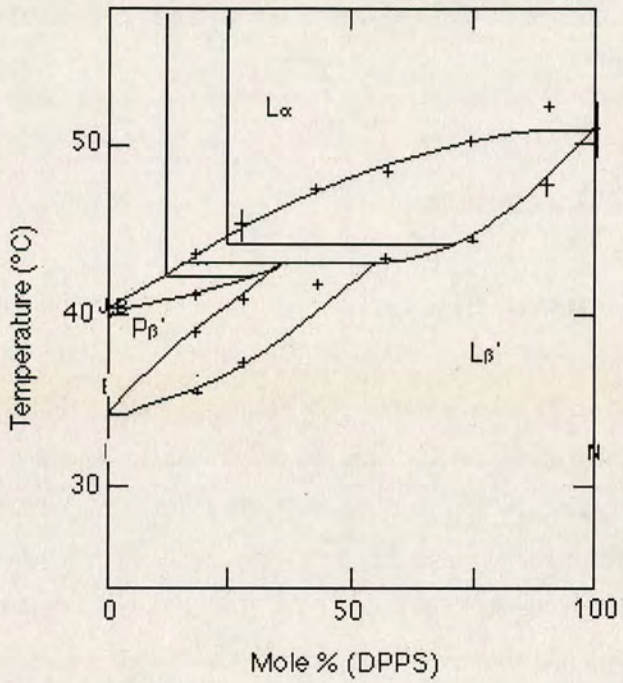

Figure 7.14: Phase diagram of the DPPC/DPPS system from Luna and McConnell 1977 [27]. The compositions 3:1 DPPC:DPPS and 7:1 DPPC:DPPS are marked on the phase diagram along with tie-lines to help the reader see the expected gel phase and its composition on entering the gel-fluid coexistence regions at these compositions. These two compositions will be discussed in the main text.

The domain morphology in 3:1 DPPC:DPPS vesicles can be seen in figures 7.16, 7.17 and 7.20. The dark gel phase domains are polygonal in shape with, at the optical resolution of my images, straight edges and sharp corners. Many of the domains appear hexagonal, including the moving domain in figure 7.16b. Many if not all of the other polygonal shapes may be made up of hexagonal building blocks in a similar way to the formation of more complicated domain shapes from the aggregation of circular domains in the DPPC/DPPE system (see figures 7.7-7.10).

Unlike three-dimensional crystals, which usually have facets, faceted domains are not allowed in two-dimensional crystals by equilibrium thermodynamics [178]; the one-dimensional perimeter of a two-dimensional crystal is prohibited from having long-range order at non-zero temperature [179]. Despite faceted two-dimensional domains not being equilibrium domain

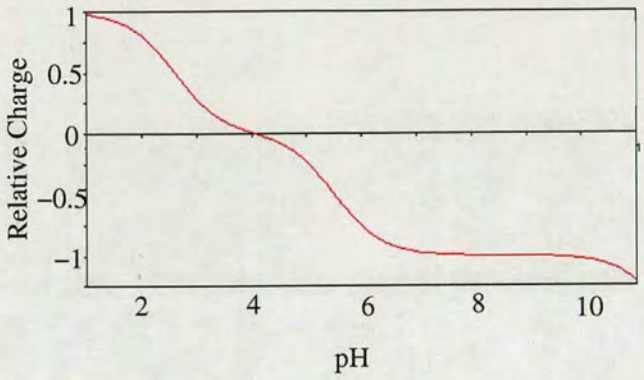

Figure 7.15: Charge per headgroup for phosphatidylserine (PS) as a function of pH in 0.1 M NaCl [15].

shapes, facets can be dynamically stable during the domain growth [180]. The slow diffusion in the gel phase probably prevents the domains rearranging from their faceted shapes during growth to an equilibrium, smooth shape on the time-scale of my observations. Berge *et al.* [180] have observed faceted crystal growth in two-dimensional SDS monolayers at the air-water interface; the observed facets were up to 50 μm long. These crystals often became unstable during growth, with their corners developing instabilities of various shapes. An instability in the faceted growth of domains in the DPPC/DPPS system could be an explanation of some of the non-hexagonal domain shapes observed.

Many of the domains observed appear to be preferentially located at points in the vesicle which are in contact with other membranes or lipid junk as shown most prominently by the vesicles in figure 7.17. These domains could have nucleated and grown at these points or have been moving domains in the 'free membrane' which become 'pinned' at points of contact with other lipid aggregates. One reason for this could be that vesicles in contact adhere and flatten against each other (see section 8.4 for a more detailed discussion of vesicle adhesion). These flatter regions of membrane on the vesicle may be preferential for rigid gel phase domains. Alternatively, moving gel domains in the free membrane may become stuck at points on the membrane where there is a rapid change in curvature since they may not be able to bend to accommodate

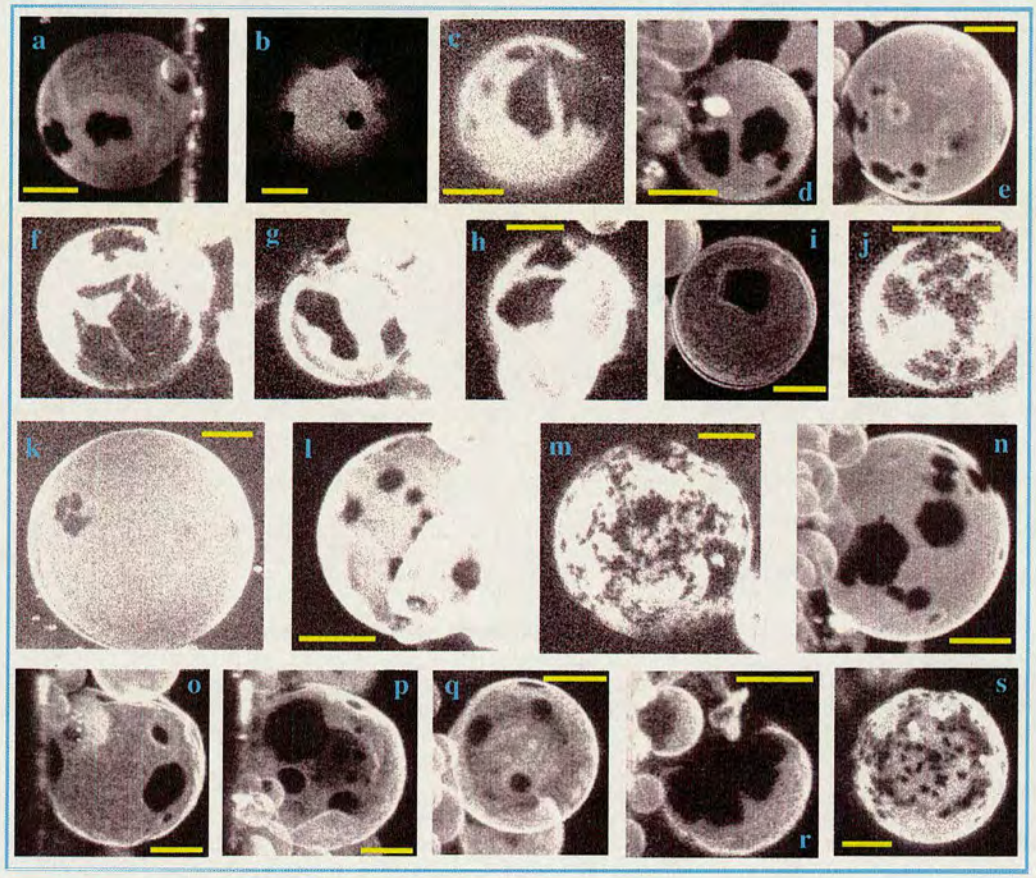

Figure 7.16: 3:1 DPPC:DPPS vesicles containing the Rh-DPPE fluorophore which is excluded from the gel phase: all full hemispheres except image *b*, which is a single image slice at the top of the vesicle showing a hexagonal domain which is moving in the membrane (as can be seen from viewing the whole z-stack of images for this vesicle). Domain shapes are polygonal with straight edges and sharp (at optical resolution) corners. (a) 39.6 °C; (b) 43.8 °C; (c) 43.9 °C; (d) 39.9 °C; (e) 39.9 °C; (f) 38.2 °C ; (g) 38.2 °C; (h) 38.2 °C; (i) 44.6 °C; (j) 37.7 °C; (k) 47.3 °C; (l) 41.8 °C; (m) 37.7 °C; (n) 39.9 °C; (o) 38.8 °C; (p) 38.8 °C; (q) 38.8 °C; (r) 38.8 °C; (s) 38.3 °C. Scale bars represent 10 μm.

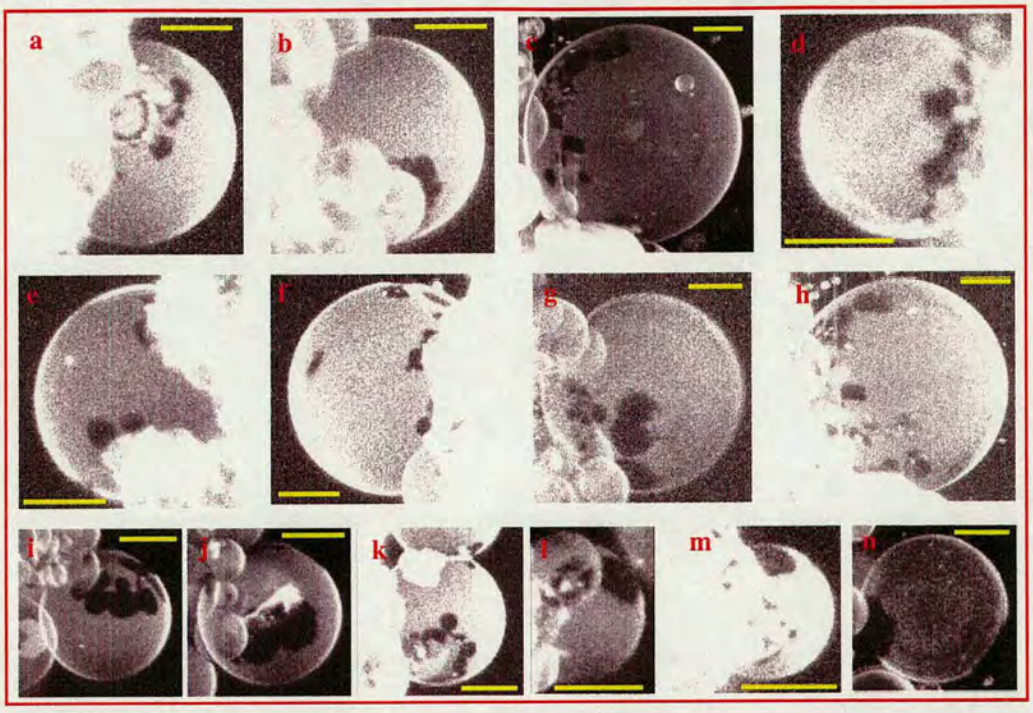

Figure 7.17: 3:1 DPPC:DPPS vesicles: domains appear to be preferentially at points on the vesicle in contact with other membranes or lipid 'junk'. (a) 51.5 °C; (b) 51.5 °C; (c) 49.2 °C; (d) 40.8 °C; (e) 41.8 °C; (f) 45.6 °C; (g) 43.8 °C; (h) 48.7 °C; (i) 45.0 °C; (j) 45.0 °C; (k) 45.5 °C; (l) 41.8 °C; (m) 42.9 °C; (n) 44.6 °C. Scale bars represent 10 μm.

this due to their rigidity. A third possibility is that gel domains are attracted to regions of osculating membranes as thermal fluctuations of the membranes would be suppressed in these regions. Gel domains are rigid with a high bending energy and so it could be entropically favourable for these gel domains to be located in regions of the membrane where membrane fluctuations are already restricted.

The angles in the polygonal domains were measured using the IDL program *sphere_angle.pro* (see section 5.5). The results of these measurement are shown in the frequency histogram in figure 7.19. These angles are strongly quantised around 120 °, the angle that would be expected from hexagonal domains. There are also a couple of measurements around 60 °and the reflex angle of 240 °, angles which could be anticipated from a hexagonally packed crystal. Other angles which were measured tended to arise from the angles between aggregated domains; it would not be surprising that defects in the crystal structure at these points of aggregation allow

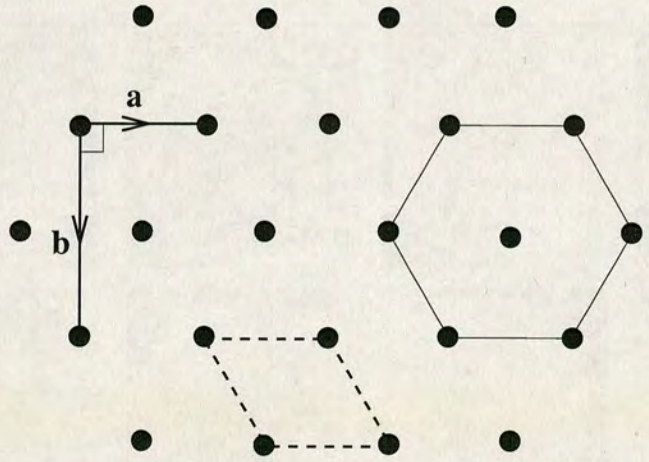

Figure 7.18: Two dimensional hexagonal packing is a special case of orthorhombic packing where the orthonormal lattice vectors **a** and **b** are shown. The dashed line indicates the unit cell for the special case of hexagonal packing.

any angle to occur. It appears from these measurements that the underlying orthorhombic packing of the gel phase is correlated on the length-scale of the domains (several microns) giving rise to the polygonal domain shapes. Note that orthorhombic packing is the technically accurate description of the packing structure since the lipid packing is near-hexagonal [18]: hexagonal packing is a special case of orthorhombic packing (see figure 7.18).

One method to investigate whether the gel phase domains form flat facets or follow the native curvature of the vesicle would be to look at the angles in the polygonal domains formed on the spherical vesicle. If a regular n-sided polygon (P), area $A(P)$, is drawn onto a sphere of radius R, the sum of angles of the polygon ($\sum \theta_{\text{sphere}}$) can be calculated by

$$\sum \theta_{\text{sphere}} = (n-2)\pi + \frac{1}{R^2} A(P) \; . \tag{7.3}$$

Using the hexagonal domains in my images, which appear to be approximately regular, each angle would be $\theta_{\text{sphere}} = \frac{1}{6} \sum \theta_{\text{sphere}}$. Alternatively, if the domain formed a flat facet, each angle of the hexagonal domain would be[5] $\theta_{\text{flat}} = \frac{n-2}{n}\pi = 120\,^{\circ}$. Are my measured angles

[5]This is simply obtained by letting $R \to \infty$ in equation 7.3 so that the second term on the right hand side of the equation becomes zero.

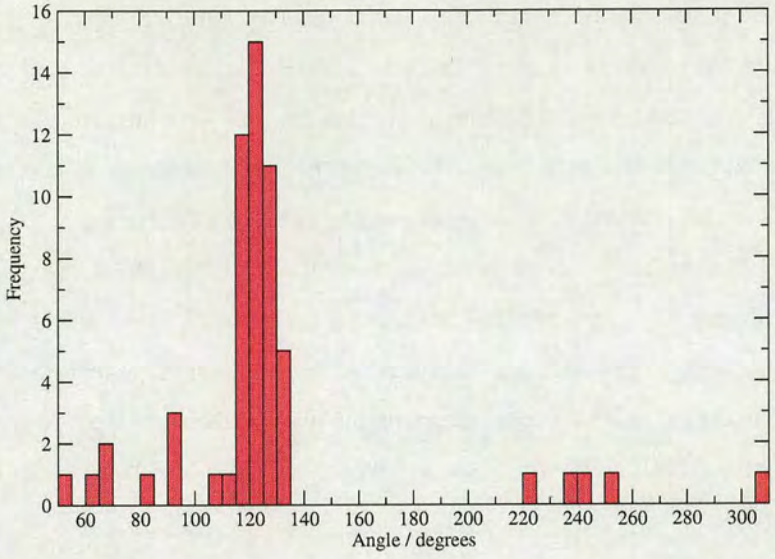

Figure 7.19: Frequency histogram of 58 angles measured for the polygonal domains in 3:1 DPPC:DPPS vesicles.

for these domains distinguishable between the predictions of these two situations so that an implication can be made about the curvature of the gel phase domains?

If we look at large hexagonal domains where the whole domain can be seen and the domain hasn't aggregated with other domains, we can calculate the anticipated angle for if the hexagonal domain has the spherical curvature of the vesicle. The area of the domain can be calculated using the IDL program *domain_finder2.pro* (see section 5.4). Firstly, if we consider the hexagonal domain slightly to the right of centre of figure 7.16n, this has a calculated area of 50.72 μm^2 and the vesicle has a radius of 17 μm. Using equation 7.3, this gives an angle of $\theta_{\text{sphere}} = 121.68$ °. Similarly for the large hexagonal domain in figure 7.16o of area 67.54 μm^2 on a vesicle of radius 15.5 μm, $\theta_{\text{sphere}} = 122.68$ °. These two angles cannot be differentiated from $\theta_{\text{flat}} = 120$ °using my angle measurement program (*sphere_angle.pro*) on my images since the deviations of the anticipated θ_{sphere} from 120 °are smaller than the error in my measurements.

Laurdan was added to the membranes for some experiments. Laurdan is thought to partition into the fluid and gel phase and so it was hoped that this probe would be able to give information on whether the gel phase domains followed the spherical curvature of the vesicle or created flat facets on the vesicle as was done for the DPPC/DPPE system (see figures 7.11 and 7.12). Unfortunately no vesicles could be found where the domains were large enough and in a suitable position on the membrane for this to be unambiguously determined. Also, Laurdan showed very weak or no fluorescence in the gel phase domains as is shown in figure 7.21. The images in figure 7.21 show the same image section through a 7:1 DPPC:DPPS vesicle[6] with the Rh-DPPE and Laurdan fluorophores; dark gel phase domains are observed in both images where the fluorophores have been excluded. This is unlike the DPPC/DPPE system where Laurdan partitioned into the gel phase domains, therefore this suggests that the gel phase domains I have observed in the DPPC/DPPS system has a different structure to the L_β domains in the DPPC/DPPE membranes.

Whether a gel phase domain forms a flat facet or follows the native curvature of the vesicle will be an interplay between the energy needed to deform the spherical vesicle and the energy cost of forming curved gel domains. The vesicles observed in my experiments are very tense, indeed they are close to the lysis tension (see section 8.5). This may mean that my experiments are in a regime where curved gel domains are formed whereas, in the regime of domain formation on a deflated vesicle, the gel phase domains may form flat facets. If gel domains were to form flat facets then the vesicle would be deformed from its spherical geometry. A vesicle of deformed geometry was observed for 3:1 DPPC:DPPS (see figure 7.20); however the 'crinkles' in the membrane do not appear to be caused by the formation of flat facets of gel domains.

Looking at the phase diagram for DPPC/DPPS (figure 7.14), at 7:1 DPPC:DPPS composition the membrane should enter a region of $L_\alpha - P_{\beta'}$ phase coexistence. Due to our conclusion that domain morphology is affected by the structure of the gel phase (see section 7.4), I observed domain formation in 7:1 DPPC:DPPS vesicles: these domains exhibited a polygonal morphology and expelled the Rh-DPPE probe. . We will see in section 7.3 that stripe domain morphologies are expected for the ripple phase which the Rh-DPPE probe preferentially partitions into. This suggests that the phase boundaries of the phase diagram in figure 7.14 are

[6]Experiments for 7:1 DPPC:DPPS will be discussed later in this section.

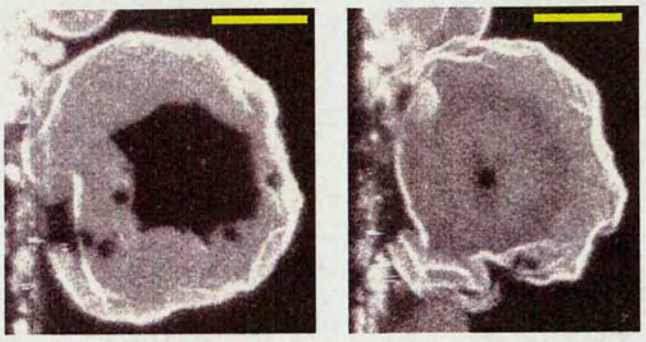

Figure 7.20: 3:1 DPPC:DPPS vesicle at 38.3 °C (one hemisphere in each image): a vesicle deformed from its usual spherical geometry. Scale bars represent 10 μm.

not in quantitative agreement with my data. My data would suggest that the $L_\alpha - P_{\beta'}$ coexistence region of the DPPC/DPPS is only accessible at lower DPPS compositions which were not studied in this work.

7.3 Observed Morphology of $P_{\beta'}$ Domains

None of the lipid mixtures with different head groups that I have looked at grow a rippled gel ($P_{\beta'}$) within the fluid phase[7]. DPPC has a pretransition to a $P_{\beta'}$ phase, but this was always the low-melting temperature component of the binary mixture and hence preferentially partitioned into the fluid phase; no region of $L_\alpha - P_{\beta'}$ phase coexistence was accessible in these systems.

Other researchers in the group have looked at GUVs with binary mixtures of lipids with the PC headgroup but with different hydrophobic acyl chain lengths. Phosphatidylcholines with chain lengths between 12 and 20 carbons long have been shown to exhibit a pretransition to the $P_{\beta'}$ phase. Catherine Blake studied mixtures of DLPC/DPPC lipids and observed stripe domains to grow in the fluid phase. This work was continued by Dr. Vernita Gordon; she studied a variety of mixtures of saturated phosphatidylcholines with different acyl chain lengths. Images courtesy of Dr. Vernita Gordon of vesicles composed of PC mixtures in the gel-fluid

[7]Although a region of $L_\alpha - P_{\beta'}$ coexistence should be accessible for DPPC/DPPS mixtures at very low DPPS compositions, the 7:1 DPPC:DPPS composition studied does not appear to be of low enough DPPS content to access this region of the phase diagram. This is because polygonal, rather than stripe, domains are observed. The proposed relationship between gel phase and domain morphology will be discussed in section 7.4.

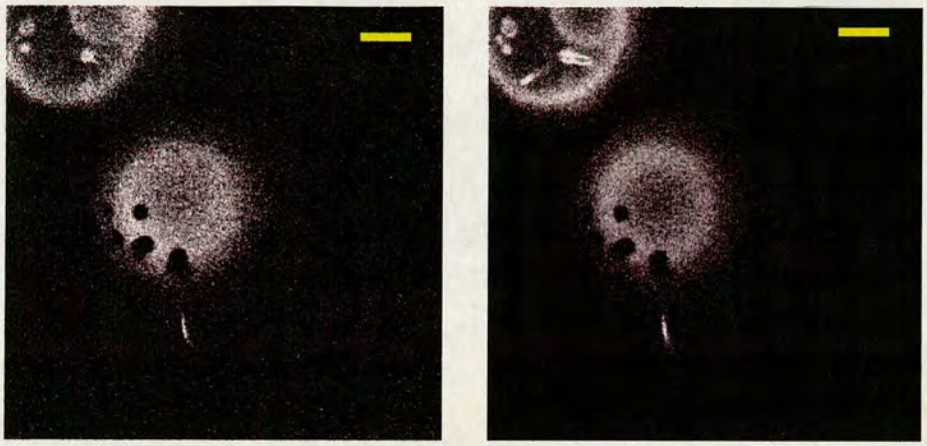

Rh–DPPE Laurdan

Figure 7.21: The same image section through a 7:1 DPPC:DPPS vesicle at 45.3 °C. Both Laurdan and Rh-DPPE are expelled from the gel phase domains. At this composition, the vesicles would be expected to enter a region of $L_\alpha - P_{\beta'}$ phase coexistence where the domains are stripes which the Rh-DPPE probe preferentially partitions into, rather than the polygonal domains observed (*see text*). Scale bars represent 10 μm.

coexistence region are shown in figure 7.22. The gel domains are a ripple gel; they form stripe domains which grow length-ways at a set stripe width. The Rh-DPPE fluorophore was found to preferentially partition into the $P_{\beta'}$ gel phase and the Bodipy-PC dye[8] was also used, which preferentially partitions into the fluid phase. Dr. Gordon also found that these stripes bend at well-defined angles quantised close to 60 °and 120 °(data not shown). Stripe domains were also observed in other systems where the gel phase formed was the $P_{\beta'}$ phase: DMPC/DPPC, DLPC/DSPC, DMPC/DSPC and DPPC/DSPC.

7.4 Gel Phase Structure Determines Domain Morphology

Much of the literature on domain morphology in lipid vesicles has concentrated on considering the line tension between phases and the bending rigidity of the membrane [71–78]. Indeed, this has been shown to be valid for liquid-liquid phase separation in giant vesicles containing

[8]2-(4,4-difluoro-5,7-dimethyl-4-bora-3a,4a-diaza-*s*-indacene-3-pentanoyl)-hexadecanoyl-*sn*-glycero-3-phosphocholine (Bodipy-PC) was obtained from Molecular Probes [112].

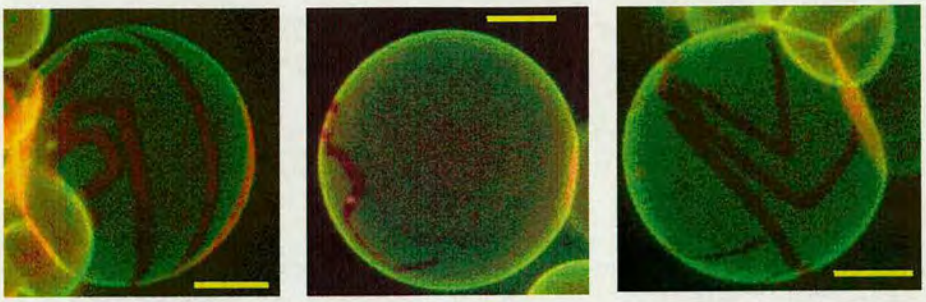

Figure 7.22: Images of vesicles in false-colour courtesy of Dr. Vernita Gordon. [*left*] 1:1 DLPC:DPPC; [*centre*] 1:1 DLPC:DSPC; [*right*] 1:1 DMPC:DSPC. The Rh-DPPE dye is in red and partitions into the $P_{\beta'}$ stripe domains. The Bodipy-PC dye is in green and partitions preferentially into the fluid phase. Scale bars represent 5 μm.

Gel Phase	Domain Shape	
L_{β}	Circles	This Work
$L_{\beta'}$	Polygons	This Work
$P_{\beta'}$	Stripes	Dr. Vernita Gordon

Table 7.1: Domain shapes that were observed for each gel phase structure formed.

cholesterol [11]. However such arguments have been unable to make reliable predictions for the observed morphology of solid-like gel phase domains formed in GUVs. The morphologies of domains observed in gel-fluid coexistence appear to be directly correlated to the structure of the gel phase formed as shown in table 7.1. Contributing to establishing this claim is indeed one of the major results from this thesis.

For mixtures of phosphatidylcholines with different acyl chain lengths, the gel phase structure formed in coexistence with the fluid phase is always $P_{\beta'}$. This ripple phase has a directional anisotropy in its structure in mutually orthogonal directions in the plane of the bilayer. This gives the domains a preferred direction of growth, consistent with the observation of stripe domains by Dr. Vernita Gordon, who has also shown that stripes bend at angles quantised about 60 °and 120 °; this characteristic presumably reflects the hexagonal packing of lipids in the ripple phase. AFM studies on supported lipid bilayers have shown elongated $P_{\beta'}$ domains which also turn at these angles [181, 182].

In DPPC/DPPE mixtures, I observe circular gel domains growing in the membrane. More complicated looking domain morphologies were formed by the aggregation of these circular domains and further growth on top of the new domain shapes. Circular structures can be expected to occur for a phase which is isotropic on the length-scale of the observed domains. NMR experiments, where different parts of the acyl chains and glycerol backbone have been labelled, suggest that DPPE has a rotational diffusion in the L_β phase about its long axis at rates of $10^5 - 10^6$ s^{-1} [183]. Rotational diffusion of a molecule which is not symmetrical under such rotations could lead to the expectation that there is no long range order in its gel phase structure, particularly on the scale of micron-sized domains. This would lead to L_β being an isotropic phase on the length-scale of the observed circular domains. However, in three dimensions, a freely rotating molecule that is in itself non-spherical gives rise to a 'plastic crystal' phase where the molecules behave as if they were perfect spheres; the analogy in two dimensions is that freely rotating lipids behave as perfect circular cylinders.

L_β is a solid-like phase and, according to theory, solid-like phases should be ordered. It is possible however that L_β is a hexatic phase. Hexatic phases are observed in liquid crystals, having orientational order but no long-range positional order [184]. Hexatic phases have also been observed in Langmuir monolayers [185]. Another possibility, but not one that I prefer, is that the domains are polycrystalline, resulting in circular domains. No long-range order has been observed in the L_β phase of DMPS from X-ray diffraction data [186], suggesting that (assuming the L_β phase of DMPS has the same structure as the L_β phase of DPPE) long-range order does not occur in the gel domains of DPPC/DPPE membranes. Currently my preferred explanation of the circular domains observed in DPPC/DPPE vesicles is that the L_β is a hexatic phase. Figure 7.23 shows a computer-generated simulation of a hexatic lattice [187]. Although short-range positional order can be seen between lattice sites, defects in the hexatic phase result in loss of positional order over large distances and hence a hexatic gel phase would be isotropic on micron length-scales.

Further NMR experiments to determine the phase diagram of the DPPC/DPPE system suggest a gradual reduction in chain tilt from $L_{\beta'}$ to L_β for a gel of increasing DPPE content [129]. This transition to the L_β phase is suggested to be complete at $40 - 50$ % DPPE and so all gel compositions accessible in fluid-gel coexistence are thought to be in the L_β phase (see figure

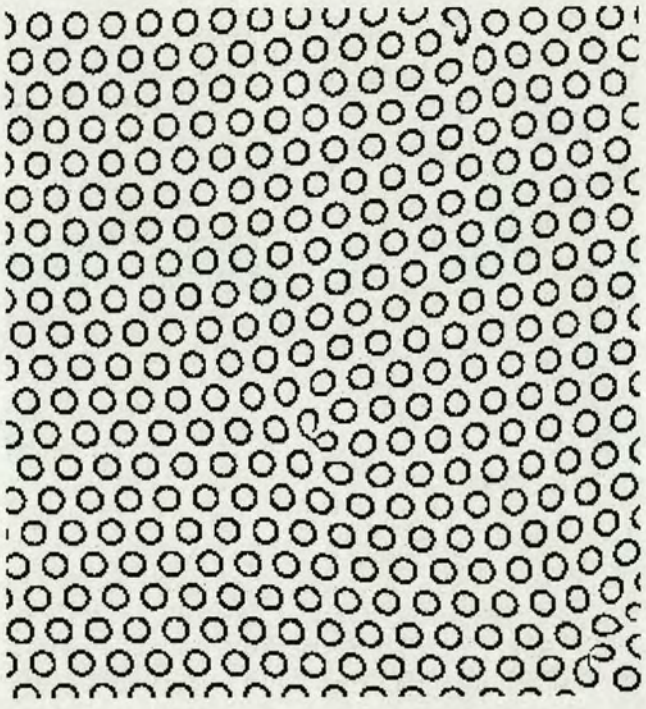

Figure 7.23: Computer-generated simulation of a hexatic lattice [187]. The lattice has short-range hexagonal order but dislocations or defects in the hexatic phase result in loss of long-range positional order.

7.24a). Therefore the gel phase observed for gel-fluid coexistence in the DPPC/DPPE system is always expected to be an L_β gel which is isotropic on the size-scale of the observed domains.

Domains observed in 3:1 DPPC:DPPS vesicles had a polygonal morphology and were often hexagonal. This kind of domain shape could be expected from a phase with orthorhombic (near-hexagonal) packing and long-range order such as the $L_{\beta'}$ gel. DPPS is known to form the L_β gel phase in singe-component systems with no long range order [28] (also see section 2.3.2). The phase diagram for DPPC/DPPS is shown in figure 7.24b; at 3:1 composition the initial gel phase formed on cooling, as shown by this phase diagram, would be $\sim$ 70 % DPPS[9]. The gel phase structure of mixtures of DPPC and DPPS has not been studied so the approximate transition compositions of the gel phase between $L_{\beta'}$ and L_β is not known although the

[9]It should be noted that the composition of the gel phase varies rapidly for small changes in overall composition in this region of the phase diagram down to $\sim$ 50 % DPPS in the gel phase for a vesicles with $\sim$ 20 % overall DPPC content. Also, observation of polygonal domains at 7:1 DPPC:DPPS composition suggest that the phase boundaries are not quantitatively accurate.

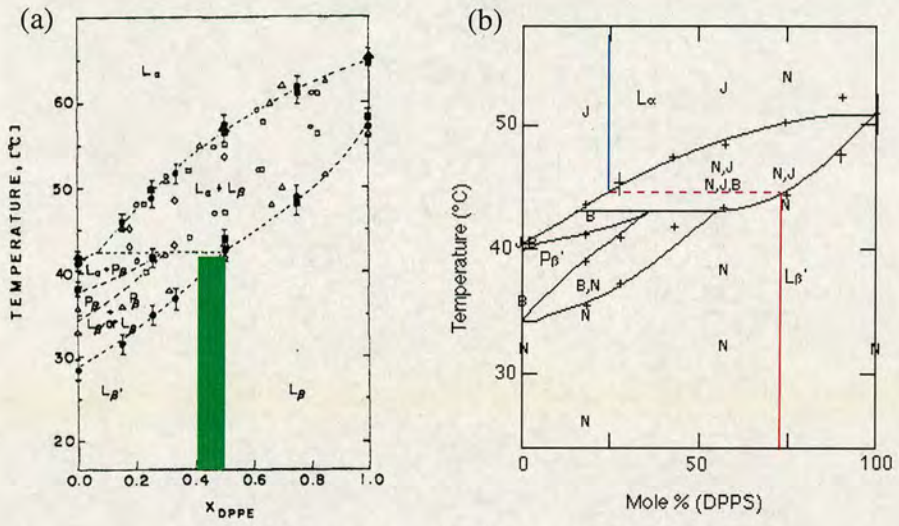

Figure 7.24: (a) Phase diagram of the DPPC/DPPE system [129]. The gradual transition between $L_{\beta'}$ and L_{β} phases is thought to be complete by $40 - 50$ % DPPE content, shown on the diagram by the green region. Therefore all gel compositions accessible in the gel-fluid coexistence region are thought to be the L_{β} phase. (b) Phase diagram for DPPC/DPPS membranes [27]. At 3:1 DPPC:DPPE composition, this phase diagram predicts an initial gel phase composition on cooling of $\sim$ 70 % DPPS.

characteristics of the observed domains suggest that the gel phase is of the $L_{\beta'}$ structure preferred by the lower melting temperature component, DPPC. This assertion is supported by my observation that Laurdan is excluded from the gel phase domains of the DPPC/DPPS membranes, unlike the L_{β} domains of the DPPC/DPPE vesicles. Experimental studies have shown the $L_{\beta'}$ phase of DPPC to exhibit long range order: X-ray diffraction of multilamellar vesicles has shown in-plane correlations between lipid positions over distances of $\sim$ 300 nm [188], which is of the order of the size of the vesicles, and optical microscopy of supported bilayers has reported $1 - 2$ μm domains[10] [189].

Why does the tilting of the acyl chains when going from an L_{β} gel phase to an $L_{\beta'}$ gel phase induce long range ordering? A possible explanation of this is shown in figure 7.25. If lipids in the $L_{\beta'}$ phase were free to rotate about their long axis in a way which was uncorrelated with their neighbouring lipids then it would be possible for the acyl chains of adjacent lipids to be tilted toward each other. Steric repulsion of the acyl chains would cause a large gap between

[10]Here a domain is defined by the correlation of the tilt angle.

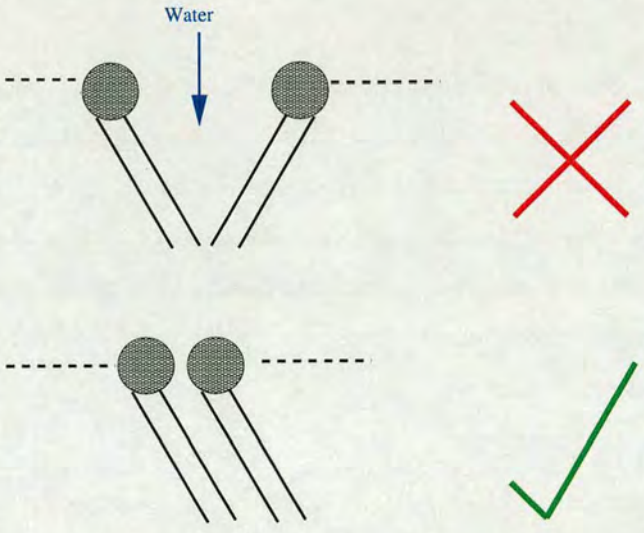

Figure 7.25: Schematic diagram to explain how chain tilt may cause long range order in the gel phases. [*top*] There is no correlation between the orientation of the tilted chains. In this scenario it is possible for adjacent sets of chains to be tilted toward each other. Steric repulsion of the chains would leave a large gap between hydrophilic headgroups allowing water to get to the hydrophobic chains. This situation is energetically highly unfavourable. [*bottom*] The orientation of chain tilt between adjacent molecules is correlated. The headgroups remain tightly packed so that water cannot reach the hydrophobic chains. This orientational as well as positional order in chain-tilted phases could cause long-range order within the gel phase compared to the L_β phase where the lipids can rotationally diffuse about their long axis.

lipid headgroups and water would be free to penetrate into the hydrophobic core of the bilayer. This situation is energetically highly unfavourable. Hence, lipids in the $L_{\beta'}$ phase will have positional order in their gel phase as well as an orientational order in their chain tilt direction which will propagate over large distances in the membrane (for example, $1 - 2$ μm in DPPC supported bilayers as mentioned above). In the L_β phase, with its untilted chains, the lipids still have local positional order in their gel phase but are less constrained in their rotation about their long axis (for example, the rotational diffusion constant measured for DPPE in the L_β phase [183]) and so this order does not propagate over long distances. Hence the L_β phase can be a hexatic phase that does not have the long range order of the $L_{\beta'}$ phase. This argument is analogous to saying that dislocations or defects in the packing structure of L_β have a lower energy cost than would be the case for the $L_{\beta'}$ phase. Similarly, long-range order is observed in the $P_{\beta'}$ phase, since non-wiggly stripe domains are observed to bend at quantise angles. The $P_{\beta'}$ phase is also thought to have tilted acyl chains (see section 2.3) although the structure is

more complicated due to the asymmetric rippling of the bilayer.

Long range positional order of the lipids induced by the tilting of the acyl chains, frustrating the rotational freedom of the lipids, could be linked to work on rotator phases of long-chain alkanes [190–192]. Alkanes can be viewed as lipid tails with the headgroups 'chopped off'. Rotator phases that 'lack long range order in the rotational degree of freedom of the molecules about its long axis' [192] have been observed between the liquid and crystal phases of normal alkanes. These rotator phases have been observed to occur at distinct angles of tilt [191].

7.5 Summary

In this chapter I have discussed the morphology of gel phase domains in binary lipid GUVs. The morphology of the gel domain is dependent on the structure of the gel phase formed: I have shown that the L_{β} phase results in circular domains and the $L_{\beta'}$ phase gives rise to polygonal domains, while Dr. Vernita Gordon has found that the $P_{\beta'}$ phase leads to stripe domains.

In the DPPC/DPPE system the gel phase is of type L_{β}. On cooling into a region of gel-fluid coexistence, circular domains are observed to be moving in the membrane due to convective flow in the fluid phase. These domains can aggregate, by a mechanism analogous to the '*moving droplet phase*' observed in the viscoelastic phase separation of polymer mixtures, to form more complicated domain shapes since slow diffusion in the gel phase prevents aggregated domains rearranging their shapes (on the time-scale of my experiments) to reduce the line tension between phases. The gel domains do not form flat facets as has been predicted in the literature but instead the gel domains follow the native curvature of the bilayer.

In 3:1 DPPC:DPPS vesicles, I argue that the gel phase formed is of type $L_{\beta'}$. Polygonal, often hexagonal, domain shapes are observed with angles quantised close to 120 °. The curvature of the gel phase could not be inferred from my data.

Chapter 8

Miscellaneous Results

This chapter contains a compendium of results and observations which were not in themselves studied in a great deal of detail, but are nevertheless interesting enough to deserve comment. Where explanations of the phenomena are attempted, these should be treated as ideas and speculation based around intelligent guess-work only.

I will firstly look at the behaviour of single component DPPE and DPPC vesicles by analysing multiphoton images of such vesicles containing the Rh-DPPE dye. These are the extreme right and left axes of the DPPC/DPPE phase diagrams in chapter 6; the single component phase behaviour of DPPE and DPPC are also detailed in section 2.3.2. I then detail some preliminary experiments on the DPPC/DPPA and DPPG/DPPE binary vesicle systems. The next section discusses the adhesion of vesicles with respect to images of all kinds of vesicle compositions studied and finally I take a look at vesicle lysis, when the membranes rupture. The final two sections on adhesion and lysis are relevant to the process of endocytosis, where two vesicles merge into one. This process requires two vesicles to adhere to each other before breaking and reforming the membranes of the vesicles at the point of opening to create a single vesicle. It should be also be noted however that vesicle fusion was never observed in any of my samples.

8.1 Single-Component Membranes

This thesis contains extensive discussions of the behaviour of DPPC/DPPE binary membranes. These observations can only be meaningful if we are aware of the behaviour of these lipids in single component vesicles. Multiphoton microscopy experiments using the Rh-DPPE fluorophore for single component DPPC and DPPE membranes were undertaken. The results of these experiments are detailed below.

8.1.1 DPPE

Electroformation of single component DPPE GUVs containing the Rh-DPPE fluorophore was found to be difficult. Low yields of vesicles were obtained compared to lipid mixtures containing lipids with the PC headgroup.

DPPE has a complex $L_\alpha \rightarrow L_\beta$ phase transition on cooling through the main transition temperature (see section 2.3.2). The phase transition is seen to be broad with a possible intermediate state (or states?). Images of DPPE vesicles on cooling through the main transition temperature are shown in figures 8.1 and 8.2.

Stripe domains are seen to form. Unlike the stripe domains seen in the DLPC-DPPC system where a $P_{\beta'}$ gel phase grows in the fluid phase (see figure 7.22), these stripes wiggle more and, instead of growing length-ways, the stripes become wider on further ripening (figure 8.1). On a faster quench through the main transition (figure 8.2), more stripes nucleated and appeared more wiggly than the slower cooling rate (figure 8.1).

Using the argument of chapter 7, where I attest that the domain morphology reflects the molecular structure and packing of the gel phase being formed, I can speculate on the nature of the intermediate phase that has been observed on cooling from the L_α phase to the L_β phase in DPPE membranes. The stripe domains suggest that there is a directional anisotropy in the plane of the bilayer in the structure of the intermediate phase so that the domain preferentially grows in one direction. The wiggling of the stripe suggests that this intermediate phase does not have the long-range (of order microns) order that is seen in the $P_{\beta'}$ phase of DPPC. The thickening of the stripes on ripening may also suggest that the energy cost to grow in the lesser

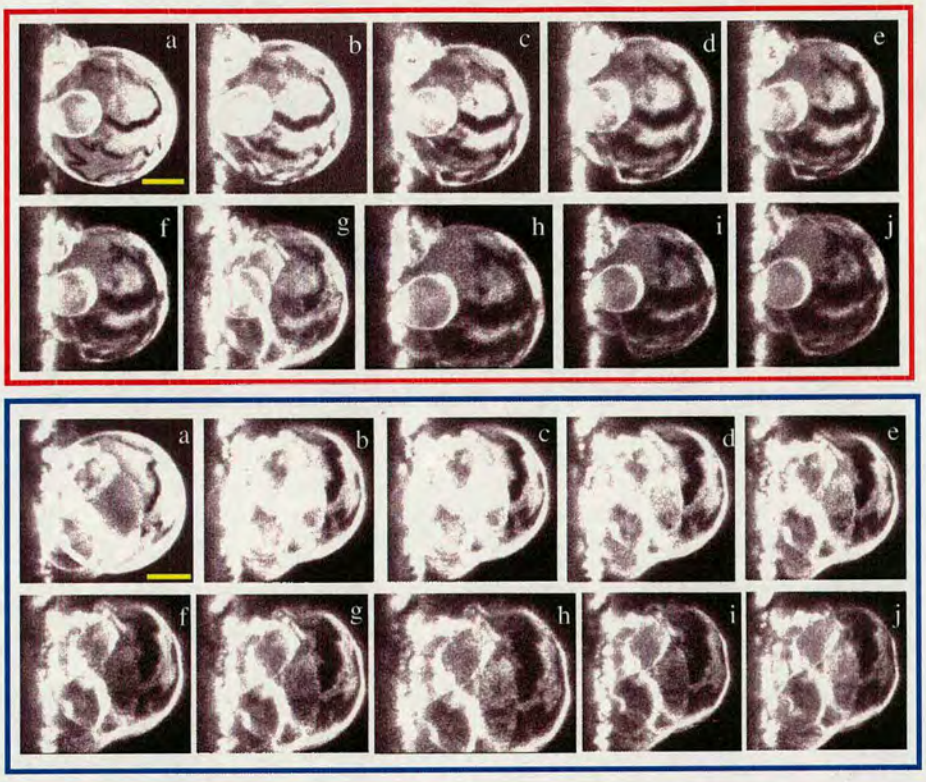

Figure 8.1: A single component DPPE vesicles cooling through images (a)-(j). The images surrounded by different colour boxes (red and blue) represent different hemispheres of the vesicle. Temperatures: (a) 62.9 °C, (b) 62.4 °C, (c) 61.9 °C, (d) 61.5 °C, (e) 61.1 °C, (f) 60.5 °C, (g) 59.8 °C, (h) 58.6 °C, (i) 57.4 °C, (j) 56.9 °C. Scale bars represent 10 μm.

preferred direction in the bilayer plane is not as great as in the DLPC/DPPC system where stripe thickness appears to be coupled to the surface tension of the membrane [193].

At higher pH (pH 12), DPPE has been seen to exhibit a pretransition to a phase with a ripple structure (see section 2.3.3). At the neutral pH of my experiments, this ripple phase is at too high an energy in the free energy landscape of DPPE to be accessible on heating. As pH is reduced, the temperature range of the DPPE ripple phase decreases until it disappears from the phase diagram, i.e. the free energy of this phase increases with respect to the other phases of DPPE until it is no longer a thermodynamically preferential state. The broad, complicated phase transition from L_α to L_β in DPPE bilayers appears to be as a result of the DPPE trying to access a thermodynamically unfavourable ripple phase in its free energy landscape: this is the

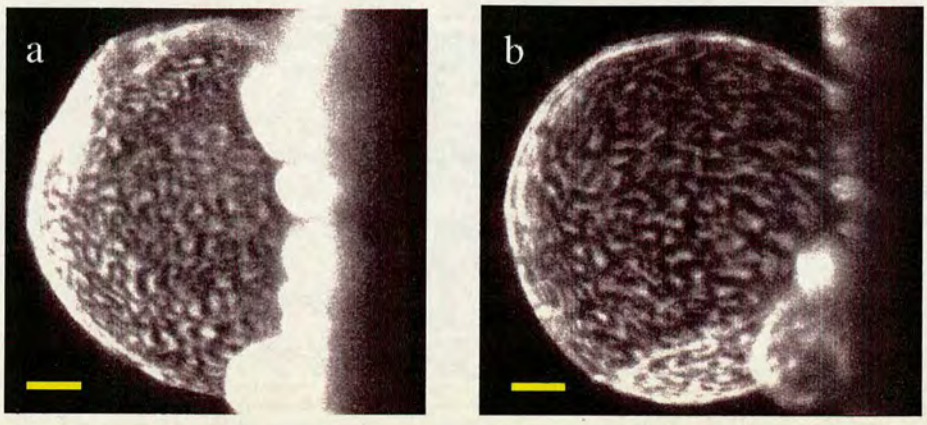

Figure 8.2: Single component DPPE vesicles below the main transition temperature after a faster rate of cooling than the vesicles in figure 8.1. (a) 62.9 °C; (b) 61.1 °C. Scale bars represent 10 μm.

Ostwald rule where a metastable state (the L_α phase of DPPE is metastable below $\sim$ 66 °C, see section 2.3.2) during a transition to a stable state doesn't undergo this transition directly but rather proceeds via intermediate metastable states which are closest in free energy to the initial state. This ripple phase is characterised by a directional anisotropy in its bilayer structure and a molecular ordering which does not persist over the long length-scale of the $P_{\beta'}$ phase of DPPC.

8.1.2 DPPC

Good yields of DPPC vesicles (containing the Rh-DPPE fluorophore) were obtained by electroformation. On cooling slowly through the main transition temperature, no heterogeneous partitioning of the Rh-DPPE was observed. Figure 8.3 shows homogeneous fluorescence from DPPC membranes below the main transition temperature. This agrees with the main transition of DPPC being highly cooperative with no detectable coexistence of $P_{\beta'}$ and L_α phases [21] as previously discussed in section 2.3.2.

8.2 DPPC/DPPA Membranes

DPPC/DPPA membranes were briefly investigated to observe the morphology of the domains which formed when cooled through the gel−fluid coexistence region of its phase diagram. This

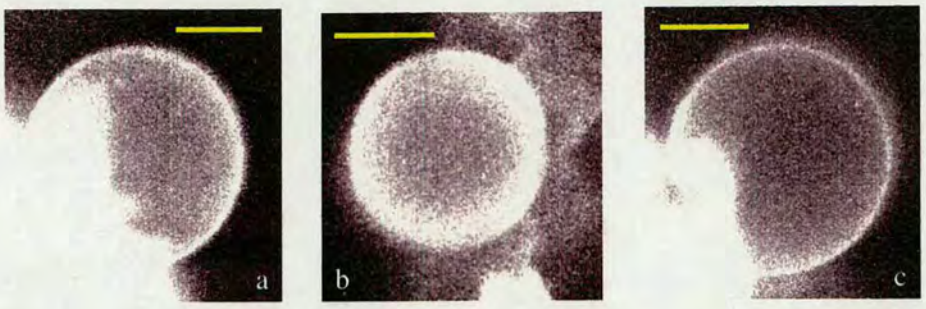

Figure 8.3: Single component DPPC vesicles below the main transition temperature showing no heterogeneous fluorophore partitioning. No heterogeneous surface structures were detected on single component DPPC vesicles around or below its main transition temperature. (a) 41.2 °C; (b) 39.8 °C; (c) 40.9 °C. Scale bars represent 10 μm.

system could also be used to study the effect of having a lipid with a net charge in the binary lipid membrane.

Electroformation in deionised water of 4:1 and 1:1 compositions of DPPC:DPPA GUVs was found to be successful. Three published phase diagrams for DPPC/DPPA membranes are shown in figure 8.4. All three phase diagrams, despite being published in the 1990s[1], do not consider how the different gel phase structures of the lipids affect the topology of the phase diagram. Indeed the phase boundaries of these three phase diagrams appear significantly different in shape even though all three phase diagrams were determined by DSC. The lipids in [137] were dissolved in unbuffered water, in [194] a pH of 7.4 was used and in [195] a pH of 7.0. This indicates that the phase transition temperatures of the DPPC/DPPA mixtures may be either sensitive to preparation method or temperature history.

The titration curve of the headgroup of DPPA is shown in figure 8.5. At neutral pH, DPPA has a charge of $-1e$ per headgroup (where e is the fundamental charge constant, $e = 1.6 \times 10^{-19}$ C). This charge per headgroup is fairly stable in a pH range down to almost pH 4 but at pHs just above neutral the charge per headgroup rapidly rises to $-2e$ at around pH 9. Due to the negative charge density that will be present on a DPPC/DPPA membrane, it can be expected that electrostatic interactions would increase the concentration of positively charged hydrogen ions close to the bilayer with respect to the bulk aqueous environment, shifting the pH local to

[1]Other published binary lipid phase diagrams have shown consideration to the different gel phases in their topologies since the early 80s.

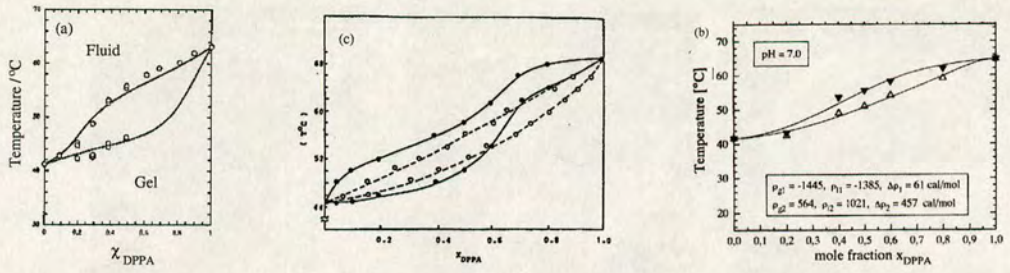

Figure 8.4: Phase diagrams of the DPPC/DPPA system from the literature (all obtained by DSC): (a) Inoue and Nibu [137], (b) Kim *et al.* [194], (c) Garidel *et al.* [195].

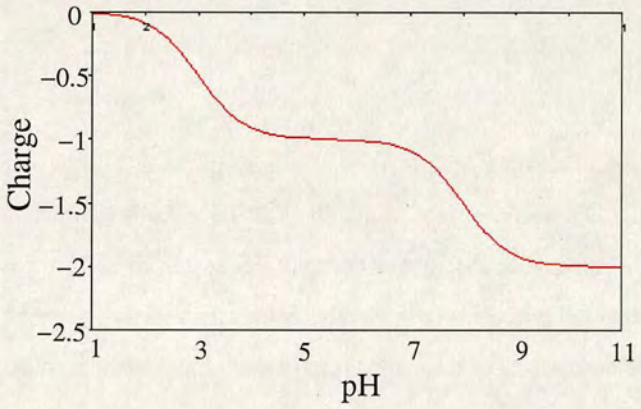

Figure 8.5: Charge per headgroup of PA as a function of pH in 0.1 M NaCl [15].

the bilayer to slightly lower values than the bulk solution. This would be likely to shift the pH in the region of the membranes to a value where the charge per lipid is relatively stable with small changes in pH (probably somewhere in the range $4 < \text{pH} < 7$).

On cooling DPPC/DPPA membranes (containing the Rh-DPPE fluorophore) from the L_α phase, domains were generally seen to form at points on a vesicle membrane where two membranes were in close contact (see figures 8.6a,b,d−g). Occasionally small moving domains were seen in the free membrane (see figure 8.6c) although most of these domains were too small to resolve whether they were circular of had angular features. A few domains did look like they may be angular, for example figure 8.6a, but the statistics due to the number of images I have is too

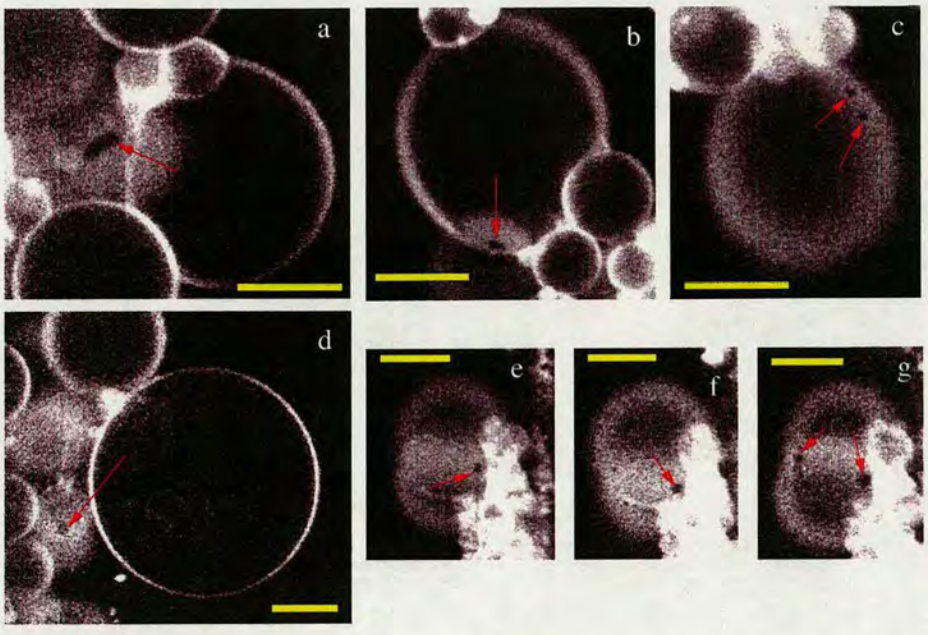

Figure 8.6: Single multiphoton sections through DPPC/DPPA membranes containing the Rh-DPPE fluorophore, red arrows are used to guide the eye to the location of the domains: (a) 4:1 DPPC:DPPA 49.1 °C; (b,c) 4:1 DPPC:DPPA 44.8 °C; (d) 1:1 DPPC:DPPA 58.1 °C; (e) 1:1 DPPC:DPPA 53.1 °C; (f) 1:1 DPPC:DPPA 50.4 °C; (g) 1:1 DPPC:DPPA 48.0 °C. Images a, b, d–g show domains at the point of contact between the membranes of different vesicles. Image c shows moving domains in the free membrane of a vesicle. Scale bars represent 10 μm.

poor to make any claims about the generic morphology of these gel phase domains. Without a 'good' phase diagram that considers the gel phase structures for the DPPC/DPPA system it is not possible to predict anything about what kind of domain morphology may be expected using the conclusions of chapter 7.

The preference of DPPA-rich gel domains to form in regions of contact with other membranes could be due to the attractive interaction between adjacent membranes causing them to adhere and flatten against each other (see section 8.4 for a further discussion on this). This flat area of membrane may provide the gel domains, which are more rigid than the fluid phase and hence require more energy to become bent, a region on the bilayer to form where they can grow flat. Alternatively, but far more unlikely, these domains could be due to a phase which is induced by the interaction between the bilayers and does not occur in the free membrane.

A possible explanation as to why the domains remain so small is that these domains may have

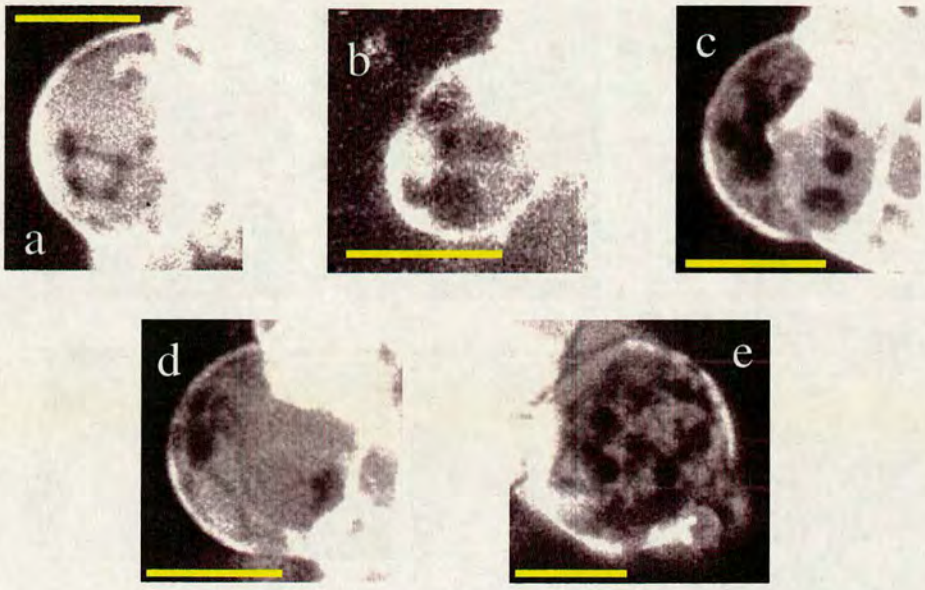

Figure 8.7: Domains in the free membrane of DPPC/DPPA vesicles; images represent a stack of multiphoton images depicting the vesicle hemisphere. All images are 1:1 DPPC:DPPA compositions: (a) 43.0 °C; (b) 42.8 °C; (c) 42.9 °C; (d) 42.9 °C; (e) 42.9 °C. Scale bars represent 10 μm.

a very high concentration of DPPA relative to DPPC. The DPPA is negatively charged whereas DPPC has no net charge. The size of these domains may become limited by electrostatic repulsion (the Debye length in deionised water is around a micron) as the energy required to add another negatively charged DPPA lipid to a domain carrying a high negative charge density could be greater than the increase in interfacial line tension between phases if a new domain was nucleated. The small size of these domains could also be due to the small amounts of dark gel phase observed on the DPPC/DPPA vesicles meaning that there is not enough of the gel phase to create large domains.

Greater abundance of the dark domains were seen on a few of the smaller vesicles (see figure 8.7) where domains also were seen to form on the free membrane. It is possible however that these domains were at one point in contact with another vesicle which later ruptured and disappeared after these domains formed (see section 8.5 for a discussion on vesicle lysis). These domains were not stripes but the resolution is not high enough to confidently state whether these domains are inherently circular or have angular features but by the arguments of chap-

ter 7, these domains consist of a lamellar gel rather than a rippled gel phase.

DPPC/DPPA membranes were not studied extensively, this discussion only represents initial observations on the phenomena of this system. The discussion is highly speculative and based on a small data set. Further investigation of this system is required in order to make any firm statements about its behaviour.

8.3 DPPG/DPPE Membranes

I wanted to look at DPPG/DPPE vesicles to see if there were any unexpected effects when substituting the lipid which was prevalent in the fluid phase of the gel-fluid coexistence region of the phase diagram. Phase diagrams for DPPG/DPPE mixtures at pH 2.0 and pH 7.0 have been published by Garidel and Blume [196] (see figure 8.8 for phase diagram at pH 7.0). These phase diagrams are of the type where the authors do not consider the effect of the different possible gel phase structures of the lipids on the phase diagram topology, despite being published as late as 2000. DPPG has the same main phase transition as DPPC, but DPPG has a charge of $-1e$ per lipid headgroup as opposed to the zwitterionic DPPC with its single positive and single negative charge per headgroup.

Several attempts were made to look at binary vesicles with DPPG and DPPE lipid components. The electroformation was attempted in a large excess of deionised water. No vesicles formed at 1:3 and 1:1 DPPG:DPPE compositions. Single component DPPE vesicles can be formed, although not in as large a yield as DPPC vesicles, so it is assumed that the presence of DPPG inhibited the electroformation. Charged lipids seem to hinder electroformation as has previously been reported [68]. Single component anionic DMPG[2] GUVs have been formed by electroformation by Riske *et al.* in 10 mM HEPES buffer (pH 7.4) plus 2 mM sodium chloride [197]. Ionic solutes are reported to hamper the electroformation of zwitterionic PC GUVs [68], but in the case of this anionic lipid it would appear to aid their formation. It has been suggested before that the electrostatic interactions between bilayers on the platinum wires are one determinant as to whether GUVs will form by electroformation [68]. It may in fact be

[2]Two 14 carbon acyl chains.

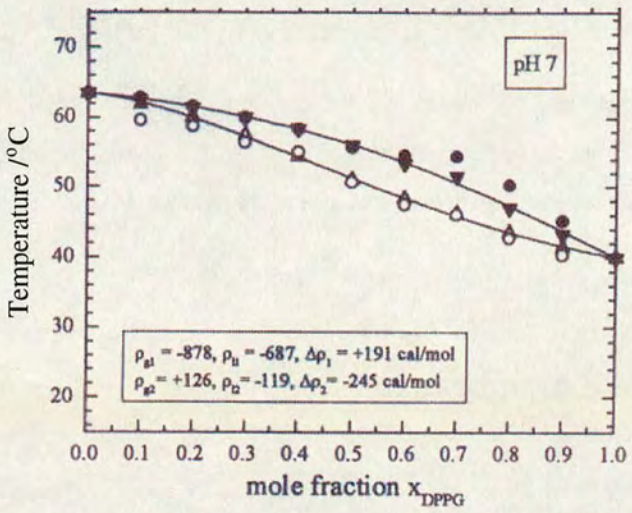

Figure 8.8: Phase diagram for the DPPG/DPPE system at pH 7.0 [196].

the case that ionic solutes in more than trace concentrations hamper the electroformation of zwitterionic membranes such as PCs but, in the appropriate concentrations, aid the formation of GUVs made from charged lipids.

DPPC/DPPG binary vesicles were not investigated as, due to being reported as having identical (or very similar) main transition temperatures, any heterogeneous partitioning of fluorophores in the membrane would be difficult to interpret in a reliable manner.

8.4 Vesicle Adhesion

Inter-membrane interactions were briefly introduced in section 3.1.4. The vesicles in my experiments are held still by adhesion to neighbouring vesicles which in turn adhere to the electrodes in the electroformation chamber. Adhesion of vesicles to each other and to surfaces has been reported and discussed previously [198, 199]. Adhesion implies an attractive energy between membranes. The only attractive interaction, as discussed in section 3.1.4, is the van der Waals interaction; all the other inter-membrane interactions are repulsive.

Adhesion energies between phospholipid bilayers have been measured to be of the order 10^{-5} Jm^{-2}

[36]. If the contact area between two vesicles is 10 μm^2 then this gives an adhesion energy of $\sim 10^{-16}$ J. The energy to deform a spherical vesicle[3] is $8\pi\kappa_b$. Taking $\kappa_b \sim 10k_BT$, this results in a bending energy of around 10^{-18} J. Since the adhesion energy is a couple of orders of magnitude larger than the bending energy, the vesicle membrane is easily deformed on adhesion to another membrane.

Deformation of vesicle shape on adhesion to other vesicles can be seen in figure 8.9. This figure illustrates vesicle adhesion for single component vesicles of the zwitterionic lipids DPPC and DPPE, vesicles with a 1:1 lipid mixture of DPPC:DPPE which has no net charge and vesicles with an overall net negative charge density with compositions 3:1 DPPC:DPPS and 1:1 DPPC:DPPA. Membrane adhesion still appears to occur when both membranes have a net negative charge density, adding an extra electrostatic repulsion to the total inter-membrane interaction energy. The hydration force is a very short range repulsion, so we will not consider its effect on membrane adhesion; we will assume that the minimum in the inter-membrane interaction energy is at a length-scale larger than about 10 Å.

Membranes are seen to flatten against each other on adhesion. The membranes in these images are under tension and no thermal fluctuations in the membranes can be observed under optical resolution. This means that the amplitude of thermal fluctuations in the membranes have an amplitude less than around 300 nm. Thermal fluctuations provide a repulsive steric interaction between adjacent bilayers.

When the vesicles are first formed by electroformation in the L_α phase, they are fully spherical with very little contact area between adjacent vesicles (see the image for Fluid Phase on the left of figure 8.10). As the temperature is decreased into a region of gel-fluid coexistence, vesicles are seen to flatten against each other (also see figure 8.10). On increasing the temperature back into the fluid phase the vesicles returned to a more spherical shape with reduced contact area but not quite as well-rounded as the initial fluid vesicles just after electroformation (again, see figure 8.10).

The observations described for figure 8.10 can be explained using a qualitative argument which considers the thermal fluctuations of the membrane. As mentioned previously, thermal fluctu-

[3]See equation 3.4, where we ignore κ_G since the integral of this term in equation 3.3 is invariant for shape variations of a given topology [36].

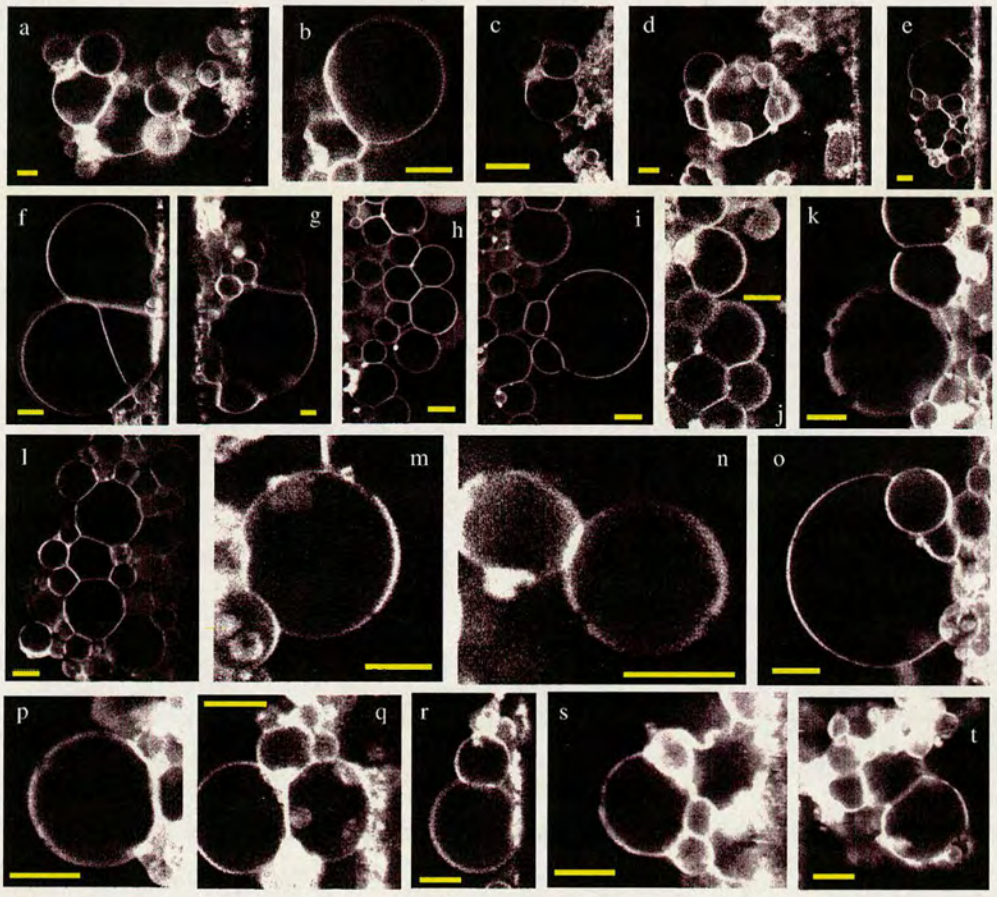

Figure 8.9: Single multiphoton image sections of adhering vesicles. Compositions: (a-d) DPPC only; (e-g) DPPE only; (h-l) 1:1 DPPC:DPPE; (m-p) 3:1 DPPC:DPPS; (q-t) 1:1 DPPC:DPPA. Temperatures: (a) 47.8 °C; (b) 41.2 °C; (c) 39.2 °C; (d) 39.1 °C; (e) 67.8 °C; (f) 67.5 °C; (g) 65.1 °C; (h) 48.8 °C; (i) 47.3 °C; (j) 46.7 °C; (k) 49.8 °C; (l) 48.3 °C; (m) 44.6 °C; (n) 42.6 °C; (o) 41.7 °C; (p) 41.9 °C; (q) 50.4 °C; (r) 48.0 °C; (s) 42.9 °C; (t) 42.9 °C. Scale bars represent 10 μm.

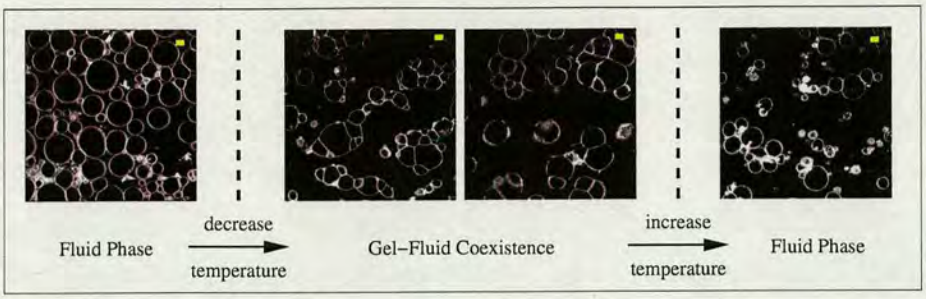

Figure 8.10: Image slices of 1:1 DPPC:DPPE vesicles in the ITO-plate formation cell. Near spherical vesicles are initially seen when the whole vesicle is in the L_α phase. The vesicles flatten against each other forming foam-like structures when the temperature is cooled to the L_β-L_α coexistence region of the phase diagram. On increasing the temperature so that the lipids are fluid again, the vesicles appear to partly regain their original near-spherical structure. Images represent different regions of the same sample during a single experiment. Scale bars represent 10 μm.

ations result in a steric repulsion between neighbouring membranes. Thermal fluctuations, and hence repulsion between membranes, increases with increasing temperature. The lateral tension in the membrane is also coupled to the amplitude of thermal fluctuations: as tension in the membrane increases, thermal fluctuations decrease and hence the steric repulsion between membranes also decreases. Membrane adhesion induced by lateral tension and a temperature-driven unbinding transition have been discussed by Helfrich, using a model of membrane interactions which only considers van der Waals attractions and steric repulsion due to thermal undulations [87]. Helfrich's model predicts that the tension (σ) in the membranes is related to the equilibrium membrane separation (D_0) by $D_0 = \sigma^{-0.5}$. Naturally, D_0 decreases as the repulsion between membranes decreases, i.e. when the membrane tension, σ, increases.

When vesicles initially form, they are under tension which reduces thermal fluctuations, but also are at high temperatures, a factor which increases thermal fluctuations. The membrane is also in the fluid phase so is free to fluctuate without too high an energy cost (relatively low κ_b). The high tension in the membrane has the consequence of increasing the energy required to bend the membrane considerably and hence suppresses the formation of flat regions of adhesion between adjacent membranes.

When the temperature is reduced into the gel-fluid coexistence region, several effects may contribute to the observed behaviour. Firstly reducing the temperature reduces the amplitude

of thermal fluctuations, reducing the repulsion between membranes. The formation of gel phase domains with a higher bending rigidity further reduces the thermal fluctuations of the membrane. The reduced repulsion between membranes results in the vesicles being able to form flat interfaces with each other due to the adhesive energy between membranes. The regions of the membrane which become flat are fluorescing with the Rh-DPPE fluorophore and are hence in the fluid phase. The fluid phase has a lower bending energy so it is easier for a fluid phase membrane to be deformed to form flat interfaces with neighbouring vesicles. Although the gel phase is more rigid than the fluid phase and is likely to prefer to be on a flat region of membrane, it would take more energy to deform a curved gel phase domain so that it flattened against neighbouring vesicles due to adhesion. It has already been seen in chapter 7 that gel domains in DPPC/DPPE vesicles form with the native curvature of the vesicle rather than forming flat facets. Whether the formation of gel domains causes an increase or a decrease in the surface tension of the vesicle is not known, although the surface tension in fluid vesicles is known to relax with time. Consideration of the effects of surface tension on membrane deformation due to adhesion is not entirely trivial since increased surface tension reduces the steric repulsion but also increases the energy required to deform a region of the membrane.

On increasing the temperature back into the fluid phase, thermal undulations increase due to the increased temperature and the regions of gel phase, which have higher bending energies, have disappeared. This increases the repulsion between vesicles and hence decreases the contact area between adjacent vesicles. The tension in the membranes has probably reduced over time and therefore the energy required to deform the membranes has reduced. This effect may dominate the increased repulsion due to the decrease in surface tension increasing the thermal fluctuations: a possible explanation as to why the vesicles do not appear to return to as spherical a shape as they began with after initial electroformation.

One further observation I wish to point out with respect to vesicle adhesion is that deformed membranes do not always form flat regions of adhesion. If we consider figure 8.9o, the smaller vesicle still appears spherical and the larger vesicle has a concave region of membrane around it. This could be due to the smaller vesicle having a larger surface tension and hence requires more energy for it to be deformed[4]. This effect can be observed in other images in figure 8.9,

[4]The energy required to deform a spherical membrane is independent of the vesicle radius (see section 3.1.2).

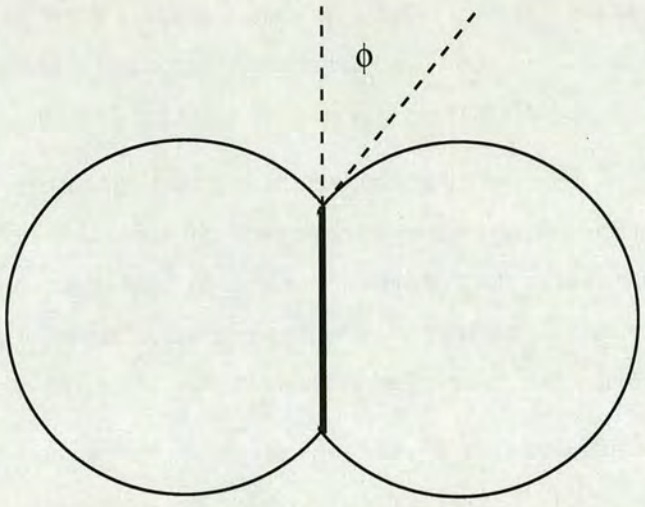

Figure 8.11: Diagram of two spherical vesicles which adhere to each other due to an attractive interaction energy between the bilayers. The magnitude of the inter-membrane adhesion energy can be calculated by measuring the half contact angle, ϕ.

but the effect in image o is the most pronounced.

The half-angle of contact between two adhering vesicles can be used to calculate the adhesion energy between vesicles (see figure 8.11) [199]. Furthermore the surface tension of the membrane can be calculated by measuring the contact area between the membranes and the vesicle diameter [200]. Such measurements were not attempted using my data since the adhesion of many vesicles to each other immensely complicates such calculations although such a problem may not be theoretically intractable. If it was desired to measure adhesion energies and surface tensions between membranes using my experimental set-up then it may be possible to search for 'nice' vesicles within a sample, i.e. a vesicle which is only in contact with one other vesicle, but such experiments would be tedious and lead to low numbers of results and poor statistics for a large number of 'man-hours that would need to be spent on this pursuit.

8.5 Vesicle Lysis

A common problem encountered when imaging vesicles was their tendency to rupture. This made it difficult to follow the evolution of domains on a single vesicle with increasing time

and decreasing temperature. The act of imaging the vesicles appeared to provide the necessary perturbation to cause vesicles to rupture. Successive multiphoton image sections of vesicles rupturing whilst scanning through the vesicle in the $z-$direction are shown in figure 8.12.

Rupturing was observed to be more common using multiphoton microscopy as opposed to single photon confocal microscopy, although vesicle lysis still occurred in the single photon case. Also, the likelihood of rupture increased with increasing laser power: this meant that a compromise had to be met between laser power and fluorescence signal due to the probability of vesicle rupture as well as the usual problem of photobleaching of the fluorophore.

The regularity of vesicle rupture also appeared to be dependent on the phase of the vesicle. Rupture appeared to be more likely at temperatures below the liquidus curve of the phase diagram although lysis was still observed when vesicles were in the fluid phase. Experimental determination of the lysis tension of POPC/DPPC vesicles by micropipette aspiration show that this critical tension decreases by 20-40 % in the L_α-gel coexistence regime compared to L_α vesicles [201]. Vesicle rupture also occurred for vesicles containing the charged lipids DPPA and DPPS although images of this are not shown in figure 8.12. The addition of anionic lipids POPG and POPA has been shown to decrease the lysis tension of POPC vesicles, with the addition of 30 % anionic lipid causing a drop in the lysis tension of 75 %; this drop can be modelled by electrostatic interactions within the membrane [202].

Generally the vesicle ruptured rapidly. If we consider figure 8.12f, the vesicle goes from being spherical to disappearing in the time it takes to scan of order 10 lines[5] (the image is being scanned line by line from top to bottom at a rate of 500 lines per second). The membrane collapses back toward the lipid bulk on the platinum electrode. Other images, particularly figure 8.12b-d, show regions of the membrane becoming flatter as the vesicle ruptures and the membrane collapses back to the lipid bulk. Figure 8.12e shows that initially there is a higher fluorescence background from the aqueous environment enclosed within the vesicle (probably due to the formation of some vesicles/aggregates of sub-optical diameters), as the membrane ruptures this fluorescence is seen to be rapidly rushing out of the bottom right of the vesicle, possibly implying that an excess pressure from the aqueous environment within the vesicle

[5]It should be noted that the vesicle never looked like the image in 8.12II, the vesicle ruptured during scanning from top to bottom.

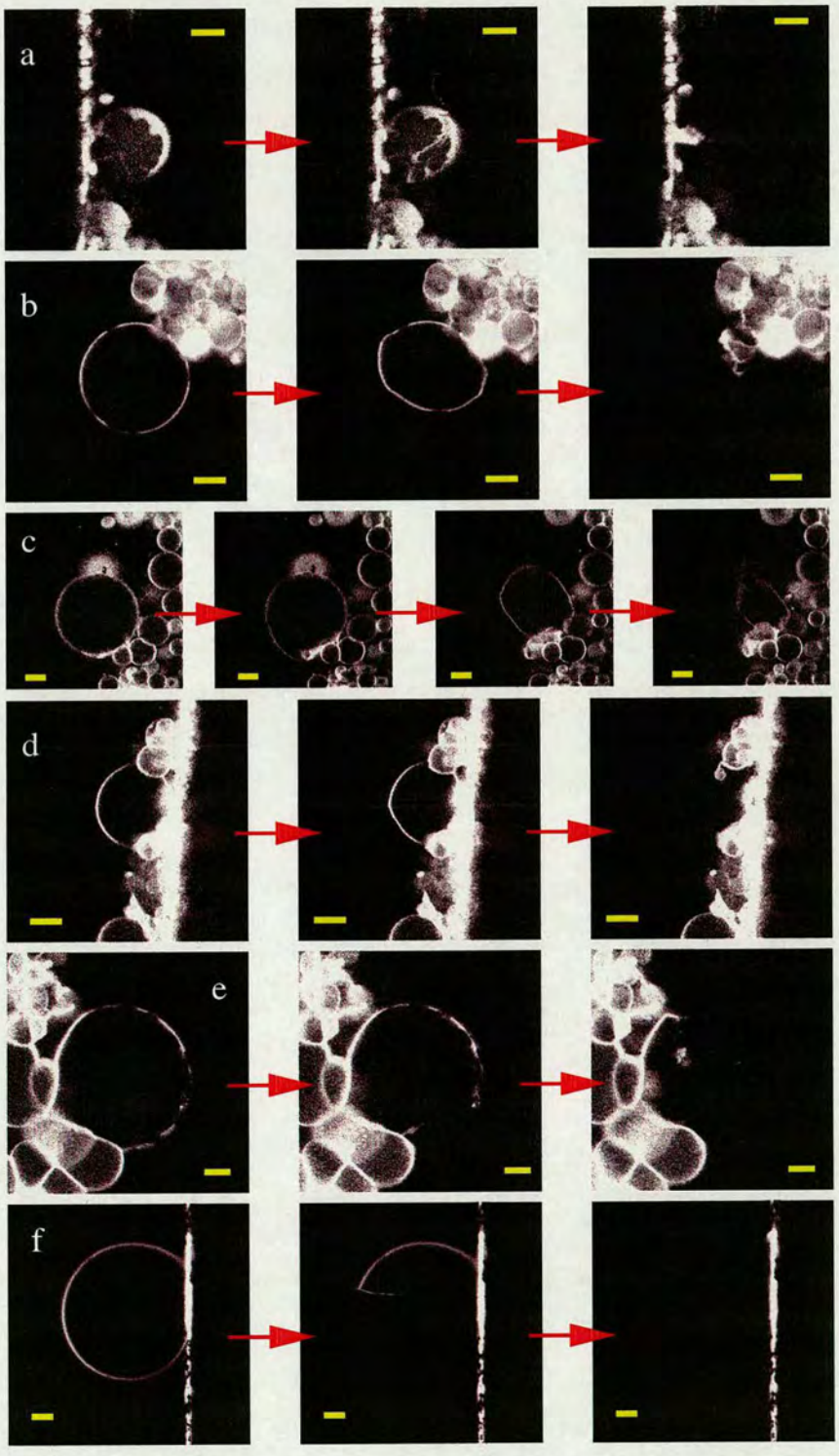

Figure 8.12: Image slices as a vesicle ruptures: (a) 1:3 DPPC:DPPE, (b)–(d) 1:3 DPPC:DPPE, (e) 1:1 DPPC:DPPE, (f) DPPE only. Temperatures: (a) 54.7 °C; (b) 43.9 °C; (c) 45.3 °C; (d) 44.9 °C; (e) 59.7 °C; (f) 64.8 °C. The time between images is approximately two seconds. Scale bars represent 10 μm.

causes it to rupture. The failure of the membrane then allows the pressure difference to be reduced as the internal fluid forces its way through the tear that has appeared. As the fluid rushes out of the vesicle, the membrane rapidly collapses back to the lipid bulk to which the vesicle adheres.

The fact that simply imaging the vesicles causes them to rupture may appear to be surprising but other authors have published observations of light increasing the membrane tension in vesicles [200,203–205]. As the membrane tension is increased, it becomes stretched according to its area compression modulus, K_A (see section 3.1.1). Lipid membranes tend to rupture when they are stretched by about $2-5$ %; this corresponds to a membrane tension of around $0.01\ \mathrm{Jm}^{-2}$ [36].

As the membrane is stretched, pores appear in the membrane which open up to allow the membrane to return to its equilibrium density (area per headgroup). If we consider the model in Boal [36], a hole of radius R forms as the system acts to minimise the enthalpy, H, (at zero temperature):

$$H = E - \tau A\,. \tag{8.1}$$

Here τ is the tension and A is an area. The energy cost to create a hole of radius R in the membrane is $2\pi R\lambda$ (see section 3.1.3). The area difference between the membrane and the membrane with a hole of radius R is simply πR^2 and so the enthalpy difference between an intact membrane and the membrane with a hole in it is:

$$\Delta H = 2\pi R\lambda - \tau\pi R^2\,. \tag{8.2}$$

For small R, ΔH increases due to the linear term dominating but at large R, the quadratic term dominates with ΔH becoming increasingly negative with increasing R. Figure 8.13 displays a schematic graph of ΔH as a function of R. This function reaches a maximum at a critical hole radius[6] of $R^* = \frac{\lambda}{\tau}$. Holes with radius $R < R^*$ will shrink whereas holes with a radius $R > R^*$ will continue to get larger, i.e. the vesicle will rupture completely. This model for R^* also tells

[6]It should be noted that there is an error in Boal as the critical radius is quoted as $R^* = \frac{\tau}{\lambda}$ [36].

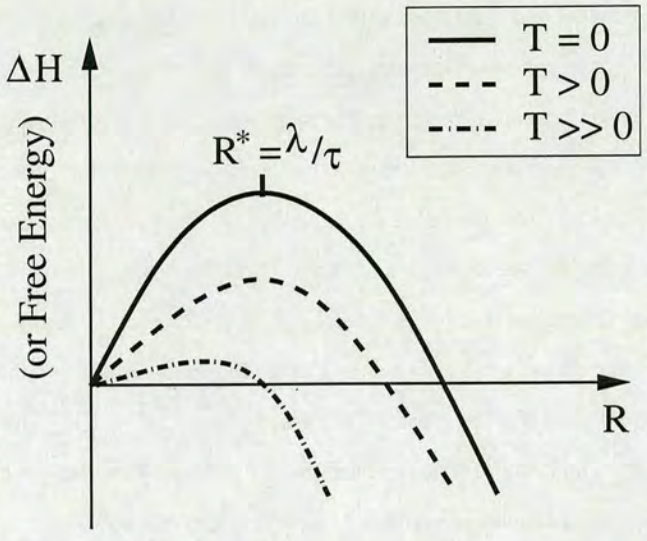

Figure 8.13: Schematic graph of the model for the enthalpy of hole formation in a membrane. The enthalpy change is modelled as $\Delta H = 2\pi R\lambda - \tau\pi R^2$ (*see text*). The critical radius above which the hole size will continue to grow (i.e. the point of vesicle lysis) is denoted R^*. The effect of increasing temperature on the height of the energy barrier is also shown where now the vertical axis should be labelled 'free energy' [36].

us that (assuming that the line tension λ is a constant value for our lipid membranes) as the tension in the membrane increases, the smaller the critical hole size becomes for the vesicle to completely rupture. For a rupture tension of 0.01 Jm^{-2} and an estimate for the line tension of 10^{-11} Jm^{-1} (see section 3.1.3), this predicts a critical hole size of order 1 nm, which is well below optical resolution and so it is not expected that I would be able to image metastable pore formation in the vesicles which I image.

This simple model predicts, at zero temperature, small metastable holes which need to cross an energy barrier of $\frac{\pi\lambda^2}{\tau}$ for the membrane to rupture. As temperature is increased, thermal energy from the environment increase the probability of small holes gaining the energy to cross this energy barrier and also entropy lowers the height of the energy barrier which needs to be overcome (see figure 8.13 where free energy rather than enthalpy change is represented by the vertical axis).

The opening and closing of membrane pores has been observed in lipid membranes using fluorescence microscopy [203, 204]. The opening of the pores is driven by the membrane

tension. When the pore opens, the fluid from within the vesicle is forced through the pore driven by the difference in Laplace pressure between the interior and exterior vesicle environments. As the interior medium exits through the pore, the membrane tension is reduced and the pore closes up driven by line tension. In a low viscosity medium such as water, these pores do not reach sizes which are optically resolvable; if the experiment is instead carried out in a viscous glycerol/water solution, the rate of leakage and hence loss of tension is reduced allowing the pores to reach sizes of several microns in diameter and therefore could be observed under a fluorescence microscope. These large pores do not contradict our simple model for a critical pore radius since the estimated surface tensions of these vesicles are $\sim 10^{-6}$ Jm^{-2} [200, 203], giving an $R^* \approx 10$ μm. Only one pore was observed at a time as transient pores opened and closed in tensed vesicle membranes. The rates of opening and closing of these pores agreed with the predicted model [203].

Among the methods that were found to increase the membrane tension and induce the appearance of pores were the adhesion of vesicles to substrates (see previous section) [203] and constant illumination by a light source [203, 204]. The light source used in these experiments was a 200 W mercury lamp, the occurrence of pores was observed to be more frequent as the light intensity was increased [204]. This is in agreement with my observation that vesicle rupture occurred much more commonly using multiphoton observation than single photon excitation since the peak illumination intensity in multiphoton is much greater. The occurrence of vesicle lysis rather than transient pores due to illumination in my experiments is probably due to the increased laser power used in multiphoton excitation, the adhesion of the vesicles to neighbouring membranes further increasing the tension and also the vesicles are already observed to be under tension after the electroformation process.

The mechanism by which light increases the membrane tension is unknown although Karatekin *et al.* speculate it could be due to lipid loss [204]. Another method of pore formation in lipid vesicles is electroporation where pore formation is induced by an intense electric field [104, 105, 206, 207]. It is not inconceivable to me that these two phenomena are linked: the electric field vector of the incident light induces a tension, and hence pore formation, in the membrane by a similar mechanism to that which causes pore formation by an electric field in electroporation. Electric fields have also been shown to interact with lipid membranes in other,

so far unexplained, ways, i.e. electroformation (see section 4.2).

8.6 Summary

In this chapter I have summarised some experimental results from systems which were not studied in detail and also I have discussed experimental observations which have not been discussed in previous chapters. Many of my attempted explanations of the observed phenomena are speculative and qualitative in nature.

Firstly I examined the behaviour of single component behaviour of DPPC and DPPE vesicles. DPPC vesicles were not seen to have any inhomogeneous fluorophore partitioning indicating a highly cooperative main transition with no detectable coexistence of L_α and $P_{\beta'}$ phases. On the other hand, the Rh-DPPE was seen to partition between two phases during the L_α to L_β transition in DPPE vesicles. Stripe domains formed which were seen to wiggle on the membrane surface. I argue that this could signify an intermediate phase within the $L_\alpha \rightarrow L_\beta$ transition. This phase could be analogous to the ripple phase which has been observed for DPPE at higher pH but without the long range molecular packing predicted for DPPC-rich $P_{\beta'}$ domains seen in DLPC/DPPC vesicles.

In DPPC/DPPA membranes, domains were seen to preferentially nucleate in regions of the membrane which were adhering to other vesicles. It was not possible to resolve whether the small domains formed were circular of angular in nature. Electroformation of DPPG/DPPE GUVs was not found to be possible for 1:3 and 1:1 DPPG:DPPE compositions.

Adjacent vesicles were observed to adhere to each other. The degree of adhesion could be qualitatively analysed by considering the attractive van der Waals interaction, the steric repulsion due to thermal fluctuations within the membrane and the energy required to bend the membrane due to its bending rigidity and surface tension. If a situation were observed where a vesicle was only adhering to one other vesicle membrane then it would be possible to make estimates of the energy of adhesion and the surface tension of the vesicle from the data collected.

Finally, I discussed vesicle lysis. Vesicles were seen to rupture whilst being imaged. This could be thought of as an increase in membrane tension caused by the incident illumination.

Increased membrane tension causes pores to form within the membrane so that the interior aqueous medium can leak out to reduce the tension. If these pores exceed a critical radius, they continue to grow without bound causing the vesicle to permanently rupture.

Chapter 9

Conclusions

This chapter summarises the results reported in this thesis on the optical study of phase separation in binary lipid GUVs.

When binary DPPC/DPPE vesicles are cooled through the region of fluid-gel coexistence, observed gel fractions do not agree with the equilibrium predictions obtained using the lever rule on the published phase diagrams. A non-equilibrium mechanism of domain growth is proposed which we term 'tree ring' growth. The lipid diffusion in the gel phase was shown to be slower than the rate of growth of the gel domain, therefore the gel domains were unable to rearrange their overall composition to the equilibrium value determined by the solidus curve. This means that the gel phase is unable to remain in equilibrium with the fluid phase and hence, on further cooling, the fluid phase behaves like an isolated system and phase separates so that a gel phase of a different composition is deposited on the outside of the existent gel domains. This process continues on cooling to give gel domains made up of compositionally different rings. The predictions of the 'tree ring' model provide a much better fit to my experimental data. The equilibrium phase diagrams, mainly produced by DSC on multi-lamellar vesicles, are probably not affected by this non-equilibrium domain growth since the system size is approximately two orders of magnitude smaller than the GUVs studied in this thesis.

On cooling into the gel-fluid coexistence region of the phase diagram, small, circular, moving gel domains appear in DPPC/DPPE membranes. These domains appear to move in convection

currents within the gel phase with velocities of a few microns per second. The domains behave viscoelastically: bouncing off each other or sticking together to form more complicated domain shapes that cannot rearrange to a circular morphology due to the slow diffusion constant of the gel phase. These gel domains do not form flat facets as has been predicted by some theorists but rather follow the native curvature of the vesicle.

Vesicles were observed composed of 3:1 DPPC:DPPS during cooling through the gel-fluid coexistence regime. The domains formed were polygonal, often hexagonal, with angles quantised close to 120 °. Results from other workers in our research group have shown that binary vesicles which grow a $P_{\beta'}$ gel in the coexistence regime exhibit domains with a stripe morphology where the stripes have been observed to bend at angles quantised about 60 °and 120 °.

A one-to-one correlation between the gel phase structure and the domain morphology has been observed. Vesicles which grow L_{β} domains (for example, DPPC/DPPE) have circular gel domains, the $L_{\beta'}$ gel (for example, 3:1 DPPC:DPPS) leads to polygonal domains and the $P_{\beta'}$ phase gives rise to stripe domain shapes. This can be understood by considering the molecular structure of these domains. No long-range ($\sim$ micron) order has been reported for the L_{β} phase, hence the domains are isotropic and a circular morphology would be expected. Long-range (hundreds of nanometres or more) order has however been reported for the $L_{\beta'}$ phase. The long-range correlation of the hexagonally packed lipids leads to growth of two-dimensional crystals with angles of $\sim$ 120 °. Finally, the $P_{\beta'}$ phase has a directional anisotropy due to the ripples in the bilayer plane. This leads to a preferred direction of growth, and hence stripes. Long range ordering has also been seen in the $P_{\beta'}$ phase with the stripes bending at quantised angles around 60 °and 120 °, a signature of the underlying hexagonal packing of the lipids.

When observing DPPC and DPPE single component vesicles, DPPC vesicles did not exhibit any optically resolvable domains in agreement with the highly cooperative phase transition described in the literature, but domains were observed when cooling through the main transition temperature of DPPE vesicles. These domains were stripes but also wiggled around on the vesicle surface. The DPPE stripe domains also broadened on ripening. A complicated $L_{\alpha} \rightarrow L_{\beta}$ transition with possible intermediate state(s)has been reported in the literature for DPPE. Using the argument that domain morphology reflects the underlying molecular structure of the

phase, this intermediate state in the $L_\alpha \rightarrow L_\beta$ transition would be expected to have directional anisotropy in the bilayer plane (similar to the $P_{\beta'}$ domains) but no long-range ordering due to their wiggly nature of the stripes. The DPPE bilayer could be trying to access the $P_{\beta'}$ phase which appears at higher pH within its phase diagram.

DPPC/DPPA membranes nucleated either circular or polygonal domains (the domain sizes were too small to resolve this) which preferentially formed at adhesion points between vesicles. The electroformation of DPPG/DPPE membranes was found not to be possible for compositions of 1:3 and 1:1 DPPG:DPPE.

Adjacent vesicles were observed to adhere to each other. This adhesion was stronger below the main transition temperature where vesicles were often seen to flatten against each other to form a foamy texture. Finally, vesicles often ruptured whilst being imaged. This was at least partly due to the light used to excite the fluorophores increasing the tension within the membrane to beyond the lysis tension of the vesicle.

9.1 Future Work

Here I will briefly outline further experiments that could be undertaken to further scientific knowledge of the phase separation in lipid GUVs.

9.1.1 What limits domain size in DPPC/DPPE GUVs?

In section 7.1 I suggest three possible mechanisms that may limit the size of the gel phase domains in DPPC/DPPE vesicles. Here I will suggest experiments that may help discriminate between these three mechanisms.

Electrostatic Repulsion

The addition of salt to the aqueous environment would decrease the Debye length (see section 3.1.4), shielding repulsive charges from one another. An increase in maximum domain size with increasing salt concentration would suggest that electrostatic repulsion between headgroup dipoles played a role in limiting domain size. However, the addition of salt would only

shield electrostatic interactions that are mediated through the aqueous environment. If the repulsion was transmitted through the hydrocarbon tails, which are of lower dielectric constant than water, the addition of salt would not affect the maximum domain size. Therefore, a null result of finding that the addition of salt does not affect the maximum domain size is not conclusive evidence that electrostatic repulsion is not the size-limiting mechanism. Finding, or even designing, an ionic molecule that would preferentially partition into the hydrocarbon region of gel phase domains would be a very challenging, maybe not far from impossible, task.

Bending Energy of Gel Domains

My initial observations as to whether the radius of curvature of the vesicle affects the maximum size of the domains were inconclusive. A smaller maximum domain size with a smaller radius of curvature would indicate that the bending energy of the gel phase is a factor in limiting the size of the domains. A greater number of observations than I have currently made would be needed to improve the statistics in order to draw any firm conclusions. One problem with the current experimental set-up could be that I have no control over the tension in the membrane. This could be remedied by using micropipette aspiration of the vesicles. Vesicle aspiration would give control over the membrane tension as well as a small amount of control over the radius of curvature of the vesicle. Micropipette aspiration could generally be a good technique to use to study the phase separation in isolated lipid vesicles where there are no inter-membrane interactions between adjacent vesicles as there are in my experiments.

Internal Tension due to 'Tree Ring' Growth

To investigate whether internal tension due to the non-equilibrium 'tree ring' growth limits the domain size, it would be necessary to devise an experiment that would allow one to alter the size of each 'ring of the tree' such that the number of internal interfacial rings per domain could be altered. My experiments have been in a cooling regime that is in the limit of a large number of 'tree rings' (see section 6.3). To decrease the number of 'tree rings', several rapid temperature quenches through the gel-fluid coexistence region could be used where domains are allowed to stop growing after each quench. This would increase the 'tree ring' step size through the two phase region. Such rapid quenches are not experimentally accessible with my current formation chambers since quench rates of up to several °C/s may be necessary.

A new observation chamber would need to be designed and built in order to carry out these experiments. If these experiments, which reduce the number of 'tree rings', result in a greater maximum domain size then it can be concluded that the internal domain tension due to the non-equilibrium domain growth is a factor in limiting domain size.

9.1.2 Other Avenues of Investigation

There are many more possible directions for experimental work to proceed based around results and observations within this thesis. I summarise a selection of possibilities below:

- **Domain interactions in systems containing charged lipids**. The interaction of moving gel domains in DPPC/DPPS and DPPC/DPPA vesicles was not investigated in the detail that it was for DPPC/DPPE membranes. The addition of lipids with a net charge per headgroup (as opposed to the zwitterionic DPPE) may affect the interaction between gel domains due to electrostatic effects. This could be investigated by taking time series of the poles of vesicles as they are slowly cooled through the two phase region. The pH of the aqueous environment could be used to 'tune' the charge per headgroup of the lipids.

- **'Tree ring' growth in systems other than DPPC/DPPE**. Other binary lipid systems could be studied by the methods of chapter 6 in order to provide evidence that 'tree ring' domain growth is a universal phenomenon for the growth of gel domains in binary lipid GUVs with any phospholipid constituents.

- **Gel phase structures of binary membranes**. All the X-ray diffraction data in the literature for gel phase structures is for single component lipid membranes. It would be useful to undertake X-ray diffraction measurements on binary lipid bilayers in the gel phase to obtain information on their structures. This would provide firm evidence of the gel phases I presume for the binary mixtures in chapter 7. Work still needs to be done on the structure of single component membranes too: for instance, resolving whether the molecular packing in the L_β phase of DPPE is polycrystalline or hexatic, and confirmation of whether the structure of the $P_{\beta'}$ phase of DPPC agrees with the simulations of de Vries *et al.* [20].

- **Faster cooling rates**. Brief observations of non-circular domain growth in a fast cooling regime for DPPC/DPPE vesicles was reported in section 7.1. This could be investigated by intentionally imaging the growth of domains in these faster cooling regimes; my current observations are from experiments where the cooling rate was not controlled properly.

- **The addition of cholesterol**. Ternary vesicles of two saturated phosphatidylcholines and cholesterol or a saturated PC, an unsaturated PC and cholesterol have been studied in the literature. However there are few reports of ternary systems of two phospholipids with different headgroups and cholesterol; the study of cholesterol with phospholipids with different headgroups by Wang and Silvius reports bulk fluorescence measurements but no optically resolved data similar to the images presented in this thesis [208]. The addition of cholesterol adds a liquid-ordered phase (L_o) to the phase diagram and so liquid-liquid[1] phase separation can be studied as opposed to the liquid-solid phase separation reported in this thesis. The effect of headgroup structure on the partitioning of cholesterol could be of biological interest although this affect may be small since cholesterol sits mainly in the hydrophobic region of the bilayer with only a small hydrophilic hydroxyl group. It may be possible to study liquid-liquid phase separation in binary lipid mixtures since a maximum in the fluidus curve has been reported by DSC for some binary mixtures at certain pHs, for instance DMPA:DPPC at pH 4.0 [195].

- **Phase diagrams that consider the effect of different gel phase structures on their topology**. Phase diagrams do exist that consider the affect of different gel phases. However, these are the exceptions. Most binary lipid phase diagrams published in the literature still do not take this into account. Phase diagrams should be constructed, for systems under study, where this is taken into consideration. This may require a combination of techniques such as DSC, X-ray diffraction and NMR.

- **Different lipid classes**. In this thesis I investigate phospholipids with different headgroups and saturated acyl chains. Binary lipid mixtures could be studied where one or both of the lipids have a different structure, for instance lipids with one or more unsat-

[1] This is, more precisely, a L_o-L_d phase separation, where L_d is analogous to the L_α phase.

urated chain, lipids whose two saturated chains are of different length, lipids with alkyl chains, lipids with a sphingoid backbone and single-chain lipids. These lipids could provide different phases and properties, which haven't been observed in this thesis, that result in rich and interesting new phenomena.

- **Diffusion constants in lipid gel phases**. It became clear in section 6.4 that published lipid diffusion constants for gel phases are currently unsatisfactory. The diffusion constant became important in my discussion of 'tree ring' domain growth (section 6.4) and the viscoelastic behaviour of gel domains (section 7.1). Reported diffusion constants for fluid-like phases appear to be satisfactory but the addition of perturbing probes to study the diffusion in solid-like gel phases results in reported diffusion constants which vary over many orders of magnitude. It would be desirable to design an experimental technique that could be used to measure the long-time diffusion in lipid bilayers without the addition of probe molecules. I have no suggestions on how to resolve this at present but this should be considered as a matter that deserves some thought by the lipid community.

The above experiments relate directly to matters involved in studying phase separation in lipid membranes. Other experimental projects of interest to observations in this thesis could involve investigations into the mechanism of electroformation, vesicle lysis and vesicle adhesion, i.e. the interactions between lipid bilayers.

9.2 Final Remarks

This thesis investigates phase separation in binary lipid vesicles. I hope the observations contained within provide new results which are of interest to members of the lipid and soft matter communities. I also hope to have highlighted some areas of the lipid literature which possibly require more thought and research. Finally, I hope the reader has found this thesis both interesting and stimulating.

Appendix A

IDL Programs

This section contains the code for IDL programs written by myself to analyse the digital images of vesicles obtained from confocal and multiphoton fluorescence microscopy experiments.

A.1 Histogram of Pixel Intensities

The program *histdatafit2.pro* analyses the intensity histogram of a vesicle and fits the data to a model of the sum of two Gaussian curves:

```
; This program makes a histogram of pixel intensities of a vesicle image.
; The binsize of the histogram can be varied and the histogram can be
; fitted to the sum of two Gaussian curves.
;
; written by Paul Beales, 2003.
;
; Vesicle diameter (in microns), the pixel defining the centre of the
; vesicle (ith and jth directions) and pixel size in microns need to be
; given in the command line.
;
; The image file analysed needs to be in PPM format.
;
; OPTIONAL PARAMETERS:
; bins specifies the binsize for data in the histogram. Default is 1. Bins must be
;  specified if curve fitting is being used.
; a0,...,a5 are initial estimates for the curve fitting parameters. If these are not
```

```
;  specified then the program will not try to curve fit the histogram data.
; a0,a3 are the max heights of the 2 Gaussians
; a1,a4 are the locations of the centres of the Gaussian maxima
; a2,a5 are the widths at half height of the two Gaussians
;
; NOTE: dualgauss.pro needs to be compiled.
;
pro histdatafit2, filename, diameter, centre_i, centre_j, PixelSize, bins, a0,a1,a2,a3,a4,a5
;
; set colour table to black/white greyscale
device, decomposed=0
loadct,0
;

; Read in vesicle image.
READ_PPM, filename, myimage
window,11
tvscl,myimage
;myimage = median(myimage,5)
;
;convert imported parameters to high precision
;so that no information is lost in calculations
myimage = Long64(myimage)
centre_i = Long64(centre_i)
centre_j = Long64(centre_j)
PixelSize = double(PixelSize)
diameter = double(diameter)
radius = diameter / 2.0
;
; set the binsize if this is specified from the command line
IF N_PARAMS() GE 6 THEN mybins = bins ELSE mybins = 1
;
; display the image file under analysis
window, 12
tvscl,myimage
;
; make a 2D array the same size as the image array.
; Set all components to zero.
; This will act as a marker for pixels inside the vesicle
location = myimage
location(*) = 0
;
; Create counter array for pixel intensities 0 to 255
```

```
y2 = LON64ARR(256)
;
; go through each pixel
; if it is within 95% of radius
; add one to the y2 array of the relevant intensity
N = n_elements(myimage(*,1))
M = n_elements(myimage(1,*))
fraction = double(1.0)  ; change the proportion of vesicle radius here
FOR I=0,N-1 DO BEGIN
FOR J=0,M-1 DO BEGIN
IF PixelSize * (SQRT((I-centre_i) * (I-centre_i) + (J-centre_j) * (J-centre_j))) LT $
(fraction * radius) THEN BEGIN
location[I,J]=100  ; mark this pixel as relevant
y2(myimage[I,J]) = y2(myimage[I,J]) + 1
;
;  draw histogram of intensity against frequency for area of interest
;
ENDIF
ENDFOR
ENDFOR
;
; display the image file with the area considered shaded brighter
z=myimage+location
window,9
tvscl,z
;
; create a histogram data set of the relevant pixels
; using the specified binsize
W = where(location eq 100)
hist = histogram(myimage(W),binsize=mybins)
binvals = FINDGEN(N_ELEMENTS(hist))*mybins + MIN(myimage(W))
; display the histogram of intensity against frequency
window, 10
plot, binvals, hist, YRANGE = [MIN(hist)-1, MAX(hist)+1], PSYM = 10, $
XTITLE = 'Intensity', YTITLE = 'Frequency',background=255,color=0, $
title='Frequency Histogram of Pixel Intensities.'
;
; Curve fitting
;
IF N_PARAMS() GE 7 THEN BEGIN
;
; Create an array of the intensity data of the histogram (x)
x = L64INDGEN(256/mybins)
```

```
x = mybins * x + (mybins-1.0)/2.0
;
; Create an array of corresponding y values
; Set these to one so that the weights function
; does not blow up.
y = LON64ARR(256/mybins)
y(*) = 1
FOR n=0,(256.0/mybins)-1 DO BEGIN
FOR counter=0,mybins-1 DO BEGIN
y(n) = y(n) + y2(mybins*n+counter)
ENDFOR
ENDFOR
;
; create an array of estimated curve fitting parameters
A = [a0,a1,a2,a3,a4,a5]
A = double(A)
weights = 1.0 / y ; specify the weights fn for CURVEFIT
y = y - 1 ; subtract the initial value of 1
;
; Fit the curve to two Gaussians using CURVEFIT method
yfit = CURVEFIT(x,y,weights,A,SIGMA,CHISQ = chi,/double,FUNCTION_NAME='dualgauss',$
ITER = iterations,YERROR = errorstd)
;
; change colour table
; plot fitted curve over histogram in red
loadct,4
OPLOT, x, yfit, Color=150, thick = 2
;
; produce individual Gaussians from fitted parameters
z1 = (A[1] - x) / (A[2]/2.0)
z2 = (A[4] - x) / (A[5]/2.0)
ez1 = EXP(-ALOG(2.0) * z1^2.0)
ez2 = EXP(-ALOG(2.0) * z2^2.0)
gauss1 = A[0] * ez1
gauss2 = A[3] * ez2
;
; Plot the two Gaussians separately over histogram
; in blue dashed lines.
OPLOT, x, gauss1, Color=50, linestyle=2, thick = 2
OPLOT, x, gauss2, Color=50, linestyle=2, thick =2
;
; Print to screen the no. of iterations used, the chi squared
; value, the error in Y and the fitted parameters A.
```

```
print, 'iterations: ', iterations
print, 'CHISQ: ', chi
print, 'YERROR: ', errorstd
print, A
ENDIF
;
; return the colour table to grey scale
; and end the program.
loadct,0
end
```

The program *dualgauss.pro* (below) needs to be compiled with *histdatafit2.pro* as this is called on to fit the Gaussian functions:

```
; For use with histdatafit.pro
;
; For fitting data to the sum of two Gaussian curves.
;
; written by Paul Beales, 2003.
;
PRO dualgauss, X, A, F, pder
z1 = (A[1] - X) / (A[2]/2.0)
z2 = (A[4] - X) / (A[5]/2.0)
ez1 = EXP(-ALOG(2.0) * z1^2.0)
ez2 = EXP(-ALOG(2.0) * z2^2.0)
F = A[0] * ez1 + A[3] * ez2
;
; partial derivatives
;
IF N_PARAMS() GE 4 THEN $
pder = [[ez1], [-4.0 * ALOG(2.0) * (A[0]/A[2]) * z1 * ez1], [2.0 * ALOG(2.0) * $
(A[0]/A[2]) * z1^2.0 * ez1], [ez2], [-4.0 * ALOG(2.0) * (A[3]/A[5]) * z2 * ez2], $
[2.0 * ALOG(2.0) * (A[3]/A[5]) * z2^2.0 * ez2]]
END
```

A.2 Area Measurements

Several programs were written to measure domain area fractions and hence the mole fraction of the gel phase. These programs are very similar to each other. The program *raft_areas2.pro* is used when a whole hemispherical vesicle with static domains is being analysed:

```
; This program calculates the proportion of raft (dark areas) and
; non-raft (light areas) on the surface of a spherical vesicle.
;
; written by Paul Beales, 2003.
;
; Vesicle diameter (in microns), the pixel defining the centre of the
; vesicle (ith and jth directions), pixel size in microns and a cut-off
; threshold defining a raft/non-raft boundary need to be given in the
; command line.
;
; The image file analysed needs to be in PPM format.
;
; OPTIONAL PARAMETERS:
; an output JPEG file may be specified which saves an image file of a
;  2 tone output of raft and non-raft areas within the area considered.
;
; NOTE: Arclength.pro also needs to be compiled.
;
pro raft_areas2, filename, diameter, centre_i, centre_j, Pixel, threshold, outfile
;
; set colour table to black/white greyscale
device, decomposed=0
loadct,0
;
; Read in vesicle image.
READ_PPM, filename, myimage
;
; Display image
window,3
tvscl, myimage
;
; Make image copies that will be manipulated
copy = myimage
copy2 = myimage
copy2(*) = 0

myimage = median(myimage,5)
window,2
tvscl,myimage
;
; specify the common variables in the group share that will be
; exported to Arclength.pro
common share,r2,Y,PixelSize
```

```
;
; Put parameters to high precision so that no information is lost
; in the calculation.
PixelSize= double(Pixel)
myimage = Long(myimage)
centre_i = Long(centre_i)
centre_j = Long(centre_j)
diameter = double(diameter)
;
; Set up variables
no_rafts=double(0.0)
rafts=double(0.0)
radius = double(diameter / 2.0)
r2 = double(radius * radius)
fluid = 0.65 ; area per headgroup of fluid phase lipid (nm^2)
gel = 0.42 ; area per headgroup of gel phase lipid (nm^2)
head_group_ratio = gel / fluid
;
; get size of image array
N = n_elements(myimage(*,1))
M = n_elements(myimage(1,*))
fraction = double(0.95)   ; change proportion of radius considered here
;
; go through each pixel
; if it is within a given fraction of radius
; then decide if it's raft or not
;
FOR I=0,(N-1) DO BEGIN
FOR J=0,(M-1) DO BEGIN ; N,M are size of bitmap array
X2 = double((I-centre_i) * PixelSize * (I-centre_i) * PixelSize)
Y2 = double((J-centre_j) * PixelSize * (J-centre_j) * PixelSize)
IF SQRT(X2 + Y2) LT (fraction * radius) THEN BEGIN
copy(I,J) = copy(I,J) + 50 ; shade area considered so that its brighter
X = double(SQRT(X2))
Y = double(SQRT(Y2))
;
; integrate area of pixel between +/- half pixel size
AREA = abs(radius * QROMB('ArcLength',X-(PixelSize/2.0),X+(PixelSize/2.0),/double))
;
; decide if this area is raft or not
; then add this area to the relevant counter.
IF myimage(I,J) GT threshold THEN BEGIN
no_rafts=no_rafts + AREA
```

```
copy2(I,J) = 255 ; make 2 Tone image bright at non-raft pixel.
ENDIF ELSE BEGIN
rafts = rafts + AREA
ENDELSE
ENDIF
ENDFOR
ENDFOR
copy2b=REBIN(copy2,N,M) ; this is here so that the 2 tone image can be
; scaled up in size by an integer times N and M
;
; Display the 2 tone image and the original image
window, 4
tvscl, copy2b
window, 5
tvscl, copy
;
; calculate area ratios
raft_ratio = 1 / (1 + ((no_rafts/rafts) * head_group_ratio))
noraft_ratio = 1 / (1 + ((rafts/no_rafts) / head_group_ratio))
;
; Print to screen data on raft areas and ratios
; as well as errors and info to check that the
; result is sensible
Print, 'proportion of molecules in gel phase : ', raft_ratio
Print, 'proportion of molecules in fluid phase : ', noraft_ratio
Print, 'Raft area : ', rafts
Print, 'Non-Raft area : ', no_rafts
TotArea = rafts + no_rafts
Print, 'Total Area : ', TotArea
Hemi = 2*!dpi*r2
Print, 'Area of hemisphere radius a : ', Hemi
AreaProp = (1-cos(asin(fraction)))
Print, 'Area fraction of the hemisphere considered : ', AreaProp
TrueArea = AreaProp * Hemi
Print, 'Total Area should be : ', TrueArea
Print, '% Error in Total Area : ', (abs(TotArea-TrueArea)/TrueArea) * 100
;
; write output JPEG file of copy2b if required.
IF N_PARAMS() GE 7 THEN $
WRITE_JPEG, outfile, copy2b, QUALITY=100, /ORDER
end
```

The program *raft_areas3.pro* is used when analysing static domains on a hemispherical vesicle

where part of the vesicle is obscurred by other vesicles and/or lipid junk. The portion of the vesicle which is analysed can be altered by making slight changes to the code below. Where these changes can be made, there are comments within the code to highlight this to the user:

```
; This program calculates the proportion of raft (dark areas) and
; non-raft (light areas) on the surface of a spherical vesicle.
;
; written by Paul Beales, 2004. Adapted from raft_areas2 so that only
; half or a quadrant of a vesicle is used for measurement.
;
; Vesicle diameter (in microns), the pixel defining the centre of the
; vesicle (ith and jth directions), pixel size in microns and a cut-off
; threshold defining a raft/non-raft boundary need to be given in the
; command line.
;
; The image file analysed needs to be in PPM format.
;
; OPTIONAL PARAMETERS:
; an output JPEG file may be specified which saves an image file of a
;  2 tone output of raft and non-raft areas within the area considered.
;
; NOTE: Arclength.pro also needs to be compiled.
;
pro raft_areas3, filename, diameter, centre_i, centre_j, Pixel, threshold, outfile
;
; set colour table to black/white greyscale
device, decomposed=0
loadct,0
;
; Read in vesicle image.
READ_PPM, filename, myimage
;
; Display image
window,3
tvscl, myimage
;
; Make image copies that will be manipulated
copy = myimage
copy2 = myimage
copy2(*) = 0
;
; specify the common variables in the group share that will be
; exported to Arclength.pro
```

```
common share,r2,Y,PixelSize
;
; Put parameters to high precision so that no information is lost
; in the calculation.
PixelSize= double(Pixel)
myimage = Long(myimage)
centre_i = Long(centre_i)
centre_j = Long(centre_j)
diameter = double(diameter)
;
; Set up variables
no_rafts=double(0.0)
rafts=double(0.0)
radius = double(diameter / 2.0)
r2 = double(radius * radius)
fluid = 0.65 ; area per headgroup of fluid phase lipid (nm^2)
gel = 0.42 ; area per headgroup of gel phase lipid (nm^2)
head_group_ratio = gel / fluid
;
; get size of image array
N = n_elements(myimage(*,1))
M = n_elements(myimage(1,*))
fraction = double(0.95)   ; change proportion of radius considered here
;
; go through each pixel
; if it is within a given fraction of radius
; then decide if it's raft or not
;
FOR I=0,(N-1) DO BEGIN
FOR J=0,(M-1) DO BEGIN ; N,M are size of bitmap array
X2 = double((I-centre_i) * PixelSize * (I-centre_i) * PixelSize)
Y2 = double((J-centre_j) * PixelSize * (J-centre_j) * PixelSize)
IF SQRT(X2 + Y2) LT (fraction * radius) THEN BEGIN
IF (I-centre_i) GE 0 THEN BEGIN ; this line can be changed to define a quadrant
; half or 3/4 of a vesicle in the image. AND/OR operator can be used.
X = double(SQRT(X2))
Y = double(SQRT(Y2))
copy(I,J) = copy(I,J) + 50 ; shade area considered so that its brighter
;
; integrate area of pixel between +/- half pixel size
AREA = abs(radius * QROMB('ArcLength',X-(PixelSize/2.0),X+(PixelSize/2.0),/double))
;
; decide if this area is raft or not
```

```
; then add this area to the relevant counter.
IF myimage(I,J) GT threshold THEN BEGIN
no_rafts=no_rafts + AREA
copy2(I,J) = 255 ; make 2 Tone image bright at non-raft pixel.
ENDIF ELSE BEGIN
rafts = rafts + AREA
ENDELSE
ENDIF
ENDIF
ENDFOR
ENDFOR
copy2b=REBIN(copy2,N,M) ; this is here so that the 2 tone image can be
; scaled up in size by an integer times N and M
;
; Display the 2 tone image and the
window, 4
tvscl, copy2b
window, 5
tvscl, copy
;
; calculate area ratios
raft_ratio = 1 / (1 + ((no_rafts/rafts) * head_group_ratio))
noraft_ratio = 1 / (1 + ((rafts/no_rafts) / head_group_ratio))
;
; Print to screen data on raft areas and ratios
; as well as errors and info to check that the
; result is sensible
Print, 'proportion of molecules in gel phase : ', raft_ratio
Print, 'proportion of molecules in fluid phase : ', noraft_ratio
Print, 'Raft area : ', rafts
Print, 'Non-Raft area : ', no_rafts
TotArea = rafts + no_rafts
Print, 'Total Area : ', TotArea
Hemi = 2*!dpi*r2
Print, 'Area of hemisphere radius R : ', Hemi
AreaProp = 0.5*(1-cos(asin(fraction)))
; extra factor of 0.5 due to measuring half a hemisphere
Print, 'Area fraction of the hemisphere considered : ', AreaProp
TrueArea = AreaProp * Hemi
Print, 'Total Area should be : ', TrueArea
Print, '% Error in Total Area : ', (abs(TotArea-TrueArea)/TrueArea) * 100
;
; write output JPEG file of copy2b if required.
```

```
IF N_PARAMS() GE 7 THEN $
WRITE_JPEG, outfile, copy2b, QUALITY=100, /ORDER
end
```

The program *raft_areas4.pro* is used for when there are moving domains on the vesicle. Individual image slices are analysed rather than a stack of images creating an image of a vesicle hemisphere:

```
; This program calculates the proportion of raft (dark areas) and
; non-raft (light areas) on the surface of a spherical vesicle.
;
; written by Paul Beales, 2004. Adapted from raft_areas2 so that single
; multiphoton sections can be considered for the case of moving domains.
; Hence a statistical average over sections can be attained to give an
; estimate of gel area fraction in vesicles with moving domains.
;
; Vesicle diameter (in microns), the pixel defining the centre of the
; vesicle (ith and jth directions), pixel size in microns and a cut-off
; threshold defining a raft/non-raft boundary need to be given in the
; command line. Also the minimum and maximum radius needs to be given so
; that the ring can be defined for the program to measure over.
;
; The image file analysed needs to be in PPM format.
;
; OPTIONAL PARAMETERS:
; an output JPEG file may be specified which saves an image file of a
;  2 tone output of raft and non-raft areas within the area considered.
;
; NOTE: Arclength.pro also needs to be compiled.
;
pro raft_areas4, filename, diameter, rad_a, rad_b, centre_i, centre_j, Pixel, threshold, outfile
;
; set colour table to black/white greyscale
device, decomposed=0
loadct,0
;
; Read in vesicle image.
READ_PPM, filename, myimage
;
; Display image
window,3
tvscl, myimage
;
```

```
; Make image copies that will be manipulated
copy = myimage
copy2 = myimage
copy2(*) = 0
copy3 = MEDIAN(myimage,5)
window,2
tvscl, copy3
;
; specify the common variables in the group share that will be
; exported to Arclength.pro
common share,r2,Y,PixelSize
;
; Put parameters to high precision so that no information is lost
; in the calculation.
PixelSize= double(Pixel)
myimage = Long(myimage)
centre_i = Long(centre_i)
centre_j = Long(centre_j)
diameter = double(diameter)
;
; Set up variables
no_rafts=double(0.0)
rafts=double(0.0)
radius = double(diameter / 2.0)
r2 = double(radius * radius)
fluid = 0.65 ; area per headgroup of fluid phase lipid (nm^2)
gel = 0.42 ; area per headgroup of gel phase lipid (nm^2)
head_group_ratio = gel / fluid
;
; get size of image array
N = n_elements(myimage(*,1))
M = n_elements(myimage(1,*))
;
; go through each pixel
; if it's between the radii considered
; then decide if it's raft or not.
;
FOR I=0,(N-1) DO BEGIN
FOR J=0,(M-1) DO BEGIN ; N,M are size of bitmap array
X2 = double((I-centre_i) * PixelSize * (I-centre_i) * PixelSize)
Y2 = double((J-centre_j) * PixelSize * (J-centre_j) * PixelSize)
IF SQRT(X2 + Y2) GE rad_a AND SQRT(X2 + Y2) LT rad_b THEN BEGIN
;IF (I-centre_i) LE 0 THEN BEGIN
```

```
copy(I,J) = copy(I,J) + 50 ; shade area considered so that its brighter
X = double(SQRT(X2))
Y = double(SQRT(Y2))
;
; integrate area of pixel between +/- half pixel size
AREA = abs(radius * QROMB('ArcLength',X-(PixelSize/2.0),X+(PixelSize/2.0),/double))
;
; decide if this area is raft or not
; then add this area to the relevant counter.
IF copy3(I,J) GT threshold THEN BEGIN
no_rafts=no_rafts + AREA
copy2(I,J) = 255 ; make 2 Tone image bright at non-raft pixel.
ENDIF ELSE BEGIN
rafts = rafts + AREA
ENDELSE
;ENDIF
ENDIF
ENDFOR
ENDFOR
copy2b=REBIN(copy2,N,M) ; this is here so that the 2 tone image can be
; scaled up in size by an integer times N and M
;
; Display the 2 tone image and the
window, 4
tvscl, copy2b
window, 5
tvscl, copy
;
; calculate area ratios
raft_ratio = 1 / (1 + ((no_rafts/rafts) * head_group_ratio))
noraft_ratio = 1 / (1 + ((rafts/no_rafts) / head_group_ratio))
;
; Print to screen data on raft areas and ratios
; as well as errors and info to check that the
; result is sensible
Print, 'proportion of molecules in gel phase : ', raft_ratio
Print, 'proportion of molecules in fluid phase : ', noraft_ratio
Print, 'Raft area : ', rafts
Print, 'Non-Raft area : ', no_rafts
TotArea = rafts + no_rafts
Print, 'Total Area : ', TotArea
Hemi = 2*!dpi*r2
Print, 'Area of hemisphere radius R : ', Hemi
```

```
Print, 'Proportional of hemisphere considered : ', TotArea/Hemi
InnerAreaProp = (1-cos(asin(rad_a/radius)))
OuterAreaProp = (1-cos(asin(rad_b/radius)))
AreaProp = OuterAreaProp - InnerAreaProp
Print, 'Area fraction of the hemisphere considered : ', AreaProp
TrueArea = AreaProp * Hemi
Print, 'Total Area should be : ', TrueArea
Print, '% Error in Total Area : ', (abs(TotArea-TrueArea)/TrueArea) * 100
;
; write output JPEG file of copy2b if required.
IF N_PARAMS() GE 9 THEN $
WRITE_JPEG, outfile, copy2b, QUALITY=100, /ORDER
end
```

The program *Arclength.pro* needs to be compiled with the above area measurement programs as it is used to solve the area integral for each pixel:

```
; for use with raft_areas2.pro (also later versions 3 & 4)
;
; for use in integrating the area of a pixel on a sphere.
;
; written by Paul Beales, 2003.
;
function ArcLength,Xcoord
common share
return, asin((Y+(PixelSize/2.0))/sqrt(r2-Xcoord^2.0)) - $
asin((Y-(PixelSize/2.0))/sqrt(r2-Xcoord^2.0))
end
```

A.3 Defining Domains

The program *domain_finder2.pro* finds indivdual domains and calculates their area and their centre of mass on the spherical membrane:

```
;
; written by Paul Beales, 2004
;
; domain_finder2 is similar to raft_areas2 at first, finding total domain
; area fractions etc. The 2-tone image of the vesicle is negative to that
; created in raft_areas2 and is used to isolate separate domains. The
; domain_finder program counts up these domains, their number of pixels
```

```
; and calculates the area of each domain (taking into account the spherical
; curvature of the vesicles).
;
;  Vesicle diameter (in microns), the pixel defining the centre of the
;  vesicle (ith and jth directions), pixel size in microns and a cut-off
;  threshold defining a raft/non-raft boundary need to be given in the
;  command line.
;
;  The image file analysed needs to be in PPM format.
;
;  OPTIONAL PARAMETERS:
;  an output JPEG file may be specified which saves an image file of a
;  2 tone output of raft and non-raft areas within the area considered.
;
;  NOTE: Arclength.pro also needs to be compiled.
;
pro domain_finder2, filename, diameter, centre_i, centre_j, Pixel, threshold, outfile
;
; set colour table to black/white greyscale
device, decomposed=0
loadct,0
;
; Read in vesicle image.
READ_PPM, filename, myimage
;
; Display image
window,3
tvscl, myimage


myimage = 0.5 * MEDIAN(myimage,2,/even) + 0.0 * MEDIAN(myimage,3) + $
; 0.2 * MEDIAN(myimage,4,/even) + 0.2 * MEDIAN(myimage,5) + 0.3 * MEDIAN(myimage,6,/even)
0.5 * MEDIAN(myimage,9)
;filter = DIGITAL_FILTER(0,0.9,50,10)
;myimage = CONVOL(myimage,filter)

window,4
tvscl, myimage
;myimage = Smooth(myimage,4)
;
; Make image copies that will be manipulated
copy = myimage
copy2 = myimage
```

```
copy2(*) = 0
;
; specify the common variables in the group share that will be
; exported to Arclength.pro
common share,r2,Y,PixelSize
;
; Put parameters to high precision so that no information is lost
; in the calculation.
PixelSize= double(Pixel)
myimage = Long(myimage)
centre_i = Long(centre_i)
centre_j = Long(centre_j)
diameter = double(diameter)
;
; Set up variables
no_rafts=double(0.0)
rafts=double(0.0)
radius = double(diameter / 2.0)
r2 = double(radius * radius)
fluid = 0.65 ; area per headgroup of fluid phase lipid (nm^2)
gel = 0.42 ; area per headgroup of gel phase lipid (nm^2)
head_group_ratio = gel / fluid
;
; get size of image array
N = n_elements(myimage(*,1))
M = n_elements(myimage(1,*))
fraction = double(0.95)    ; change proportion of radius considered here
;
; go through each pixel
; if it is within a given fraction of radius
; then decide if it's raft or not
;
FOR I=0,(N-1) DO BEGIN
FOR J=0,(M-1) DO BEGIN ; N,M are size of bitmap array
X2 = double((I-centre_i) * PixelSize * (I-centre_i) * PixelSize)
Y2 = double((J-centre_j) * PixelSize * (J-centre_j) * PixelSize)
IF SQRT(X2 + Y2) LT (fraction * radius) THEN BEGIN
copy(I,J) = copy(I,J) + 50 ; shade area considered so that its brighter
X = double(SQRT(X2))
Y = double(SQRT(Y2))
;
; integrate area of pixel between +/- half pixel size
AREA = abs(radius * QROMB('ArcLength',X-(PixelSize/2.0),X+(PixelSize/2.0),/double))
```

```
;
; decide if this area is raft or not
; then add this area to the relevant counter.

; threshold = threshold * (1 + (x2 + y2)/(radius*radius)
IF myimage(I,J) GT threshold THEN BEGIN
no_rafts=no_rafts + AREA

ENDIF ELSE BEGIN
rafts = rafts + AREA
copy2(I,J)=255
ENDELSE
ENDIF
ENDFOR
ENDFOR
;copy2b=REBIN(copy2,N,M) ; this is here so that the 2 tone image can be
; scaled up in size by an integer times N and M
;
; Display the 2 tone image and the

window, 5
tvscl, copy
;
; calculate area ratios
raft_ratio = 1 / (1 + ((no_rafts/rafts) * head_group_ratio))
noraft_ratio = 1 / (1 + ((rafts/no_rafts) / head_group_ratio))
;
; Print to screen data on raft areas and ratios
; as well as errors and info to check that the
; result is sensible
Print, 'proportion of molecules in gel phase : ', raft_ratio
Print, 'proportion of molecules in fluid phase : ', noraft_ratio
Print, 'Raft area : ', rafts
Print, 'Non-Raft area : ', no_rafts
TotArea = rafts + no_rafts
Print, 'Total Area : ', TotArea
Hemi = 2*!dpi*r2
Print, 'Area of hemisphere radius R : ', Hemi
AreaProp = (1-cos(asin(fraction)))
Print, 'Area fraction of the hemisphere considered : ', AreaProp
TrueArea = AreaProp * Hemi
Print, 'Total Area should be : ', TrueArea
```

```
Print, '% Error in Total Area : ', (abs(TotArea-TrueArea)/TrueArea) * 100


; label the individual domains in the image
domain = label_region(copy2)
window,0
loadct,22 ; colourful table to show up different domains
tvscl, domain
loadct,0 ; revert to greyscale
window,1
tvscl, copy2
; Get population and members of each domain:
h = HISTOGRAM(domain)

; Each region
FOR k=1, N_ELEMENTS(h)-1 DO BEGIN
domain_area = 0 ; counter for area of the domain
com_i = 0 ; counter for centre of mass in x direction
com_j = 0 ; counter for centre of mass in y direction

FOR I=0,(N-1) DO BEGIN
FOR J=0,(M-1) DO BEGIN ; N,M are size of bitmap array
IF domain(I,J) eq k THEN BEGIN
X2 = double((I-centre_i) * PixelSize * (I-centre_i) * PixelSize)
Y2 = double((J-centre_j) * PixelSize * (J-centre_j) * PixelSize)
X = double(SQRT(X2))
Y = double(SQRT(Y2))
;
; integrate area of pixel between +/- half pixel size
AREA = abs(radius * QROMB('ArcLength',X-(PixelSize/2.0),X+(PixelSize/2.0),/double))
domain_area = domain_area + AREA

com_i = com_i + (I - centre_i) * PixelSize * AREA
com_j = com_j + (J - centre_j) * PixelSize * AREA

ENDIF
ENDFOR
ENDFOR

;calculate centre of mass coordinates in x,y plane
centre_of_mass_i = com_i / domain_area
centre_of_mass_j = com_j / domain_area
```

```
; label centre of mass of domain with dot on original image
pixel_i = Fix((centre_of_mass_i / PixelSize) + centre_i)
pixel_j = Fix((centre_of_mass_j / PixelSize) + centre_j)
myimage(pixel_i,pixel_j) = 255

; print domain data
PRINT, 'Domain ', k, $
     ', Population = ', h[k], $
      ', Area = ', domain_area, ' microns^2', $
      ', Centre of Domain = (', centre_of_mass_i, ',', centre_of_mass_j, ') microns'


ENDFOR

; show image with centre of masses marked on
window,2
tvscl, myimage
;
; write output JPEG file of copy2b if required.
IF N_PARAMS() GE 7 THEN $
WRITE_JPEG, outfile, copy2, QUALITY=100, /ORDER
end
```

The program *domain_finder3.pro* is a variant of *domain_finder2.pro* which is used when analysing a single image slice (i.e. moving domains) rather than an image stack of a vesicle hemisphere:

```
;
; written by Paul Beales, 2004
;
; domain_finder3 is to domain_finder2 what raft_areas4 is to raft_areas2,
; i.e. isolating domains (number and individual areas) in single image
; slices of a vesicle.
;
; Vesicle diameter (in microns), the pixel defining the centre of the
;  vesicle (ith and jth directions), pixel size in microns and a cut-off
;  threshold defining a raft/non-raft boundary need to be given in the
;  command line. Also the minimum and maximum radius needs to be given so
;  that the ring can be defined for the program to measure over.
;
;  The image file analysed needs to be in PPM format.
;
;  OPTIONAL PARAMETERS:
;  an output JPEG file may be specified which saves an image file of a
```

```
;  2 tone output of raft and non-raft areas within the area considered.
;
;  NOTE: Arclength.pro also needs to be compiled.
;
pro domain_finder3, filename, diameter, rad_a, rad_b, centre_i, centre_j, Pixel, $
threshold, outfile
;
; set colour table to black/white greyscale
device, decomposed=0
loadct,0
;
; Read in vesicle image.
READ_PPM, filename, myimage
;
; Display image
window,3
tvscl, myimage
;
; Make image copies that will be manipulated
copy = myimage
copy2 = myimage
copy2(*) = 0
copy3 = Smooth(myimage,4)
window,2
tvscl, copy3
;
; specify the common variables in the group share that will be
; exported to Arclength.pro
common share,r2,Y,PixelSize
;
; Put parameters to high precision so that no information is lost
; in the calculation.
PixelSize= double(Pixel)
myimage = Long(myimage)
centre_i = Long(centre_i)
centre_j = Long(centre_j)
diameter = double(diameter)
;
; Set up variables
no_rafts=double(0.0)
rafts=double(0.0)
radius = double(diameter / 2.0)
r2 = double(radius * radius)
```

```
fluid = 0.65 ; area per headgroup of fluid phase lipid (nm^2)
gel = 0.42 ; area per headgroup of gel phase lipid (nm^2)
head_group_ratio = gel / fluid
;
; get size of image array
N = n_elements(myimage(*,1))
M = n_elements(myimage(1,*))
;
; go through each pixel
; if it's between the radii considered
; then decide if it's raft or not.
;
FOR I=0,(N-1) DO BEGIN
FOR J=0,(M-1) DO BEGIN ; N,M are size of bitmap array
X2 = double((I-centre_i) * PixelSize * (I-centre_i) * PixelSize)
Y2 = double((J-centre_j) * PixelSize * (J-centre_j) * PixelSize)
IF SQRT(X2 + Y2) GE rad_a AND SQRT(X2 + Y2) LT rad_b THEN BEGIN
;IF (I-centre_i) GE 0 THEN BEGIN
copy(I,J) = copy(I,J) + 50 ; shade area considered so that its brighter
X = double(SQRT(X2))
Y = double(SQRT(Y2))
;
; integrate area of pixel between +/- half pixel size
AREA = abs(radius * QROMB('ArcLength',X-(PixelSize/2.0),X+(PixelSize/2.0),/double))
;
; decide if this area is raft or not
; then add this area to the relevant counter.
IF copy3(I,J) GT threshold THEN BEGIN
no_rafts=no_rafts + AREA
; make 2 Tone image bright at non-raft pixel.
ENDIF ELSE BEGIN
rafts = rafts + AREA
copy2(I,J) = 255
ENDELSE
;ENDIF
ENDIF
ENDFOR
ENDFOR
;copy2b=REBIN(copy2,N,M) ; this is here so that the 2 tone image can be
; scaled up in size by an integer times N and M
;
; Display the 2 tone image and the
;window, 4
```

```
;tvscl, copy2b
window, 5
tvscl, copy
;
; calculate area ratios
raft_ratio = 1 / (1 + ((no_rafts/rafts) * head_group_ratio))
noraft_ratio = 1 / (1 + ((rafts/no_rafts) / head_group_ratio))
;
; Print to screen data on raft areas and ratios
; as well as errors and info to check that the
; result is sensible
Print, 'proportion of molecules in gel phase : ', raft_ratio
Print, 'proportion of molecules in fluid phase : ', noraft_ratio
Print, 'Raft area : ', rafts
Print, 'Non-Raft area : ', no_rafts
TotArea = rafts + no_rafts
Print, 'Total Area : ', TotArea
Hemi = 2*!dpi*r2
Print, 'Area of hemisphere radius R : ', Hemi
Print, 'Proportional of hemisphere considered : ', TotArea/Hemi
InnerAreaProp = (1-cos(asin(rad_a/radius)))
OuterAreaProp = (1-cos(asin(rad_b/radius)))
AreaProp = OuterAreaProp - InnerAreaProp
Print, 'Area fraction of the hemisphere considered : ', AreaProp
TrueArea = AreaProp * Hemi
Print, 'Total Area should be : ', TrueArea
Print, '% Error in Total Area : ', (abs(TotArea-TrueArea)/TrueArea) * 100

myimage2 = copy2 - threshold

for i = 0, (N-1) do begin
for j = 0, (M-1) do begin
if myimage2(I,J) LT 0 then begin
myimage2(I,J) = 0
endif
endfor
endfor
domain = label_region(myimage2)
window,0
tvscl, domain
window,1
tvscl, myimage2
; Get population and members of each blob:
```

```
h = HISTOGRAM(domain)

; Each region
FOR k=1, N_ELEMENTS(h)-1 DO BEGIN
domain_area = 0
com_i = 0
com_j = 0
FOR I=0,(N-1) DO BEGIN
FOR J=0,(M-1) DO BEGIN ; N,M are size of bitmap array
IF domain(I,J) eq k THEN BEGIN
X2 = double((I-centre_i) * PixelSize * (I-centre_i) * PixelSize)
Y2 = double((J-centre_j) * PixelSize * (J-centre_j) * PixelSize)

X = double(SQRT(X2))
Y = double(SQRT(Y2))



;
; integrate area of pixel between +/- half pixel size
AREA = abs(radius * QROMB('ArcLength',X-(PixelSize/2.0),X+(PixelSize/2.0),/double))
domain_area = domain_area + AREA

com_i = com_i + (I - centre_i) * PixelSize * AREA
com_j = com_j + (J - centre_j) * PixelSize * AREA

ENDIF
ENDFOR
ENDFOR

centre_of_mass_i = com_i / domain_area
centre_of_mass_j = com_j / domain_area

pixel_i = Fix((centre_of_mass_i / PixelSize) + centre_i)
pixel_j = Fix((centre_of_mass_j / PixelSize) + centre_j)
myimage(pixel_i,pixel_j) = 255

   PRINT, 'Domain ', k, $
      ', Population = ', h[k], $
      ', Area = ', domain_area, ' microns^2'

ENDFOR

window,2
```

```
tvscl, myimage

;
; write output JPEG file of copy2b if required.
IF N_PARAMS() GE 9 THEN $
WRITE_JPEG, outfile, copy2b, QUALITY=100, /ORDER
end
```

A.4 Distances and Angles

The program *distance.pro* is used to measure the distance (arc length) between two points on a sphere when the two dimensional coordinates of the points on the hemisphere are inputs with the centre of the sphere being the origin:

```
; distance.pro measures the arc length moved along a vesicle
; between two points specified in microns from the centre of
; the vesicle in a 2D projection.
;
; command line needs to contain vesicle diameter (in microns)
; and the 2D cartesian position coordinates of the 2 points on
; the vesicle surface (the centre of the vesicle is the origin
; and units need to be in microns).
;
; written by Paul Beales, 2004
;

pro distance, diameter, x1, y1, x2, y2

radius = diameter / 2.0 ; calculate radius of vesicle
radius2 = radius * radius ; radius squared (used in calculations)

z1 = sqrt(radius2 - x1 * x1 - y1 * y1) ; z coordinate of point 1 by pythagoras
z2 = sqrt(radius2 - x2 * x2 - y2 * y2) ; z coordinate of point 2

theta = acos((x1 * x2 + y1 * y2 + z1 * z2) / radius2)
; take dot product of radial vectors
; to find angle between them

arc_distance = radius * theta ; calculate arc length

print, 'distance moved is ', arc_distance, ' microns'; print result to screen
```

```
end
```

The program *sphere_angle.pro* measures the angle on the surface of a sphere where two lines intersect. The lines are defined by two dimensional coordinates (on a hemispherical vesicle projection) of the apex where the lines meet and another point on each of the lines:

```
;
; Calculate angle on sphere by inputing 3 points from a 2D projection.
;
; Program calculates the two tangential vectors at the apex of the angle.
; Then the angle between these two tangents is calculated.
;
; Input: diameter (microns)
; centre pixel (i^{th} then j^{th} coordinates)
; coordinates of apex
; coordinates of the other two points
; pixel size in microns
;
; Written by Paul Beales, 2004
;

pro sphere_angle, diameter, centre_i, centre_j, xa, ya, xb, yb, xc, yc, pixel

radius = double(diameter / 2.0)
radius2 = double(radius * radius)

; rescale coordinates to microns with the origin
; as the centre of the sphere

xa = double((xa - centre_i) * pixel)
ya = double((ya - centre_j) * pixel)
xb = double((xb - centre_i) * pixel)
yb = double((yb - centre_j) * pixel)
xc = double((xc - centre_i) * pixel)
yc = double((yc - centre_j) * pixel)

; find the z coords for points a,b,c
; on surface of sphere using Pythagoras

za = double(sqrt(radius2 - xa * xa - ya * ya))
zb = double(sqrt(radius2 - xb * xb - yb * yb))
zc = double(sqrt(radius2 - xc * xc - yc * yc))
```

```
; find plane OAB in the form kx + ly + mz = 0
; set k=1 as l,m should scale with this.

k = double(1.0)
m = double(k * (xa * yb - xb * ya) / (zb * ya - yb * za))
l = double(-1 * (m * za + k * xa) / ya)

print, 'plane OAB: kx + ly + mz = 0'
print, 'k = ',k
print, 'l = ',l
print, 'm = ',m

; similarly for plane OAC, in form px + qy + rz = 0, set p=1

p = double(1.0)
r = double(p * (xa * yc - xc * ya) / (zc * ya - yc * za))
q = double(-1 * (r * za + p * xa) / ya)

print, 'plane OAC: px + qy + rz = 0'
print, 'p = ',p
print, 'q = ',q
print, 'r = ',r

; find tangential vector tb.
; first find point pb on tb, since pb.a = r^2

pbx = double(1.0)
pbz = double((l * (xa * pbx - radius2) - k * pbx * ya) / (m * ya - l * za))
pby = double((radius2 - pbx * xa - pbz * za) / ya)

; tb = pb - a

tbx = double(pbx - xa)
tby = double(pby - ya)
tbz = double(pbz - za)

; make sure tb is in same direction as A-B

; find A-B
abx = double(xb - xa)
aby = double(yb - ya)
abz = double(zb - za)
```

```
i=1
while i GE 1 do begin
; find length of A-B and length of tb

ab = double(sqrt(abx * abx + aby * aby + abz * abz))
tb = double(sqrt(tbx * tbx + tby * tby + tbz * tbz))
theta_b = acos((abx*tbx + aby*tby + abz*tbz) / (ab*tb))
theta_b = theta_b * 180 / !dpi
print, 'angle between tb and a-b is ',theta_b

if theta_b GT 90 then begin
tbx = double(-1*tbx)
tby = double(-1*tby)
tbz = double(-1*tbz)
i = i+1
endif else begin
i = 0
endelse

if i GE 3 then begin
print,'think about tangent directions more carefully'
exit
endif

endwhile

; similarly, find tangential vector tc.
; first find point pc on tc, since pc.a = r^2

pcx = double(1.0)
pcz = double((q * (xa * pcx - radius2) - p * pcx * ya) / (r * ya - q * za))
pcy = double((radius2 - pcx * xa - pcz * za) / ya)

; tc = pc - a

tcx = double(pcx - xa)
tcy = DOUBLE(pcy - ya)
tcz = double(pcz - za)

; make sure tc is in same direction as A-C

; find A-B
acx = double(xc - xa)
```

```
acy = double(yc - ya)
acz = double(zc - za)
j=1
while j GE 1 do begin
; find length of A-C and length of tc

ac = double(sqrt(acx * acx + acy * acy + acz * acz))
tc = double(sqrt(tcx * tcx + tcy * tcy + tcz * tcz))
theta_c = acos((acx*tcx + acy*tcy + acz*tcz) / (ac*tc))
theta_c = theta_c * 180 / !dpi
print, 'angle between tc and a-c is ',theta_c

if theta_c GT 90 then begin
tcx = double(-1*tcx)
tcy = double(-1*tcy)
tcz = double(-1*tcz)
j = j+1
endif else begin
j = 0
endelse

if j GE 3 then begin
print,'think about tangent directions more carefully'
exit
endif

endwhile

; angle by vernita's method
THETA2 = double(acos((abx*acx + aby*acy + abz*acz)/(ac*ab)))
THETA2 = double(THETA2*180/!dpi)
print,'a rougher measure of the angle is ',THETA2

; finally find the angle between tc and tb

THETA = double(acos((tbx*tcx + tby*tcy + tbz*tcz)/(tc*tb)))
THETA = double(THETA * 180 / !dpi)
print, 'angle on the sphere is ',THETA

end
```

Bibliography

[1] Singer S.J. and Nicolson G.L. The fluid mosaic model of the structure of cell membranes. *Science*, 175(4023):720–731, 1972.

[2] Korlach J., Schwille P., Webb W.W., and Feigenson G.W. Characterization of lipid bilayer phases by confocal microscopy and fluorescence correlation spectroscopy. *Proceedings of the National Accademy of Sciences, USA*, 96:8461–8466, 1999.

[3] Bagatolli L.A. and Gratton E. Two photon fluorescence microscopy of coexisting lipid domains in giant unilamellar vesicles of binary phospholipid mixtures. *Biophys. J.*, 78:290–305, 2000.

[4] Bagatolli L.A., Parasassi T., and Gratton E. Giant phospholipid vesicles: comparison among the whole lipid sample characteristics using different preparation methods. a two photon fluorescence microscopy study. *Chemistry and Physics of Lipids*, 105:135–147, 2000.

[5] Bagatolli L.A. and Gratton E. A correlation between lipid domain shape and binary phospholipid mixture composition in free standing bilayers: A two-photon fluorescence microscopy study. *Biophysical Journal*, 79:434–447, 2000.

[6] Dietrich C., Bagatolli L.A., Volovyk Z.N., Thompson N. L., Levi M., Jacobson K., and Gratton E. Lipid rafts reconstituted in model membranes. *Biophysical Journal*, 80:1417–1428, 2001.

[7] Feigenson G.W. and Buboltz J.T. Ternary phase diagram of dipalmitoyl-pc/dilauroyl-pc/cholesterol: Nanoscopic domain formation driven by cholesterol. *Biophysical Journal*, 80:2775–2788, 2001.

[8] Veatch S.L. and Keller S.L. Organisation in lipid membranes containing cholesterol. *Physical Review Letters*, 89(26):268101–1 – 268101–4, 2002.

[9] Veatch S.L. and Keller S.L. Separation of liquid phases in giant vesicles of ternary mixtures of phospholipids and cholesterol. *Biophysical Journal*, 85:3074–3083, 2003.

[10] Scherfeld D., Kahya N., and Schwille P. Lipid dynamics and domain formation in model membranes composed of ternary mixtures of unsaturated and saturated phosphatidylcholines and cholesterol. *Biophysical Journal*, 85:3758–3768, 2003.

[11] Baumgart T., Hess S.T., and Webb W.W. Imaging coexisting fluid domains in biomembrane models coupling curvature and line tension. *Nature*, 425:821–824, 2003.

[12] Veatch S.L., Polozov I.V., Gawrisch K., and Keller S.L. Liquid domains in vesicles investigated by nmr and fluorescence microscopy. *Biophysical Journal*, 86:2910–2922, 2004.

[13] http://www.chem.qmul.ac.uk/iupac/lipid/.

[14] Cevc G., editor. *Phospholipids Handbook*. Marcel Dekker, Inc., 1993.

[15] http://www.avantilipids.com.

[16] http://scattering.tripod.com/erich.html.

[17] Israelachvili J. *Intermolecular & Surface Forces*. Academic Press, 2nd edition, 1991.

[18] Nagle J.F. and Tristram-Nagle S. Structure of lipid bilayers. *Biochimica et Biophysica Acta*, 1469:159–195, 2000.

[19] Kirchner S. and Cevc G. On the origin of thermal $L_{\beta'} \rightarrow P_{\beta'}$ pretransition in the lamellar phospholipid membranes. *Europhysics Letters*, 28(1):31–36, 1994.

[20] de Vries A.H., Yefimov S., Mark A.E., and Marrink S.J. Molecular structure of the lecithin ripple phase. *PNAS*, 102(15):5392–5396, 2005.

[21] Koynova R. and Caffrey M. Phases and phase transitions of the phosphatidylcholines. *Biochimica et Biophysica Acta*, 1376:91–145, 1998.

[22] Koynova R., Koumanov A., and Tenchov B. Metastable rippled gel phase in saturated phosphatidylcholines: calorimetric and densitometric characterization. *Biochimica et Biophysica Acta*, 1285:101–108, 1996.

[23] Koynova R. and Caffrey M. Phases and phase transitions of the hydrated phosphatidylethanolamines. *Chemistry and Physics of Lipids*, 69:1–34, 1994.

[24] Tenchov B., Koynova R., and Rapp G. New ordered metastable phases between the gel and subgel phases in hydrated phospholipids. *Biophysical Jounal*, 80:1873–1890, 2001.

[25] Lewis R.N.A.H. and McElhaney R.N. Calorimetric and spectroscopic studies of the thermotropic phase behaviour of lipid bilayer model membranes composed of a homologous series of linear saturated phosphatidylserines. *Biophysical Journal*, 79:2043–2055, 2000.

[26] Hauser H., Paltauf F., and Shipley G.G. Structure and thermotropic behaviour of phosphatidylserine bilayer membranes. *Biochemistry*, 21:1061–1067, 1982.

[27] Luna E.J. and McConnell H.M. Lateral phase separations in binary mixtures of phospholipids having different charges and different crystalline structures. *Biochimica et Biophysica Acta*, 470:303–316, 1977.

[28] Petrache H.I., Tristram-Nagle S., Gawrisch K., Harries D., Parsegian V.A., and Nagle J.F. Structure and fluctuations of charged phosphatidylserine bilayers in the absence of salt. *Biophysical Journal*, 86:1574–1586, 2004.

[29] Cevc G., Watts A., and Marsh D. Titration of the phase transition of phosphatidylserine bilayer membranes. effect of ph, surface electrostatics, ion binding, and head-group hydration. *Biochemistry*, 20:4955–4965, 1981.

[30] Cevc G. How membrane chain melting properties are regulated by the polar surface of the lipid bilayer. *Biochemistry*, 26:6305–6310, 1987.

[31] Blume A. Apparent molar heat capacities of phospholipids in aqueous dispersion. effects of chain length and head group structure. *Biochemistry*, 22:5436–5442, 1983.

[32] Jacobson K. and Papahadjopoulos D. Phase transitions and phase separations in phospholipid membranes induced by changes in temperature, ph, and concentration of bivalent cations. *Biochemistry*, 14(1):152–161, 1975.

[33] Harlos K. and Eibl H. Hexagonal phases in phospholipids with saturated chains: Phosphatidylethanolamines and phosphatidic acids. *Biochemistry*, 20:2888–2892, 1981.

[34] Wilkinson D.A. and McIntosh T.J. A subtransition in a phospholipid with a net charge, dipalmtoylphosphatidylglycerol. *Biochemistry*, 25:295–298, 1986.

[35] Cevc G. Isothermal lipid phase transitions. *Chemistry and Physics of Lipids*, 57:293–307, 1991.

[36] David Boal. *Mechanics of the Cell*. Cambridge University Press, 2002.

[37] http://omega.dawsoncollege.qc.ca/ray/cellmemb/membrane.jpg.

[38] Lommerse P.H.M., Spaink H.P., and Schmidt T. In vivo plasma organization: results of biophysical approaches. *Biochimica et Biophysica Acta*, 1664:119–131, 2004.

[39] Vereb G., Szöllősi J., Matkó J., Nagy P., Farkas T., Vigh L., Mátyus L., Waldmann T.A., and Damjanovich S. Dynamic, yet structured: The cell membrane three decades after the singer-nicolson model. *PNAS*, 100(14):8053–8058, 2003.

[40] Hao M. and Maxfield F.R. Analyzing microdomains in biological membranes using fluorescence techniques. *Journal of Fluorescence*, 11(4):287–295, 2001.

[41] Rietveld A. and Simons K. The differential miscibility of lipids as the basis for the formation of functional membrane rafts. *Biochimica et Biophysica Acta*, 1376:467–479, 1998.

[42] Kasahara K. and Sanai Y. Possible roles of glycosphingolipids in lipid rafts. *Biophysical Chemistry*, 82:121–127, 1999.

[43] Shin J.-S. and Abraham S.N. Caveolae - not just craters in the cellular landscape. *Science*, 293:1447–1448, 2001.

[44] Edidin M. Lipids on the frontier: a century of cell-membrane bilayers. *Nature Reviews Molecular Cell Biology*, 4(5):414–418, 2003.

[45] Edidin M. Lipid microdomains in cell surface membranes. *Current Opinion in Structural Biology*, 7:528–532, 1997.

[46] Gouaux E. and White S.H. Membranes: Lipids lost, lipids regained. *Current Opinion in Structural Biology*, 11:393–396, 2001.

[47] Simons K and Ikonen E. Functional rafts in cell membranes. *Nature*, 387:569–572, 1997.

[48] Kurzchalia T.V. and Parton R.G. Membrane microdomains and caveolae. *Current Opinion in Cell Biology*, 11:424–431, 1999.

[49] Edidin M. The state of lipid rafts: From model membranes to cells. *Annual Review of Biophysics and Biomolecular Structure*, 32:257–283, 2003.

[50] Kusumi A., Sako A., and Yamamoto M. Confined lateral diffusion of membrane receptors as studied by single particle tracking (nanovid microscopy). effects of calcium-induced differentiation in cultured epithelial cells. *Biophysical Journal*, 65:2021–2040, 1993.

[51] Kusumi A. and Sako Y. Cell surface organization by the membrane skeleton. *Current Opinion in Cell Biology*, 8:566–574, 1996.

[52] Fujiwara T., Ritchie K., Murakoshi H., Jacobson K., and Kusumi A. Phospholipids undergo hop diffusion in compartmentalized cell membrane. *Journal of Cell Biology*, 157:1071–1081, 2002.

[53] This work was presented by P. D. Olmsted in a seminar at the Isaac Newton Institute for Mathematical Sciences, Cambridge in May 2004. As far as I know this work has not yet been published.

[54] de Almeida R.F.M., Fedorov A., and Prieto M. Sphingomyelin/phosphatidylcholine/cholesterol phase diagram: Boundaries and composition of lipid rafts. *Biophysical Journal*, 85:2406–2416, 2003.

[55] McConnell H.M. and Vrljic M. Liquid-liquid immiscibility in membranes. *Annual Review of Biophysics and Biomolecular Structure*, 32:469–492, 2003.

[56] Dietrich C., Yang B., Fujiwara T., Kusumi A., and Jocobson K. Relationship of lipid rafts to transient confinement zones detected by single particle tracking. *Biophysical Journal*, 82:274–284, 2002.

[57] Pralle A., Keller P., Florin E.L., Simons K., and Hörber J.K. Sphingolipid-cholesterol rafts diffuse as small entities in the plasma membrane of mammalian cells. *Journal of Cell Biology*, 148:997–1008, 2000.

[58] Sharma P., Varma R., Sarasij R.C., Ira K.G., Krishnamoorthy G., Rao M., and Mayor S. Nanoscale organization of multiple gpi-anchored proteins in cell plasma membranes. *Cell*, 116:577–589, 2004.

[59] Schütz G.J., Kada G., Pastushenko V.P., and Schindler H. Properties of lipid microdomains in a muscle cell membrane visualized by single molecule microscopy. *EMBO Journal*, 19:892–901, 2000.

[60] Taniguchi Y., Stanley H.E., and Ludwig H., editors. *Biological Systems under Extreme Conditions. Structure and Function.* Springer Verlag, 2002.

[61] Bouwstra J.A., Thewalt J., Gooris G.S., and Kitson N. A model membrane approach to the epidermal permeability barrier: An x-ray diffraction study. *Biochemistry*, 36:7717–7725, 1997.

[62] Stoffel W. and Bosio A. Myelin glycolipids and their functions. *Current Opinion in Neurobiology*, 7:654–661, 1997.

[63] Wolf D.E. Microheterogeneity in biological membranes. *Current Topics in Membranes*, 40:143–165, 1994.

[64] Wolf D.E. Lipid domains in sperm plasma membranes. *Molecular Membrane Biology*, 12:101–104, 1995.

[65] http://www.lipidat.chemistry.ohio-state.edu.

[66] Allen T.M. and Cullis P.R. Drug delivery systems: Entering the mainstream. *Science*, 303(5665):1818–1822, 2004.

[67] Alper J. Drug delivery - breaching the membrane. *Science*, 2002.

[68] Luisi P.L. and Walde P., editors. *Giant Vesicles*, volume 6 of *Perspectives in Supramolecular Chemistry*. John Wiley & Sons, Ltd, 2000.

[69] Paul Davies. *The Fifth Miracle*. The Penguin Press, 1998.

[70] Dworkin J.P., Deamer D.W., Sandford S.A., and Allamandola L.J. Self-assembling amphiphilic molecules: Synthesis in simulated interstellar/precometary ices. *PNAS*, 98(3):815–819, 2001.

[71] Harden J.L. and MacKintosh F.C. Shape transformations of domains in mixed-fluid films and bilayer-membranes. *Europhysics Letters*, 28(7):495–500, 1994.

[72] Raudino A. Lateral inhomogeneous lipid membranes: Theoretical aspects. *Advances in Colloid and Interface Science*, 57:229–285, 1995.

[73] Taniguchi T. Shape deformation and phase separation dynamics of two-component vesicles. *Physical Review Letters*, 76(23):4444–4447, 1996.

[74] Sunil Kumar P.B. and Rao M. Shape instabilities in the dynamics of a two-component fluid membrane. *Physical Review Letters*, 80(11):2489–2492, 1998.

[75] Góźdź W.T. and Gompper G. Shape transformations of two-component membranes under weak tension. *Europhysics Letters*, 55(4):587–593, 2001.

[76] Lipowsky R. and Dimova R. Domains in membranes and vesicles. *Journal of Physics: Condensed Matter*, 15:S31–S45, 2003.

[77] Laradji M. and Sunil Kumar P.B. Dynamics of domain growth in self-assembled fluid vesicles. *Physical Review Letters*, 93(19):198105, 2004.

[78] Schneider S. and Gompper G. Shapes of crystalline domains on spherical fluid vesicles. *Europhysics Letters*, 70(1):136–142, 2005.

[79] Schneider M.B., Jenkins J.T., and Webb W.W. Thermal fluctuations of large cylindrical phospholipid vesicles. *Biophysical Journal*, 45:891–899, 1984.

[80] Méléard P., Gerbeaud C., Pott T., Fernandez-Puente L., Bivas I., Mitov M.D., Dufourcq J., and Bothorel P. Bending elasticities of model membranes: influences of temperature and sterol content. *Biophysical Journal*, 72:2616–2629, 1997.

[81] Evans E. and Rawicz W. Entropy-driven tension and bending elasticity in condensed-fluid membranes. *Physical Review Letters*, 64(17):2094–2097, 1990.

[82] Rawicz W., Olbrich K.C., McIntosh T., Needham D., and Evans E. Effect of chain length and unsaturation on elasticity of lipid bilayers. *Biophysical Journal*, 79:328–339, 2000.

[83] Helfrich W. The size of bilayer vesicles generated by sonication. *Physics Letters*, 50A(2):115–116, 1974.

[84] Fromherz P. Lipid-vesicle structure: size control by edge-active agents. *Chemical Physics Letters*, 94(3):259–266, 1983.

[85] Safran S.A. *Statistical Thermodynamics of Surfaces, Interfaces, and Membranes*. Addison-Wesley, 1990.

[86] Leckband D. and Israelachvili J. Intermolecular forces in biology. *Quarterly Reviews of Biophysics*, 34(2):105–267, 2001.

[87] Helfrich W. Spontaneous and induced adhesion of fluid membranes. In Riste T. and Sherrington D., editors, *Phase Transitions in Soft Condensed Matter*. Plenum Press, New York, 1989.

[88] Rand R.P. and Parsegian V.A. Hydration forces between phospholipid bilayers. *Biochimica et Biophysica Acta*, 988:351–376, 1989.

[89] Planck M. *Treatise on Thermodynamics*. Dover Publications, Inc., 3rd edition, 1990.

[90] Lee A.G. Lipid phase transitions and phase diagrams ii. mixtures involving lipids. *Biochimica et Biophysica Acta*, 472:285–344, 1977.

[91] Kemp R.B., editor. *From Macromolecules to Man*, volume 4 of *Handbook of Thermal Analysis and Calorimetry*. Elsevier, 1999.

[92] Needham D. and Evans E. Structure and mechanical properties of giant lipid (dmpc) vesicles bilayers from 20 °c below to 10 °c above the liquid crystal-crystalline phase transition at 24 °c. *Biochemistry*, 27:8261–8269, 1988.

[93] Yang L. and Glaser M. Formation of membrane domains during the activation of protein kinase c. *Biochemistry*, 35:13966–13974, 1996.

[94] Moscho A., Orwar O., Chiu D.T., Modi B.P., and Zare R.N. Rapid preparation of giant unilamellar vesicles. *PNAS*, 93:11443–11447, 1996.

[95] Mathivet L., Cribier S., and Devaux P. Shape changes and physical properties of giant phospholipid vesicles prepared in the presence of an ac electric field. *Biophysical Journal*, 70:1112–1121, 1996.

[96] Oku N., Scheerer J.F., and MacDonald R.C. Preparation of giant liposomes. *Biochimica et Biophysica Acta*, 692:384–388, 1982.

[97] Oku N. and MacDonald R.C. Differential effects of alkali metal chlorides on formation of giant liposomes by freezing and thawing and by dialysis. *Biochemistry*, 22:855–863, 1983.

[98] Hargreaves W.R. and Deamer D.W. Liposomes from ionic, single-chain amphiphiles. *Biochemistry*, 17:3759–3763, 1978.

[99] Angelova M. and Dimitrov D.S. A mechanism of liposome electroformation. *Progress in Colloid & Polymer Science*, 76:59–67, 1988.

[100] Angelova M.I. and Dimitrov D.S. Liposome electroformation. *Faraday Discuss. Chem. Soc.*, 81:303–311, 1986.

[101] Dimitrov D.S. and Angelova M.I. Lipid swelling and liposome formation on solid surfaces in external electric fields. *Progress in Colloid & Polymer Science*, 73:48–56, 1987.

[102] Lee C.-H., Lin W.-C., and Wang J. All-optical measurements of the bending rigidity of lipid-vesicle membranes across structural phase transitions. *Physical Review E*, 64:020901–1–020901–4, 2001.

[103] Dimitrov D.S. and Angelova M.I. Lipid swelling and liposome formation mediated by electric fields. *Bioelectrochemistry and Bioenergetics*, 19:323–336, 1988.

[104] Isambert H. Understanding the electroporation of cells and artificial bilayer membranes. *Physical Review Letters*, 80(15):3404–3407, 1998.

[105] Neu J.C. and Krassowska W. Asymptotic model of electroporation. *Physical Review E*, 59(3):3471–3482, 1999.

[106] Stoicheva N.G. and Hui S.W. Electrofusion of cell-sized liposomes. *Biochimica et Biophysica Acta*, 1195:31–38, 1994.

[107] Joseph R. Lakowicz. *Principles of Fluorescence Spectroscopy*. Kluwer Academic/Plenum Publishers, New York, 2nd edition, 1999.

[108] Herschel. Sir J. F. W. On a case of superficial colour presented by a homogeneous liquid internally colourless. *Phil. Trans. R. Soc. London*, 135:143–145, 1845.

[109] Stokes G.G. On the change of refrangibility of light. *Phil. Trans. R. Soc. London*, 142:463–562, 1852.

[110] Kasha M. Characterization of electronic transitions in complex molecules. *Disc. Faraday Soc.*, 9:14–19, 1950.

[111] Molecular Expressions. http://micro.magnet.fsu.edu/primer/java/fluorescence/photobleaching/.

[112] http://www.probes.com.

[113] Nichols J.W. and Pagano R.E. Use of resonance energy transfer to study the kinetics of amphiphile transfer between vesicles. *Biochem.*, 21:1720–1726, 1982.

[114] Parasassi T., De Stasio G., Ravagnan G., Rusch R.M., and Gratton E. Quantitation of lipid phases in phospholipid vesicles by the generalized polarization of laurdan fluorescence. *Biophysical Journal*, 60:179–189, 1991.

[115] Corle T.R. and Kino G.S. *Confocal Scanning Optical Microscopy and Related Imaging Systems*. Academic Press, 1996.

[116] Hecht E. *Optics*. Addison-Wesley, 3^{rd} edition, 1998.

[117] Sheppard C.J.R. and Shotton D.M. *Confocal Laser Scanning Microscopy*. BIOS Scientific Publishers, 1997.

[118] Gu M. *Principles of Three-Dimensional Imaging in Confocal Microscopes*. World Scientific, 1996.

[119] http://microscopy.bio-rad.com/reference/technical.htm.

[120] http://www.chroma.com.

[121] Riley K.F., Hobson M.P., and Bence S.J. *Mathematical Methods for Physics and Engineering*. Cambridge University Press, 1997.

[122] Press W.H., Teukolsky S.A., Vetterling W.T., and Flannery B.P. *Numerical Recipes in C: the art of scientific computing*. Cambridge University Press, 2nd edition, 1999.

[123] Shimshick E.J. and McConnell H.M. Lateral phase separation in phospholipid membranes. *Biochemistry*, 12(12):2351–2360, 1973.

[124] Blume A. and Ackermann T. A calorimetric study of the lipid phase transitions in aqueous dispersions of phosphorylcholine-phosphorylethanolamine mixtures. *FEBS Letters*, 43(1):71–74, 1974.

[125] Sklar L.A., Hudson B.S., and Simon R.D. Conjugated polyene fatty acids as fluorescent probes: Synthetic phospholipid membrane studies. *Biochemistry*, 16(5):819–828, 1977.

[126] Mendelsohn R. and Koch C.C. Deuterated phospholipids as raman spectroscopic probes of membrane structure. phase diagrams for the dipalmitoylphosphatidylcholine (and its d_{62} derivative)-dipalmitoylphosphatidylethanolamine system. *Biochimica et Biophysica Acta*, 598:260–271, 1980.

[127] Arnold K., Lösche A., and Gawrisch K. ^{31}p-nmr investigations of phase separation in phosphatidylcholine/phosphatidylethanolamine mixtures. *Biochimica et Biophysica Acta*, 645:143–148, 1981.

[128] Petrov A.G., Gawrisch K., Brezesinski G., Klose G., and Möps A. Optical detection of phase transitions in simple and mixed lipid-water phases. *Biochimica et Biophysica Acta*, 690:1–7, 1982.

[129] Blume A., Wittebort R.J., Das Gupta S.K., and Griffin R.G. Phase equilibria, molecular conformation and dynamics in phosphatidylcholine/phosphatidylethanolamine bilayers. *Biochemistry*, 21:6243–6253, 1982.

[130] Tenchov B.G., Brankov J.G., and Koynova R.D. Lateral lipid-lipid interactions in dppc/dppe bilayers. *Studia Biophysica*, 103(2):89–96, 1984.

[131] Boyanov A.I., Koynova R.D., and Tenchov B.G. Effect of lipid admixtures on the l-dipalmitoylphosphatidylcholine subtransition. *Chemistry and Physics of Lipids*, 39:155–163, 1986.

[132] Silvius J.R. Solid- and liquid-phase equilibria in phosphatidylcholine/phosphatidylethanolamine mixtures. a calorimetric study. *Biochimica et Biophysica Acta*, 857:217–228, 1986.

[133] Caffrey M. and Hing F.S. A temperature dradient method for lipid phase diagram construction using time-resolved x-ray diffraction. *Biophysical Journal*, 51:37–46, 1987.

[134] Caffrey M. and Bywater M.T. Two new and rapid approaches for studying the phase properties of cosmetic lipids and oils. *Journal of the Society of Cosmetic Chemists*, 39:159–167, 1988.

[135] Ipsen J.H. and Mouritsen O.G. Modelling the phase equilibria in two-component membranes of phospholipids with different acyl-chain lengths. *Biochimica et Biophysica Acta*, 944:121–134, 1988.

[136] Dörfler H.-D., Miethe P., and Meyer H.W. Phase diagrams of pseudo-binary phospholipid systems iv. preliminary results about the effects of licl and $cacl_2$ on the phase transitions of amphoteric phospholipids in aqueous dispersions. *Chemistry and Physics of Lipids*, 54:181–192, 1990.

[137] Inoue T. and Nibu Y. Phase behavior of hydrated lipid bilayer composed of binary mixture of phospholipids with different head groups. *Chemistry and Physics of Lipids*, 100:139–150, 1999.

[138] Dörfler H.-D. Relationships between miscibility behavior and chemical structure of phospholipids in pseudobinary systems. *Colloid Polymer Science*, 278:130–136, 2000.

[139] http://www.lipidat.chemistry.ohio-state.edu/lipidag/homelipidag.asp.

[140] Koynova R. and Caffrey M. An index of lipid phase diagrams. *Chemistry and Physics of Lipids*, 115:107–219, 2002.

[141] Vaz W.L.C., Derzko Z.I., and Jacobson K.A. Photobleaching measurements of the lateral diffusion of lipids and proteins in artificial phospholipid bilayer membranes. *Cell Surface Reviews*, 8:83–136, 1982.

[142] Vaz. W.L.C., Goodsaid-Zalduondo F., and Jacobson K. Lateral diffusion of lipids and proteins in bilayer membranes. *FEBS Letters*, 1740(2):199–207, 1984.

[143] Wade C.G. Lateral diffusion of lipids. *Structure and Properties of Cell Membranes*, 1:51–76, 1985.

[144] Jovin T.M. and Vaz W.L.C. Rotational and translational diffusion in membranes measured by fluorescnece and phosphorescence methods. *Methods in Enzymology*, 172:471–513, 1989.

[145] Tocanne J.-F., Dupou-Cézanne, and Lopez André. Lateral diffusion of lipids in model and natural membranes. *Progress in Lipid Research*, 33(3):203–237, 1994.

[146] Almeida P.F.F. and Vaz W.L.C. Lateral diffusion in membranes. In Lipowsky R. and Sackmann E., editors, *Structure and Dynamics of Membranes: From Cells to Vesicles*, pages 305–357. Elsevier, 1995.

[147] Saxton M.J. and Jacobson K. Single-particle tracking: Application to membrane dynamics. *Annual Review of Biophysics and Biomolecular Structure*, 26:373–399, 1997.

[148] Saxton M.J. Lateral diffusion of lipids and proteins. *Current Topics in Membranes*, 48:229–282, 1999.

[149] Derzko Z. and Jacobson K. Comparative lateral diffusion of fluorescent lipid analogues in phospholipid multibilayers. *Biochemistry*, 19:6050–6057, 1980.

[150] Schneider M.B., Chan W.K., and Webb W.W. Fast diffusion along defects and corrugations in phospholipid $P_{\beta'}$ liquid crystals. *Biophysical Journal*, 43:157–165, 1983.

[151] Timbs M.M. and Thompson N.L. Slow rotational mobilities of antibodies and lipids associated with substrate-supported phospholipid monolayers as measured by polarized fluorescence photobleaching recovery. *Biophysical Journal*, 58:413–428, 1990.

[152] Almeida P.F.F., Vaz W.L.C., and Thompson T.E. Lateral diffusion and percolation in two-phase, two-component lipid bilayers. topology of the solid-phase domains in-plane and across the lipid bilayer. *Biochemistry*, 31:7198–7210, 1992.

[153] Timbs M.M. and Thompson N.L. Measurement of restricted rotational diffusion of fluoresent lipids in supported planar phospholipid monolayers using angle-dependent polarized fluorescence photobleaching recovery. *Biopolymers*, 33:45–57, 1993.

[154] Böckmann R.A., Hac A., Heimburgh T., and Grubmüller H. Effect of sodium chloride on a lipid bilayer. *Biophysical Journal*, 85:1647–1655, 2003.

[155] Hac A.E., Seeger H.M., Fidorra M., and Heimburg T. Diffusion in two-component lipid membranes - a fluorescence correlation spectroscopy and monte carlo simulation study. *Biophysical Journal*, 88:317–333, 2005.

[156] Sonneleitner A., Schütz G.J., and Schmidt Th. Free brownian motion of individual lipid molecules in biomembranes. *Biophysical Journal*, 77:2638–2642, 1999.

[157] Soong R. and MacDonald P.M. Lateral diffusion of peg-lipid in magnetically aligned bicelles measured using stimulated echo pulsed field gradient ^{1}h nmr. *Biophysical Journal*, 88:255–268, 2005.

[158] Fisher R.W. and James T.L. Lateral diffusion of the phospholipid molecule in dipalmitoylphosphatidylcholine bilayers. an investigation using nuclear spin-lattice relaxation in the rotating frame. *Biochemistry*, 17(7):1177–1183, 1978.

[159] Arnold A., Paris M., and Auger M. Anomalous diffusion in a gel-fluid lipid environment: A combined solid-state nmr and obstructed random-walk perspective. *Biophysical Journal*, 87:2456–2469, 2004.

[160] König S., Bayerl T., Coddens G., Richter D., and Sackmann E. Hydration dependence of chain dynamics and local diffusion in 1-*alpha*-dipalmitoylphosphatidylcholine multilayers studied by incoherent quasi-elastic neutron scattering. *Biophysical Journal*, 68:1871–1880, 1995.

[161] Vaz W.L.C. and Almeida P.F. Microscopic versus macroscopic diffusion in one-component fluid phase lipid bilayer membranes. *Biophysical Journal*, 60:1553–1554, 1991.

[162] Harms G.S., Sonnleitner M., Schütz G.J., Gruber H.J., and Schmidt Th. Single-molecule anisotropy imaging. *Biophysical Journal*, 77:2864–2870, 1999.

[163] Boggs J.M. Lipid intermolecular hydrogen bonding: influence on structural organisation and membrane function. *Biochimica et Biophysica Acta*, 906:353–404, 1987.

[164] Tanaka H. Viscoelastic phase separation. *Journal of Physics: Condensed Matter*, 12:R207–R264, 2000.

[165] Knobbler C. Seeing phenomena in flatland: Studies of monolayers by fluorescence microscopy. *Science*, 249(4971):870–874, 1990.

[166] Krügger P. and Lösche M. Molecular chirality and domain shapes in lipid monolayers on aqueous surfaces. *Physical Review E*, 62(5):7031–7043, 2000.

[167] McConlogue C.W., Malamud D., and Vanderlick T.K. Interaction of dppc monolayers with soluble surfactants: electrostatic effects of membrane perturbants. *Biochimica et Biophysica Acta*, 1372:124–134, 1998.

[168] Klingler J.F. and McConnell H.M. Brownian motion and fluid mechanics of lipid monolayer domains. *Journal of Physical Chemistry*, 97(22):6096–6100, 1993.

[169] Möhwald H. Phospholipid and phospholipid-protein monolayers at the air/water interface. *Annual Review of Physical Chemistry*, 41:441–476, 1990.

[170] McConnell H.M. Structures and transitions in lipid monolayers at the air-water interface. *Annual Review of Physical Chemistry*, 42:171–195, 1991.

[171] Wohlert J. and Edholm O. The range of shielding of dipole-dipole interactions in phospholipid bilayers. *Biophysical Journal*, 87:2433–2445, 2004.

[172] Sedgwick H., Egelhaaf S.U., and Poon W.C.K. Clusters and gels in systems of sticky particles. *Journal of Physics: Condensed Matter*, 16(42):S4913–S4922, 2004.

[173] Stradner A., Sedgwick H., Cardinaux F., Poon W.C.K., Egelhaaf S.U., and Schurtenberger P. Equilibrium cluster formation in concentrated protein solutions and colloids. *Nature*, 432:492–495, 2004.

[174] Sedgwick H., Kroy K., Salonen A., Robertson M.B., Egelhaaf S.U., and Poon W.C.K. Non-equilibrium behaviour of sticky colloidal particles: beads, clusters and gels. *European Physical Journal E*, 16(1):77–80, 2005.

[175] Parasassi T., Gratton E., Yu W.M., Wilson P., and Levi M. Two-photon fluorescence microscopy of laurdan gerneralized polarization domains in model and natural membranes. *Biophysical Journal*, 72:2413–2429, 1997.

[176] Miller A., Knoll W., and Möhwald H. Fractal growth of crystalline phospholipid domains in monomolecular layers. *Physical Review Letters*, 56(24):2633–2636, 1986.

[177] Miller A. and Möhwald H. Diffusion limited growth of crystalline domains in phospholipid monolayers. *Journal of Chemical Physics*, 86(7):4258–4265, 1987.

[178] Gallavotti G. The phase separation line in the two-dimensional ising model. *Communications in Mathematical Physics*, 27:103–136, 1972.

[179] Landau L.D. and Lifshitz E.M. *Statistical Physics*, volume 5 of *Course of Theoretical Physics*. Butterworth Heinemann, 3^{rd} edition, 1997.

[180] Berge B., Faucheux L., Schwab K., and Libchaber A. Faceted crystal growth in two dimensions. *Nature*, 350:322–324, 1991.

[181] Leidy C., Kaasgaard T., Crowe J.H., Mouritsen O.H., and Jorgensen K. Ripples and the formation of anisotropic lipid domains: imaging two-component double bilayers by atomic force microscopy. *Biophysical Journal*, 83:2625–2633, 2002.

[182] Kaasgaard T., Leidy C., Crowe J.H., Mouritsen O.H., and Jorgensen K. Temperature-controlled structure and kinetics of ripple phases in one- and two-component supported lipid bilayers. *Biophysical Journal*, 85:350–360, 2003.

[183] Blume A., Rice D.M., Wittebort R.J., and Griffin R.G. Molecular dynamics and conformation in the gel and liquid-crystalline phases of phosphatidylethanolamine bilayers. *Biochemistry*, 21:6220–6230, 1982.

[184] Nelson D.R. and Halperin B.I. Solid and fluid phases in smectic layers with tilted molecules. *Physical Review B*, 21(11):5312–5329, 1980.

[185] Peterson I.R., Kenn R.M., Goudot A., Fontaine P., Rondelez F., Bouwmann W.G., and Kjaer K. Chiral and herringbone symmetry breaking in water-surface monolayers. *Physical Review E*, 53:667–673, 1996.

[186] John F. Nagle. Private Communication.

[187] http://legacywww.coventry.ac.uk/cmbs/hexatic.htm.

[188] Sun W.-J., Suter R.M., Knewtson M.A., Worthington C.R., Tristram-Nagle S., Zhang R., and Nagle J.F. Order and disorder in fully hydrated unoriented bilayers of gel phase dipalmitoylphosphatidylcholine. *Physical Review E*, 49(5):4665–4676, 1994.

[189] Lee C.-W., Decca R.S., Wassall S.R., and Breen J.J. Direct imaging of domains in the $L_{\beta'}$ state of 1,2-dipalmitoylphosphatidylcholine bilayers. *Physical Review E*, 67:061914–1 – 061914–5, 2003.

[190] King Jr. H.E., Sirota E.B., Shao H., and Singer D.M. A synchrotron x-ray scattering study of the rotator phases of the normal alkanes. *Journal of Physics D: Applied Physics*, 26(8B):B133–B136, 1993.

[191] Sirota E.B., King Jr. H.E., Singer D.M., and Shao H.H. Rotator phases of the normal alkanes: An x-ray scattering study. *Journal of Chemical Physics*, 98(7):5809–5824, 1993.

[192] Sirota E.B., Singer D.M., and King Jr. H.E. Structural effects of high pressure gas on the rotator phases of normal alkanes. *Journal of Chemical Physics*, 100(2):1542–1551, 1994.

[193] Vernita D. Gordon. Private Communication.

[194] Kim N.H., Roh S.B., and Park W.W. A study of phase transition of lipids and lipid mixtures by differential scanning calorimetry. *Bulletin of the Korean Chemical Society*, 11(6):508–511, 1990.

[195] Garidel P., Johann C., and Blume A. Nonideal mixing and phase separation in phosphatidylcholine-phosphatic acid mixtures as a function of acyl chain length and ph. *Biophysical Journal*, 72:2196–2210, 1997.

[196] Garidel P. and Blume A. Miscibility of phosphatidylethanolamine-phospatidylglycerol mixtures as a function of ph and acyl chain length. *European Biophysics Journal*, 28:629–638, 2000.

[197] Riske K.A., Amaral L.Q., Döbereiner H.-G., and Lamy M.T. Mesoscopic structure in the chain-melting regime of anionic phospholipid vesicles: Dmpg. *Biophysical Journal*, 86:3722–3733, 2004.

[198] Seifert U. and Lipowsky R. Adhesion of vesicles. *Physical Review A*, 42(8):4768–4771, 1990.

[199] Bailey S.M., Chiruvolu S., Israelachvili J.N., and Zasadzinski J.A.N. Measurements of forces in vesicle adhesion using freeze-fracture electron microscopy. *Langmuir*, 6:1326–1329, 1990.

[200] Puech P.-H. and Brochard-Wyart F. Membrane tensiometer for heavy giant vesicles. *European Physical Journal E*, 15:127–132, 2004.

[201] Shoemaker S.D. and Vanderlick T.K. Material studies of lipid vesicles in the L_α and L_α-gel coexistence regimes. *Biophysical Journal*, 84:998–1009, 2003.

[202] Shoemaker S.D. and Vanderlick T.K. Intramembrane electrostatic interactions destabilize lipid vesicles. *Biophysical Journal*, 83:2007–2014, 2002.

[203] Sandre O., Moreaux L., and Brochard-Wyart F. Dynamics of transient pores in stretched vesicles. *Proceedings of the National Academy of Sciences USA*, 96:10591–10596, 1999.

[204] Karatekin E., Sandre O., Guitouni H., Borghi N., Puech P.-H., and Brochard-Wyart F. Cascades of transient pores in giant vesicles: Line tension and transport. *Biophysical Journal*, 84:1734–1749, 2003.

[205] Puech P.-H., Borghi N., Karatekin E., and Brochard-Wyart F. Line thermodynamics: Adsorption at a membrane edge. *Physical Review Letters*, 90(12):128304(4), 2003.

[206] Ramos C. and Teissié J. Electrofusion: A biophysical modification of cell membrane and a mechanism in exocytosis. *Biochimie*, 82:511–518, 2000.

[207] Tekle E., Astumian R.D., Friauf W.A., and Chock P.B. Asymmetric pore distribution and loss of membrane lipid in electroporated dopc vesicles. *Biophysical Journal*, 81:960–968, 2001.

[208] Wang T.-Y. and Silvius J.R. Cholesterol does not induce segregation of liquid-ordered domains in bilayers modeling the inner leaflet of the plasma membrane. *Biophysical Journal*, 81(5):2762–2773, 2001.

List of Figures

List of Tables